2017

A study on the variability of pavement foundation properties

Jia Li
Iowa State University

A study on the variability of pavement foundation properties

by

Jia Li

A dissertation submitted to the graduate faculty

in partial fulfillment of the requirements for the degree of

DOCTOR OF PHILOSOPHY

Major: Civil Engineering (Geotechnical Engineering)

Program of Study Committee:
David J. White, Co-major Professor
Vernon R Schaefer, Co-major Professor
Pavana K.R. Vennapusa, Co-major Professor
W. Robert Stephenson
Hyungseok David Jeong

The student author, whose presentation of the scholarship herein was approved by the program of study committee, is solely responsible f or the content of this dissertation. The Graduate College will ensure this dissertation is globally accessible and will not permit alterations after a degree is conferred.

Iowa State University
Ames, Iowa
2017

TABLE OF CONTENTS

LIST OF TABLES

LIST OF FIGURES

ACKNOWLEDGEMENTS

I would like to express my deepest gratitude to my co-major professors, Drs. David White, Vernon Schaefer, and Pavana Vennapusa for their inspirations, guidance, and patience. Without their constant supports, this work would not have been possible.

I would like to thank my committee members Drs. W. Robert Stephenson and Hyungseok David Jeong for providing constructive suggestions to my research and providing kind help on finishing my degree. I would also like to thank Dr. Christianna White for helping me to improve my technical writing and presentation skills.

The research projects were sponsored by the Federal Highway Administration under agreement No. DTFH61-06-H-00011 and the Iowa Department of Transportation under Transportation Pooled Fund Program TPF-5(183).

I also want to express my deepest love to my parents for their supports and encouragements throughout my study and life.

ABSTRACT

Variations in resilient modulus (M_r) values of unbound materials as determined in accordance with AASHTO T307 are studied. Three different granular materials and an elastic polyurethane (control) sample were tested using commercially available laboratory test equipment. A field test bed was also constructed to measure vehicle (Class 3) induced loading conditions at the bottom of an unbound granular layer underlying new hot-mix asphalt pavement to determine stress-pulse duration as a function of vehicle speed. Various interpretation issues were identified within the framework of the testing methods and equipment including: (1) insufficient laboratory sensor sampling rate (per standard); (2) the laboratory specified 0.1 second load-pulse duration and haversine shape are not matching the field stress-pulse duration and shape; (3) the need for careful tuning of the load system gain settings; (4) the number of LVDTs used in the vertical strain calculation; (5) limiting quality control and quality assurance to deformation ratio values in the preconditioning sequence; (6) limiting the load step calculations to the last 5 of 100 load cycles; and (7) the k_3 coefficient used in the MEPDG suggested generalized universal model function generally not being statistically significant.

Detailed geostatistical analysis procedures are presented in this study to provide a guide for pavement engineers to study spatial variability of pavement foundation properties with consideration of choosing the best fit semivariogram model and characterization of anisotropy. Measurements from two densely gridded pavement reconstruction sites are presented in studying the geostatistical modelling parameters that characterize spatial variability of stiffness and compaction properties. Preliminary study on anisotropy in spatial variability of pavement foundation properties is performed, but different major and minor anisotropic directions were identified in the two small square study sections. Comparisons of three theoretical

semivariogram models (i.e., spherical, exponential, and Matérn with k=1) in studying different pavement foundation properties shows that there is no single best fit model. The isotropic semivariogram model works as well as the anisotropic semivariogram model in estimating the data at unsampled locations across the studied small square area. The range that indicates the spatial correlation length is less than 5 m in all studied properties of both test sections, without considering anisotropy behavior. When anisotropy behavior is considered, longer spatial correlation length, up to about 11 m, can be expected in the major direction.

The second objective of this study is to investigate variability of pavement foundation properties (e.g., $E_{LWD\text{-}Z3}$, γ_d, and w) that are determined from four major in-situ tests (i.e., FWD, LWD, NG, and DCP) over 18 test sections of 6 project sites. Change in variation of in-situ measured properties has been studied in relationship to the number of compaction passes. Univariate statistics of pavement foundation properties is documented for providing references to pavement engineers and researchers to know the range of variability that in-situ measured properties can have. In addition to univariate statistics, spatial analysis was performed on selected sites that contain relatively large data sets for spatial analysis. The difference in spatial variation can be expected in longitudinal and transverse direction. The correlation length of about 2 m to 3 m in the minor or less uniform direction was quantified for spatial variability of dense gridded data on the base layer. The spatial variability of in-situ measured properties along the longitudinal direction could be expected to be 15 m to 23 m in the CTB layer. This study on spatial variability shows that the correlation length can be different in different pavement foundation layers and materials.

CHAPTER 1. INTRODUCTION

Stiffness is an important input parameter in pavement design and laboratory determined resilient modulus values can be used as an input for the stiffness present in the whole pavement foundation layer. Uniform support is desired for pavement structures to have longer service life, but the variability of in-situ measurements on pavement foundations reveals nonuniform support to the pavement surface. This chapter discusses the importance of studying variability of pavement foundation properties, presents the research goal and objectives of this study, and details the organization of the dissertation.

1.1. Problem Statement

Pavement foundation structures are constructed to provide uniform support for upper pavement layers and traffic load. However, material properties of existing pavement foundation structures are generally non-homogeneous. Non-uniform subbase/subgrade stiffness will induce fatigue cracking and other types of pavement distresses and shorten the pavement service life (Titi et al. 2014; White et al. 2004). Dilip abd Babu (2014) concluded that critical strains will be underestimated without considering spatial variability of resilient moduli. Roesler et al. (2016) showed peak concrete slab tensile stresses increases up to 39% in nonuniform compared to uniform support conditions. However, pavement design assumes that uniform layers are achieved and uses a single modulus of subgrade reaction to represent the whole layer.

Resilient modulus (M_r) is a pavement foundation input value used in the mechanistic-empirical pavement design method and is often measured using laboratory equipment in accordance with AASHTO T307 (2007). Pavement foundation stress conditions are simulated in the laboratory test by applying transient cyclic load pulses for a series of deviator and confining stress conditions. AASHTO T307 (2007) specifies cyclic loading with each cycle having a

haversine-shaped load pulse with a 0.1 s pulse duration (load time) and 0.9 s rest period (dwell time). M_r values are well studied by many researchers, but the testing standard and testing system should be assessed for obtaining accurate resilient modulus. According to Witczak (2004), "inaccurate determination of the resilient modulus of the unbound materials in the pavement structure will contribute to erroneous predictions of overall pavement response and pavement performance."

To achieve a reliable pavement design, variability of engineering properties should be properly quantified. Phoon and Kulhawy (1999) suggested estimating the variability of soil parameters to develop and apply reliability-based design. Otake and Honjo (2013) also suggested evaluating the effects of spatial variability of material properties on pavement structures.

Variability was identified in constructed pavement foundations. Allen and Graves (1994) obtained falling weight deflectometer (FWD) and Road Rater deflection measurements data at 25 foot intervals along a 500 ft long test section and observed a 75% coefficient of variation in subgrade moduli within the section. Yoder (1975) reported a range of standard deviation of layer thickness from 0.6 to 0.72 with 9749 tests on cement treated base, 0.72 to 0.84 with 7046 on aggregate base, and 0.96 to 1.44 with 10758 tests on aggregate subbase. Yoder (1975) reported that a typical range for the standard deviation of percent compaction on embankment/subgrade went from 2.0 to 7.0 percent and on subbase/base went from 2.0 to 3.5 percent. Siddharthan et al. (1992) studied layer moduli that were determined from back calculation of FWD tests perfomed on asphalt concrete pavement and reported the layer moduli vary in a range of 5 to 65 percent for the coefficient of variation.

However, the nonuniformity of pavement foundation (subbase/subgrade) layers has not been well studied. The univariate statistical analysis of pavement foundation properties shows a range

of the property can vary within the studied area, but it does not describe the spatial uniformity. Several previous studies (Facas et al. 2010; Lea and Harvey 2015a; Lea and Harvey 2015b; Vennapusa 2004; Vennapusa et al. 2010; White et al. 2004) performed spatial variability analysis on pavement related properties (i.e., stiffness, layer thickness, intelligent compaction measurement values), and anisotropy in the studied properties was observed that roller-integrated compaction measurements (Facas et al. 2010; Vennapusa et al. 2010) varied with longer correlation length in the longitudinal direction than in the transverse direction.

Geostatistical methods have been well studied in other fields (i.e., mining, geology, soil science) and details in understanding general spatial variation had appeared in many books (Clark and Harper 2002; Cressie 1993; Deutsch and Journel 1998; Goovaerts 1997; Isaaks and Srivastava 1989; Journel and Huijbregts 1978; Olea 2006). Lea and Harvey (2015b) introduced model types with analysis on pavement layer thickness. However, the details in using geostatistical analysis methods on charactering pavement foundation properties with closer spacing (about 0.6 m) was not studied.

Although variation of in-situ properties in pavement construction has been noticed, there is no documentation of pavement foundation properties variability for people to have ideas on how variable the pavement foundation properties could be. Selective sampling by the inspector, often as ordered by the engineer has played an important part in the failure to recognize the magnitude of the actual variations occurring in embankment and base construction.

Pavement foundation properties are studied by investigating the results $E_{LWD\text{-}Z3}$, $\gamma_{d,}$ w, $DCPI_{subbase}$, and $DCPI_{subgrade}$ that are obtained from the light weight deflectometer (LWD) test, nuclear gauge (NG) test, and dynamic cone penetrometer (DCP) test. Following the pavement construction process that the material was spread on the ground and then roller compacted to the

target density, the data on pavement foundation properties may not be statistically independent. Data values that at locations that are closer together tend to be more similar than data values collected at locations that are farther apart. However, how much the pavement foundation properties can vary, univariate and spatially, has not been reported sufficiently. Therefore, in this research, the assessment of testing method in obtaining the design stiffness input, characterization and quantification of variability of in-situ measured pavement foundation properties will be discussed.

1.2. Research Goal and Objectives

The main goals of this research are to provide assessment procedures for verifying the reliability of laboratory determined M_r values that will be used in pavement design and to study variability of in-situ pavement foundation properties after pavement construction. To address these goals, the objectives of the research are to:

- Assess the laboratory testing standard and system for improving the reliability of obtaining M_r values with simulated in-situ conditions,
- Provide the detailed procedures for performing spatial variability analysis on pavement foundation properties using a geostatistical method,
- Document univariate and spatial variability of pavement foundation properties as a reference for pavement engineers.

1.3. Organization of the Dissertation

This dissertation consists of five chapters: a general introduction, three research articles, and conclusions and recommendations for further research.

Following this general introduction, Chapter 2 explains equipment related considerations on differences between the lab and field conditions that can lead to variations in resilient modulus

(M_r) values of unbound materials as determined in accordance with AASHTO T307. Chapter 3 demonstrates detailed geostatistical analysis procedures to provide a guide for pavement engineers to study spatial variability of pavement foundation properties with consideration of choosing the best fitted semivariogram model and characterization of anisotropy. Two densely gridded test sections are studied to characterize the behavior of spatial correlation of pavement foundation properties in both longitudinal and transverse directions within a small study area. Chapter 4 documents the variability of pavement foundation properties by analyzing data collected from 6 project sites and provides a reference for pavement engineers and researchers to know how variable the in-situ measured pavement foundation properties can be. Chapter 5 summarizes the conclusions and outcomes derived from this study, and offers several suggestions and directions for future research.

CHAPTER 2. CONSIDERATIONS FOR LABORATORY RESILIENT MODULUS TESTING OF UNBOUND MATERIALS

A paper submitted to *Geotechnical Testing Journal*

Jia Li, David J. White, and W. Robert Stephenson

2.1. Abstract

This paper explains equipment related considerations on differences between the lab and field conditions that can lead to variations in resilient modulus (M_r) values of unbound materials as determined in accordance with AASHTO T307. Three different granular materials and an elastic polyurethane (control) sample were tested using commercially available laboratory test equipment. A field test bed was also constructed to measure vehicle (Class 3) induced loading conditions at the bottom of an unbound granular layer underlying new hot-mix asphalt pavement to determine stress-pulse duration as a function of vehicle speed. Various interpretation issues were identified within the framework of the testing methods and equipment including: (1) insufficient laboratory sensor sampling rate (per standard); (2) the laboratory specified 0.1 second load-pulse duration and haversine shape are not matching the field stress-pulse duration and shape; (3) the need for careful tuning of the load system gain settings; (4) the number of LVDTs used in the vertical strain calculation; (5) limiting quality control and quality assurance to deformation ratio values in the preconditioning sequence; (6) limiting the load step calculations to the last 5 of 100 load cycles; and (7) the k_3 coefficient used in the MEPDG suggested generalized universal model function generally not being statistically significant. The goal of this paper is to provide equipment users and specification developers with user knowledge concerning laboratory resilient modulus determination.

2.2. Introduction

Resilient modulus (M_r) is a pavement foundation input value used in the state-of-the-art AASHTOWare™ pavement design software based on the mechanistic empirical design principles (2015) and is often measured using laboratory equipment in accordance with AASHTO T307 (2007). Pavement foundation stress conditions are simulated in the laboratory test by applying transient cyclic load pulses for a series of deviator and confining stress conditions. By using a selected portion of the laboratory data, results are then used to develop a nonlinear stress-dependent model of resilient modulus.

AASHTO T307 (2007) specifies cyclic loading with each cycle having a haversine-shaped load pulse with a 0.1 s pulse duration (load time) and 0.9 s rest period (dwell time). The specified minimum sampling rate is 200 Hz. Following an initial 500 to 1000 cycles conditioning phase, 15 different load sequences are specified with 100 load cycles each. There are two different load sequence schedules followed depending on whether the material is an unbound granular material (high stress sequence) or a subgrade soil (low stress sequence). The average M_r of the last five in the 100 cycles is calculated to represent M_r of the specimen under the specified stress state. Further, AASHTO T307 (2007) requires two externally mounted spring-loaded linear variable differential transducers (LVDTs) to measure vertical axial deformation for determining resilient strain.

This paper discusses practical considerations that affect interpretation of results from a commercially available laboratory M_r test system. Laboratory M_r tests were conducted on three unbound granular materials and one polyurethane control specimen (representing an elastic material). For comparison to the laboratory load pulse duration and shape, a pavement test bed was instrumented and then trafficked with a Class 3 vehicle with two axles (Hallenbeck et al.

2014). According to Witczak (2004), "inaccurate determination of the resilient modulus of the unbound materials in the pavement structure will contribute to erroneous predictions of overall pavement response and pavement performance."

Laboratory related equipment factors were studied and characterized including, stress-pulse shape and duration, sensor sampling rates, control system proportional and integral gain factors, an equipment/software error issue that resulted in an examination of differences between deformation measurements of one versus two LVDTs, and criteria used for quality control and quality assurance in M_r tests. Considering several test parameters, statistical analyses were performed to characterize how the test method and materials influence the calculated M_r values and development of the non-linear universal stress-dependent resilient modulus model.

2.3. Background

Although AASHTO T307 (2007) is widely used to obtain M_r values for unbound materials, research on many factors affecting pavement foundation stress conditions and alterative concepts for M_r testing have been studied for years. Barksdale (1971) and Brown (1973) reported that the equivalent stress pulse shapes changed from sinusoidal to triangular with increased depth beneath pavement surfaces and that the stress pulse duration increases with depth and decreases with increasing vehicle speed. Seed et al. (1967) reported that 20 % greater M_r values were obtained by decreasing load application duration that correspond to a vehicle's travel speed. Allen and Thompson (1974) reported that the M_r of well-graded granular materials under moving wheel loads between about 24 and 113 km/h is independent of stress pulse duration and used 0.15 s stress pulse duration for further M_r tests.

In contrast to AASHTO T307, the NCHRP 1-28A method (2004) requires that each load cycle have a haversine-shaped load pulse with 0.2 s pulse duration and 0.8 s rest period for

subgrade soils and 0.1 s pulse duration and 0.9 s rest period for base and subbase materials and a special provision allows for a 0.15 s load pulse and 0.4 s rest period for non-plastic granular materials. Irwin (2009) suggested that load pulse durations of 0.2 s for base course and 0.25 s for subgrade materials would more accurately represent in situ conditions.

AASHTO T307 (2007) uses the average deformation measurements of two LVDTs mounted outside the pressure chamber, while the NCHRP 1-28A method (2004) requires internally mounted LVDTs. Although average values of two outside mounted LVDTs measured deformations are used in calculating M_r values to reduce the effects of imperfect top specimen surfaces, Groeger et al. (2003) suggested that, with careful inspection (e.g., prevent LVDTs from slipping), more accurate deformation values can be obtained with LVDTs mounted inside the pressure chamber. Camargo et al. (2012) compared M_r results determined from internal and external LVDTs deformation measurements and reported that internal M_r values are generally higher than external M_r values. However, the ratio of internal to external M_r values increases with increasing internal M_r values and this ratio is related to material types. Based on Camargo et al. (2012) results, ratios of internal to external M_r values ranges from 1.0 to 2.2 and have a median value of 1.5 for tested base and recycled aggregate materials. Bozyurt et al. (2012) also found that ratios of internal to external were greater than 1.0 (ratio equal to about 3.6 for two recycled aggregate materials).

The NCHRP 1-28A method (2004) and AASHTO T307 (2007) require quality assurance/quality control (QA/QC) checks on deformation measurements of two LVDTs. Both standard methods specify an acceptable value for the vertical deformation ratio (R_v) that is the ratio of Y_{max} to Y_{min} where the largest deformation measurement of the two LVDTs is Y_{max} and smallest is Y_{min}. NCHRP 1-28A defines an acceptable maximum defamation ratio of 1.1 and the

test should be stopped if an unacceptable ratio is obtained during the preconditioning (PC) sequence. Per AASHTO T 307 (2007) the desired R_v value is 1.1 and the load sequence contains R_v values larger than 1.3 should be withdrawn. Kim et al. (2007) suggests to have three QA/QC criteria including angle of rotation, signal to noise ratio (SNR) and coefficient of variation (c_v) for checking measured M_r values. Angle of rotation is a criteria for checking uniformity of three deformation measurements but this check cannot be done with only two deformation measurements.

AASHTO T307 (2007) specified a loading schedule with 500 to 1000 load cycles for conditioning the specimen and 100 load cycles for each load sequence. Setting the number of cycles to 100 assumes that a representative M_r values can be obtained at 100 load cycles. Seed et al. (1967) reported that increases in M_r values with increasing number of load cycles could be 50 % to 100 % for specimens with different moisture contents and dry densities. Moore et al. (1970) also reported that M_r increased with the number of load cycles. Morgan (1966) tested two sandy materials and reported that constant M_r values were often obtained only after about 10,000 load cycles. Both Moore et al. (1970) and Morgan (1966) examined results from about one million load cycles and moisture loss may have been a contributing factor to the M_r increase. In other studies such as Hicks and Monismith (1971) test results show that M_r values obtained after 50 to 100 load cycles are reasonable estimates for some granular materials. Allen and Thompson (1974) also reported that the “representative” values M_r can be obtained after 25 to 100 cycles. Boyce et al. (1976) found that steady resilient strain values can be reached after 200 to 1000 load cycles if no substantial permanent strain occurs. Based on testing a subgrade material, Elliott and Thornton (1988) reported that M_r values only differed by about 6 % when 50 instead of 200 load cycles was applied instead.

AASHTO T307 (2007) and NCHRP 1-28A (2004) require a minimum sampling rate of 200 Hz. Groeger et al. (2003), however, suggested that 200 readings/second is not sufficient to fully characterize the true shape of a load pulse cycle and that 500 Hz should be implemented.

Given the range of recommendations in the literature concerning load pulse time, deformation measurement, and loading cycles, this study set out to examine these issues for the specific equipment purchased for this study. AASHTO T307 was selected as the reference testing method as this was being used by several state agencies for unbound materials and was specified for the equipment purchased for the experiments.

2.4. Materials and Methods

2.4.1. Laboratory Test Specimens

AASHTO T307 (2007) M_r tests were conducted on three granular materials: crushed limestone, recycled asphalt pavement (RAP), and recycled portland cement concrete with RAP particles (RPCC/RAP), and one polyurethane control specimen. Fines contents and moisture contents were determined for each material according to ASTM D422 (2007) and ASTM D2216 (2010) respectively. A total of thirty-six 101.6 mm diameter by 203.2 mm high specimens were compacted in five equal lifts using a vibration hammer in a split mold. For granular materials, AASHTO T307 (2007) requires vibratory compaction to prepare test specimens with 5 lifts and height and mass of each lift were carefully controlled to ensure the test specimens resulted in uniform density. Samples were compacted to target densities for each lift and then the total sample density measured. Three specimens of each material with the same fines content were compacted to different dry unit weights (i.e., 85 %, 90 %, 95 % relative density). Table 2.1 summarizes properties for all test specimens.

Table 2.1. Properties of the test specimens.

Material	Fines Content, %	Dry Unit Weight, kN/m^3		Moisture content, %	
		Mean	Standard Deviation	Mean	Standard Deviation
Crushed limestone	2.2	19.28	0.18	2.3	0.09
	5.8	19.76	0.20	2.4	0.00
	7.9	17.76	0.06	2.5	0.05
	12.6	20.58	0.19	2.5	0.00
RAP	1.6	15.94	0.12	2.9	0.12
	2.0	15.13	0.10	2.8	0.05
	5.6	17.19	0.14	2.9	0.00
	12.5	17.86	0.16	2.9	0.05
RPCC/RAP	0.8	15.49	0.16	5.9	0.08
	3.5	16.22	0.19	6.5	0.85
	6.0	16.98	0.19	6.2	0.24
	12.4	17.77	0.16	6.1	0.09
Polyurethane	—	11.53	—	—	—

Note: Only one polyurethane specimen was tested

Fourteen tests were performed on the polyurethane specimen to study the effects of proportional gain (P) and integral gain (I) values and to study the effects of stress and strain sampling rates on the resulting calculated M_r values. P and I values are generally only adjusted in the PC sequence when M_r test equipment with proportional-integral (PI) control parameters are used. This adjustment minimizes the difference between the actual applied and target stresses. However, adjustments on P and I values are controlled by operators without specification. Only two external LVDTs were used to measure vertical deformations of each specimen. The uniformity ratio (R_v) of Y_{max} to Y_{min} was calculated for all load sequences in addition to the PC sequence. The desired R_v value is 1.1 (AASHTO 2007) and if the load sequence contains R_v values larger than 1.3 they should be withdrawn. In addition to R_v quality criteria during testing, coefficient of variation (c_v) and signal to noise ratio (SNR) were calculated for checking measured M_r values. According to Kim and Labuz (2007), c_v is calculated as the ratio of the standard deviation (s_d) to the average of the last five M_r values and load sequences. The SNR value is determined by comparing the peak load or displacement to the standard deviation (s_d) of

the noise. Kim and Labuz (2007) recommend that c_v values exceeding 10 % and SNR values less than 3 for each LVDT and 10 for load at each of the last five cycles used to calculate average M_r at each stress level should be withdrawn. SNR is calculated as a ratio of peak load or displacement to three times the baseline s_d using Eq 2.1 while s_d of baseline is calculated using Eq 2.2.

$$\text{SNR}=\frac{\text{Peak}}{3\times s_d(\text{baseline})} \tag{2.1}$$

$$s_d(\text{baseline}) = \sqrt{\frac{\sum_1^N (Y(n)-\mu)^2}{N-1}} \tag{2.2}$$

where

μ = mean value of baseline readings,

Y(n) = stress or displacement reading at point n of baseline, and

N = total data points of baseline.

For this study on the effects of P and I values and sampling rates, a polyurethane specimen was used to mitigate the differences among the specimens. Also, three M_r tests were conducted on RPCC/RAP material to study differences in M_r values using different load-pulse durations. Loading period was controlled as 0.1 s, 0.5 s, and 1.0 s for each test separately while the rest period was controlled as 0.9 s for all tests. The specimens were compacted to the values as listed in Table 2.2.

Table 2.2. Properties of the RPCC/RAP specimens for loading duration test.

Test	Fines Content, %	Dry Unit Weight, kN/m^3	Moisture content, %	Loading Time, s
1	0.4	16.38	5.8	0.1
2	0.4	16.41	5.8	0.5
3	0.4	16.40	5.8	1.0

2.4.2. Instrumented Pavement Foundation

In situ drive tests were performed on a newly constructed asphalt pavement to study the relationship between driving speed and stress-pulse duration and to determine the in situ stress-pulse shape. A one-half ton truck (Class 3 vehicle) was used for the drive test with tire pressures of 290 kPa. The test pavement has a nominal 152.4 mm pavement surface, a 152.4 mm aggregate base, and a 304.8 mm silty clay subgrade. A triangular aperture geogrid was placed between the subgrade and the base layer. Details for the test section are presented in White et al. (2013). Three piezoelectric earth pressure cells were installed at the unbound aggregate base/subgrade interface. Figure 2.1 shows the field installation of the earth pressure cells (EPC) embedded in a thin layer of silica sand. Stress-time recording were made at controlled speeds in 16.1 km/h increments from 32.2 km/h to 96.6 km/h. The sampling rate was set at 2500 Hz and a low pass filter (100 Hz finite impulse response) was used to produce the final stress-time plots.

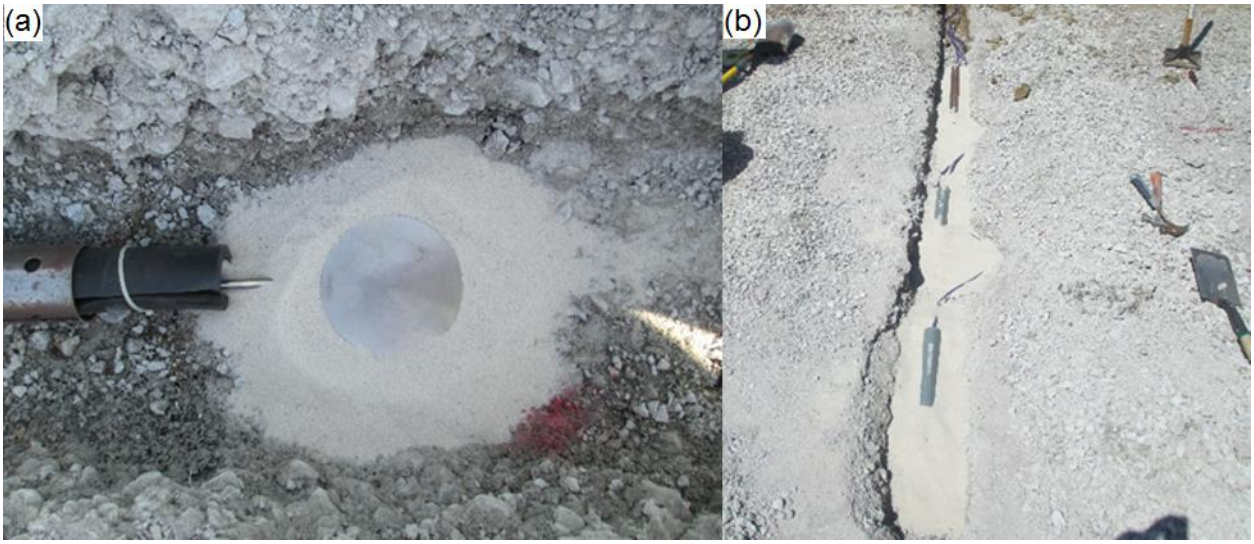

Figure 2.1. Field installation of (a) individual EPC embedded in thin layer of silica sand, and (b) transverse trench with array of three EPCs.

2.5. Results and Analysis

Statistical analyses of variations in M_r were conducted to determine effects of material type, stress level, and load cycle selection. Moreover, nonlinear regression analyses were performed on 36 granular material specimens to study the significance of the three regression coefficients of the universal model.

2.5.1. Characterization of Stress Pulse

The laboratory stress-time pulse shape and duration and influences from sensor sampling rate and P and I gain settings were studied and compared. Results were also compared to the measured in situ trafficking test results. Note that the cross-section area of the specimen is considered constant according to AASHTO T307 for purposes of calculating stress and results are presented in terms of stress and not load.

Stress pulse shape and duration

The laboratory and field stress-pulse shape and duration is compared with the in situ stress pulse in Figure 2.2. Results show that the stresses measured from the drive test are small in comparison to the laboratory test sequences. The peaks of the in situ front tire and one laboratory test stress pulse were matched for comparison in terms of the stress-pulse time history. From the piezoelectric earth pressure cells, the initial front tire stress-pulse is followed by a smaller amplitude stress-pulse for the rear tire (corresponding to heavier front axle). The shapes of the lab and field results are similar. Here the in situ dwell time between front and rear tires is comparatively short (e.g., about 0.14 sec when the test truck traveled at 96.6 km/h), as would be expected for all vehicles traveling at highway speeds. In general, longer stress pulse durations and different pulse shapes were observed with the in situ drive tests compared to the laboratory

test. Note that the commercially available laboratory test system sampling intervals result in closely spaced groups of two to four points per the equipment manufacturer's setup.

The theoretical haversine cyclic load pulse shape as specified in AASHTO T307 (2007) was compared with the laboratory and in situ stress pulses. Results show that the laboratory stress pulses do not merge with the haversine shape in the regions of the stress-pulse initialization and dissipation (Figure 2.2). The haversine curve shape is described using equation $((1 - \cos\theta) / 2)$ with target peak stress and loading duration. The haversine model was fitted to the data obtained from the in situ test for the 96.6 km/h test using 0.1 s pulse duration and the same peak stress obtained in the lab test. This exercise demonstrated that a haversine cyclic stress-pulse shape does not match the initialization and dissipation regions.

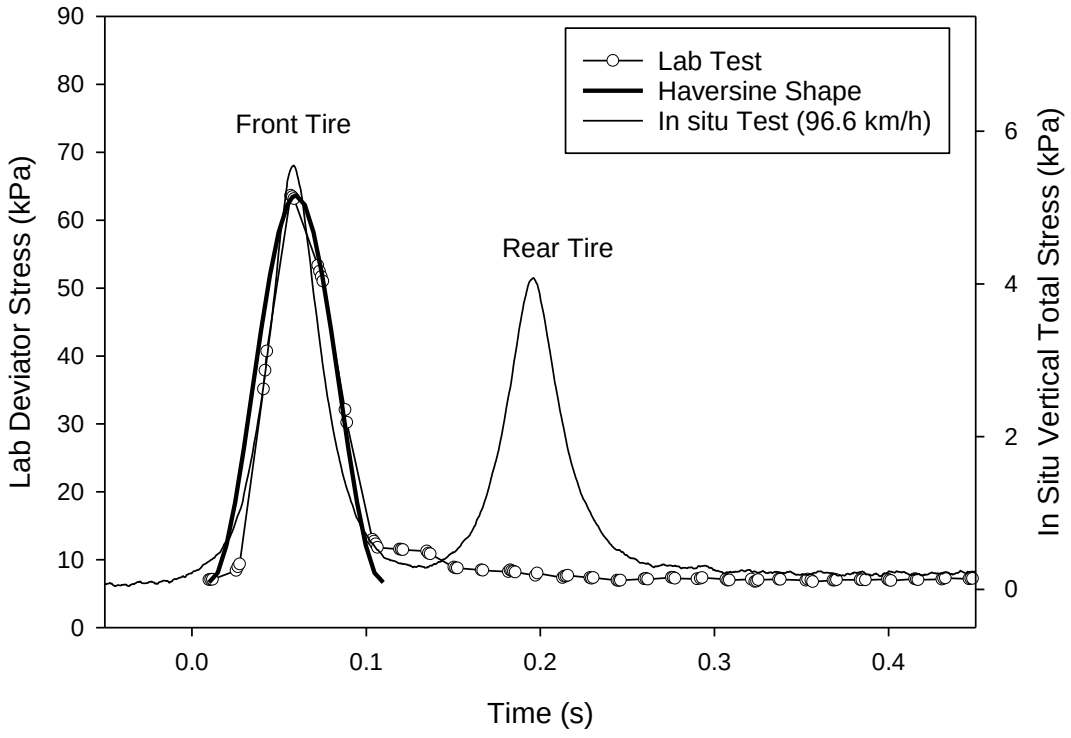

Figure 2.2. Comparison of laboratory and in situ measured stress pulse shape and duration.

Through investigation of several alternative shapes, it was determined that a modified Gaussian pulse shape fits both the laboratory and field data. Eq 2.3 shows the parameters for this model.

$$\sigma=\sigma_o+ae^{\left[-0.5\left(\frac{|t-t_0|}{b}\right)^c\right]} \quad (2.3)$$

where

σ = laboratory deviator stress or in situ vertical total stress,

σ_0 = minimum stress at initialization,

t = time,

t_0 = time at peak stress, and

a, b, and c = regression coefficients.

An example of the modified Gaussian model fit to the in situ test data for both front and rear tire stress pulses is provided in Figure 2.3. Although the modified Gaussian model fits the in situ data better than the haversine model, comparison of the actual and modeled results shows that the model may slightly over-predict the maximum stress. The actual peak stresses can be matched by changing values of the modified Gaussian model coefficients and/or by adjusting the low pass filtering parameters to process the raw EPC measurements. The peak stress occurs at time t_0 and parameter a indicates the peak stress from the modified Gaussian model fit, parameter b and c may be adjusted to change the width of the peak curve that affect stress pulse duration. The examples of the modified Gaussian fit to the measured in situ stress shows that the minimum stress in initialization (σ_0 in Eq 2.3) is zero for the front tire but 0.043 for the rear tire. The reason is that the short period between the front and rear peak stress (e.g., about 0.16 s for drive tests at 80.5 km/h) will not allow the full stress to be dissipated before the rear tire stress is

initiated and dissipation of the stress is not a sudden decrease but is slowly decreased to zero (e.g., a rate of decrease of about 0.45 kPa/s for the rear tire stress for drive tests at 80.5 km/h).

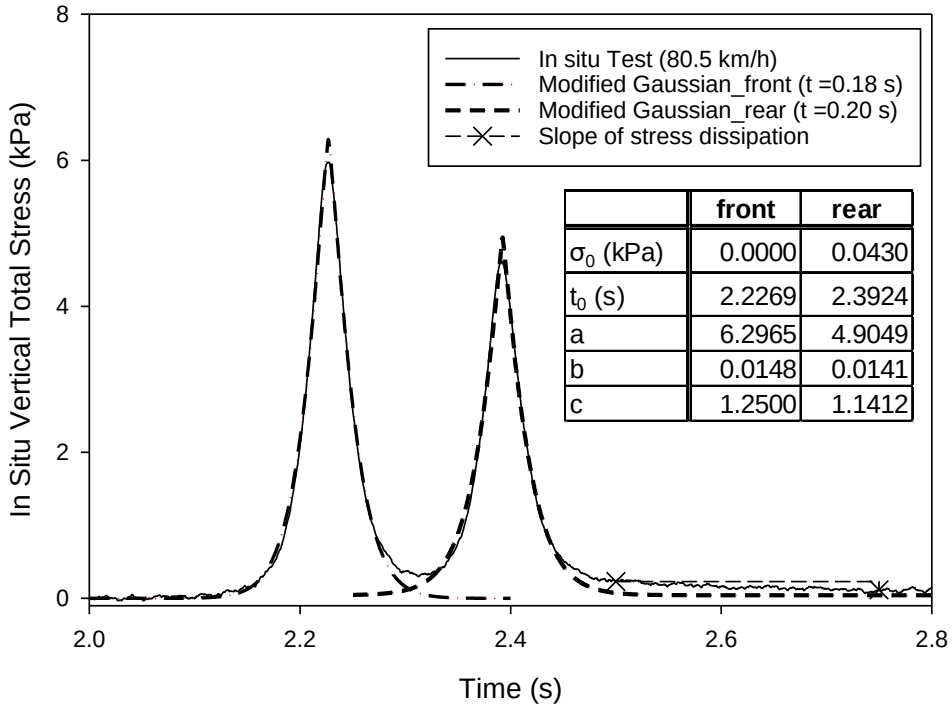

Figure 2.3. Modified Gaussian model fit for in situ 80.5 km/h driving test.

Consequently, the modified Gaussian model was used to determine the in situ stress pulse durations for all of the in situ drive tests and the relationship between stress pulse duration and driving speed was also studied. The modified Gaussian model was fitted to front and rear tire stress pulses separately by non-linear regression analysis. The stress pulse duration is calculated as the time difference when stress σ-σ_0 is equal to 0.05 kPa at stress initialization and dissipation using Eq 3. The duration of rear tire stress pulse at a given speed was slightly longer than the stress pulse duration of front tire. The average stress pulse duration of front and rear tires decreased from 0.50 s to 0.15 s as drive speed increased from 32.2 km/h to 96.6 km/h. Eq 2.4 describes the relationship between stress pulse durations and vehicle driving speeds:

$$\Delta t = t_o + \frac{a}{v} \qquad (2.4)$$

Where: Δt = the stress-pulse duration (s), t_0 = time correction for model fit (s), v = vehicle velocity (km/h), and a = a regression coefficient.

Analysis of stress pulse duration vs. drive speed shows that to achieve the AASHTO T307 specified 0.1 s stress-pulse duration at the in situ sensor location (152.4 mm beneath the bottom of pavement), the vehicle speed would need to be about 128 km/h (Figure 2.4). However, considering that the in situ test response is a composite response of the pavement foundation layers, including the underlying subgrade layer, the non-linear nature of the stress-pulse vs. vehicle speed suggests that the rebound rate of the subgrade may influence the in situ test results.

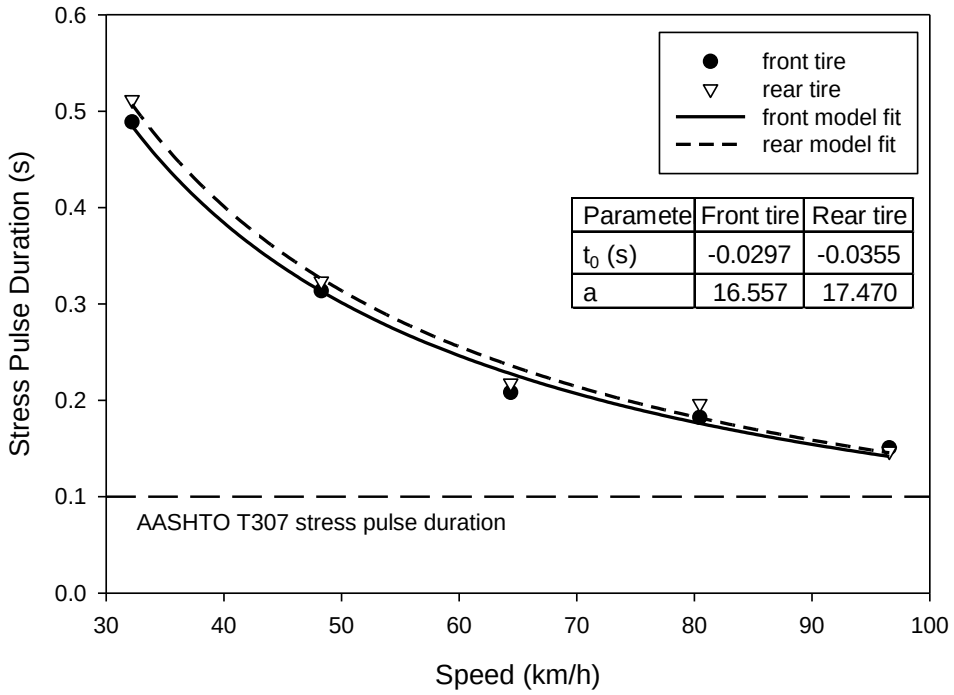

Figure 2.4. Stress pulse duration at varied drive speeds.

To investigate the influence of stress pulse duration on the laboratory M_r test results, laboratory specimens were prepared using the RPCC/RAP material. The stress-pulse duration was set at 0.1 s, 0.5 s or 1.0 s. Figure 2.5 shows the resilient modulus plotted as a function of the bulk stress. The raw data and the Mechanistic-Empirical Pavement Design Guide (MEPDG) suggested generalized model (NCHRP 2004) curves are presented. Results show that the

specimen loaded with the 0.5 s stress-pulse duration produced higher M_r values than the specimen tested at 0.1 s for most of the applied bulk stresses. Lower M_r values were obtained with the 1.0 s stress-pulse duration compared to the 0.5 s duration at most bulk stresses. A definite relationship between stress pulse duration and M_r values needs to be studied further in respect to the fact that the in situ response is a composite response, not just one layer or material. Previously, Marr et al. (2003) suggested that a simpler and less expensive M_r test could be conducted with loading period of 0.5 s.

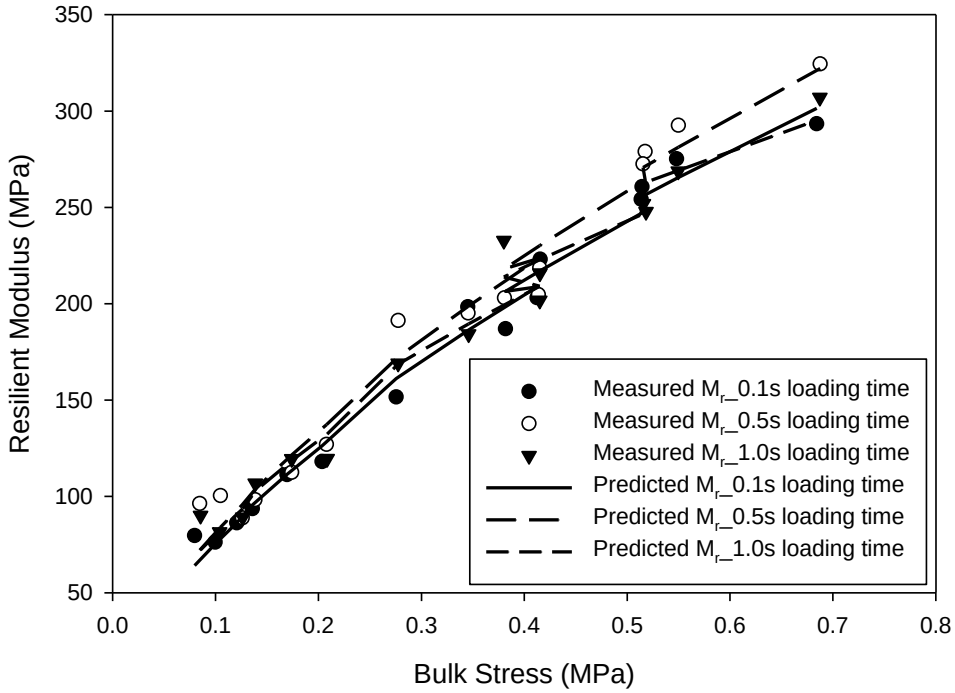

Figure 2.5. M_r values from laboratory tests with varied pulse duration.

Influence of Laboratory Sampling Rate

AASHTO T307 requires a 200 Hz minimum sampling rate. An experiment was performed on a uniform polyurethane specimen to investigate the effects of 200 Hz, 500 Hz, 1000 Hz, and 1250 Hz sampling rates on peak load values. The polyurethane specimen was used to minimize effects of different specimen properties on the resulting M_r values. Figure 2.6 shows an example

of the load-time history at the 200 Hz sample rate. The sampling rate and pattern results in an obvious miss in terms of peak value determination with characteristic aliasing effect from under sampling. This observation confirmed that the sampling pattern and rate at 200 Hz is not sufficient to quantify the peak load.

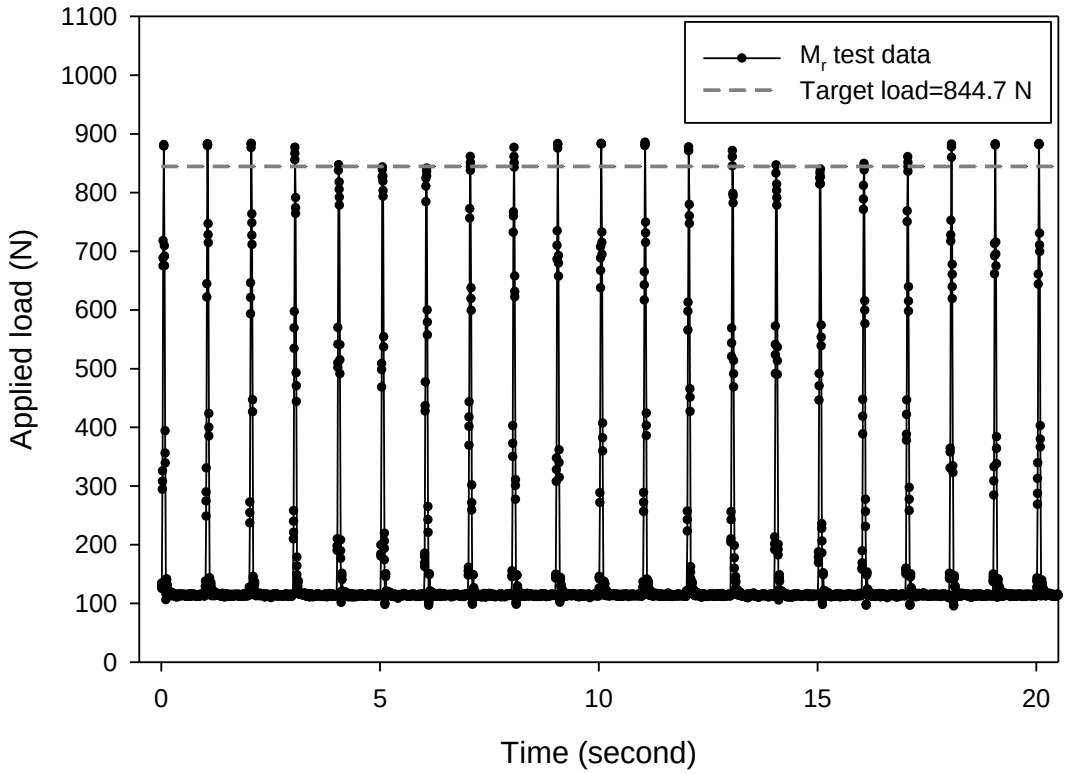

Figure 2.6. Example of M_r test on the polyurethane specimen with 200 Hz sampling rate.

With increasing sampling rate, variation in the maximum load was reduced along with a reduction in variation of the minimum applied load during the dwell period. Improvement by reduced variability was observed at all stress levels. Figure 2.7 shows a frequency plot of peak loads and the differences in recorded peak loads with the selected sampling rates. Although a higher sampling rate means more data could be recorded to identify the actual peak load, the test with 1250 Hz target sampling rate had lower consistency in peak loads than the test with 1000 Hz target sampling rate. The reason could be that the actual recorded data is less than 1250

points per load cycle as the result of capability of the data acquisition system used to collect a large amount of data points in a short period of time. However, based on the results presented herein, a minimum sampling rate of 500 Hz would provide a significant improvement relative to the existing minimum rate of 200 Hz.

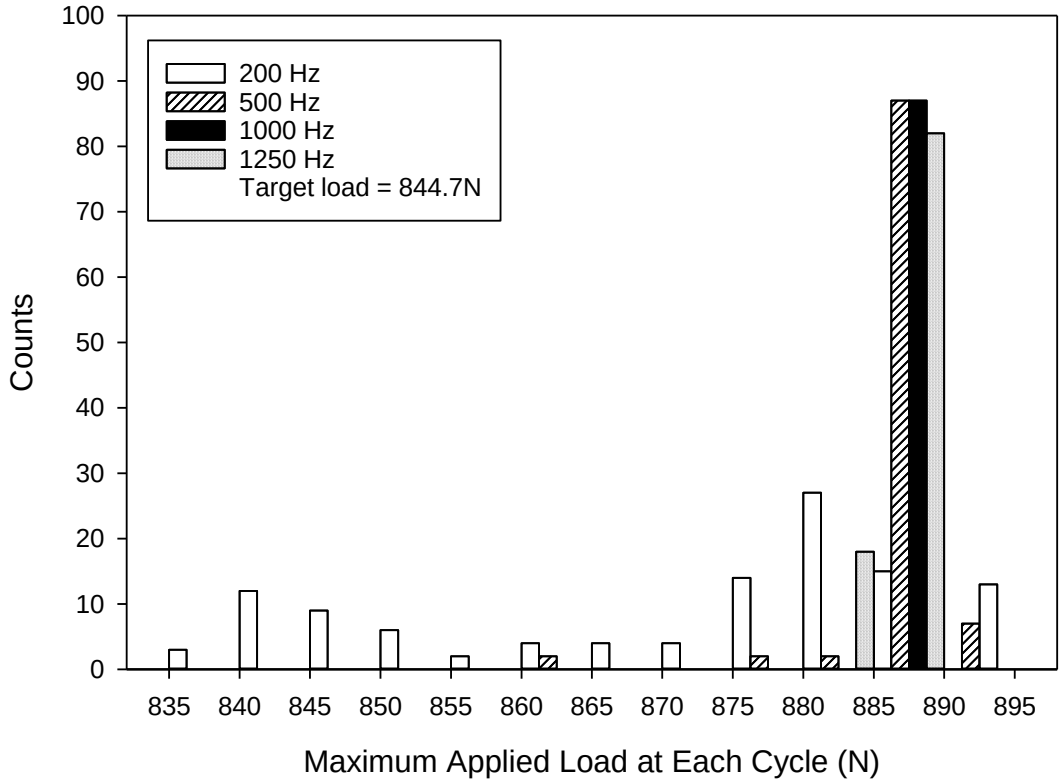

Figure 2.7. Frequency plot for maximum applied loads within a load sequence with different sampling rates.

P and I Gain Settings

P and I gain settings are tuned during the PC load sequence to minimize the difference between the applied and target maximum load. The effect of selected gain settings, within a narrow range of optimal settings per the equipment manufacturer, were studied by conducting several laboratory M_r tests on the polyurethane specimen per the details provided in Figure 2.8 (see legend notes). This study demonstrated that the differences among M_r values of the

polyurethane specimen are about 6 % of the maximum M_r value at each stress level for varied initial P and I settings. Each point in Figure 2.8 shows the average M_r values of the last five load cycles in each load sequence. Compared to the I value, the P value was considered the more dominate parameter for the range of values selected. Careful adjustment of P and I signal values are necessary for each M_r test.

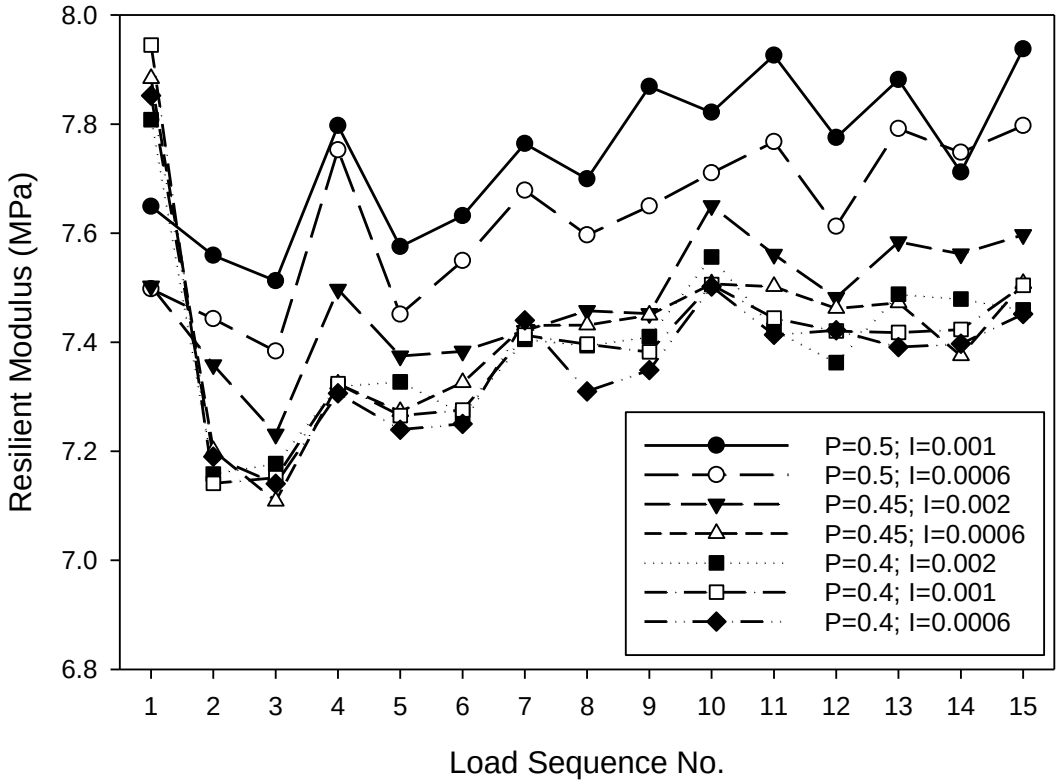

Figure 2.8. M_r values of a polyurethane specimen with varied P and I signal values.

Although P and I values are varied in a small range for seven M_r tests on the polyurethane specimen, differences in the determined M_r values are obvious. Three selected load sequences that have different deviator and confining stresses were studied for determining relationships between P or I values and the average peak load or displacement of the last five load cycles in the given load sequence. Although changes in response associated with the I values are much smaller compared to P values, signal I is adjusted by multiplying the I value by the sum of the

previous load errors and signal P is adjusted by multiplying the P value by the load error. The P and I values were estimated only in the PC sequence for the target deviator stress of 103.4 kPa and confining pressure of 103.4 kPa, so the P and I values are not always giving the closest actual load to the target load that varied in different load sequences.

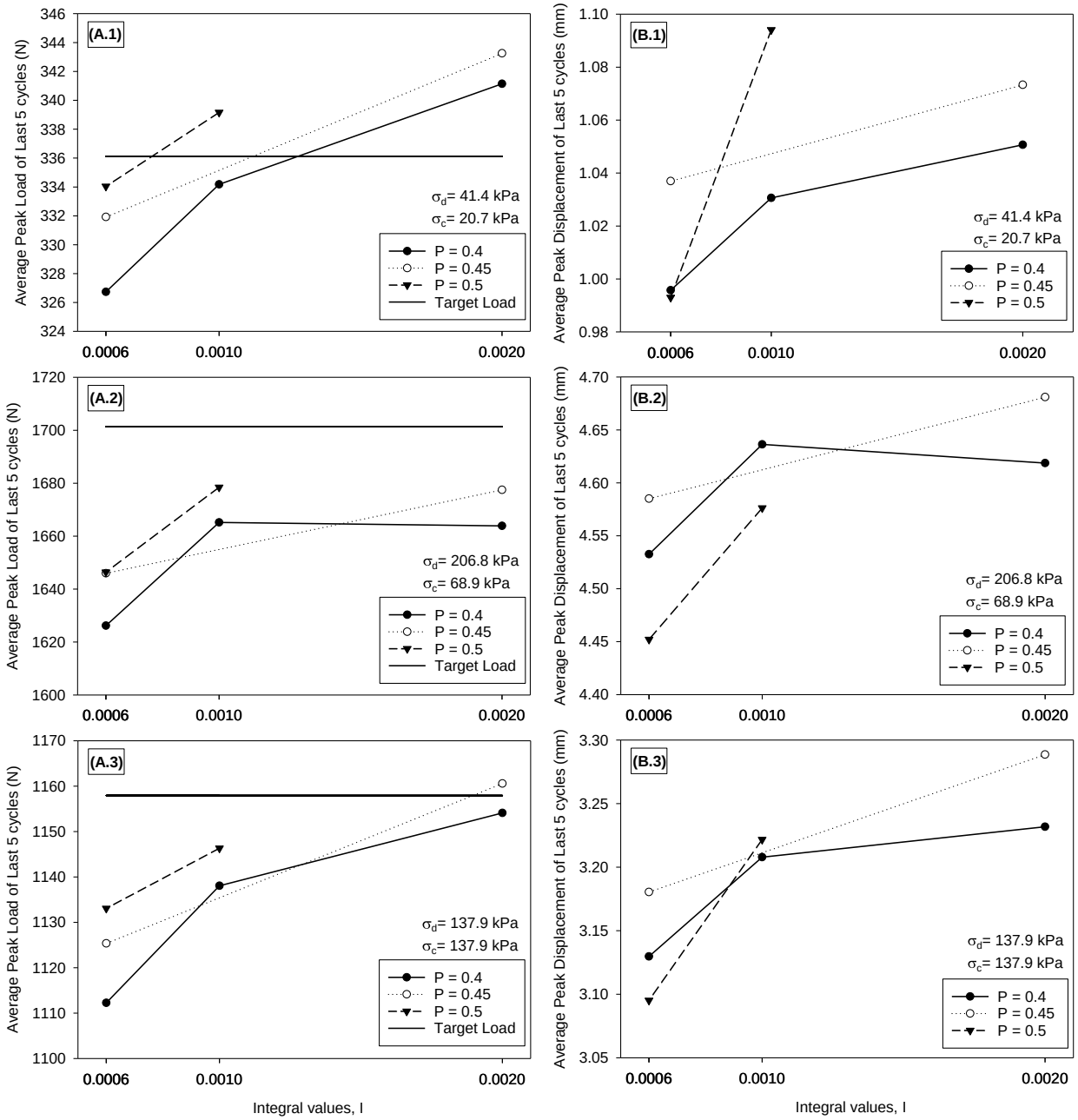

Figure 2.9. M_r values of a polyurethane specimen at selected load sequences with varied P and I signal values.

Figure 2.9 shows that the average peak load at the same P and I values is close, undershooting, and overshooting the target load for different load sequences. Increases in P and I values generally give higher actual peak load and displacement, except the actual peak load and displacement decreased about 0.5 % when the I value increased from 0.001 to 0.002 at P equal to 0.4. To get the best possible control, P and I values should be adjusted during the first few load cycles in each load sequence that has deviator stress changed from 20.7 kPa to 275.8 kPa.

2.5.2. Influence of Deformation Measurements

Vertical deformations were measured using two outside mounted LVDTs according to AASHTO T307 (2007). Figure 2.10 shows an example dataset comparing results using one LVDT versus the average of two LVDTs measurements. Surprisingly, the commercially available equipment was programmed to read only from LVDT1. This suggests that new users should carefully study how the sensors are integrated into the data collection and analysis software provided by the manufacturer. Based on the results presented in Figure 2.10, the differences between M_r values determined using LVDT1 and LVDT2 deformation measurements are up to about 60 % of the M_r values calculated with average deformation measurements of LVDT1 and LVDT2. If one LVDT is used, the determined M_r values will overestimate or underestimate the actual resilient properties of the test specimen. Because the top surface of the specimen may rotate during loading, one or even two LVDTs may not be sufficient to characterize the rotation and check uniformity of the test specimen. (see, Ping et al. (2003), Bozyurt et al. (2012), Camargo et al. (2012)).

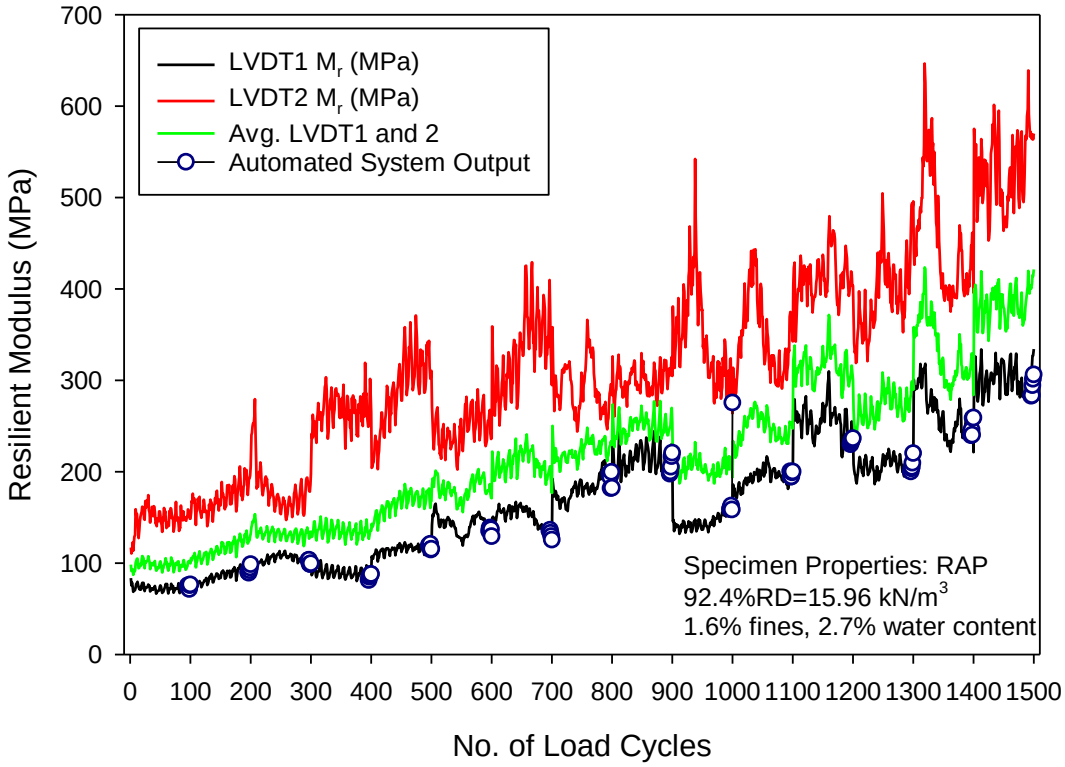

Figure 2.10. M_r test results with varied LVDT measurements for a RAP specimen.

2.5.3. Quality Control and Quality Assurance

Variation of the calculated M_r values cannot be eliminated but needs to be maintained below a maximum value that reflects the quality of the test. Therefore, quality verification was done by checking the signal to noise ratio (SNR), deformation ratio (R_v), and coefficient of variation (c_v) for the last five M_r values in a load sequence.

SNR is calculated for each load cycle using Eq 2.1 and Eq 2.2, and Kim et al. (2007) suggested that the minimum SNR of 10 for each load *is* acceptable. Figure 2.11 shows an example of SNR values for checking the peak load to the noise of 90 % baseline data of a polyurethane specimen with varied sampling rate and three granular materials with target 85 % RD. All measurements met the minimum SNR value of 10 for each load, except the first load sequence at the first (lowest) peak loading sequence. SNR values of load for the polyurethane specimen with 200 Hz sampling rate varied in a relatively constant range for the last 14 load

sequences. But for aggregate specimens, the SNR values increase with the number of load sequences. This can be explained as the standard deviation (s_d) is not increasing significantly with increasing bulk stress.

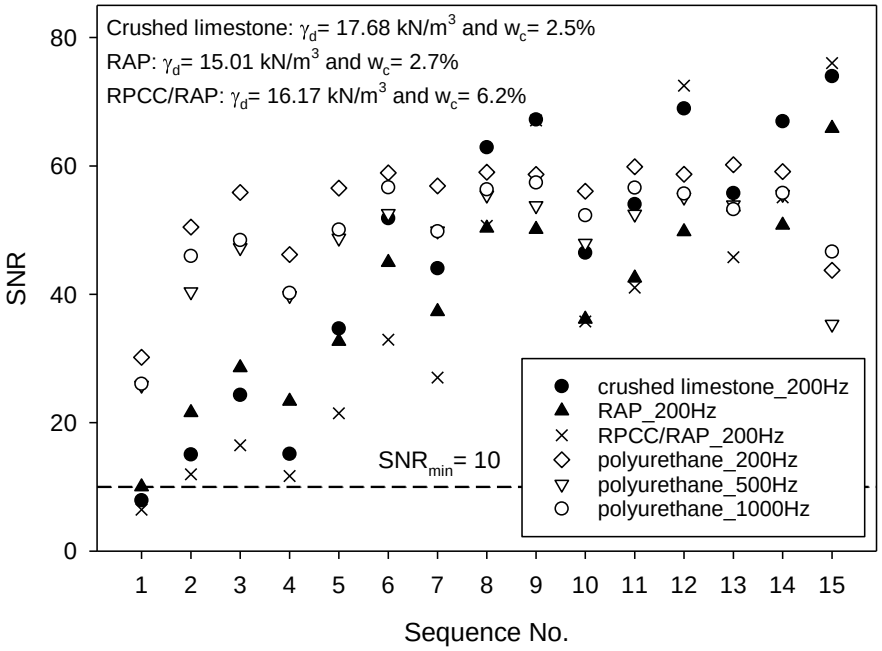

Figure 2.11. Average SNR for load measurements of last five cycles at all load sequences

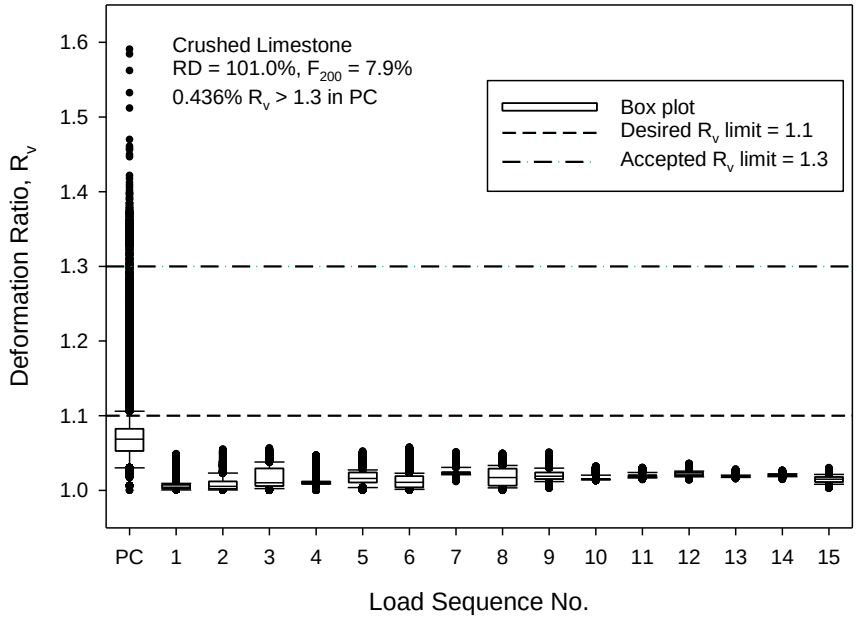

Figure 2.12. R_v for all deformation measurements at each load sequence of one M_r test on crushed limestone.

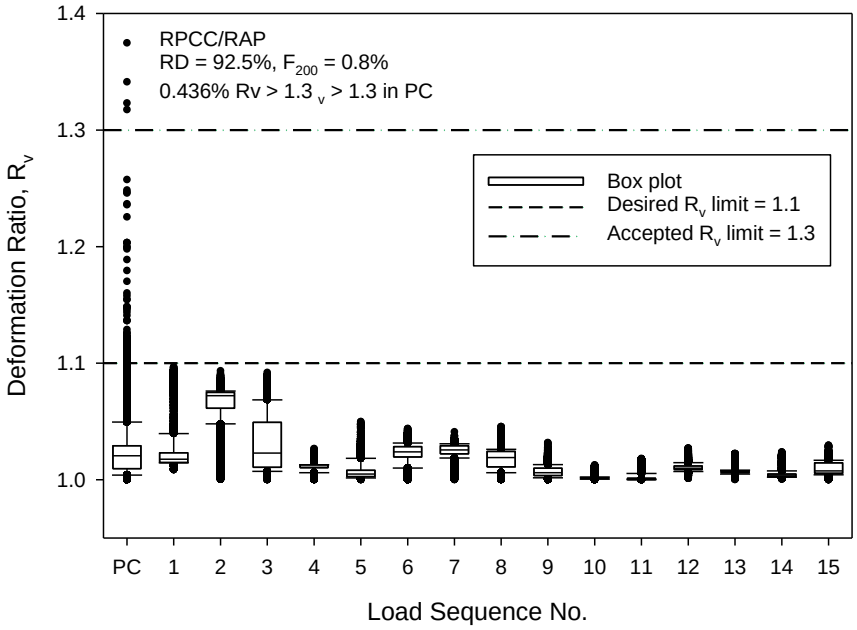

Figure 2.13. R_v for all deformation measurements at each load sequence of one M_r test on RPCC/RAP.

As described previously, AASHTO T307 (2007) requires quality verification assessment of the deformation ratio (R_v). It is desired that $R_v \leq 1.1$ and it is considered unacceptable if $R_v > 1.30$ during the PC phase of the test. However, the comparative checks might be conducted for all load sequences not only the PC sequence as an additional measure of quality testing. Two examples of R_v values for M_r tests on crushed limestone and RPCC/RAP are shown by box-plots in Figure 2.12 and Figure 2.13, respectively. All box plots in this paper are plotted to show the 10 % and 90 % quartile with boundary of the upper and lower whiskers, the 25 % and 75 % quartile with the upper and lower boundary of the box, the median with the horizontal line inside the box, and the values that are out of the range (10 % to 90 % quartile) with single points. Results show that all load sequences, except the PC sequence, have R_v values less than the desired limit of 1.1. In general, the results for both test samples show that the R_v values are highest during the PC sequence and that virtually all the R_v values meet the desired limit of 1.1 for the subsequent 15 loading cycles.

In addition to the comparison of paired R_v values, the resilient strain (ε_r) for each load cycle that is calculated from the deformation measurement of each LVDT was compared. Figure 2.14 shows an example of the resilient strain ratio ($R_{\varepsilon r}$) calculated as the ratio of resilient strain determined from LVDT1 to LVDT2 on the same RPCC/RAP specimen that was used for calculating R_v values in Figure 2.13. $R_{\varepsilon r}$ varied from 0.7 up to 1.9 for all load cycles, and values of $R_{\varepsilon r}$ varied differently from R_v values for all load sequences. Figure 2.13 shows that the PC sequence is the only load sequence that has R_v values exceeding 1.1, but Figure 2.14 shows that the first load sequence where the lowest stresses were applied has the highest $R_{\varepsilon r}$.

Large differences between LVDT1 and LVDT2 measured resilient strains result in larger errors in M_r calculation. Both deviator stress and confining pressure applied in the first load sequence are lower than stresses applied in the PC sequence, but they all have deviator stress to confining pressure ratio of one. During the transition between the PC sequence and the first load sequence, stresses at a lower stress level are applied. Per the raw data obtained in several M_r tests, the displacements that were measured by both LVDTs decrease with increasing number of load cycles in the first load sequence. This analysis suggests that cyclic densification and/or particle rearrangement leading to non-uniform vertical strain might contribute to differences in all paired resilient strains in the first load sequence.

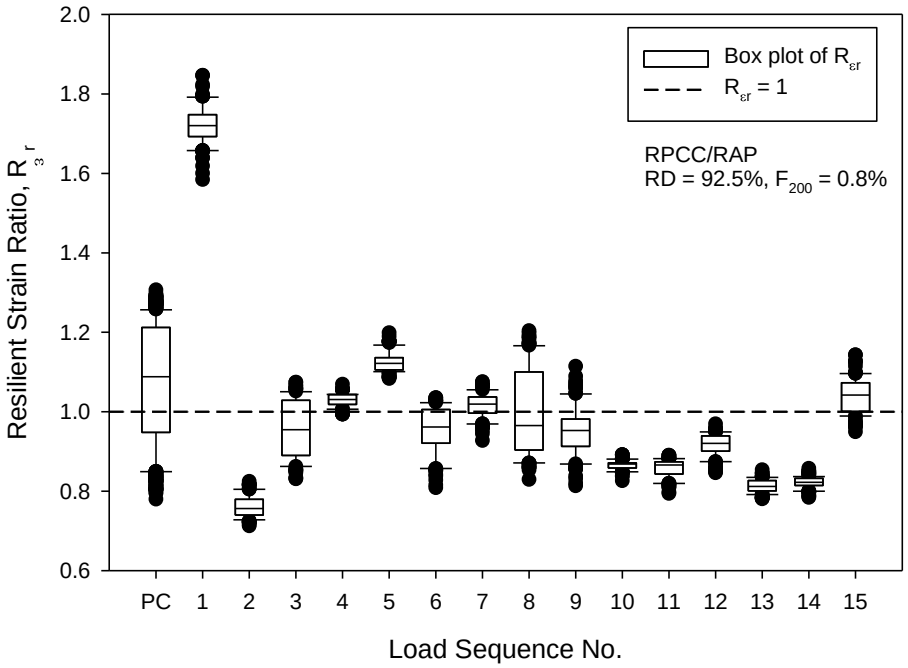

Figure 2.14. $R_{\varepsilon r}$ for all load cycles at each load sequence of one M_r test on RPCC/RAP.

In addition to the observation of variation of M_r values in a load sequence, the variation of M_r values within the last five load cycles was also studied based on the suggestion of Kim et al. (2007) for quality verification of the test results that c_v for the last five M_r values should be below the limit of 10 %. In this present study, all 36 M_r tests on granular soils have c_v less than 10 % at all load sequences. The distribution of c_v values for each test was presented in box-plots and summarized in Figure 2.15. Properties of each test specimen are noted above each box-plot. Figure 2.15 shows that all tests that were performed on crushed limestone material have 50 % of the c_v values less than 4 % and 75 % of the c_v values less than 5 %. The tests that were performed on RPCC and RAP materials agreed with the results summarized from tests on crushed limestone, except the first RAP test. However, this c_v value only shows variation among the last five load cycle that cannot identify the variation of M_r values of the entire 100 load cycle of each load sequence that shows if the average M_r of the last five load cycles is representative for that load sequence.

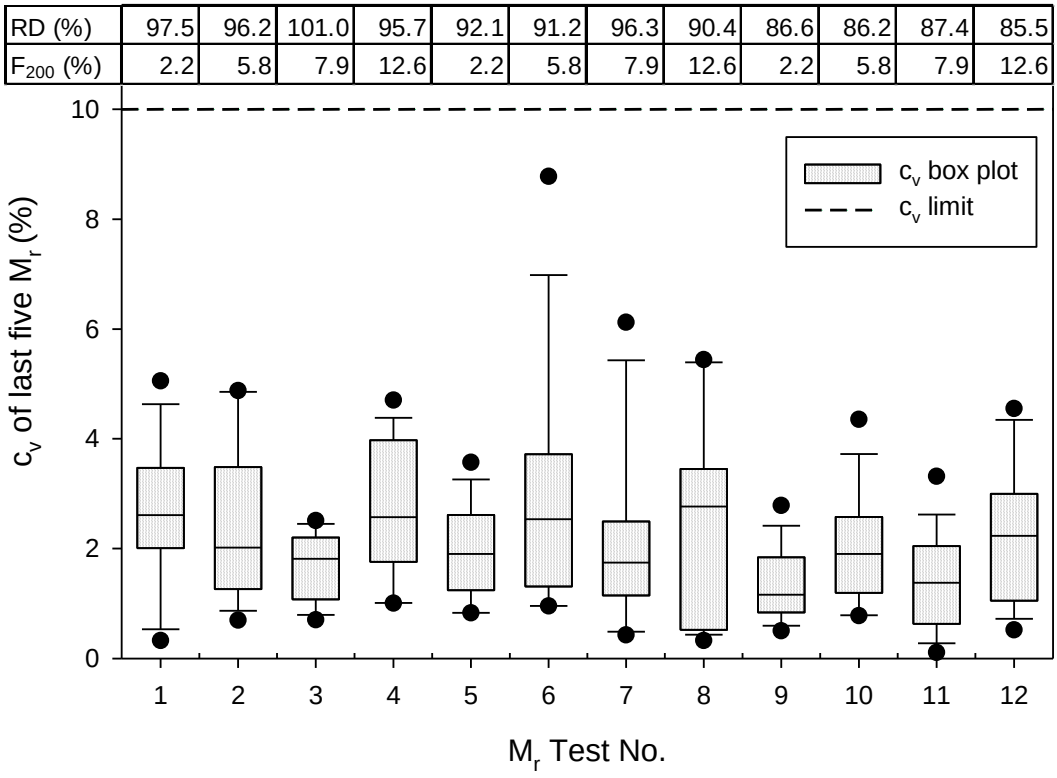

Figure 2.15. c_v of last five M_r values for all M_r tests on crushed limestone.

Further study on variation of M_r values was accomplished by comparing the average M_r of the last 5 load cycles to the average maximum M_r and the average minimum M_r separately. The average maximum M_r is calculated using the maximum and 4 adjacent M_r values.

2.5.4. Statistical Analysis of M_r Variation and Model Coefficients

All 36 M_r test results were used to study the variation in M_r values as a function of the different stress levels. Analysis was performed to characterize the statistical importance of factors that influence M_r values. Coefficients fit to the universal prediction model were also determined using non-linear regression analysis. Moreover, the significance of each coefficient was determined from the statistical analysis.

M_r variation

Morgan (1966) and Moore et al. (1970) reported that M_r values generally increased with number of load cycles, so the average M_r of the last 5 load cycles should be nearly the same as the maximum M_r value. However, observation of variation in M_r values within each load sequence indicates that the average M_r of the last 5 load cycles is not always the maximum value nor representative of the load sequence.

Figure 2.16 shows an example where the M_r values decrease near the end of the 100 load cycles and the minimum M_r value was obtained at the last load cycle. Another example (Figure 2.17) shows that the M_r value decreased first and then increased. Consequently, the variation of M_r values within each 100 load cycle sequence was identified by comparing the average M_r of the last 5 load cycles to the average 5-pt. maximum and the average 5-pt. minimum M_r values. By observation, the first 10 load cycles were excluded because these cycles often result in significant changes.

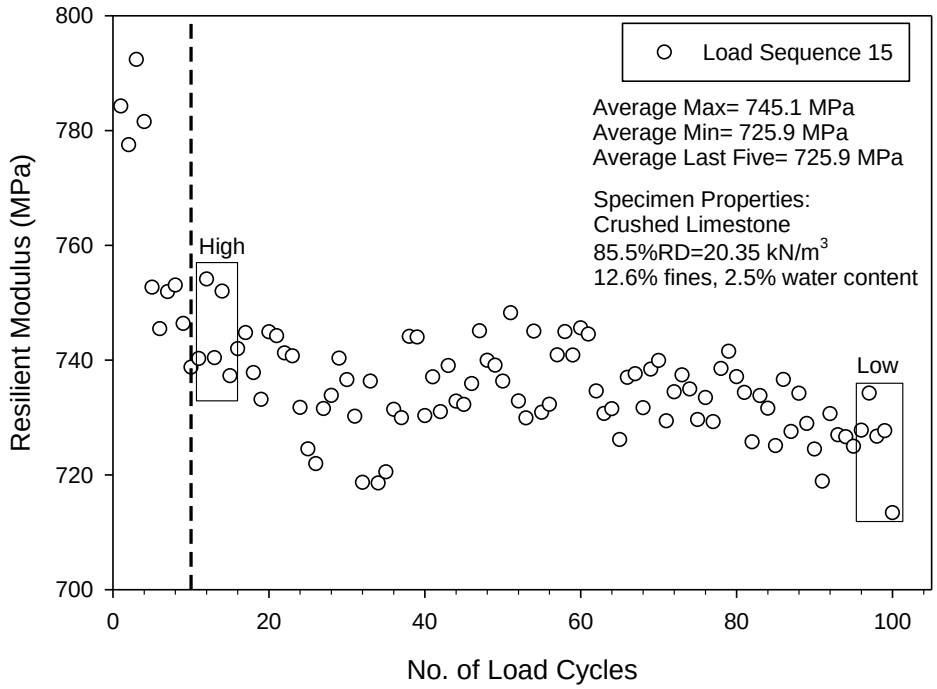

Figure 2.16. M_r variation in a load sequence of M_r test on limestone specimen.

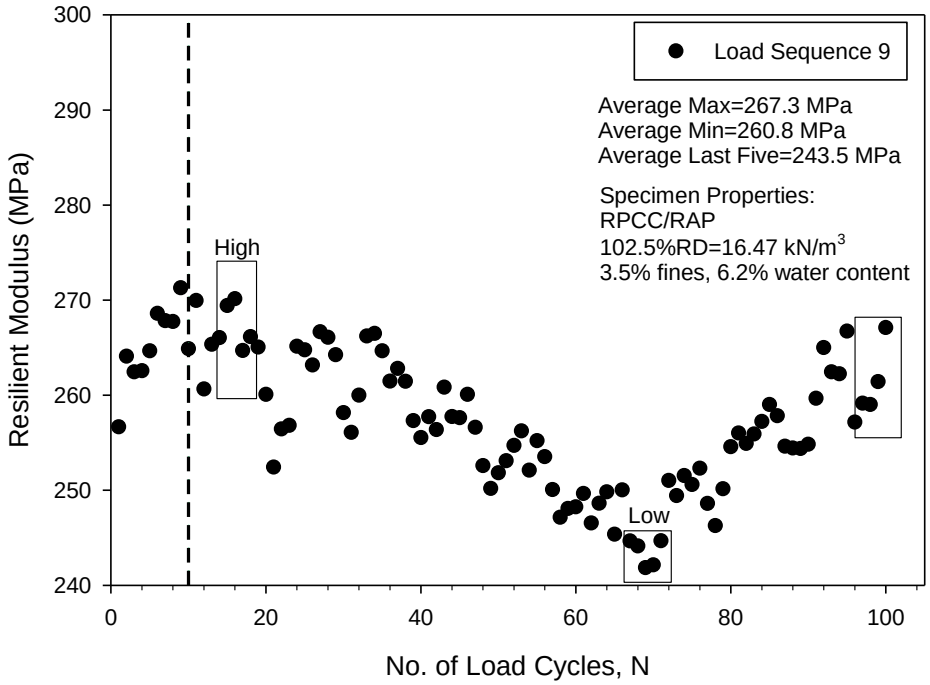

Figure 2.17. M_r variation in a load sequence of M_r test on RPCC/RAP specimen.

By plotting the ratio of the average maximum of 5 consecutive values to the average of the last 5 M_r cycles (FIG. 18) it can be seen that the RAP specimens have larger ratios than crushed limestone and RPCC/RAP specimens, and the ratio is up to 1.45 which means the average maximum M_r is up to 45 % higher than the average M_r of the last 5 load cycles. Studying all tests on crushed limestone, 78.3 % of the load sequences have an average maximum M_r larger than the average M_r of the last 5 load cycles. A similar result was found for 86.1 % of the load sequences for RAP and 82.2 % of the load sequences for RPCC/RAP. This finding suggests that selection of the last five load cycles does not necessarily provide a representative maximum M_r value for the load sequence.

In addition, the average minimum M_r was not necessarily obtained at the beginning of the load sequence (examples are shown in Figure 2.16 and Figure 2.17), so ratios of the average minimum M_r to the average M_r of the last 5 load cycles for each load sequence were calculated and summarized (Figure 2.18). Studying all tests and materials, less than 5 % of the load

sequences have an average minimum M_r at the end of the load sequence. The ratios larger than one indicate large variation among the five points, because the average minimum M_r was calculated using the minimum M_r from five consecutive points. Results show that the RAP specimens have larger ratios than crushed limestone and RPCC/RAP specimens, and the ratio is up to 1.04.

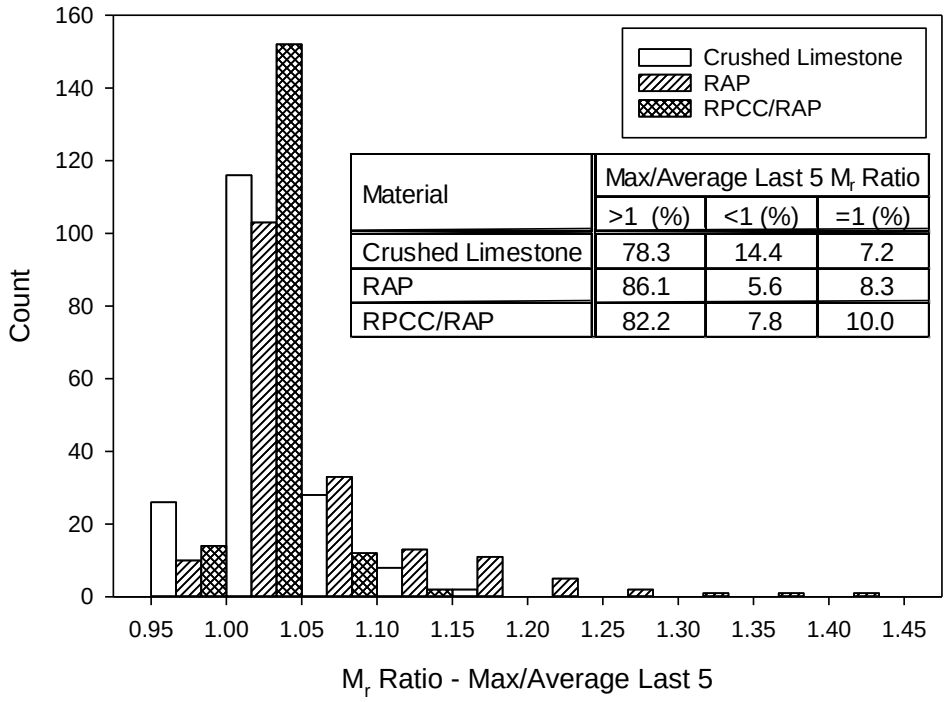

Figure 2.18. Ratios of the average maximum M_r to average M_r of last 5 load cycles for 36 granular specimens.

Statistical analysis was performed on test results to determine the significance of material types, load sequence number, and 5-point average M_r value (considering average maximum/minimum/last 5 load cycles). P-values less than 0.05 were used to indicate significant effects of the tested factors. Results summarized in Table 2.3 show that material type, load sequence, and 5-point M_r values all have significant effects. The least square means of M_r values (Figure 2.19) showed that the deviator stress (σ_d) and confining pressure (σ_c) have positive effects on M_r values and M_r values of crushed limestone are very different from that of RAP and

RPCC/RAP. Tukey HSD (honest significant difference) tests were also performed to study statistical differences in average M_r values among levels of a factor.

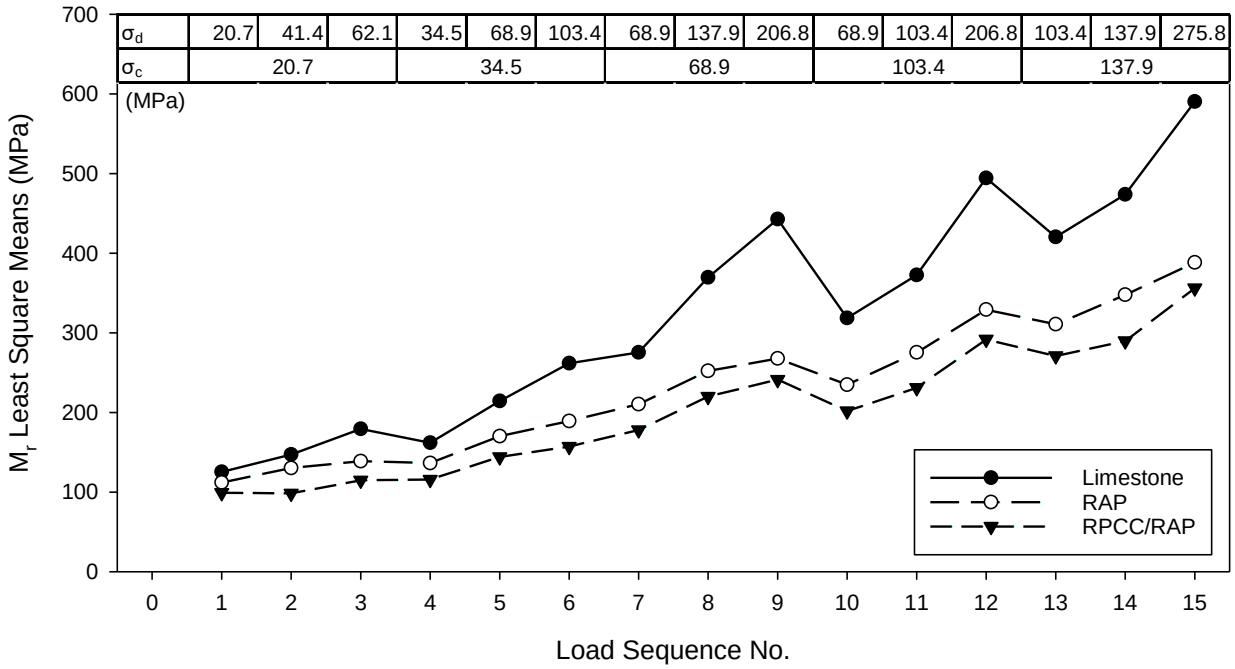

Figure 2.19. Least square means plot for M_r tests on 3 base/subbase materials.

Table 2.3. Tests for fixed and random effects of analysis of variance.

Source of Variation	Sum of Squares	Mean Square	DF	F	p-value
Material	4361301	2180650	2	23.40	<.0001**
Test No.[Material]&Random	3075393	93194	33	94.59	<.0001**
Load Sequence #	16052914	1146637	14	1163.84	<.0001**
Material*Load Sequence #	1302376	46513	28	47.21	<.0001**
M_r Calculation	111770	55885	2	56.72	<.0001**
Material*M_r Calculation	26717	6679	4	6.78	<.0001**
Load Sequence #*M_r Calculation	26036	930	28	0.94	0.5498
Material*Load Sequence #*M_r Calculation	15516	277	56	0.28	1.0000
Error	1430532	985	1452		

Note: * = interaction of factors; ** = significant at α = 0.01; p-value = probability that larger than F ratio

Tukey's HSD test compares all possible pairs of factor level means by first computing the pairwise differences in mean M_r values. Each pairwise difference is compared to a critical value (HSD) to determine the statistical significance of all pairwise differences. The critical HSD value

uses a value from the studentized range distribution. Values of the studentized range are based on Type I error rate (α), number of groups or factor levels (k), and degrees of freedom (df) for error. In JMP, a statistical program, the critical HSD value is calculated as $Q\sqrt{MS_{error}\left(\frac{1}{n_i}+\frac{1}{n_j}\right)}$ where MS_{error} is mean square error, n_i and n_j are numbers of observations for factor levels i and j and Q is derived from the distribution of the studentized range. If the absolute value of the pairwise difference between two factor level means is less than the HSD value, these two factor levels are not significantly different and marked by the same letter. Otherwise, the factor level means are significantly different and marked by different letters.

Table 2.4 shows results of two Tukey HSD tests that were performed on material type and M_r calculation separately, each set of alphabetically listed letters indicates the statistical significance of the difference between mean M_r values of any two levels of each factor. The Tukey HSD test on material type shows that the differences in mean M_r between recycled materials (RAP, RPCC/RAP) and virgin materials (crushed limestone) are statistically significant while the difference in mean M_r between the two recycled materials is not. Moreover, the differences in the mean M_r values calculated using each of the three M_r calculation methods are significantly different from the other two.

Table 2.4. Tukey HSD test on material type and M_r calculation method.

Factors	Levels	Letter			Least Square Mean
Material	Limestone	A			323.2401
	RAP		B		232.9138
	RPCC/RAP		B		200.6457
M_r Calculation	Avg M_r of max and adjacent 4 load cycles	A			261.9112
	Avg M_r of last 5 load cycles		B		253.2517
	Avg M_r of min and adjacent 4 load cycles			C	241.6368

Note: Levels that are not connected by same letter are significantly different and α=0.05.

Coefficients of M_r prediction model

Values of universal prediction model coefficients are determined from non-linear regression analysis as the direct inputs for the AASHTOWare design software (AASHTO 2015). This model predicts M_r values based on the bulk stress (σ_B) and octahedral stress (τ_{oct}) with three coefficients, k_1, k_2, k_3, as given by Eq 2.5, in which P_a is atmosphere pressure.

$$M_r = k_1 P_a \left(\frac{\sigma_B}{P_a}\right)^{k_2} \left(1+\frac{\tau_{oct}}{P_a}\right)^{k_3} \quad (2.5)$$

M_r values are positive, so values of k_1 are positive. Values of k_2 are also positive, because k_2 is the exponent coefficient of bulk stress and M_r is positively related to bulk stress. Strain hardening of the material is caused by increasing bulk stress, so a higher M_r value is obtained. In addition, negative values of k_3 should be obtained to account for strain softening effects of increasing octahedral shear stresses. Negative values for k_3 are generally obtained for fine-grained soils, but not always for coarse-grained or granular materials. Strain softening of granular materials generally occurs at high stress levels where volumetric strains are increasing. Mr testing is normally limited to strains <5 %. Therefore, it is not surprising that 33 of the 36 M_r tests resulted in positive values of k_3. In addition, all 36 M_r tests have positive values for k_1 and k_2 coefficients.

The significance of k_1, k_2, and k_3 coefficients was determined for all 36 M_r tests at a significance level of 0.001. Results show that k_1 and k_2 are significant for all 36 tests, but only 13 of the 36 tests produce a statistically significant k_3 value. Figure 2.20 shows the p-values for all 36 k_3 coefficients. As indicated, the RAP specimens produced least significant k_3 coefficients compared to crushed limestone and RPCC/RAP. The insignificant k_3 coefficients indicate that octahedral shear stress is not a significant factor in controlling resilient modulus for the materials

tested. Examining the data with respect to statistical significance in lieu of just a curve fitting exercise thus reveals useful information about the material properties.

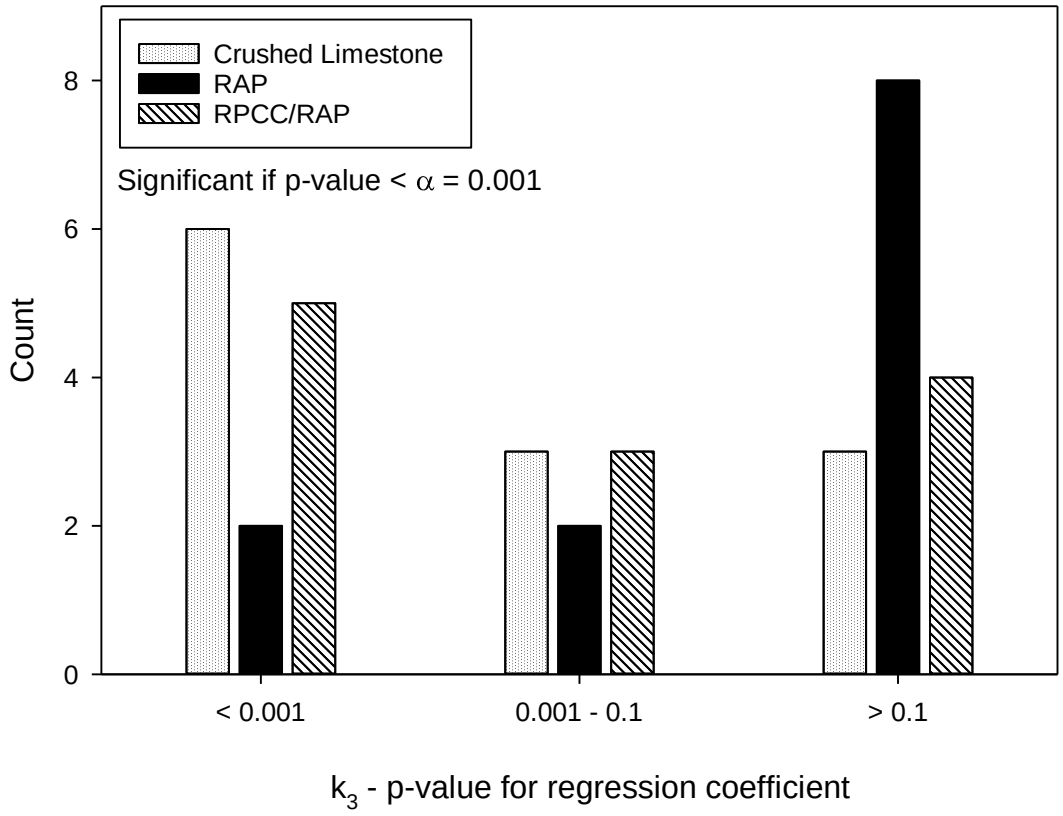

Figure 2.20. P-values for coefficient k_3 of 36 M_r tests on granular materials.

2.6. Conclusions

This paper characterizes sources of error associated with laboratory M_r tests conducted with a commercially available M_r system. Laboratory M_r tests conducted on three unbound granular materials and one polyurethane specimen and in situ drive tests performed on a flexible pavement revealed some sources of error related to strain and stress measurements for granular materials.

The errors related to stress measurements were characterized by identifying the difference between in situ and laboratory stress pulse shape and duration, studying the effects of sampling

rates, and P and I signal values. A comparison of randomly selected raw data of a AASHTO T307 test with the required theoretical haversine-shaped stress pulse and in situ stress pulses revealed inadequate simulation of in situ stress pulse shapes and fast stress pulse durations in laboratory tests. The haversine-shaped stress pulse does not simulate the actual slow stress initialization and dissipation that in situ stress pulse experienced. A modified Gaussian model with 5 parameters can better simulate in situ stress pulses. Stress pulse duration of 0.1 s is too fast compared to in situ stress pulse duration of 0.14 s at 304.8 mm beneath the pavement surface and base layer when the test vehicle was driving at 96.6 km/h. In addition, a 0.1 s stress pulse duration might be obtained at the same position when the test vehicle is driving at 128 km/h. Although M_r values varied with different stress pulse durations, three laboratory tests are not sufficient to conclude effects of stress pulse duration on M_r values. Therefore, the effects of the inadequate simulation on M_r values needs to be studied further to determine if a revision is needed for the laboratory tests. Further, the specified 200 Hz sampling rate for laboratory tests is insufficient to fully characterize the true shape of stress pulses, especially the applied peak stresses. After tests with different sampling rates, rates of 500 Hz or greater can capture applied peak stresses better than the 200 Hz rate and result in less variation in M_r values. However, the different M_r test appliance may perform better or worse with the same sampling rate. Different sampling rates during the loading and rest period might be used with capable software to save computer storage and time for processing data. Initial adjustments of P and I signal values and automatic adaptation with time within the PC sequence is good when applying the target load in the PC sequence but not for achieving target loads for subsequent sequences where different stress levels are required. Therefore, careful adjustments of P and I signal values in each load sequence might be suggested when M_r test equipment with a PID controller is used.

The differences between deformation measurements of two LVDTs were studied. In some cases, large differences were observed perhaps because top surfaces of the test specimens were not perfectly flat and the unit weights of the specimens were not uniform. In some cases, large differences in two LVDTs measurements were not observed in the PC sequence but in other load sequences. The larger the difference in two LVDTs measurements, the lower the accuracy in M_r values. Therefore, quality control and quality assurance (QC/QA) are needed to determine the reliability of the M_r tests results. SNR values of loads, the AASHTO T307 required displacement ratio R_v in the PC sequence, a proposed resilient strain ratio $R_{\varepsilon r}$ of LVDT1 to LVDT2, and c_v of the last five M_r values in each load sequence were studied for QC/QA. Most of the SNR values met the requirement except for the first load sequence. The first load sequence has most SNR values less than 10, the minimum criteria. A possible reason for this is particle rearrangement in the specimen. Values of R_v in the PC sequence are not representative of R_v values for all load sequences, so R_v values should be checked for all load sequences. The highest $R_{\varepsilon r}$ values were obtained in the first load sequence not the PC sequence this suggests a possible particle rearrangement might have occurred in that load sequence. Therefore, $R_{\varepsilon r}$ should be studied to check the uniformity of the specimen response. However, two LVDTs may not be sufficient for checking the uniformity of the specimen response and more LVDTs are suggested. In addition, c_v was calculated for the last five load cycles of selected M_r tests and all the values met the requirement. However, this only shows that variations within the last five load cycles were acceptable and that the average of the last five M_r values is used to represent the M_r at the given stress for the tested material.

However, M_r values varied in different ways than the average of the last five M_r values, they could be higher than the maximum or lower than the minimum M_r values. This suggests steady

M_r values were not obtained at the end of the 100 load cycles. According to the statistical analysis on all 36 M_r tests on three granular materials, variations among the average of the last five M_r values, the average of the maximum and adjacent four M_r values, and the average of the minimum and adjacent four M_r values are statistically different. In addition, crushed limestone specimens had higher average M_r than RAP and RPCC/RAP specimens, and material type is a statistically significant factor affecting M_r values. Although increasing use of recycled materials can help environmental sustainability and reduce costs, careful investigation of the properties of the recycled materials should be conducted. Moreover, regression coefficient k_3 is not necessary for granular materials because the effects of shear stress that k_3 interprets in the universal model can be negative or positive.

Assessments of testing errors are necessary to ensure accurate M_r values. Practitioners who perform AASHTO T307 M_r tests with similar equipment can use these findings to evaluate their equipment and identify possible sources of error.

2.7. Acknowledgements

This study was sponsored by the Federal Highway Administration under agreement No. DTFH61-06-H-00011 and the Iowa Department of Transportation under Transportation Pooled Fund Program TPF-5(183).

CHAPTER 3. STUDYING SPATIAL VARIATION OF PAVEMENT FOUNDATION PROPERTIES WITH GEOSTATISTICAL ANALYSIS METHOD

A paper submitted to *Journal of Geotechnical and Geoenvironmental Engineering*

Jia Li, David J White, Philip M Dixon, and Pavana Vennapusa

3.1. Abstract

Geostatistical analysis procedures are presented in this study to provide a guide for geotechnical and pavement engineers to quantify spatial variability of pavement foundation properties with consideration of choosing the best fitted semivariogram model and characterization of anisotropy. Characterization of spatial variability of stiffness and compaction properties are presented from two Interstate projects sites in Michigan (I-94 and I-96). . Geospatial analysis of anisotropy for the geotechnical measurements shows different major and minor anisotropic directions for densely tested spatial areas. Comparisons of three theoretical semivariogram models (i.e., spherical, exponential, and Matérn with k=1) using elastic modulus, moisture/density, and penetration resistance show that there is no single best fitted model for all measurement types. The isotropic semivariogram model works as well as the anisotropic semivariogram model in estimating the data at unsampled locations across the studied areas. The range values (indicating the spatial correlation length) are almost all less than 5 m for all measurements without considering the anisotropic behavior. When anisotropy is considered, longer spatial correlation lengths up to 11 m were determined in the longitudinal direction of the road alignment. The importance of this research is that with high quality field measurements, different anisotropic behaviors were observed and therefore careful assessment of geospatial modeling is required to adequately characterize spatial variability of pavement foundation layer properties.

3.2. Introduction

Non-uniform subbase/subgrade stiffness can accelerate fatigue cracking and other types of pavement distresses and shorten the pavement service life (Titi et al. 2014; White et al. 2004). Dilip abd Babu (2014) concluded that critical strains will be underestimated without considering the spatial variability of resilient moduli. Roesler et al. (2016) showed peak concrete slab tensile stresses increase up to 39% in nonuniform compared uniform support conditions. However, there have been very limited studies that documented the fundamental aspects of nonuniformity modeling of the foundation layer properties. In part, the lack of study in this area is due to the state of practice that relies on sparse data collected. The univariate statistical analysis of pavement foundation properties shows a range of engineering parameters values can vary within the studied area, but it does not describe the spatial variability. Several previous studies (Facas et al. 2010; Lea and Harvey 2015a; Lea and Harvey 2015b; Vennapusa 2004; Vennapusa et al. 2010; White et al. 2004) performed spatial variability analysis on pavement foundation layer properties (i.e., stiffness, layer thickness, intelligent compaction measurement values). Anisotropy in engineering parameters has been observed and characterized using roller-integrated compaction measurements (Facas et al. 2010; Vennapusa et al. 2010) where longer correlation lengths were observed in the longitudinal direction compared to the transverse direction.

Geostatistical methods have been well studied in other fields (i.e., mining, geology, soil science) and details of understanding general spatial variation have been introduced in many books (Clark and Harper 2002; Cressie 1993; Deutsch and Journel 1998; Goovaerts 1997; Isaaks and Srivastava 1989; Journel and Huijbregts 1978; Olea 2006). Lead and Harvey (2015b) introduced model types with analysis of pavement layer thickness. However, the details in using

geostatistical analysis methods for charactering pavement foundation properties with closer spacing (about 0.6 m) was not studied.

Herein pavement foundation properties were studied by investigating the in-situ stiffness, penetration resistance, and compaction properties. Stiffness properties include elastic modulus ($E_{LWD\text{-}Z3}$) determined from the light weight deflectometer (LWD) test. Penetration resistance was determined from the dynamic cone penetration index (DCPI) (ASTM D6951-03) of subbase layer and subgrade layers ($DCPI_{subbase}$, and $DCPI_{subgrade}$). Compaction properties include dry unit weight (γ_d) and moisture content (w), as determined from the nuclear gauge (NG) test method (ASTM D6938-10). In-situ testing was performed shortly after pavement foundation construction process was completed. Observation of the construction processes were noted in terms of how the materials were placed, spread, and compacted.

The in-situ measurements were taken at several test locations with consideration for the depth of measurement that the values represent. For example, the LWD test is a spot test where the $E_{LWD\text{-}Z3}$ values represent stiffness for the composite subgrade and subbase layers at the test location. Other measurments were interpreted to represent the target layer, like DCP and the NG tests results.. Interpretation of the in-situ test results is important for further interpretation of the geospatial results.

This paper focuses on quantifying spatial variability using a geostatistical method, comparing efficiency of different theoretical semivariogram models in fitting the semivariogram of studied properties, describing different methods in identifying anisotropic spatial variance, and comparing isotropic and anisotropic semivariogram models in describing the spatial variability. The interpretation and modelling of experimental measures of spatial variability are discussed and demonstrated using data collected at two projects MI I-94 and MI I-96 in Michigan. This

paper introduces researchers and engineers to quantifying spatial variability, examines how the correlation of the pavement foundation properties could be in different directions, and guides readers to plan future sampling programs for studying the spatial variability of the pavement foundation sections.

3.3. Geostatistical Analysis

The semivariogram γ(h) is a tool in geostatistical studies to describe and quantify spatial variability of studied variables. A semivariogram γ(h) measures the average dissimilarity of paired data separated by a vector ***h*** (Goovaerts 1997). The semivariogram γ(h) is defined as half of the average squared differences between a number, N(h), of data values pairs separated at a distance h as calculated in Eq. 3.1 (Isaaks and Srivastava 1989).

$$\gamma(h)=\frac{1}{2N(h)}\sum_{(i,j)|h_{ij}\approx h}\left(Z(\mathbf{s}_i)-Z(\mathbf{s}_j)\right)^2 \quad (3.1)$$

The random function Z(**s**) where s denotes spatial location is second order stationary, which means that the mean value (μ) is a constant and the covariance between any pair of data values separated by the vector with vector distance ***h*** is the same across the study area. Although semivariance, variance, semivariogram, and variogram have been used in different studies (Bachmaier and Backes 2011), the semivariogram, γ(h) given in Eq. 3.1, will be used in this study.

A semivariogram plot is composed of sill (C) that includes nugget effect (C_0) and partial sill (C_s), and range (a) or effective range (a') for a single semivariogram model with nugget effect. Figure 3.1 shows a typical spherical semivariogram fitted to the experimental semivariogram data.

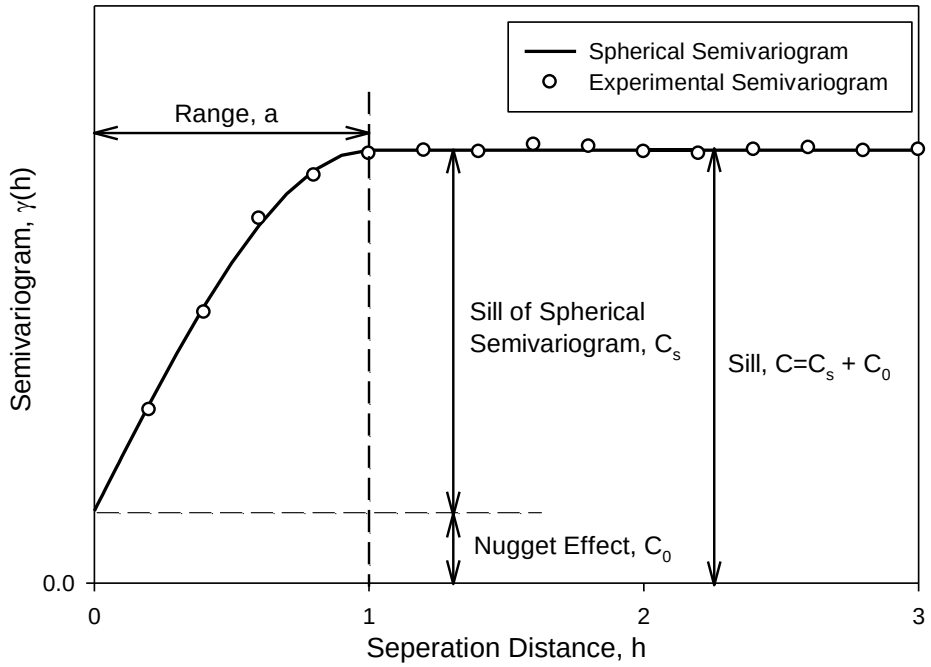

Figure 3.1. Typical semivariogram graph

Three major semivariogram parameters are the nugget effect (C_0), the sill ($C=C_0+C_s$), and the range (a). The brief description of each parameter will be summarized from geostatistical books (Goovaerts 1997; Isaaks and Srivastava 1989).

The nugget effect (C_0) is the sudden increase in the semivariogram value as the separation distance goes from 0 m at the origin to an extremely small distance. This nugget effect can be the result of sampling error and short scale variability. The nugget effect can be determined by fitting the straight line through the first few semivariogram values to the intercept with the vertical axis. The relative nugget effect tends to increase with the lag (h) tolerance and data sparsity. Data sparsity or measurement errors may lead to a semivariogram with noisy values and can only be presented with a pure nugget effect. In general, the nugget effect is modelled as an isotropic component, but it could be modeled as an anisotropic spatial structure if the range value is smaller than the shortest sampling distance.

The sill ($C=C_0+C_s$) is the value of semivariogram that no longer increases with increasing separation distance, that is the semivariogram reaches a plateau with value C_0. The sill of the semivariogram may not be equal to the sample variance (Barnes 1991; Goovaerts 1997) and so forcing the sill to be equal to the sample variance (s^2) is a questionable practice.

The range (a) is the separation distance at which the semivariogram reaches the sill plateau. In most models, the effective range (a') is determined as the semivariogram reaches 95% of the sill plateau. More and better data tends to produce a semivariogram with longer range.

Some properties of a semivariogram are that the semivariogram values are identical when computed on opposite directions, the omnidirectional semivariogram is computed on the data pairs in all directions that have an angular tolerance ($\Delta\theta$) greater than or equal to 90°, the directional semivariogram is computed when $\Delta\theta$ less than 90°, and semivariogram values are sensitive to extreme data or outlier values (Goovaerts 1997). The $\Delta\theta$ extend the vector $\boldsymbol{h}$ angle θ to include all distance vector falls in the direction $\theta\pm\Delta\theta$.

The appropriate lag or separation distance should be chosen according to the average minimum spacing among the sampling locations. The lag tolerance is commonly one half of the lag spacing. The default setting in the statistical program R is to study the semivariogram values of the data pairs separated at a distance up to 1/3 of the maximum length of the studied area. In general, 10 to 15 bins is desired at separation distance up to ½ of the maximum distance over the sampling area, but the number of data pairs within each bin is more important.

The discrepancies in semivariogram values reflect experimental fluctuation that result from the small number of data pairs available for each lag. Generally, the minimum of 30 and preferred 50 or more data pairs is desired within each bin (Journel and Huijbregts 1978). Erratic behaviors could be found in experimental semivariogram for data that is skewed or has

extremely high or low values (outliers). If the sampled data is highly skewed (skewness is out the range of -1 to 1), the data may be transformed before performing spatial analysis. If the experimental semivariogram keeps increasing with increasing separation distance between data pairs, there could be a trend in the sampled data that should be removed before spatial analysis (Gringarten and Deutsch 2001). The reason for this is that it is unreasonable to expect a constant mean value over the study area, as is assumed in spatial analysis, if a significant trend is identified.

3.4. Project Overview

Two dense gridded test sections with the minimum spacing of about 0.6 m were studied for investigating and quantifying the spatial variability of the pavement foundation properties. The in situ test data used in this study were collected from one test section from each of the MI I-94 and the MI I-96 reconstruction projects.

3.4.1. Test section

The first dense gridded test section (TS1b) is part of the MI I-94 project which involved pavement reconstruction. The new pavement was constructed with a 280 mm (11 in.) thick JCPC pavement surface and a 406 mm (16.0 in.) thick OGDC base layer that sat on the subgrade layer of silty clay which was classified as ML in the USCS classification system with a geotextile layer in between. TS1b involved testing a 7 m × 7 m area in a dense grid pattern with 121 test points on the newly constructed trimmed OGDC base layer. The second dense gridded test section (TS1) is part of the MI I-96 project which also involved pavement reconstruction. The new pavement was constructed with a 292 mm (11.5 in.) thick jointed PCC pavement, 127 mm (5 in.) cement treated base (CTB) layer with recycled PCC (RPCC) material and 279 mm (11 in.) of existing or new sand subbase with a geotextile separator at the CTB/subbase interface. TS1 involved

testing an 8.5 m × 8.5 m area in a dense grid pattern with 73 test points on the final compacted and trimmed sand subbase layer. Soil properties of these two test sections determined by laboratory tests, are summarized in Table 3.1.

Table 3.1. Soil properties summary for studied test sections

Project Site		MI I-94	MI I-96
Pavement Foundation Layer	**Soil Properties**	**TS1b**	**TS1**
Base/subbase	r_{dmax}(kN/m^3) (ASTM D4253-00)	16.23	20.06
	r_{dmin}(kN/m^3) (ASTM D4254-00)	14.05	14.98
	AASHTO Classification	A-1-a	A-1-b
	USCS Classification	GP	SP-SM
Subgrade	r_{dmax} (ASTM D698-07)	18.58	20.1
	w_{opt} (ASTM D698-07)	13.8	9.5
	AASHTO Classification (ASTM D3282-09)	A-4(0)	A-4
	USCS Classification (ASTM D2487-00)	ML	SC

3.4.2. In-situ tests

The following in situ tests were conducted on test sections MI I-94 TS 1b and MI I-96 TS1 to evaluate the variability in properties of pavement foundation systems: real-time kinematic global positioning system (RTK-GPS); Zorn light weight deflectometer (LWD); dynamic cone penetrometer (DCP); and Humboldt nuclear gauge (NG).

Real-Time Kinematic Global Positioning System

RTK GPS system was used to obtain global spatial coordinates (i.e., northing, easting, and elevation) of in situ test locations and tested pavement layers. The local spatial coordinates (x, y, and z) were determined for all tested sections from their global coordinates. A Trimble SPS 851 was established on site to provide base station correction for a Trimble SPS 851 receiver. This system has manufactured accuracies of < 10 mm in the horizontal direction and < 20 mm in the vertical direction.

Zorn Light Weight Deflectometer

Zorn LWD tests were performed according to manufacturer's recommendations (Zorn G. 2003) on base and subbase layers to determine elastic modulus. These LWD testes were set up with a 300-mm diameter plate and a 71 cm drop height. Elastic modulus ($E_{LWD\text{-}Z3}$) from LWD results were determined using Eq. 3.2 where E is elastic modulus (MPa); D_0 is measured deflection under the plate (mm); η is Poisson's ratio (0.4); σ_0 is applied stress (MPa); r is radius of the plate (mm); and F = shape factor = 8/3 per Vennapusa and White (2009).

$$E = \frac{(1-\eta^2)\sigma_0 r}{D_0} \times F \tag{3.2}$$

Nuclear gauge

A nuclear moisture-density gauge (NG) device was calibrated and used to measure in situ soil dry unit weights (γ_d) and moisture contents (*w*) in the base and subbase materials. Tests were performed according to ASTM D6938-10 (2010) at each test location. The average values of γ_d and *w* are reported for spatial analysis.

Dynamic Cone Penetrometer

DCP tests were performed following ASTM D6951-03 (2003) to evaluate the in situ strength of compacted base, subbase, and subgrade materials, and dynamic penetration index (DCPI) and penetration depth were determined at each test point. The weighted average DCPI was calculated for each identified subbase and subgrade layer at each test point to evaluate variability of the in-situ strength at different pavement foundation layers. The first reading of the DCPI from the beginning of the test was excluded from the calculation of the weighted average DCPI. The reason is that the initial large DCPI value was obtained at the near surface of the subbase. After compaction of the subgrade and subbase, the lack of confining pressure of the unbound layer will

have less resistance to penetration. Since the pavement surface will be constructed on the top of the subbase layer that will provide confining pressure, the exclusion of the first reading will result in a more accurate average DCPI value for the subbase layer. By evaluating the test results, MI I-94 DCPI was calculated into the weighted average value for base and subgrade layers, and MI I-96 DCPI was calculated into the weighted average value for subbase andsubgrade layers.

3.4.3. Test plan

The test point locations of MI I-94 TS1b and MI I-96 TS1 are shown in Figure 3.2 and Figure 3.3. All three LWD, NG, DCP tests were conducted at all test points in MI I-94 TS1b (Figure 3.2). Both LWD and NG tests were conducted at all tests points in MI I-96 TS1 and DCP tests were conducted at fewer test points as shown in Figure 3.3.

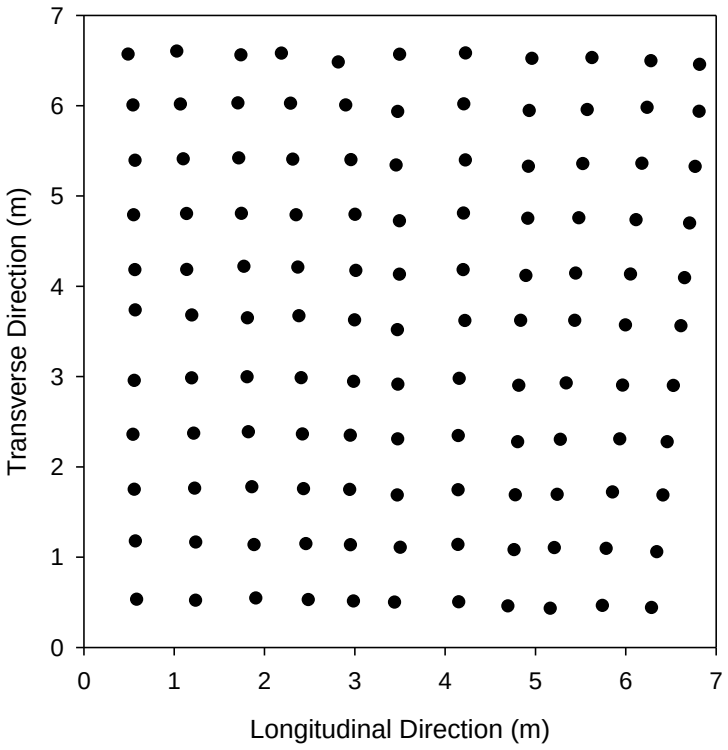

Figure 3.2. Test points in MI I-94 TS1b

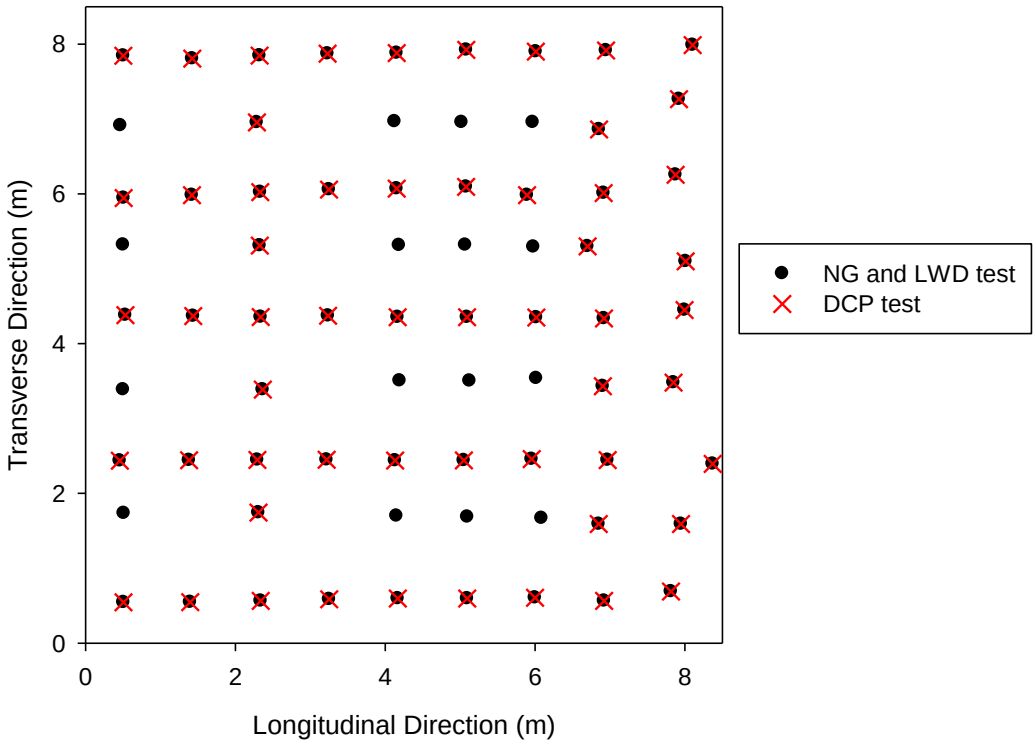

Figure 3.3. Test points in MI I-96 TS1

3.5. Method

Spatial analysis of pavement foundation properties was performed using the statistical analysis program R (Bivand et al. 2013; Pebesma 2001). the R program calculates the experimental semivariogram efficiently, fits a theoretical semivariogram model with statistical criteria to obtain the best fit to the calculated semivariogram values, and uses ordinary kriging to visualize the fitted semivariogram prediction results over the studied area.

The basic steps are summarized below:

- Calculate the omnidirectional experimental semivariogram values with adjustment on lag distance (h), angle tolerance ($\Delta\theta$), and the maximum distance.
- Plot the variogram map as a preliminary study of anisotropy of the experimental semivariogram values of the studied variable.

- Calculate the semivariogram values in four major directions withazimuth angle (θ) is equal to 0°, 45°, 90°, 135° separately to identify existence and type of anisotropy (geometric, zonal, or both), and investigate major and minor anisotropy directions that are generally perpendicular to each other.
- Fit a theoretical model to the omnidirectional experimental semivariogram if isotropic or directional semivariogram if anisotropy is identified, and record values of a, C_0, C_s and sum of square errors (SSErr).
- Perform cross-validation with the fitted semivariogram model and calculate the mean square of the prediction error (MSPE).
- Use ordinary kriging with the fitted model to predict the values at unsampled locations among the sampled points and use contour plotting to present the results.

The calculation of an omnidirectional semivariogram is useful in starting the spatial analysis for investigating the distance parameters to produce a clearer structure without having insufficient bins or amount of data pairs in each bin. The omnidirectional semivariogram can indicate an erratic directional variogram when it exists. Several tolerances (Δθ) should be tried to use the smallest tolerance value that still provide good results (Isaaks and Srivastava 1989).

Although several commercially available geostatistical analysis software are available for calculating and plotting experimental semivariograms and fitting theoretical semivariogram models, the R program allows fitting theoretical semivariograms with a weighted least square method that can provide a better statistically fitted model and allow comparison between different theoretical models.

The maximum cutoff length is controlled to be 1/3 to ½ of the maximum distance of the studied area to exclude the effect of fewer data pairs at larger separation distances when studying

the spatial variability over the test area. Figure 3.4 shows an example of a calculating experimental semivariogram of the variable E_{LWD-Z3} calculated from LWD tests performed on MI I-94 TS1b. The example shows fewer data pairs were obtained with increasing separation distances, the variance of the semivariogram values is larger at larger separation distance, and semivariogram values start to decrease at about 2/3 of the maximum distance of the studied area when number of data pairs is smaller.

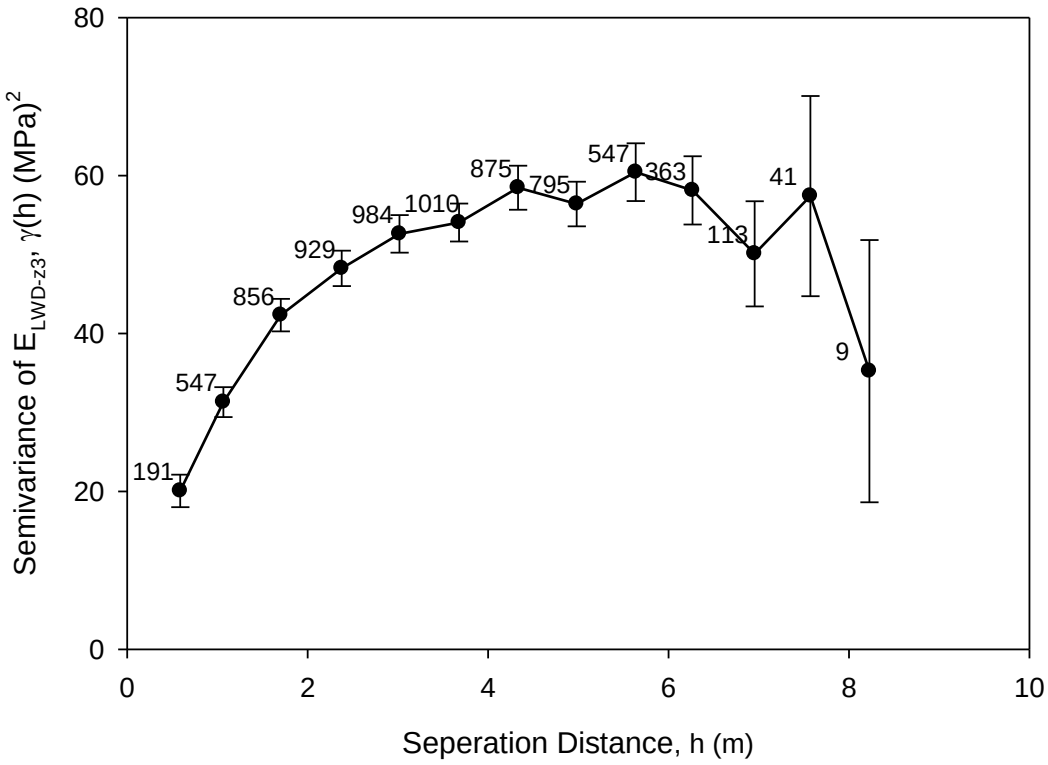

Figure 3.4. Illustration of choosing the maximum cutoff length (MI I-94 TS1b)

Extreme values or outliers should be identified and removed before calculating the experimental semivariogram, because the semivariogram values are sensitive to these extreme values that can introduce errors in studying the spatial continuity. For example, univariate statistical analysis of DCPI values on the subbase layer indicate there might be an outlier value. Figure 3.5 clearly shows the location where the extreme value, 22.648 blows/mm, was obtained.

The extreme value will significantly affect the calculation of semivariance. A bubble plot, like the one in Figure 3.5, is useful in visually identifying the location of extreme values.

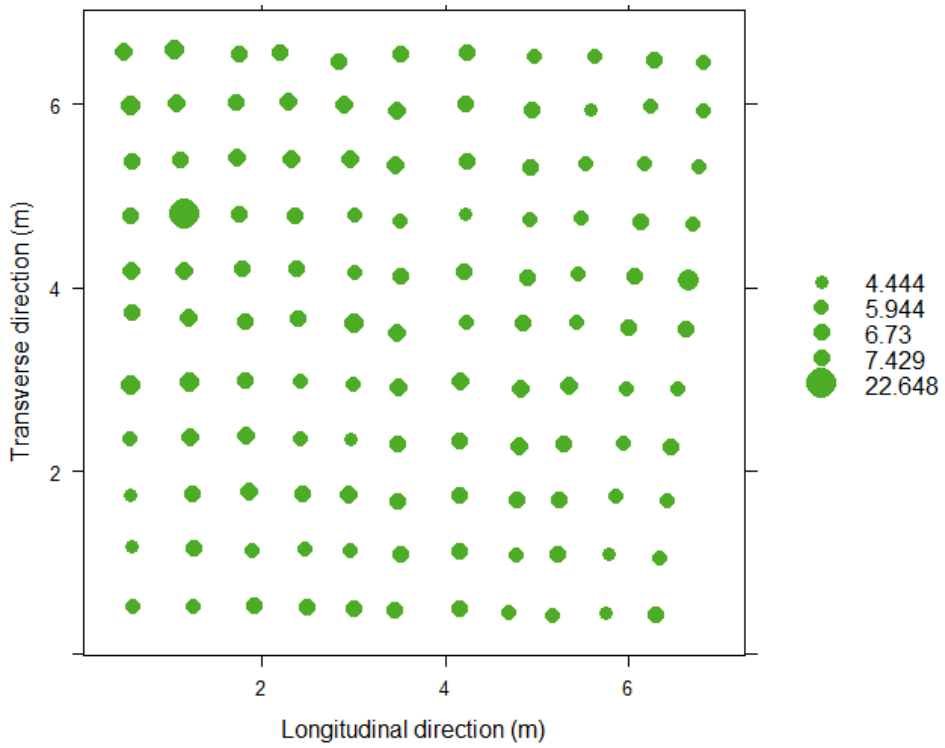

Figure 3.5. Bubble plot of DCPI values of subbase layer

3.5.1. Model types

Although the experimental semivariogram summarized the mean semivariogram for each lag distance (h), it does not give the value of correlation length that should be obtained by fitting the theoretical semivariogram models. The most important characteristic for the choice of the variogram model is the interpretation of the behavior at the origin. The objective of fitting theoretical semivariogram models to the experimental semivariogram is to capture the major spatial features of the studied variable (Goovaerts 1997). Webster and Oliver (2007) summarized several semivariogram models and there are selected model types is summarized in Table 3.2.

Table 3.2. Semivariogram models

Model	R code	Equation	Parameter note
Nugget	Nug	$\hat{\gamma}(h)=\begin{cases}0 & h=0\\ C_0 & h\neq 0\end{cases}$	
Spherical	Sph	$\hat{\gamma}(h)=\begin{cases}C_s\left(\frac{3}{2}\frac{h}{r}-\frac{1}{2}\left(\frac{h}{r}\right)^3\right) & 0\le h\le r\\ C_s & h>r\end{cases}$	$a = r$ (range reaches 100% of C_s)
Gaussian (Matérn, $k=\infty$)	Gau	$\hat{\gamma}(h)=\begin{cases}0 & h=0\\ C_s\left(1-e^{-\left(\frac{h}{r}\right)^2}\right) & h>0\end{cases}$	$a' = \sqrt{3}r$ (effective range reaches 95% of C_s)
Exponential (Matérn, $k=0.5$)	Exp	$\hat{\gamma}(h)=\begin{cases}0 & h=0\\ C_s\left(1-e^{-\frac{h}{r}}\right) & h>0\end{cases}$	$a' = 3r$ (effective range reaches 95% of C_s)
Whittles (Matérn, $k=1$)	Bes	$\hat{\gamma}(h)=\begin{cases}0 & h=0\\ C_s\left(1-\left(\frac{h}{r}\right)K_1\left(\frac{h}{r}\right)\right) & h>0\end{cases}$	$a' = 4r$ (effective range reaches 95% of C_s)
Matérn	Mat	$\hat{\gamma}(h)=\begin{cases}0 & h=0\\ C_s\left(1-\frac{1}{2^{k-1}\Gamma(k)}\left(\frac{h}{r}\right)^k K_k\left(\frac{h}{r}\right)\right) & h>0\end{cases}$	k (smoothness parameter)

Note: $\Gamma(k)$ and $K_k(h/r)$ are Gamma function and modified Bessel function of the second kind with order k respectively, r is the range parameter obtained in R program.

Goovaerts (1997) suggested that models with parabolic behavior at the origin (i.e., Gaussian model) should be used for highly continuous properties (i.e., Ground water level) and Wackernagel (2003) said that the Gaussian model is “pathological”. The Gaussian model is not suggested (Wackernagel 2003; Webster and Oliver 2007) for describing the spatial variability of general properties that are not highly continuous. Pavement foundation properties are not be expected to be highly continuous variable, so a Gaussian model will be not be used in this paper.

This paper will instead consider application of a spherical (Sph) model, an exponential (Exp) model, and Matérn (Mat, $k=1$) models in describing spatial variability of pavement foundation properties.

The Matérn model class has a smoothness parameter (*k*) to describe the behavior of the semivariogram at the origin. The exponential model, Whittle's model, and Gaussian model are particular cases of the Matérn model with *k* equal to 0.5, 1, and infinity, respectively. With $k=\infty$ the Gaussian model describes the most continuous origin behavior.

An experimental semivariogram is meaningless with only a pure nugget effect model fitted that indicates the studied properties lack spatial continuity within the studied area (Olea 2006). Therefore, the nugget model is generally nested with other models. Nested models are combinations of different models where properties of the original models are not changed. There are many possible combinations of semivariogram models. A combination of basic models is generally required to satisfactorily fit the directional experimental semivariogram, but overfitting the semivariogram with complicated a model that consists of three or more basic models usually will not result in more accurate estimates than using the simpler models.

Olea (2006) reported that nested models are often a combination of two simple models and one pure nugget effect model as shown in Eq. 3.3.

$$\hat{\gamma}(h)=\sum_{i=0}^{k} C_0+C_i\gamma_i(h) \tag{3.3}$$

Equation 3.4 shows a nested model consisting of a nugget effect model, an exponential model, and a Gaussian model:

$$\hat{\gamma}(h)=\begin{cases} 0 & h=0 \\ C_0+C_{s1}\left(\frac{3}{2}\frac{h}{a_1}-\frac{1}{2}\left(\frac{h}{a_1}\right)^3\right)+C_{s2}\left(1-e^{-3\left(\frac{h}{a_2}\right)}\right) & h\neq 0 \end{cases} \tag{3.4}$$

Figure 3.6 shows semivariogram plots of these four models with values assigned to C and a and a′ where sill = 1.

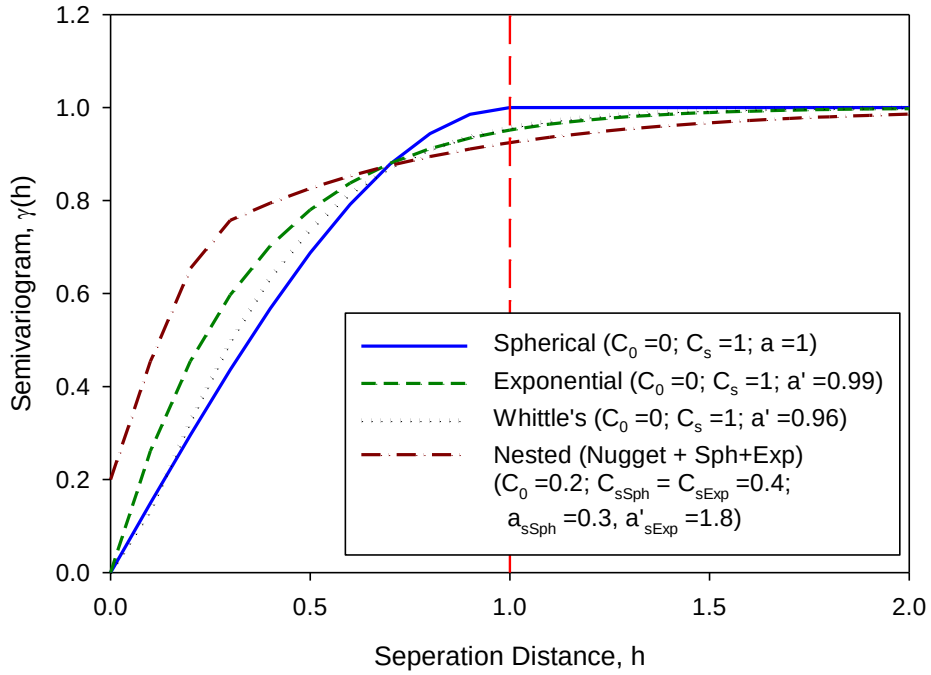

Figure 3.6. Sample semivariogram plots of spherical, exponential, Gaussian, and nested models with values assigned to C and a and a′ where sill = 1

3.5.2. Model selection

The theoretical model can be fit to the experimental semivariogram to describe the spatial variability of the data with quantified parameters. The theoretical model can be selected based on one of two methods; one method chooses the model that best fits the calculated experimental semivariogram values, another method chooses the model that gives the best predictions. Four statistical criteria are discussed here. Three methods for defining the "best fit" use either the squared errors (SSErr), Akaike information criterion (AIC), or Cressie goodness of fit (GoF). The mean squares prediction error (MSPE) can be used to choose the model that give the "best" predictions.

Fitting a semivariogram model by eye relies on the averaged semivariance values at each lag distance and ignores the number of pairs of data spaced at that lag distance. A weighted least squares method as Cressie (1985) suggested will be used for this study. The weighted least

squares method gives the most weight to the early lags and less weight to those lags that have fewer data pairs. Therefore, the weighted least squares method allows fitting the theoretical model to capture the major spatial characteristics of the variable, rather than not to be the closest to the experimental values.

There are several methods for calculating the weight (w_i) for the weighted least squares fit, the weight calculation method used in this study is presented in Eq. 3.5 with N_i is the number of data pairs that are separated by a distance h_i.

$$w_i = \frac{N_i}{h_i^2} \tag{3.5}$$

In this study, exponential, spherical, and Matérn (k=1) model will be fitted to the experimental semivariogram and the nested model of more than one structure might be used to better describe the anisotropic experimental semivariogram. The sum of square errors (SSErr) is calculated for each fitted theoretical semivariogram to describe how well the model fits the experimental semivariogram. In calculation of SSErr (Eq. 3.6), $\hat{\gamma}(h_j)$ is the predicted semivariogram value with the fitted theoretical model and $\gamma(h_i)$ is the average experimental semivariogram value at a set of lag distance h_i.

$$SSErr = \sum_{i=1}^{n} w_i \left[\hat{\gamma}(h_i) - \gamma(h_i)\right]^2 \tag{3.6}$$

Akaike information criterion (AIC) can also be used to assess the goodness of fit as well as the parsimony of the model (Jian et al. 1996; Webster and Oliver 2007). Equation 3.7 is used to calculate AIC where n is the number of experimental semivariogram values and p is the number of parameters in that theoretical model. Since the three models (i.e., spherical, exponential, Matérn with k=1) have the same p is equal to three, using the AIC criteria is not different from using SSErr.

$$\widehat{AIC} = n \ln\left(\frac{SSErr}{n}\right) + 2p \tag{3.7}$$

Clark and Harper (2002) suggested a modified Cressie goodness of fit (GoF) criteria to measure how well the model fits the data. Smaller GoF indicates better fit of the theoretical semivariogram model to the experimental semivariogram values. GoF is calculated with Eq. 3.8 that N_h is the number of data pairs used to calculate the average experimental semivariogram $\gamma(h)$ at lag or separation distance h, and $\hat{\gamma}(h)$ is the fitted theoretical semivariogram at h.

$$GoF=\frac{1}{\sum_h N_h}\sum_h N_h\left(\frac{\hat{\gamma}(h)-\gamma(h)}{\gamma(h)}\right)^2 \quad (3.8)$$

SSErr, AIC and GoF are used to measure how well the theoretical model fits the experimental semivariogram values. However, they may not measure the goodness of using the fitted model to describe the spatial variability of the studied variable. Therefore, the mean squared prediction error (MSPE) using the fitted model to predict the variable values at unsampled locations, calculated from cross-validation, can be used to evaluate the better semivariogram model for that variable.

The objective of fitting the experimental semivariogram is to describe the spatial continuity of the studied variable and ultimately to estimate the variable values at the unsampled locations. The impacts of different models on interpolating experimental semivariogram results can be compared through cross-validation (Isaaks and Srivastava 1989). The cross-validation process involves removing the first data value $Z(\mathbf{s}_i)$ at location $\mathbf{s}_i$ (i=1 to N) and using the rest (N-1) of the data values sampled over the study area to fit the theoretical semivariogram model and predicted $\hat{Z}(\boldsymbol{s}_i)$ and calculating the squared error for the first data value. The cross-validation process is repeated for all data values sampled at all N locations $\mathbf{s}_i$, and the average squared error in the cross-validation process is calculated as the mean squared prediction error (MSPE) in Eq. 3.9.

$$MSPE = \frac{1}{N}\left[Z(\boldsymbol{s}_i) - \hat{Z}(\boldsymbol{s}_i)\right]^2 \quad (3.9)$$

The idea consists of removing one datum at a time from the data set and re-estimating this value from the remaining data using the different semivariogram models. Interpolated and actual values are compared, and the model that yields the most accurate predictions is retained

3.5.3. Anisotropy

Anisotropy is the phenomenon that the spatial variability is a function of the magnitude and the direction of the separation distance vector ***h***. Two types of two-dimensional anisotropy are defined as geometric anisotropy and zonal anisotropy (Goovaerts 1997) and shown in Figure 3.7. Eriksson and Siska(2000) clarified the details in calculations of modelling anisotropy in spatial analysis with defining the types of anisotropy to be nugget anisotropy, range anisotropy, and sill anisotropy. Isaaks and Srivastava (1989) and Goovaerts (1997) presented the concept of geometric and zonal anisotropy in spatial analysis.

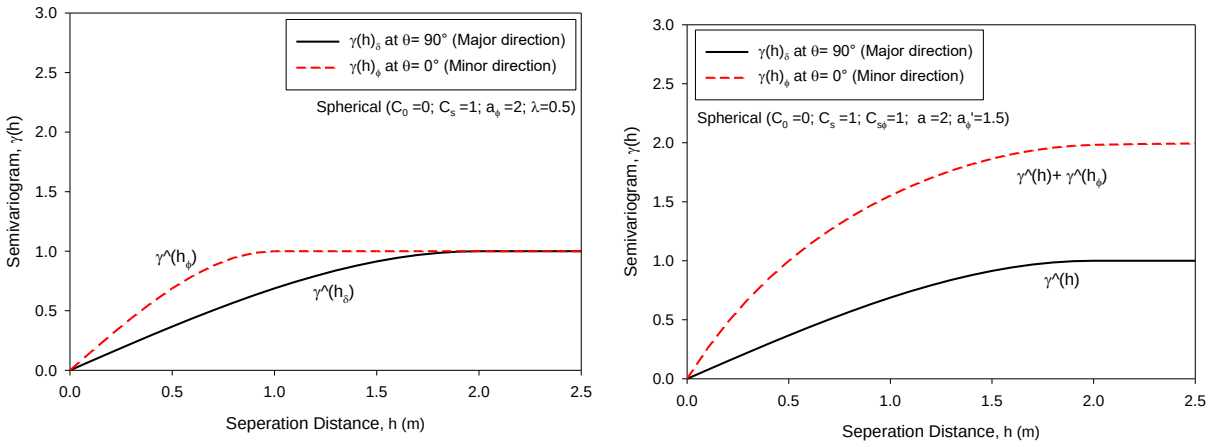

Figure 3.7. Types of anisotropy: geometric anisotropy (left); zonal anisotropy (right)

Geometric anisotropy can be identified when the directional semivariograms have the same shape and sill values (C_0 and C_s) but different range values and the rose diagram or plot of range values versus the azimuth θ of the direction is an ellipse (Goovaerts 1997). Azimuth angle θ is counted clockwise from the north. The anisotropy ratio ($\lambda<1$) is the ratio of the minor range (a_ϕ) to the major range (a_δ) of the directional semivariograms that are generally perpendicular to each

other. Zonal anisotropy can be identified when the directional semivariograms have different partial sill values.

Geometric anisotropic semivariogram can be modeled by clockwise rotating the coordinate system to make the major direction (δ) that has the longer range to be aligned with an axis and rescale the anisotropic range to be the minor range a_ϕ (Eq. 3.10).

$$\gamma(\boldsymbol{h}) = \gamma(\boldsymbol{h}^*) \quad \text{with} \quad \boldsymbol{h}^* = \begin{bmatrix} 1 & 0 \\ 0 & \lambda \end{bmatrix} \begin{bmatrix} cos\delta & -sin\delta \\ sin\delta & cos\delta \end{bmatrix} \boldsymbol{h} \tag{3.10}$$

Zonal anisotropic semivariogram can be modeled by clockwise rotating the coordinate system to have the direction that shows the maximum continuity (lowest C_s) aligned with an axis and set the range (a_δ) in that direction to be a very large value towards infinity (λ) is very small towards zero) (Eq. 3.11).

$$\gamma(\boldsymbol{h}) = \gamma_1(\mathrm{h}) + \gamma_2(\boldsymbol{h}^*) \quad \text{with} \quad \boldsymbol{h}^* = \begin{bmatrix} 1 & 0 \\ 0 & 0 \end{bmatrix} \begin{bmatrix} cos\delta & -sin\delta \\ sin\delta & cos\delta \end{bmatrix} \boldsymbol{h} \tag{3.11}$$

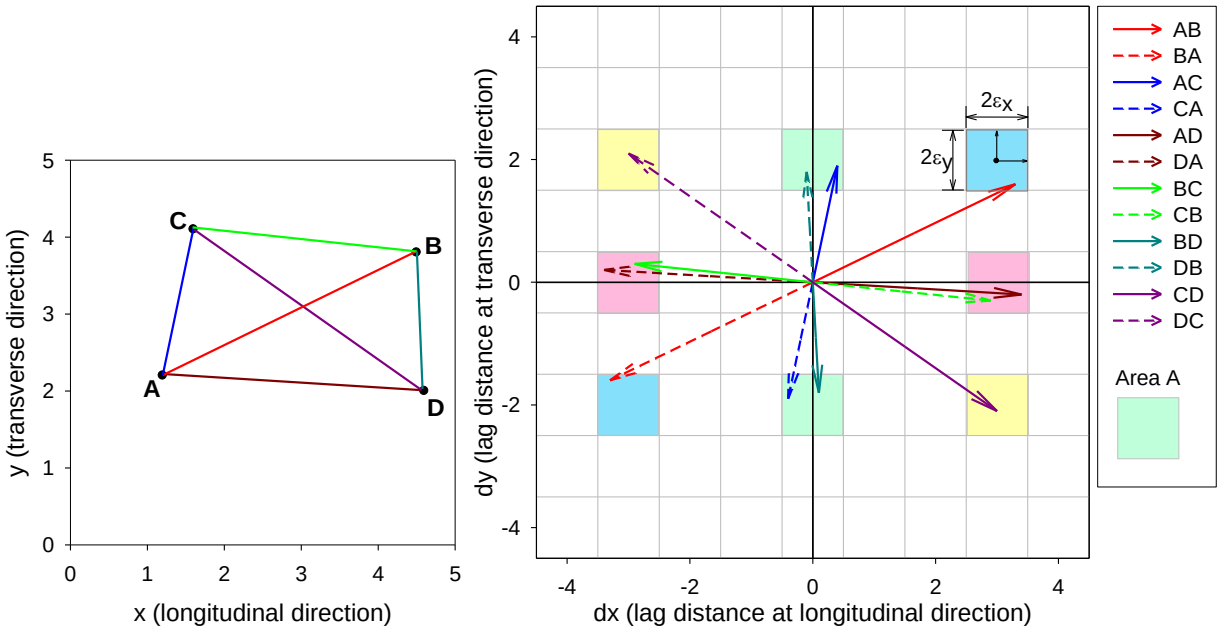

Figure 3.8. Methodology of plotting semivariogram map

Semivariogram maps (Goovaerts 1997; Isaaks and Srivastava 1989) can be used as a tool that can detect anisotropy directions. The computation of a semivariogram map requires considering

many directions and lags. A semivariogram map can be a useful tool in the preliminary study of the major and minor spatial continuity directions. However, the spatial resolution of the semivariogram map will be largely reduced when sparse and irregular spaced data are collected (Facas et al. 2010). Figure 3.8 shows the process of plotting the semivariogram map and also shows semivariogram values are the same in the opposite direction.

Another tool that can quickly reveal anisotropy is a semivariogram contour map (Isaaks and Srivastava 1989) which is similar to the semivariogram map but the average values calculated in each area cell will be used for the contour plot. We don't know the actual population mean of the studied variable, so we will use ordinary kriging to estimate the value at unsampled locations. Simple kriging requires input of the population mean that means we know the actual mean value, but we cannot say the sample mean is the population mean.

3.5.4. Kriging

The word kriging means optimal prediction (Cressie 1993). Kriging is used to make prediction on values of a continuous variable Z at unsampled locations using the observed value at sampled locations of the study area. Kriging makes no distributional assumptions and the variates are statistically correlated. Ordinary kriging and the minimum mean squared prediction error will be used in this study to present the fitted semivariogram model. The two assumptions in ordinary kriging are that the local mean is unknown but constant and the sum of the coefficients of the linear predictor is equal to one. The assumptions guarantee that the mean of the predicted values is the same as the observed values over the study area (Cressie 1993; Goovaerts 1997; Journel and Huijbregts 1978). The brief description of ordinary kriging is only to introduce the basics of understanding how the kriged contour map is created. The ordinary

kriging estimator $Z_{OK}^{*}(\mathbf{s})$ at location **s** is written as a linear combination of the n(s) random variables $Z(s_i)$ with the kriging weights forced to be equal to 1 (Eq. 3.12).

$$Z_{OK}^{*}(\mathbf{s}) = \sum_{i=1}^{n(\mathbf{s})} \varepsilon_i^{OK}(\mathbf{s}) Z(\mathbf{s}_i) \quad \text{with} \quad \sum_{i=1}^{n(\mathbf{s})} \varepsilon_i^{OK}(\mathbf{s}) = 1 \tag{3.12}$$

3.6. Univariate statistical analysis

The univariate statistics of pavement foundation properties $E_{LWD\text{-}Z3}$, γ_d, w, $DCPI_{subbase}$, and $DCPI_{subgrade}$ of both test sections MI I-94 TS1a (Figure 3.2) and MI I-96 TS1 (Figure 3.3) are summarized in Table 3.3. Each variable was studied by plotting a histogram, examining skewness, and identifying outliers. The collected data for each property variable do not show extremely skewed and no transformation of the data was made for spatial variability analysis. One extreme value or outlier of $DCPI_{subbase}$ was identified at a sample location in MI I-94 TS1b (Figure 3.5) and removed for spatial variability analysis.

Table 3.3. Soil properties summary for studied test sections

Project Test Section	Univariate Statistics	$E_{LWD\text{-}Z3}$ (MPa)	γ_d (kN/m^3)	w (%)	$DCPI_{subbase}$ (mm/blow)	$DCPI_{subgrade}$ (mm/blow)
MI I-94 TS1b	Mean ($\bar{x}$)	58.5	20.00	2.3	7	43
	Median	58.6	20.00	2.3	7	43
	Variance (s^2)	50.5	0.38	0.1	1.3	61.3
	Std Dev (s)	7.1	0.61	0.3	1.1	7.8
	COV	12	3	14	17	18
	N	121	121	121	120	121
	Skewness	0.43	-0.13	-0.70	0.48	-0.07
MI I-96 TS1	Mean ($\bar{x}$)	30.9	20.16	7.8	19	8
	Median	31.3	20.15	7.7	19	7
	Variance (s^2)	124.1	0.34	1.0	20.7	6.3
	Std Dev (s)	11.1	0.59	1.0	4.5	2.5
	COV	36	3	13	24	32
	N	73	73	73	57	57
	Skewness	-0.20	-0.03	0.47	0.37	0.92

The overall sample mean ($\bar{x}$) of $E_{LWD\text{-}Z3}$ determined LWD test is higher in MI I-94 TS1b than in MI I96 TS1, the reason could be that the LWD tests were performed on top of the base layer in MI I-94 TS1b and on top of the subbase layer in MI I96 TS1 while $E_{LWD\text{-}Z3}$ presents the stiffness of the composite pavement foundation layers not a single layer. However, the coefficient of variation (COV) is higher in MI I96 TS1 than in MI I-94 TS1b. This indicates there are some possible soft spots that could be identified in MI I96 TS1.

Histograms of each variable are created as shown in Figure 3.9 to Figure 3.13. Univariate statistics show that dry unit weight (γ_d) and moisture content (w) that determined NG test at a desired point within the base/subbase layer are less variable in both test sections than the other variables. DCPI of both subbase and subgrade layer determined from DCP tests shows high COV and higher COV was obtained in MI I96 TS1. The sample mean value of DCPI is lower in the subgrade layer than the base layer of MI I-94 TS1b. This means the subbase layer could be stiffer than the subgrade layer, on average. However, the sample mean value of DCPI is higher in the subgrade layer than the subbase layer of MI I-96 TS1. This means the subbase layer could be insufficiently compacted in some areas. The preliminary analysis of the pavement foundation properties with univariate statistics should be further studied with spatial variability analysis.

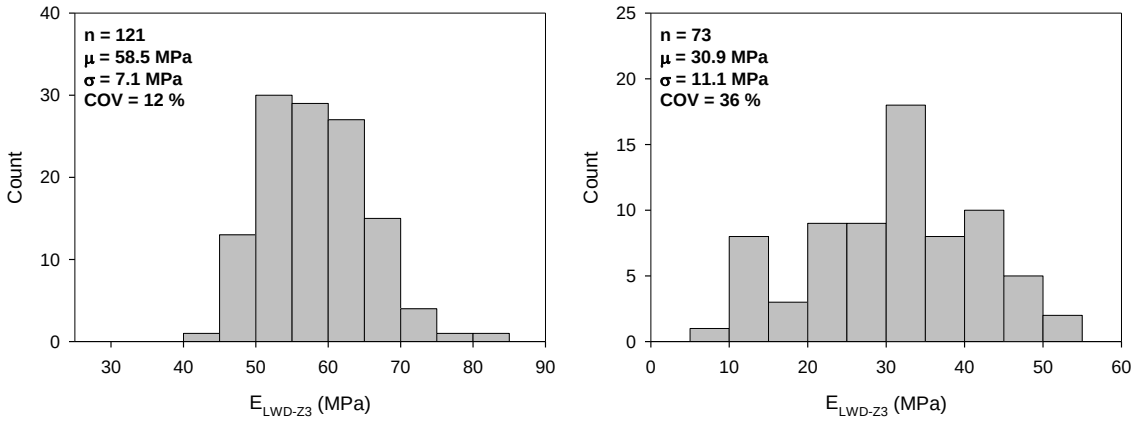

Figure 3.9. Histogram of $E_{LWD\text{-}Z3}$ on MI I94 TS1b (left) and MI I96 TS1 (right)

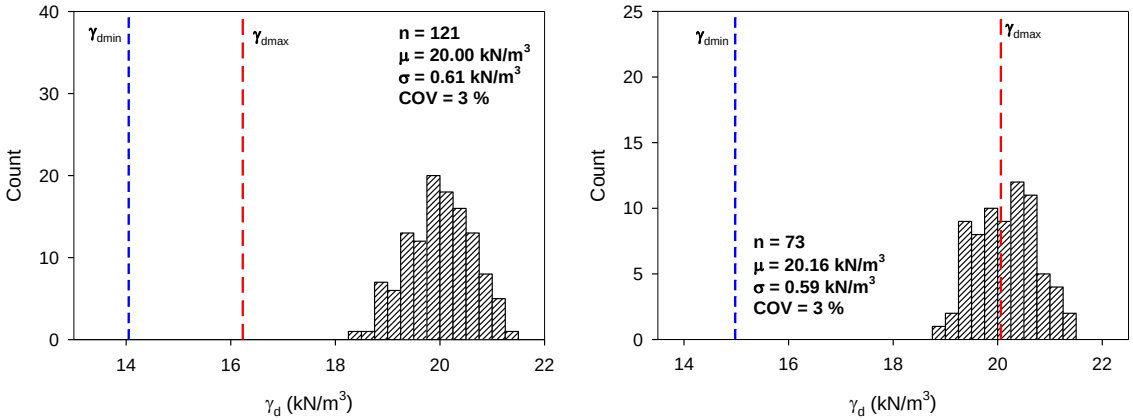

Figure 3.10. Histogram of γ_d on MI I94 TS1b (left) and MI I96 TS1 (right)

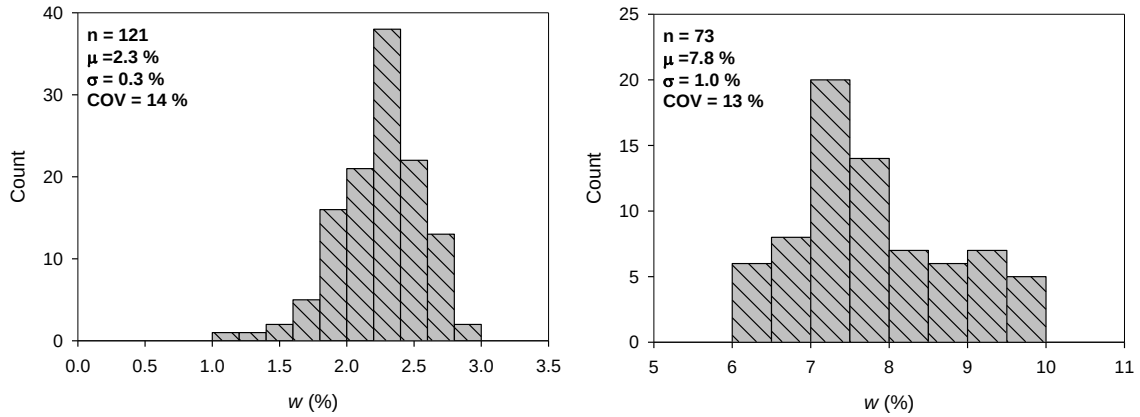

Figure 3.11. Histogram of *w* on MI I94 TS1b (left) and MI I96 TS1 (right)

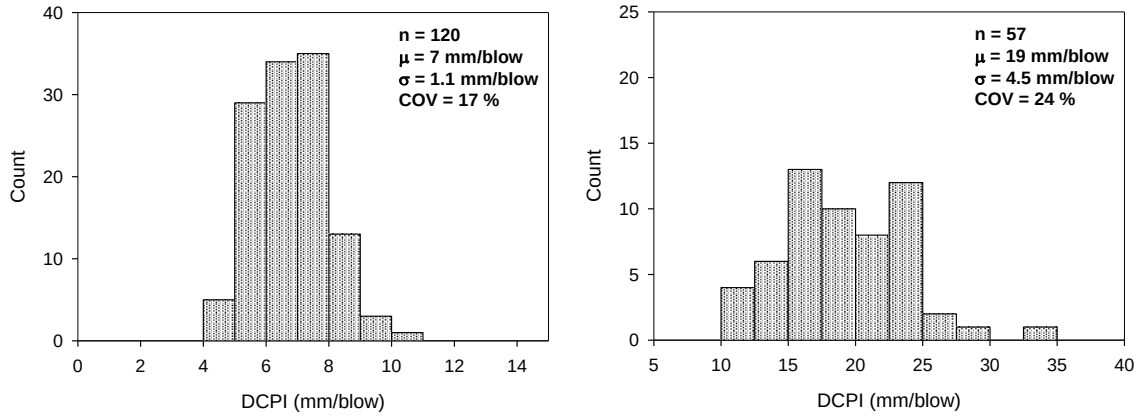

Figure 3.12. Histogram of $DCPI_{subbase}$ on MI I94 TS1b (left) and MI I96 TS1 (right)

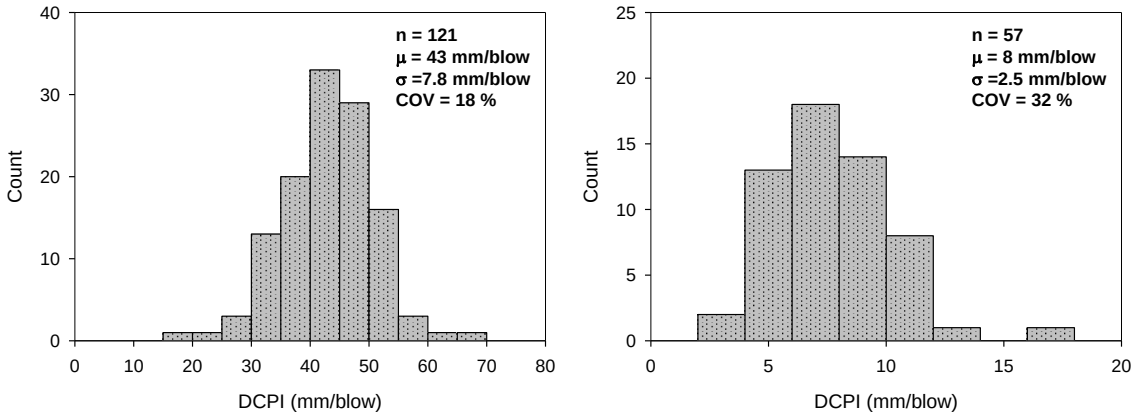

Figure 3.13. Histogram of $DCPI_{subgrade}$ on MI I94 TS1b (left) and MI I96 TS1 (right)

3.7. Spatial variability analysis

Spatial variability analysis is used to characterize and quantify the spatial continuity of the five studied pavement foundation property variables $E_{LWD\text{-}Z3}$, γ_d, w, $DCPI_{subbase}$, and $DCPI_{subgrade}$. The omnidirectional semivariogram which neglects the directions is the isotropic semivariogram modelling. The omnidirectional semivariogram and directional semivariogram will be studied to explore the anisotropy of each variable over each of the studied test sections and to examine the need of modeling the possible anisotropy.

3.7.1. Omnidirectional semivariogram

The experimental semivariogram of each property variable was calculated as omnidirectional, the spatial variability is only investigated with the distance h that data pairs are apart and assumes isotropic spatial correlation. Three theoretical semivariogram models, spherical, exponential, and Matérn (k=1), are used to fit the experimental semivariogram using weighted least square methods. The model parameters are estimated and the statistical criteria of choosing the better fitted model that including SSErr, GoF, and MSPE are summarized in Table 3.4.

Table 3.4. Summary of spatial analysis with omnidirectional semivariogram

Project Site		MI I-94 TS1b			MI I-96 TS1		
Properties	$\hat{\gamma}(\mathbf{h})$ **estimation parameters**	**Model Type**			**Model Type**		
		Sph	**Exp**	**Mat, k=1**	**Sph**	**Exp**	**Mat, k=1**
$E_{LWD\text{-}Z3}$ (MPa)	C_0	11.45	4.145	12.52	0	0	12.18
	Cs	41.54	54.644	44.04	146.6	212.2	161.43
	r	3.167	1.45	0.9489	3.437	2.772	1.247
	a or a′	3.167	4.35	3.7956	3.437	8.316	4.988
	SSErr	15829	15555	16009	159196	170814	164420
	GoF	0.0050	0.0055	0.0054	0.0412	0.0442	0.0417
	MSPE	22.84	22.77	23.08	46.25	44.74	43.72
γ_d (kN/m^3)	C_0	0.1522	0.1283	0.1635	0.05901	0.03935	0.08359
	Cs	0.2088	0.2818	0.2256	0.34	0.34	0.34
	r	3.412	1.885	1.121	6.891	2.966	2.238
	a or a′	3.412	5.655	4.484	6.891	8.898	8.952
	SSErr	0.1845	0.1702	0.1723	0.1156	0.189	0.1293
	GoF	0.0024	0.0022	0.0022	0.0104	0.0170	0.0117
	MSPE	0.2106	0.2107	0.2115	0.135	0.1372	0.1362
w (%)	C_0	0.06975	0.04562	0.07216	0.07296	0.01137	0.1771
	Cs	0.27523	0.98209	0.3576	1.00653	1.48051	1.1507
	r	48.46	128.3	12.34	3.757	2.69	1.484
	a or a′	48.46	384.9	49.36	3.757	8.07	5.936
	SSErr	0.02271	0.9678	0.01504	5.168	5.39	5.277
	GoF	0.0031	0.0784	0.0021	0.0399	0.0427	0.0421
	MSPE	0.0807	0.08093	0.0811	0.3937	0.4124	0.4085
$DCPI_{subbase}$ (mm/blow)	C_0	0.5344	0.3036	0.51	0	0	0
	Cs	0.6974	0.9745	0.7569	26.57	46.05	30.95
	r	2.197	0.817	0.6018	3.8	3.923	1.232
	a or a′	2.197	2.451	2.4072	3.8	11.769	4.928
	SSErr	5.364	5.565	5.31	2387	2608	2302
	GoF	0.0027	0.0025	0.0024	0.0728	0.0737	0.0702
	MSPE	0.9048	0.8679	0.8701	11.76	11.97	11.95
$DCPI_{subgrade}$ (mm/blow)	C_0	0	0	0	2.11	0	0
	Cs	57.61	58.79	58.61	3.995	5.954	5.551
	r	0.848	0.3019	0.211	4.091	1.101	0.5887
	a or a′	0.848	0.9057	0.844	4.091	3.303	2.3548
	SSErr	16893	21970	19925	179.5	170.2	169.4
	GoF	0.0022	0.0022	0.0021	0.0390	0.0424	0.0461
	MSPE	60.3	60.41	60.48	3.455	3.514	3.56

The estimated model parameters for each variables summarized in Table 3.4 show that there is no single best model type that can better fit the experimental semivariogram than the other two

models. The exponential $\hat{\gamma}(h)$ model estimates the largest range or effective range value, a, in most of the cases while the Matérn (k=1) model estimates the largest nugget effect, C_0, in all cases. The better fitted model is chosen according the statistical criteria to present the results in characterizing and quantifying the isotropic or omnidirectional spatial variability. The smaller value of each of three statistical criteria SSErr, GoF, and MSPE is desired and indicate a better fitted model. Since the range value of the studied variables is close to or larger than the 1/3 of the maximum distance that data pairs are apart over the study area, the difference of three models in the initial part of the semivariogram cannot be identified for the experimental semivariogram without $\gamma(h)$ values at distance smaller than 0.5 m in MI I94 TS1b and 0.7 m in MI I96 TS1.

MI I94 TS1b

The sill of the omnidirectional experimental semivariogram of $E_{LWD\text{-}Z3}$ is higher than the sample variance slightly (Figure 3.14) which indicates a possible trend or an anisotropic semivariogram.

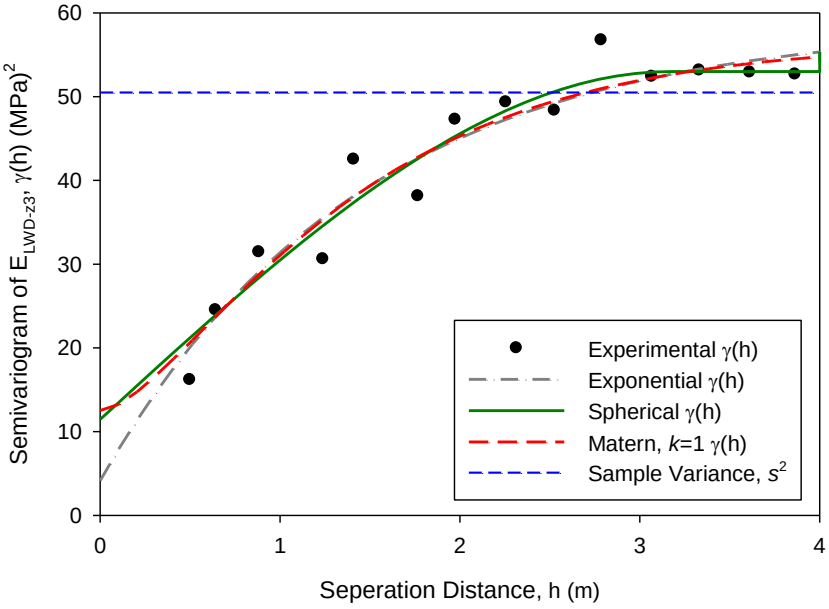

Figure 3.14. Omnidirectional $\gamma(h)$ of $E_{LWD\text{-}Z3}$ with fitted $\hat{\gamma}(h)$ on MI I94 TS1b

Figure 3.15 shows the contour plot of the ordinary kriging values with the selected exponential model has smaller MSPE in the three studied models. A less variable E_{LWD-Z3} with distance in the transverse direction is presented in Figure 3.15 and further analysis with directional variability should be performed to identify correlation length in different directions.

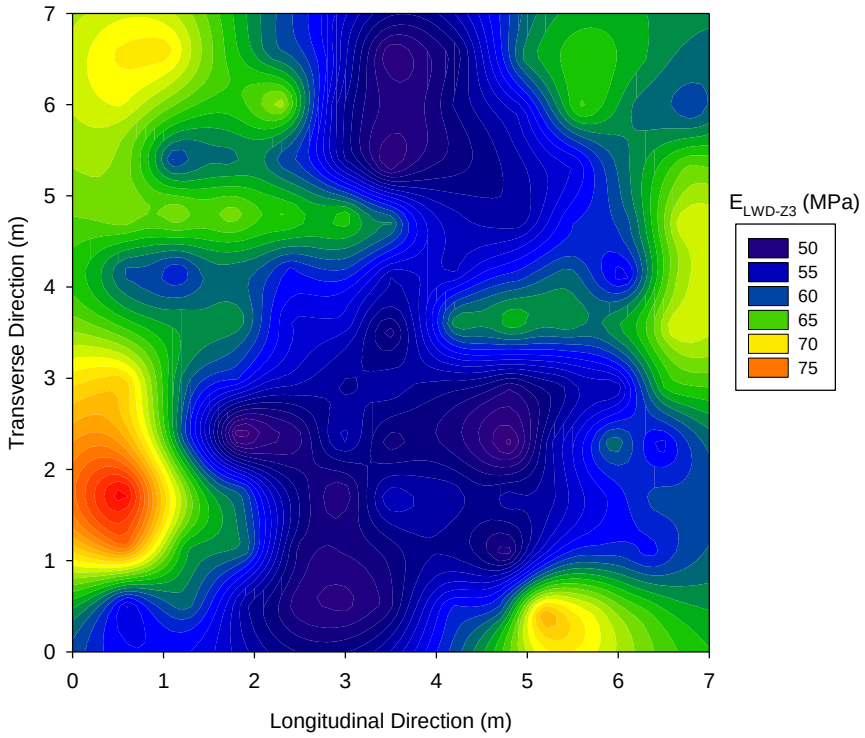

Figure 3.15. Ordinary kriging of E_{LWD-Z3} with fitted omnidirectional exponential $\hat{\gamma}(\mathbf{h})$ on MI I94 TS1b

Omnidirectional $\gamma(h)$ of γ_d is calculated and fitted with three models that shows increasing $\gamma(h)$ with separation distance and close to the sample variance (Figure 3.16), but the nugget values of $\hat{\gamma}(h)$ is relatively larger compared to its sill value. The measurement error or insufficient sampling at smaller spacing might be the cause for the relatively high nugget value. The ordinary kriging values of γ_d with the selected spherical model plotted in Figure 3.17 that less compacted area can be observed at the upper left portion of the studied area.

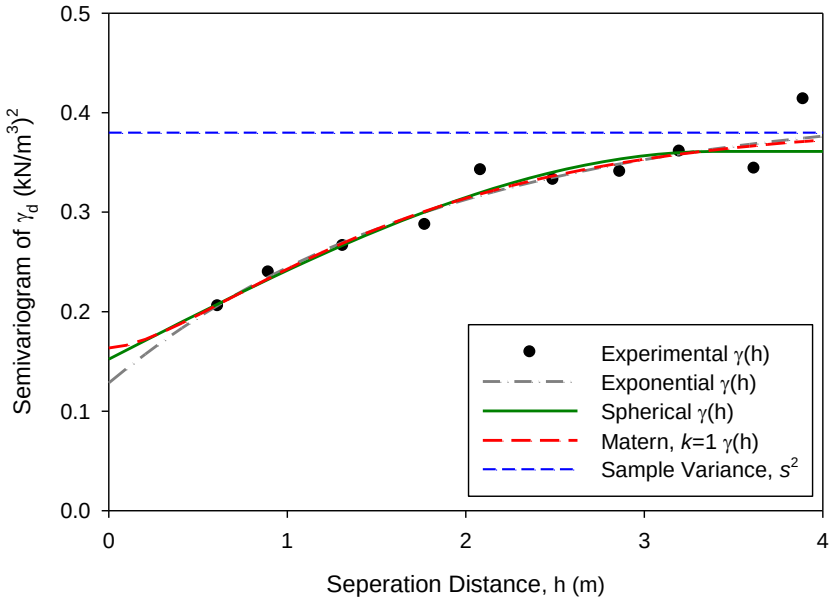

Figure 3.16. Omnidirectional γ(h) of γ_d with fitted $\hat{\gamma}(\mathbf{h})$ on MI I94 TS1b

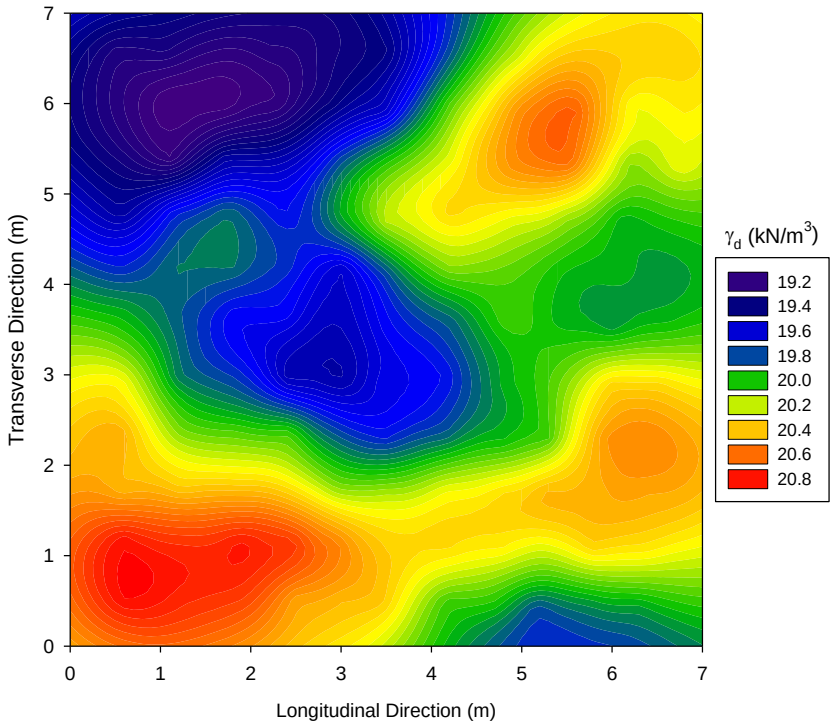

Figure 3.17. Ordinary kriging of γ_d with fitted omnidirectional spherical $\hat{\gamma}(\mathbf{h})$ on MI I94 TS1b

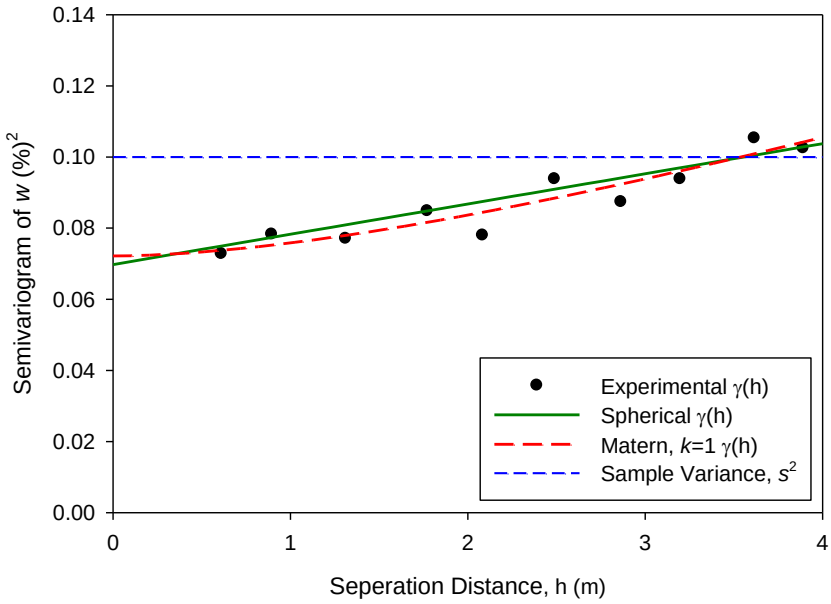

Figure 3.18. Omnidirectional γ(h) of *w* with fitted $\hat{\gamma}(\mathbf{h})$ on MI I94 TS1b

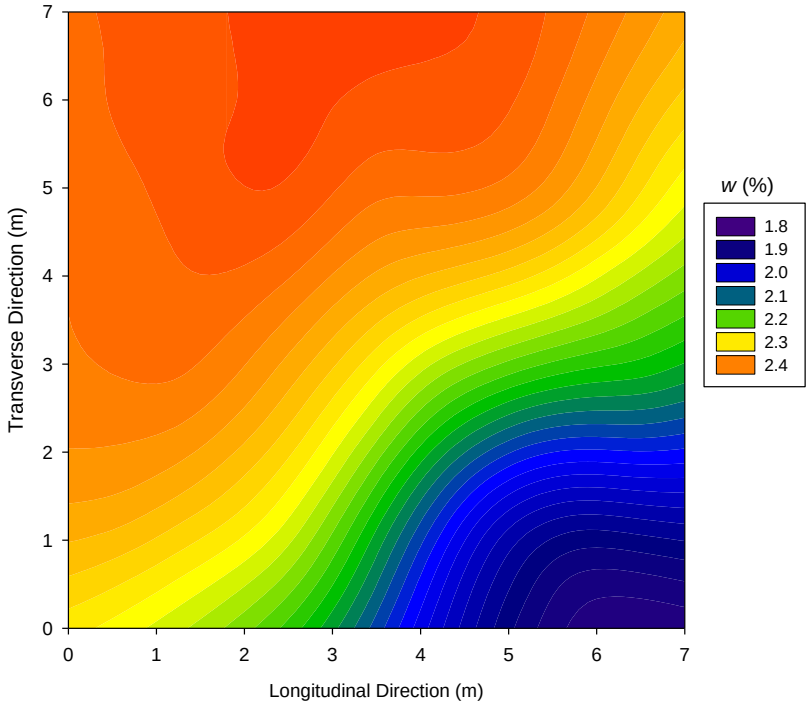

Figure 3.19. Ordinary kriging of *w* with fitted omnidirectional exponential $\hat{\gamma}(\mathbf{h})$ on MI I94 TS1b

Omnidirectional γ(h) of moisture content as shown in (Figure 3.18) shows a very large nugget effect compared to the sample variance and a trend can be observed in the fitted

semivariogram with range estimated as about 50 m. The experimental omnidirectional γ(h) calculated in this study area is close to a straight line, this could be caused by a leaking water tank in the study area during the pavement base construction except a leaking of water tank at the study area. The raw data should be examined for reliability. The ordinary kriging plot of *w* with all three models, like the example with the fitted Matérn (*k*=1) model (Figure 3.19) shows clear trend that *w* is higher in upper left triangle portion than the lower right portion of the studied area. However, with knowledge of in-situ measured *w* values, the raw data could have possible mistakes.

The weighted average DCPI values of subbase and subgrade indication average ability of that layer to resist penetration and higher DCPI indicates less stiffness would be expected at that location. The omnidirectional γ(h) of $DCPI_{subbase}$ and $DCPI_{subgrade}$ are shown in Figure 3.20 and Figure 3.22 separately. A longer range value was observed in $DCPI_{subbase}$ than $DCPI_{subgrade}$ which indicates higher spatial correlation could be observed in weighted average DCPI of the subbase layer than the subgrade layer. The experimental semivariogram calculated for $DCPI_{subbase}$ shows a nearly zero nugget effect, only a few γ(h) values within the first 1 m separation distance show a possible correlation of $DCPI_{subgrade}$ with spacing distance. The zero nugget effect and short range value modelled in $DCPI_{subgrade}$ predicted values at unsampled location around the sampled location with variation equal to the sill value which shows up as a small circle areas with similar values in the ordinary kriging plot of $DCPI_{subgrade}$ shown in Figure 3.23. The longer range value indicated correlation of $DCPI_{subbase}$ with longer spacing distance up to 2 m is presented with the ordinary kriging contour plot (Figure 3.21) that larger area of unsampled locations around the sampled locations have similar values.

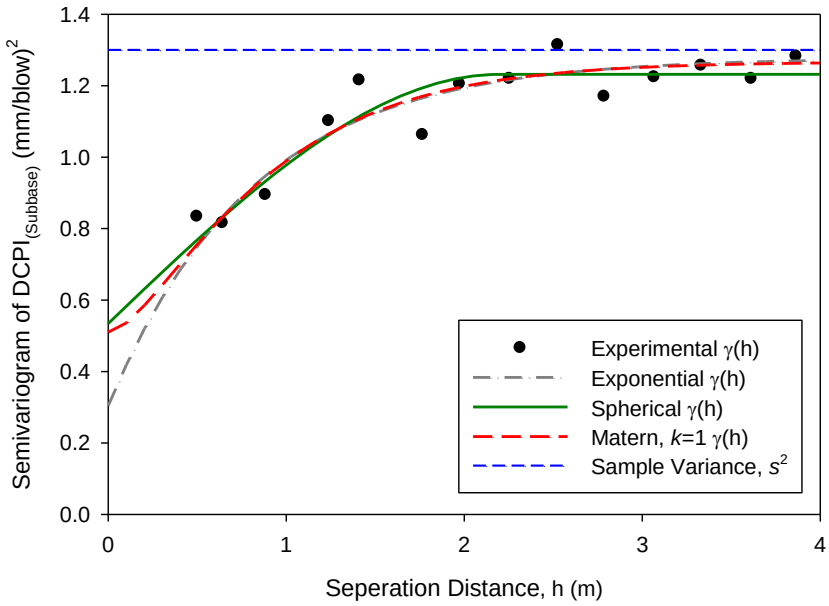

Figure 3.20. Omnidirectional γ(h) of $DCPI_{subbase}$ with fitted $\hat{\gamma}(h)$ on MI I94 TS1b

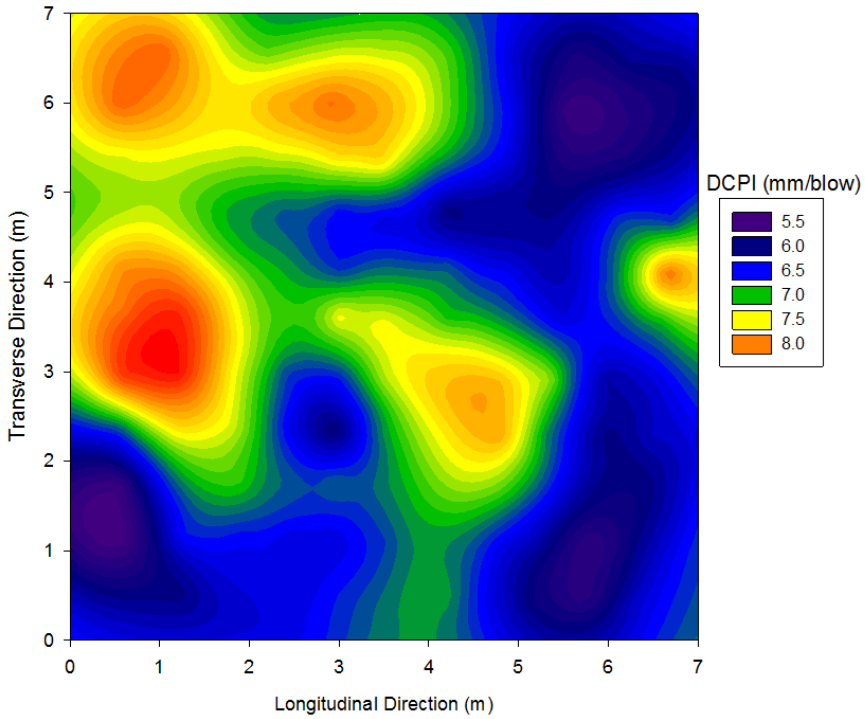

Figure 3.21. Ordinary kriging of $DCPI_{subbase}$ with fitted omnidirectional spherical $\hat{\gamma}(h)$ on MI I94 TS1b

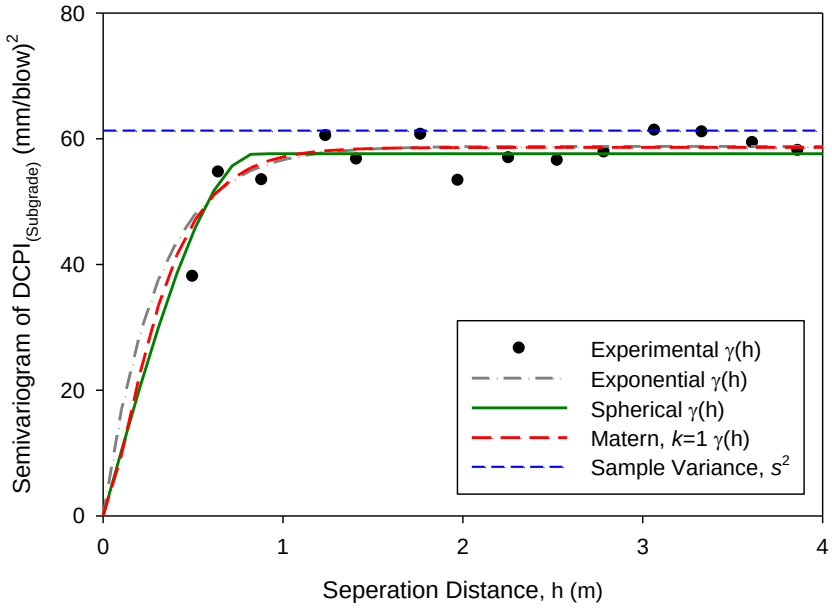

Figure 3.22. Omnidirectional γ(h) of $DCPI_{subgrade}$ with fitted $\hat{\gamma}(\mathbf{h})$ on MI I94 TS1b

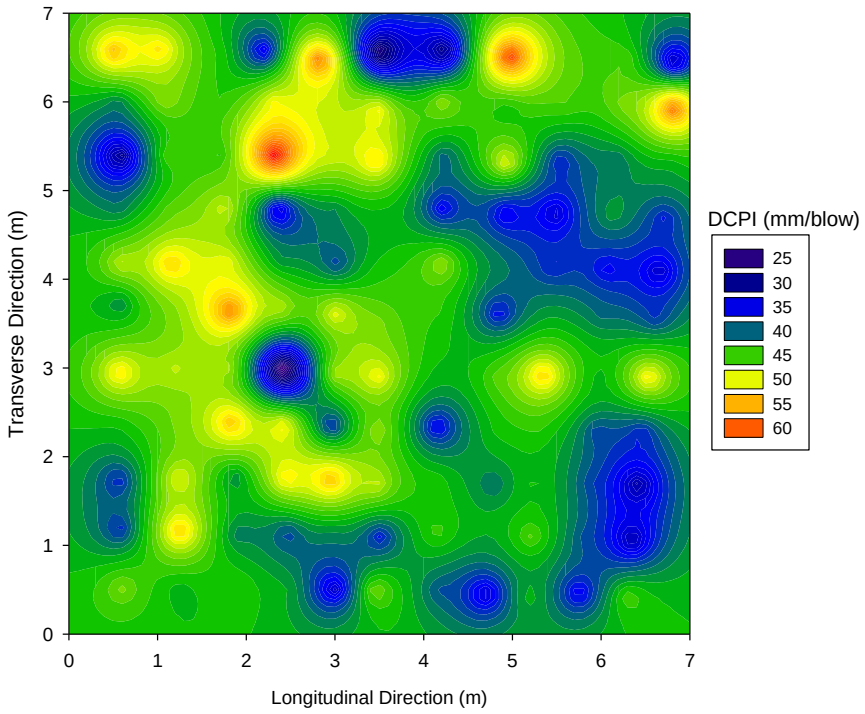

Figure 3.23. Ordinary kriging of $DCPI_{subgrade}$ with fitted omnidirectional spherical $\hat{\gamma}(\mathbf{h})$ on MI I94 TS1b

MI I96 TS1

Omnidirectional experimental semivariogram γ(h) of $E_{LWD\text{-}Z3}$ increases with separation distance and exceeds the sample variance before the fitted model predicted range is reached (Figure 3.24). This γ(h) behavior shows a possible trend or anisotropy behavior in the collected $E_{LWD\text{-}Z3}$ values through the study area. There could be an insufficiently compacted roller pass in compacting the study area in MI I96 TS1 as shown in Figure 3.25, because the roller width is about two meters and there are consistently lower $E_{LWD\text{-}Z3}$ values obtained in the transverse direction while the roller travels along the longitudinal direction in compacting materials. Anisotropy of the directional semivariogram should be investigated for this data.

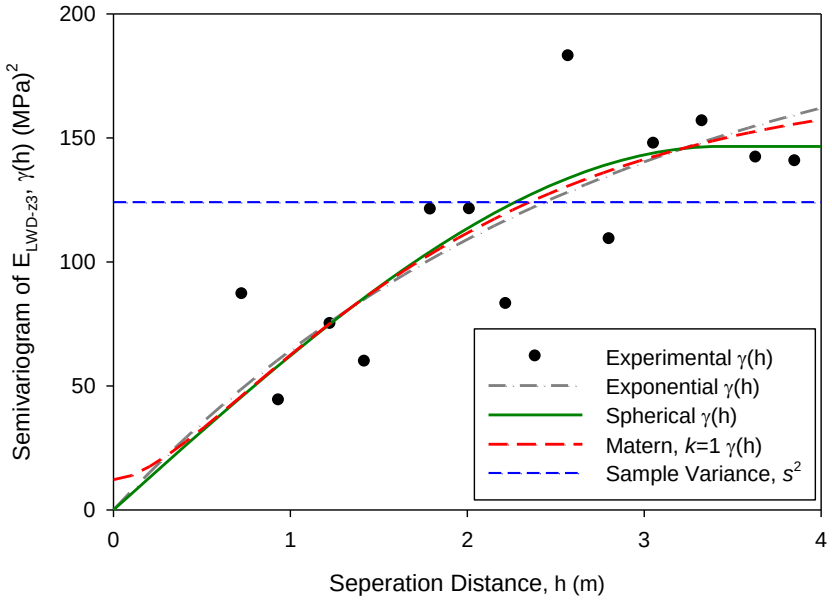

Figure 3.24. Omnidirectional γ(h) of $E_{LWD\text{-}Z3}$ with fitted $\hat{\gamma}(h)$ on MI I96 TS1

The calculated experimental semivariogram of γ_d measurements shows a possible trend with long spatial correlation. The range value, estimated as 6.891 m with spherical model,is larger than the maximum semivariogram study distance of 4 m (Figure 3.26). The ordinary kriging contour plot (Figure 3.27) of γ_d shows two sections with consistently higher predicted values at

the upper portion of the plot and consistently lower value at the lower portion. This indicates that anisotropy should be investigated for the collected γ_d values.

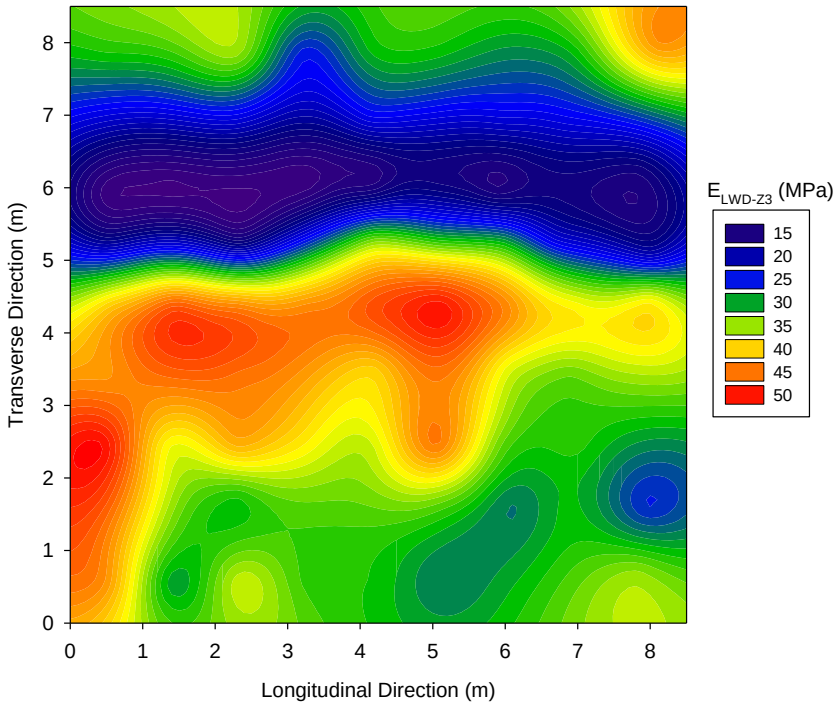

Figure 3.25. Ordinary kriging of $E_{LWD\text{-}Z3}$ with fitted omnidirectional Matérn (k=1) $\hat{\gamma}(\mathbf{h})$ on MI I96 TS1

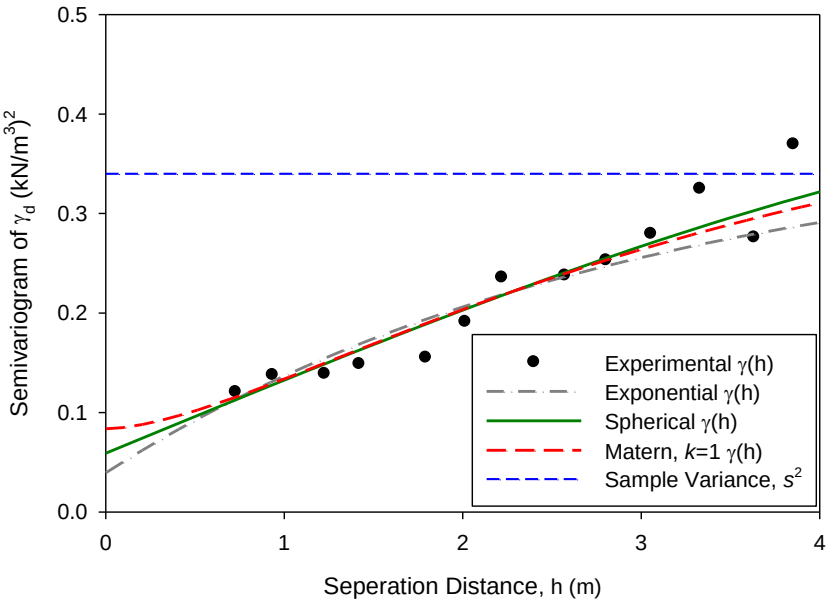

Figure 3.26. Omnidirectional γ(h) of γ_d with fitted $\hat{\gamma}(\mathbf{h})$ on MI I96 TS1

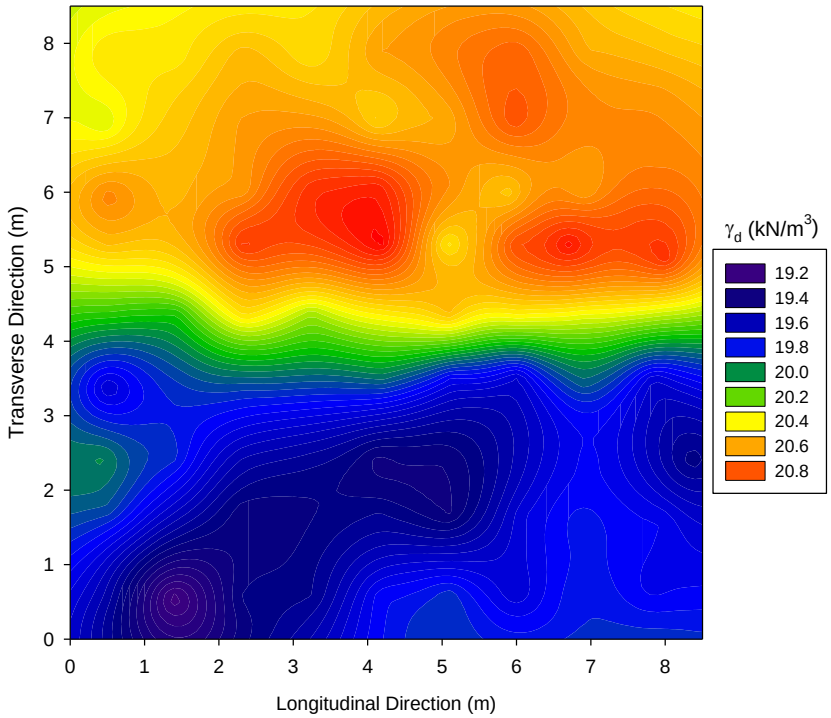

Figure 3.27. Ordinary kriging of γ(h) with fitted omnidirectional spherical $\hat{\gamma}(\mathbf{h})$ on MI I94 TS1b

The calculated experimental semivariogram of *w* measurements shows a possible trend because γ(h) tends to be larger than the sample variance after about 3 m in separation distance (Figure 3.28). The ordinary kriging contour plot (Figure 3.29) of *w* also shows two sections with consistently higher predicted values at the lower portion of the plot and consistently higher values at the upper portion which is with the reverse of the kriging contour plot of γ_d. Investigating anisotropy is advised for the collected *w* values.

The calculated experimental semivariogram of $DCPI_{subbase}$ also shows a possible trend that γ(h) tends to be larger than the sample variance after about 2 m in separation distance (Figure 3.30). The ordinary kriging contour plot (Figure 3.31) of $DCPI_{subbase}$ also shows an approximate 2.5 m wide strip along the longitudinal direction possibly due to insufficient compacted. This is similar to what the ordinary kriging plot of $E_{LWD\text{-}Z3}$ shows.

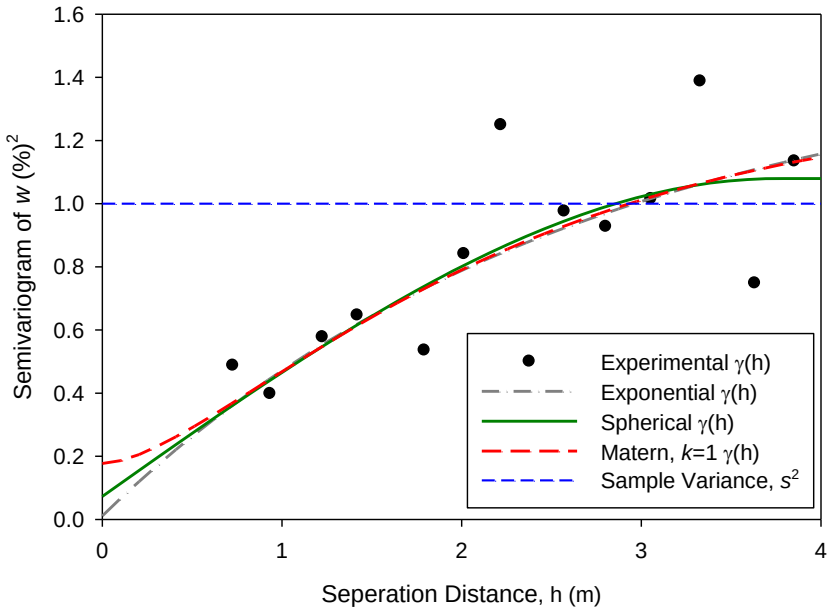

Figure 3.28. Omnidirectional γ(h) of *w* with fitted $\hat{\gamma}(\mathbf{h})$ on MI I96 TS1

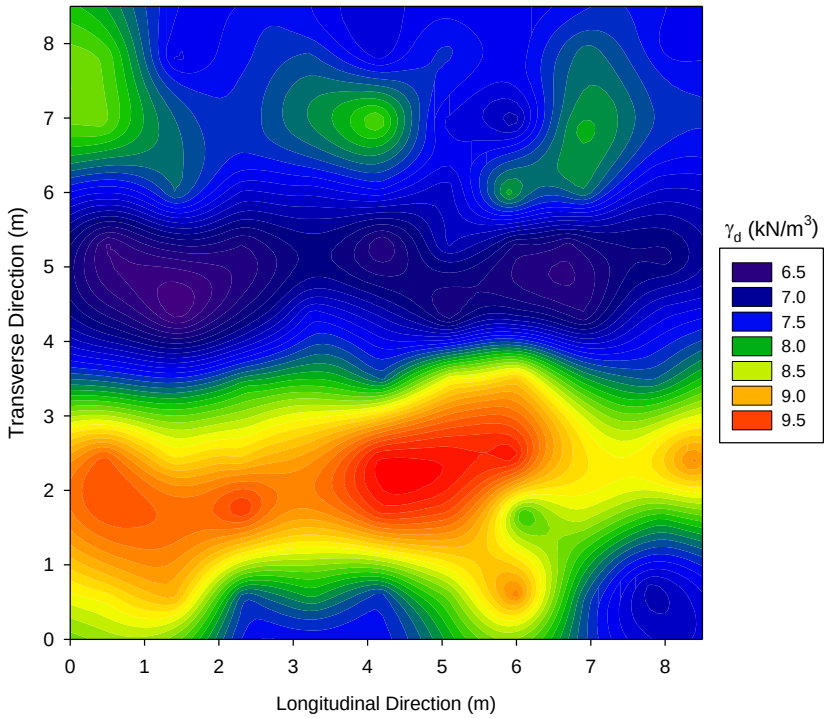

Figure 3.29. Ordinary kriging of *w* with fitted omnidirectional spherical $\hat{\gamma}(\mathbf{h})$ on MI I96 TS1

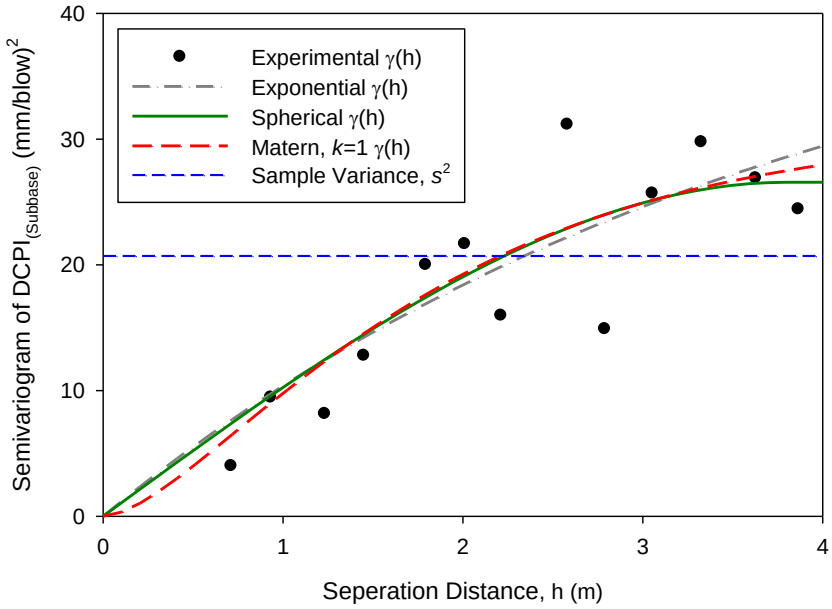

Figure 3.30. Omnidirectional γ(h) of $DCPI_{subbase}$ with fitted $\hat{\gamma}(h)$ on MI I96 TS1

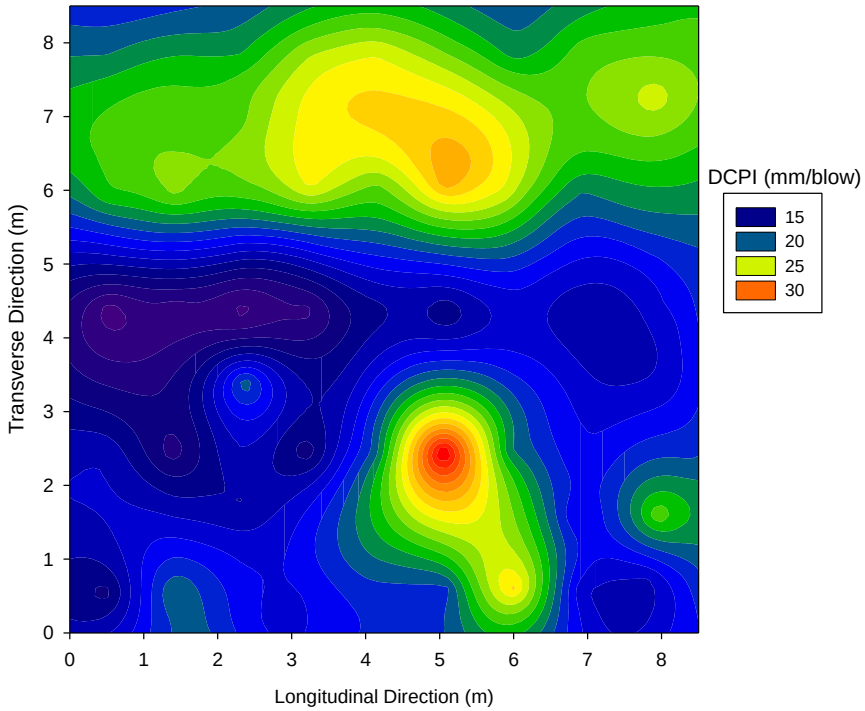

Figure 3.31. Ordinary kriging of $DCPI_{subbase}$ with fitted omnidirectional spherical $\hat{\gamma}(h)$ on MI I96 TS1

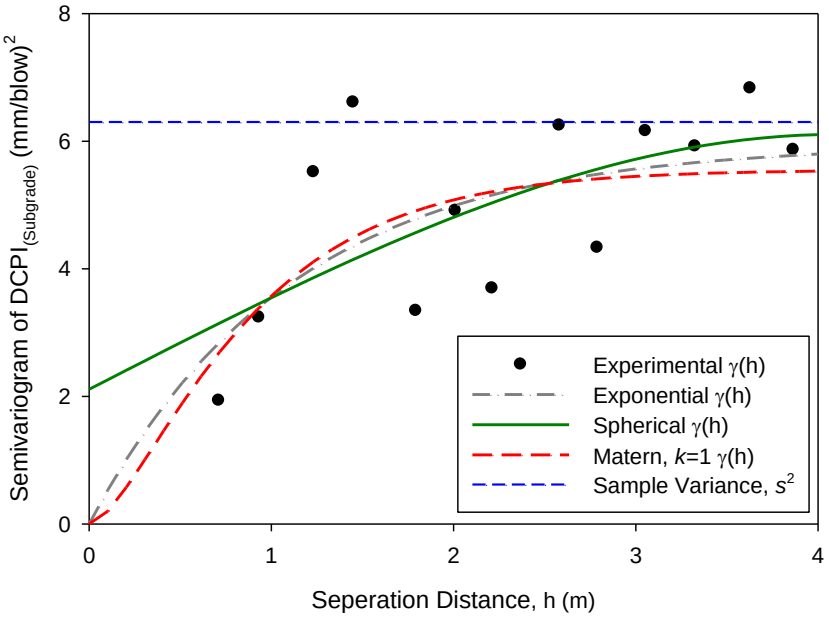

Figure 3.32. Omnidirectional γ(h) of $DCPI_{subgrade}$ with fitted $\hat{\gamma}(h)$ on MI I96 TS1

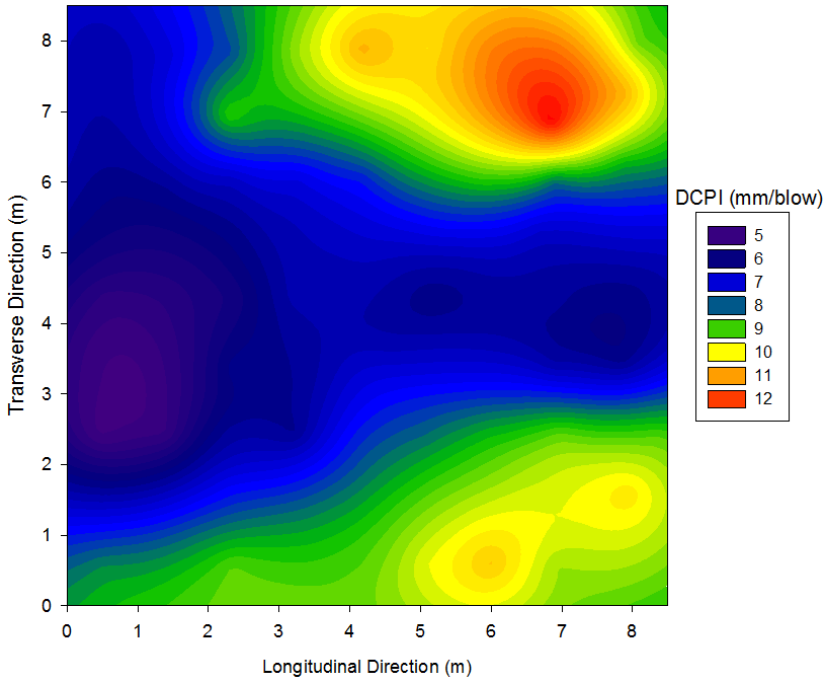

Figure 3.33. Ordinary kriging of $DCPI_{subgrade}$ with fitted omnidirectional spherical $\hat{\gamma}(h)$ on MI I96 TS1

The erratic experimental semivariogram values of $DCPI_{subgrade}$ does not show clear correlation of $DCPI_{subgrade}$ measurements with separation distance. The overall weighted average DCPI of the subgrade layer is higher than that of the subbase layer as shown in ordinary kriging

contour plots in Figure 3.31 and Figure 3.33. The difference could be the result of the material used in construction of the subbase and subgrade layers having similar maximum dry unit weight but less confinement in the subbase layer which is exposed to air while it providing confinement to the underlying subgrade layer. Another possible reason could be more fines in the subgrade material may result in a larger contact area between aggregate particles making it harder to penetrate.

3.7.2. Directional semivariogram anisotropy study

Directional experimental semivariograms can be studied in order to identify anisotropic behavior of variables throughout the study area. A rose diagram, semivariogram map, semivariogram contour map, and plotting the directional semivariogram in several directions on the plot could help in identifying anisotropic behavior. The ordinary kriging contour plots with omnidirectional experimental semivariogram of some pavement foundation properties studied on MI I94 TS1b and MI I96 TS1 revealed the need for directional semivariograms. The obvious anisotropic $\gamma(h)$ will be modelled by fitting the theoretical semivariogram model with identified anisotropy ratio (λ), major direction (δ) for both geometric and zonal anisotropy, and a nested model for zonal anisotropy.

Directional $\gamma(h)$ is calculated in four major directions ($\theta = 0°, 45°, 90°, 135°$) and the major and minor directions are generally at θ equals to 0° and 90° which aligns with transverse and longitudinal directions of pavement sections. One exception is the study on the moisture content measurements on MI I-94 TS1b where a possible error was identified in omnidirectional semivariogram study. All three theoretical models (i.e., spherical, exponential, and Matérn with k=1) are fitted to the $\gamma(h)$ in major and minor direction individually, and the best fitted model of the three are selected based on the smallest SSErr value and summarized in Table 3.5.

Table 3.5. Summary of theoretical model fitted to major and minor directional γ(h)

Properties	Project Site	MI I-94 TS1b		MI I-96 TS1	
	$\hat{\gamma}(h)$ estimation parameters	Transverse Direction, y, θ=0°	Longitudinal Direction, x, θ=90°	Transverse Direction, y, θ=0°	Longitudinal Direction, x, θ=90°
E_{LWD-z3} (MPa)	Model	Exp	Sph	Sph	Mat, k=1
	C_0	20.3	3.229	3.931	0
	Cs	38.78	59.79	161.37	203.5
	r	3.674	2.993	2.624	2.071
	a or a′	11.022	2.993	2.624	8.284
	SSErr	6481	6112	193699	151449
	GoF	0.0066	0.0087	0.0652	0.2323
r_d (kN/m^3)	Model	Sph	Sph	Sph	Mat, k=1
	C_0	0.1523	0.14	0	0
	Cs	0.1965	0.4844	0.674	0.1661
	r	2.328	9.86	7.482	0.558
	a or a′	2.328	9.86	7.482	2.232
	SSErr	0.07408	0.4511	0.3866	0.1554
	GoF	0.0014	0.0107	0.0375	0.1090
w (%)	Model	Sph (θ=45°)	Mat, k=1 (θ=135°)	Sph	Exp
	C_0	0.075137	0.06748	0	0
	Cs	0.006446	512.38299	1.406	0.8321
	r	1.971	604.6	3.531	1.785
	a or a′	1.971	2418.4	3.531	5.355
	SSErr	0.01376	0.01185	3.826	4.215
	GoF	0.0087	0.0024	0.0276	0.1813
$DCPI_{subbase}$ (mm/blow)	Model	Sph	Mat, k=1	Matern, k=1	Spherical
	C_0	0.6996	0.1071	0	0.4807
	Cs	0.4956	1.189	30.21	27.5117
	r	1.732	0.5448	1.072	4.603
	a or a′	1.732	2.1792	4.288	4.603
	SSErr	7.769	1.201	2705	2015
	GoF	0.0094	0.0021	0.1781	0.1367
$DCPI_{subgrade}$ (mm/blow)	Model	*		Spherical	Spherical
	C_0			0	0
	Cs			5.865	4.152
	r			1.068	2.289
	a or a′			1.068	2.289
	SSErr			469.8	283.2
	GoF			0.1352	0.1760

Note: *directional experimental semivariogram of $DCPI_{subgrade}$ on MI I94 TS1b shows close pure nugget effect, no directional semivariogram was modelled.

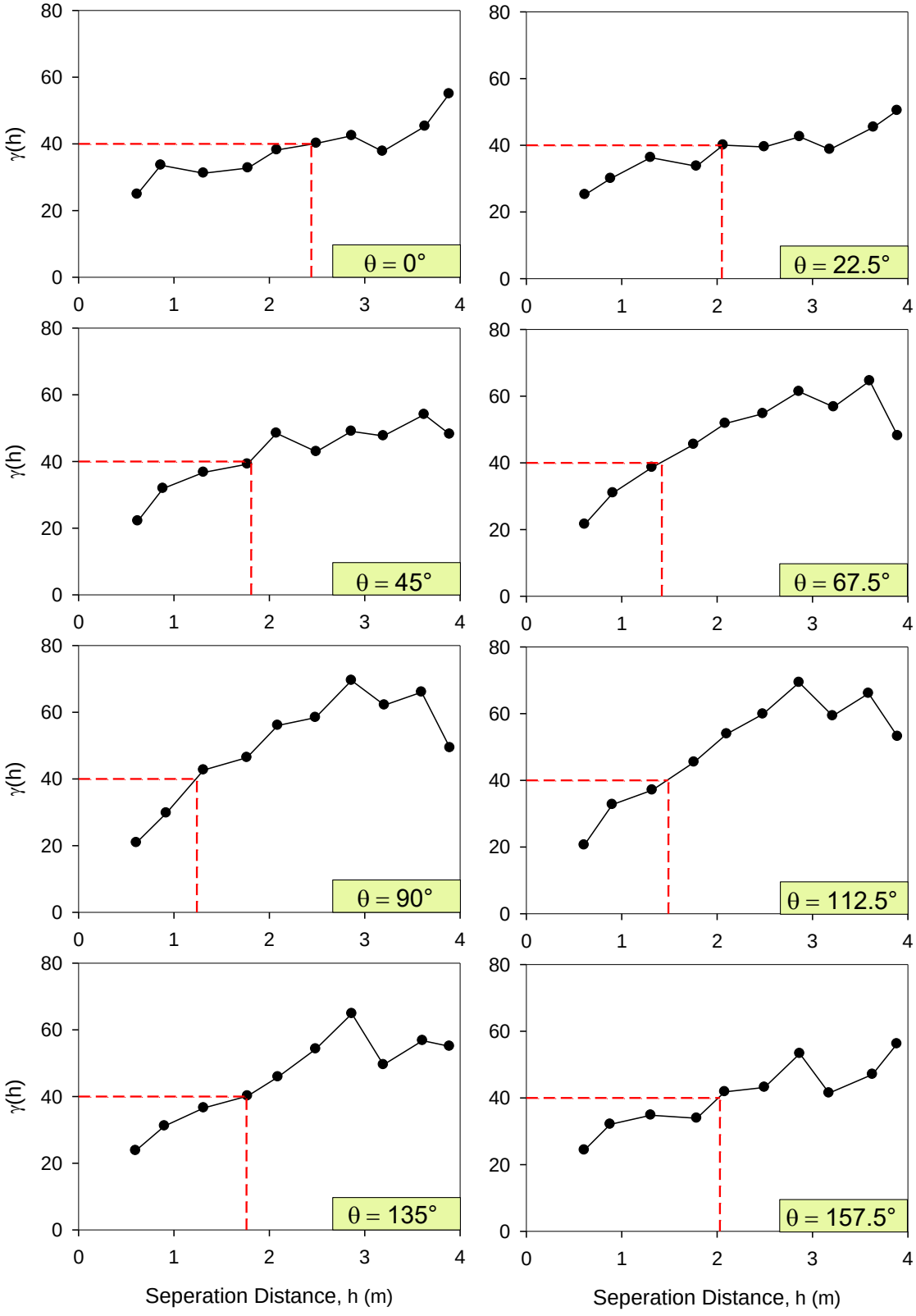

Figure 3.34. Directional γ(h) of E_{LWD-Z3} on MI I94 TS1b

The detailed study process for constructing directional semivariograms of all studied pavement foundation properties for both study test sections are not provided, but examples of procedures in studying the anisotropy behavior will be shown in this section. Three types of plots, a rose diagram, a semivariogram map, and a semivariogram contour map for preliminary examination of the directional variation of sill and range parameters are presented for $E_{LWD\text{-}Z3}$ collected on MI I94 TS1b.

A rose diagram of range values is created by identifying the range values at each directional γ(h) with a selected γ(h) that is not the initial value nor the constant γ(h) in all directions. Range values are determined and recorded at each directional γ(h) plot, as Figure 3.34 shows. Then, the rose diagram is created with ranges as distance from the center to the end point along each axial direction as shown in Figure 3.35. An ellipse that indicates geometric anisotropy is closely fitted to the end points of range values along the axial directions (Figure 3.35). Note that possible zonal anisotropy could be expected at larger γ(h).

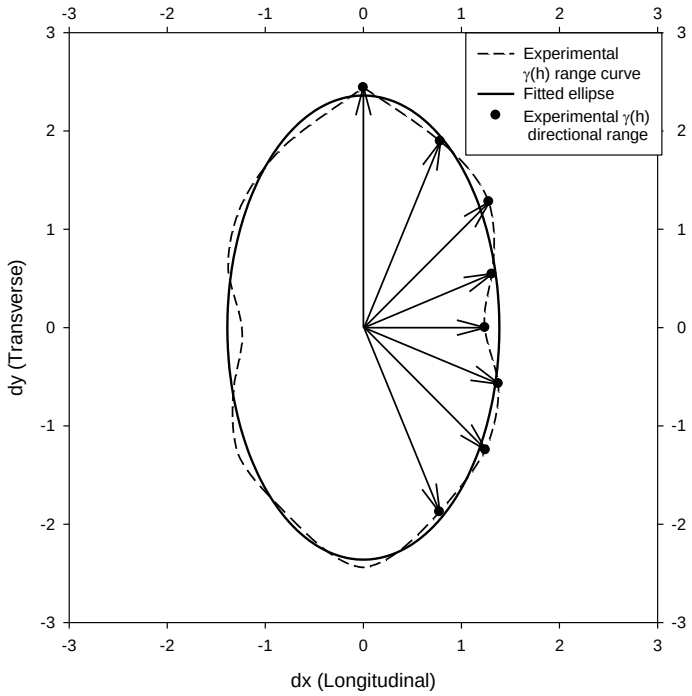

Figure 3.35. Rose diagram of $E_{LWD\text{-}Z3}$ on MI I94 TS1b

A semivariogram map is created by setting a lag distance and calculating the average value of all $\gamma(\boldsymbol{h})$ falling into the area cell with the side distance the same as the lag distance which was discussed in the method section. The lag distance should be chosen as a value not smaller than the minimum spacing that point pairs are apart. Figure 3.36 is the semivariogram plot using a color scheme to represent the value of the average $\gamma(h)$ in each area cell and Figure 3.37 is the semivariogram contour map that plots the same values in a contour line. Both of these two plot a show zonal anisotropy that $E_{LWD\text{-}Z3}$ is less variable in transverse direction compared to the longitudinal direction. The reason could be the dense gridded sampling test section, MI I94 TS1b, is sampled from a small area that may not catch the variance in the longitudinal direction. According the ordinary kriging contour plot (Figure 3.15) of the same data, $E_{LWD\text{-}Z3}$ on MI I94 TS1b, the consistently low $E_{LWD\text{-}Z3}$ values were estimated along the transverse direction at an approximate range from 2 m to 5 m that may indicate insufficient compaction in that area.

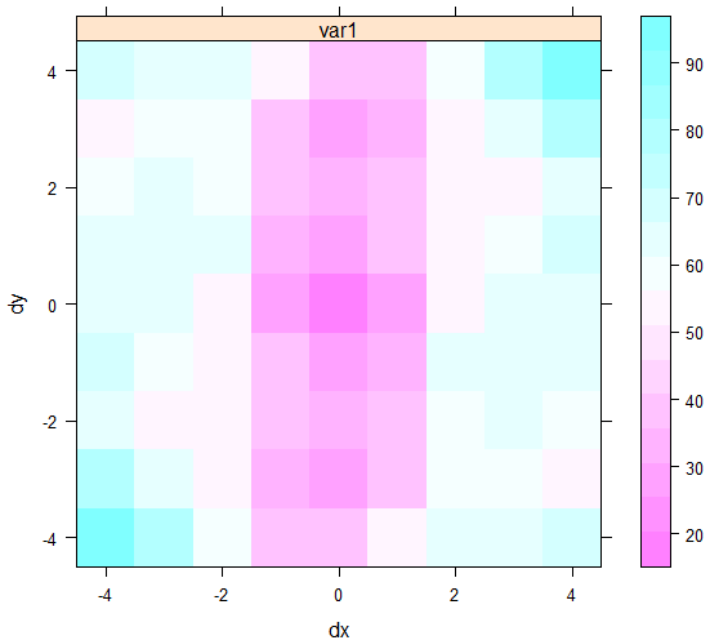

Figure 3.36. Semivariogram map of $E_{LWD\text{-}Z3}$ on MI I94 TS1b

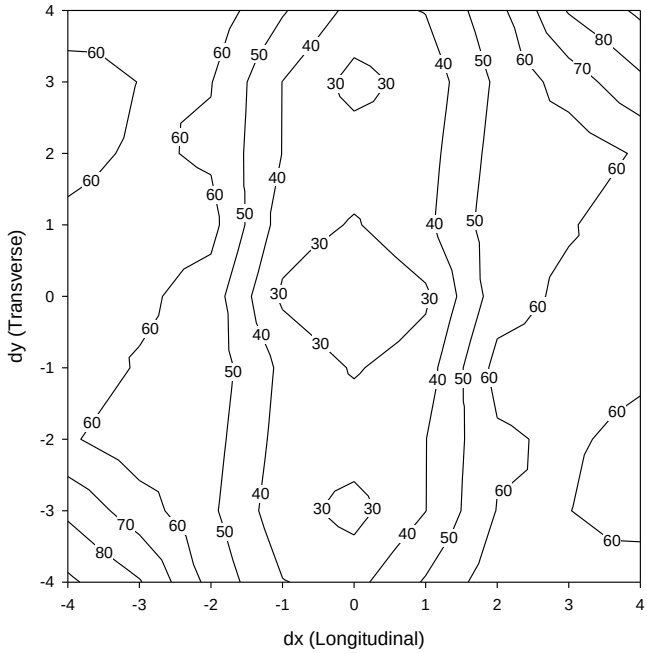

Figure 3.37. Semivariogram contour map of E_{LWD-Z3} on MI I94 TS1b

The three models fitted to transverse (y) direction and longitudinal (x) direction separately as Figure 3.38 shows and the fitted $\hat{\gamma}(h)$ in the longitudinal direction exceed the sample variance while the fitted $\hat{\gamma}(h)$ in transverse direction is reach a constant value that below the sample variance at a small range value. However, the experimental semivariogram $\gamma(h)$ tends to increase at separation distances over 3 m which may indicate a possibly higher variation could be observed in the transverse direction.

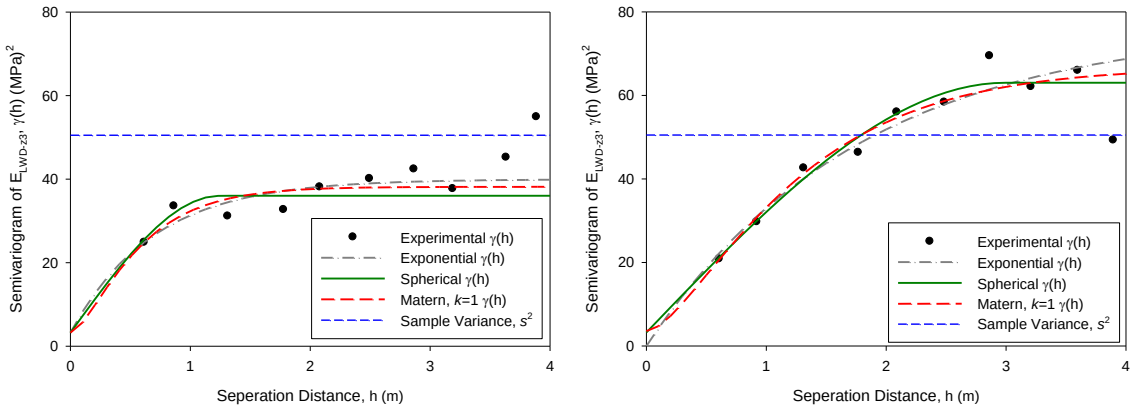

Figure 3.38. Fitted $\hat{\gamma}(h)$ for E_{LWD-Z3} on MI I94 TS1b, transverse direction (left) and longitudinal (right)

With the fitted $\hat{\gamma}(h)$ $E_{LWD\text{-}Z3}$ on MI I94 TS1b in both transverse and longitudinal directions, the best fitted model could be selected with the smaller SSErr and GoF values. The first isotropic part of zonal anisotropy is modelled with the selected model for the transverse direction $\hat{\gamma}_1(h)$ that has the lower sill than the longitudinal direction, and the second part of zonal anisotropy $\hat{\gamma}_2(\boldsymbol{h})$ is modelled with the model selected for the longitudinal direction that sill is the difference between the fitted $\hat{\gamma}(h)$ in transverse and longitudinal direction and range is set to be extremely large (e.g., 10^9) with zonal anisotropy ratio (λ) that $\lambda \times 10^9$ will be same as the selected fitted $\hat{\gamma}(h)$ in longitudinal direction.

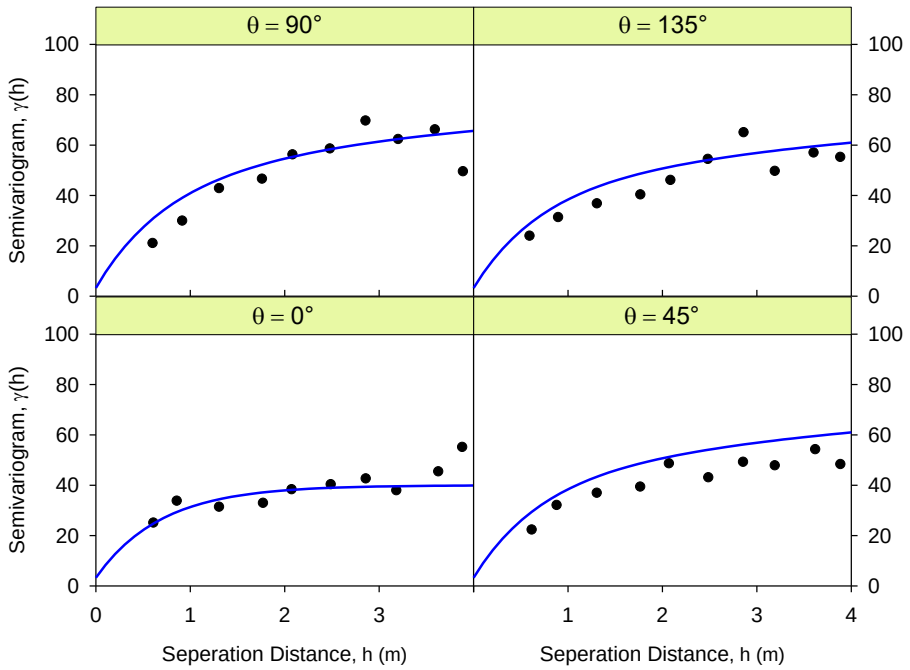

Figure 3.39. Modelling γ(h) with zonal anisotropy for $E_{LWD\text{-}Z3}$ on MI I94 TS1b

The nested model with zonal anisotropy fitted $\hat{\gamma}(h)$ is shown as a continuous curve with the experimental semivariogram of $E_{LWD\text{-}Z3}$ shown as black dots which clearly shows the zonal anisotropic model describing the variation of $E_{LWD\text{-}Z3}$ in different directions (Figure 3.39), but the quality of prediction using the zonal anisotropic model should be verified using the cross-validation MSPE value. The ordinary kriging plot using the zonal anisotropic model for $E_{LWD\text{-}Z3}$

on MI I-94 TS1a is shown in Figure 3.40 which is similar to the ordinary kriging plot using the omnidirectional model shown in Figure 3.15.

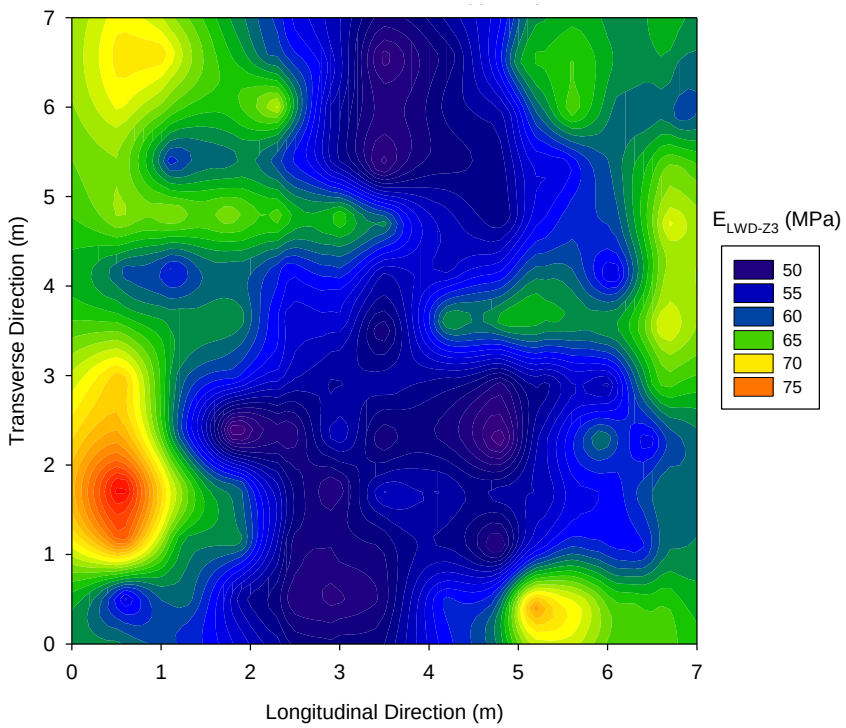

Figure 3.40. Ordinary kriging contour plot of E_{LWD-Z3} on MI I94 TS1b

The detailed study on anisotropic behavior of E_{LWD-Z3} on MI I96 TS1 is also discussed. The semivariogram map of E_{LWD-Z3} on MI I96 TS1 (Figure 3.41) shows that E_{LWD-Z3} is more uniform and continuously varied along the longitudinal direction which is similar to what the literature study suggests. Directional semivariograms calculated in all four directions with angle tolerance ($\Delta\theta$) equal to 45° (Figure 3.42) tend to reach the same sill at separation distance equal to 4 m. However, the zonal anisotropy as semivariogram map (Figure 3.41) indicates can be observed when angle tolerance decreased to 25° (Figure 3.42) to narrow the searching angle that less data pairs will be counted. Therefore, a different tolerance angle should be studied to accurately characterize the spatial anisotropic variability.

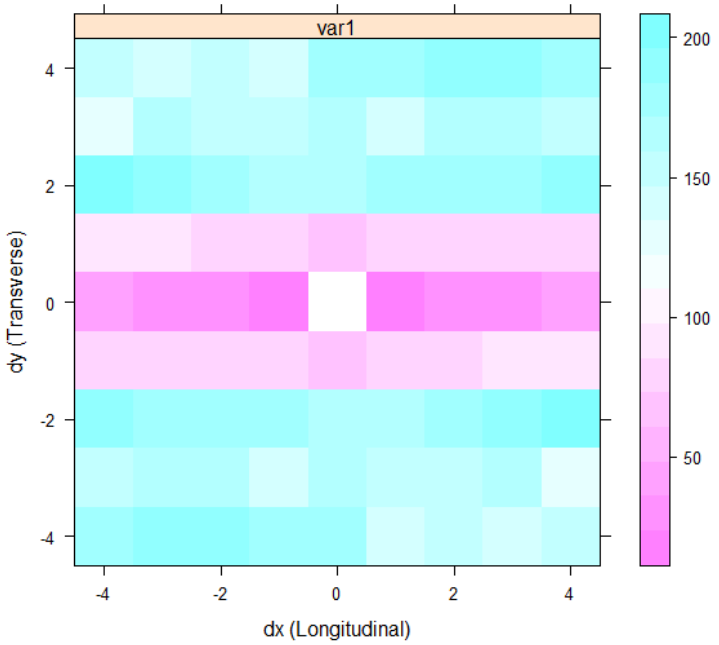

Figure 3.41. Semivariogram map of E_{LWD-Z3} on MI I96 TS1

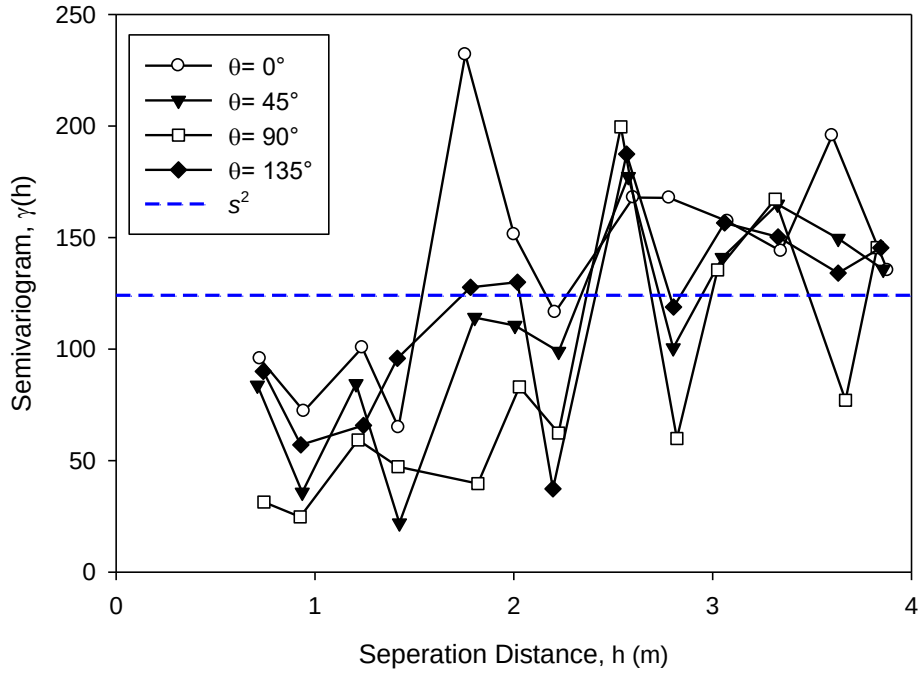

Figure 3.42. Directional γ(h) of E_{LWD-Z3} on MI I96 TS1b with Δθ=45°

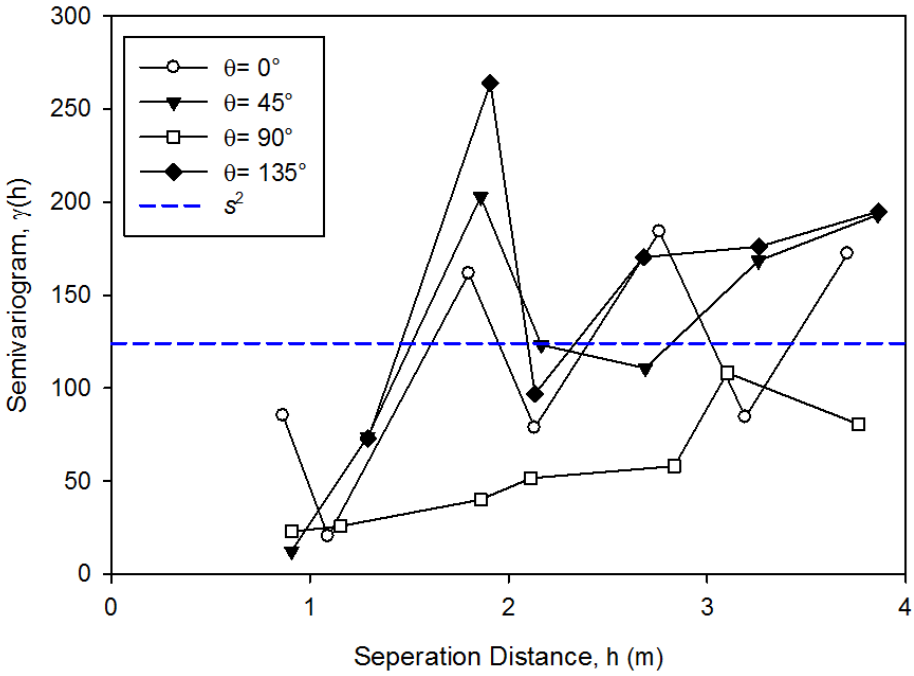

Figure 3.43. Directional γ(h) of E_{LWD-Z3} on MI I96 TS1b with Δθ=25°

The zonal anisotropy behavior of E_{LWD-Z3} on MI I96 TS1 is modelled using the same process as that used on E_{LWD-Z3} on MI I94 TS1b. The nested semivariogram that modelled zonal anisotropy with major direction along the longitudinal direction is shown in Figure 3.44. Besides fitting the theoretical model, the pattern of the experimental semivariogram can also tell some characteristics of how the data varied at the study area. Both of $\hat{\gamma}(h)$ and $\gamma(h)$ in longitudinal direction (θ=90°) tends to increase at the end the studied maximum separation distance of 4 m as shown in Figure 3.44. This could be an indication of a longer range or correlation length could be obtained in longitudinal direction. Moreover, the experimental semivariogram in the transverse direction (θ=0°) shows a cyclic behavior which may indicate stripes of lower and higher data along the longitudinal direction. The ordinary kriging contour plot with the fitted zonal anisotropic model shown in Figure 3.44 predicts the lower E_{LWD-Z3} values more precisely and the continuity of estimated data along the longitudinal direction is increased.

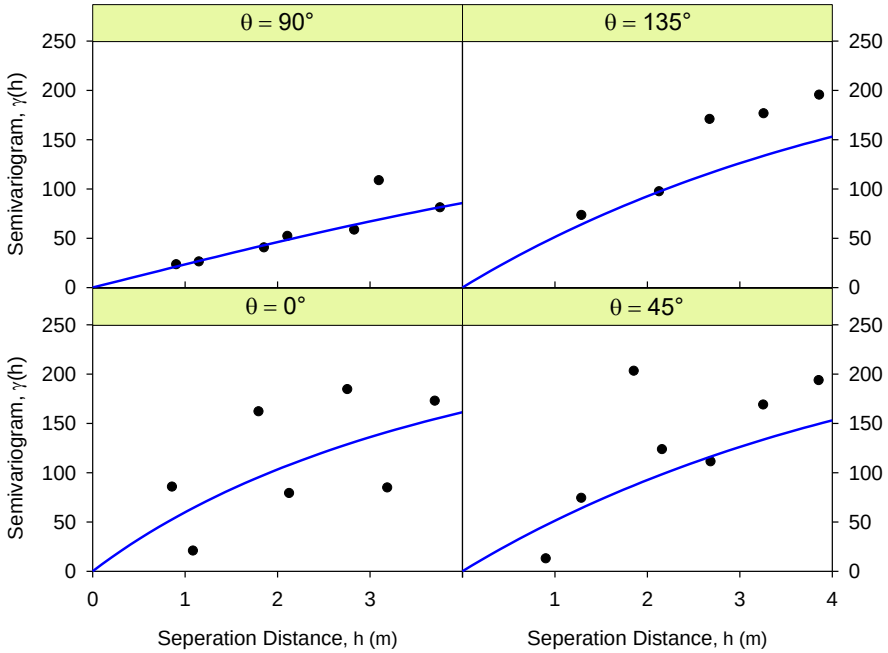

Figure 3.44. Modelling γ(h) with zonal anisotropy for E_{LWD-Z3} on MI I96 TS1

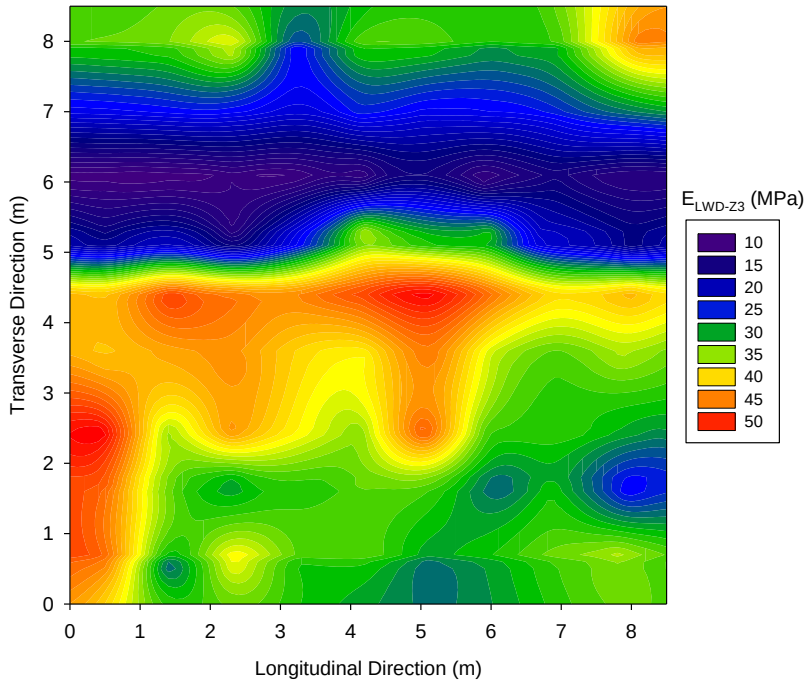

Figure 3.45. Ordinary kriging contour plot of E_{LWD-Z3} on MI I94 TS1b

The MSPE value should be used as the statistical criteria for comparing the ability of selected omnidirectional semivariogram model and anisotropic semivariogram models to predict the data at the missing location. The omnidirectional semivariogram model will be chosen for describing

the spatial variation for the studied variable if a similar MSPE value is obtained. Comparing the fitted semivariogram models for omnidirectional semivariograms and directional semivariograms with anisotropy behavior, the isotropic semivariogram models show similar accuracy as anisotropic semivariogram models in predicting the pavement foundation properties at unknown locations cross the studied area. The MSPE of each fitted semivariogram for both isotropic and anisotropic experimental semivariogram are summarized in Table 3.6.

Table 3.6. Summary of fitted isotropic and anisotropic semivariogram model parameters

Project Site		**MI I-94 TS1b**		**MI I-96 TS1**	
Properties	**$\hat{\gamma}(\mathbf{h})$ estimation parameters**	**Anisotropic**	**Isotropic**	**Anisotropic**	**Isotropic**
$E_{LWD\text{-}Z3}$ (MPa)	Anisotropy	Zonal	—	Geometric	—
	Model 1	Exponential	Exponential	Matern, k=1	Matern, k=1
	Model 2	Spherical			
	C_0	3.229	4.145	0	12.18
	C_{s1} or C_s	36.736	54.644	203.5	161.43
	C_{s2}	23.054			
	a_{s1} or r	0.6913	1.45	2.071	1.247
	a_{s2}	1E9			
	λ	2.994E-09		0.45	
	δ	0°		90°	
	MSPE	23.61	**22.77**	46.28	**43.72**
γ_d (kN/m^3)	Anisotropy	Zonal	—	Zonal	—
	Model 1	Spherical	Spherical	Matern, k=1	Spherical
	Model 2	Spherical	—	Spherical	—
	C_0	0.1523	0.1522	0	0.05901
	C_{s1} or C_s	0.1965	0.2088	0.1661	0.34
	C_{s2}	0.2756		0.5079	
	a_{s1} or r	2.328	3.412	0.558	6.891
	a_{s2}	1E9	—	1E9	—
	λ	0.00000001	—	7.692E-09	—
	δ	0°	—	90°	—
	MSPE	0.215	**0.2106**	0.136	**0.135**

Note: — means not available

Table 3.6 Continued. Summary of fitted isotropic and anisotropic semivariogram model parameters

Project Site		MI I-94 TS1b		MI I-96 TS1	
Properties	**$\hat{\gamma}(\mathbf{h})$ estimation parameters**	**Anisotropic**	**Isotropic**	**Anisotropic**	**Isotropic**
w (%)	Anisotropy	Zonal	—	Zonal	—
	Model 1	Matern, k=1	Spherical	Exponential	Spherical
	Model 2	Matern, k=1	—	Spherical	—
	C_0	0.06748	0.06975	0	0.07296
	C_{s1} or C_s	0.01381	0.27523	0.8321	1.00653
	C_{s2}	512.36918		0.5739	
	a_{s1} or *r*	0.2965	48.46	1.785	3.757
	a_{s2}	10E9	—	10E9	—
	λ	6.667E-07	—	3.571E-09	—
	δ	45°	—	90°	—
	MSPE	0.08006	**0.0807**	0.4085	**0.3937**
$DCPI_{subbase}$ (mm/blow)	Anisotropy	Geometric	—	Geometric	—
	Model 1	Matern, k=1	Exponential	Spherical	Spherical
	Model 2	Matern, k=1	—	—	—
	C_0	0.06748	0.3036	0.4807	2.11
	C_{s1} or C_s	1.189	0.9745	27.5117	26.57
	C_{s2}	—	—	—	—
	a_{s1} or *r*	0.5448	0.817	4.603	3.8
	a_{s2}	—	—	—	—
	λ	0.5	—	0.8	—
	δ	90°	—	90°	—
	MSPE	**0.8343**	0.8701	12.81	**11.76**
$DCPI_{subgrade}$ (mm/blow)	Anisotropy	—	—	Zonal	—
	Model 1		Spherical	Spherical	Spherical
	Model 2		—	Spherical	—
	C_0		0	0	2.11
	C_{s1} or C_s		57.61	4.152	3.995
	C_{s2}		—	1.713	—
	a_{s1} or *r*		0.848	2.289	4.091
	a_{s2}		—	1E9	—
	λ		—	1.068E-09	—
	δ		—	90°	—
	MSPE		**60.3**	**2.335**	3.455

Note: — means not available

Table 3.7. Summary of spatial variability estimates

In-situ properties	Directions	MI I-94 TS1b		MI I-96 TS1	
		Sill ($C+C_0$)	Range (a or a'), m	Sill ($C+C_0$)	Range (a or a'), m
E_{LWD-Z3} (MPa)	Omnidirection	58.789	4.35	173.61	4.988
	Transverse Direction (y)	59.08	11.022	165.301	2.624
	Longitudinal Direction (x)	63.019	2.993	203.5	8.284
γ_d (kN/m^3)	Omnidirection	0.361	3.412	0.39901	6.891
	Transverse Direction (y)	0.3488	2.328	0.674	7.482
	Longitudinal Direction (x)	0.6244	9.86	0.1661	2.232
w (%)	Omnidirection	0.34498	48.46*	1.07949	3.757
	Transverse Direction (y)	—		1.406	3.531
	Longitudinal Direction (x)			0.8321	5.355
$DCPI_{subbase}$ (mm/blow)	Omnidirection	1.2781	2.451	26.57	4.091
	Transverse Direction (y)	1.1952	1.732	30.21	4.288
	Longitudinal Direction (x)	1.2961	2.1792	27.9924	4.603
$DCPI_{subgrade}$ (mm/blow)	Omnidirection	57.61	0.848	6.105	3.8
	Transverse Direction (y)	—		5.865	1.068
	Longitudinal Direction (x)			4.152	2.289

Note: * possible measurement error

A summary of sill and range values estimated by weighted least squares fitted theoretical semivariogram models are summarized in Table 3.7. The fitted semivariogram model estimated range values that indicates the separation distance that the data pairs are no longer correlated. E_{LWD-Z3} is spatially correlated within 4.35 m in the test point in MI I-94 TS1b test section and about 5 m in MI I-96 TS1 test section without considering the directions. The anisotropic behavior of E_{LWD-Z3} in MI I-94 TS1b is different from MI I-96 TS1 that E_{LWD-Z3} is more spatially correlated in the transverse direction in MI I-94 TS1b and is more spatially correlated in the

longitudinal direction in MI I-96 TS1. Since the sample variance is relatively small in MI I-94 TS1b in the smaller sampling area, the different anisotropic behavior might be expected in the larger sampling area. The spatial correlation length or range of dry unit weight in MI I-96 TS1 is about twice as in MI I-94 TS1b without considering anisotropy. The similar anisotropic behavior of $E_{LWD\text{-}Z3}$ is observed in γ_d. Anisotropic behavior of the questioned moisture content data in MI I-94 TS1b is not reported, but the anisotropic behavior of *w* in MI I96 TS1 is similar to $E_{LWD\text{-}Z3}$ and γ_d. Spatial variability of weighted average DCPI in subbase and subgrade layer is almost the same in all directions. The reason could be the weighted average DCPI value averaged the difference in vertical direction to present as a point for horizontal direction analysis.

3.8. Conclusions

Detailed geostatistical analysis procedures are presented in this study to provide a guide for pavement engineers to study spatial variability of pavement foundation properties with consideration of choosing the best fitted semivariogram model and characterization of anisotropic behavior. Isotropic semivariogram modelling indicates that the studied measurement values has the same spatial correlation between data pairs separated at distance *h* in all directions, but anisotropic semivariogram modelling shows that the spatial correlation between data pairs separated at distance *h* is different in different directions. Measurements obtained in a relatively dense grid pattern from two sections of pavement reconstructions sites (MI I-94 and MI I-96) are presented in studying the geostatistical modelling parameters that characterize spatial variability of stiffness and compaction properties. Preliminary study on anisotropy of spatial variability of pavement foundation properties is allowed with the dense gridded measurements, but different anisotropic behavior was identified in two test sections that may

only represent the local sample area. More data in the longitudinal direction should be provided for further anisotropy analysis.

Experimental semivariogram of layer averaged DCPI values are nearly isotropic with possible anisotropic behavior in the horizontal direction on both subbase and subgrade layers. Zonal anisotropy with the major anisotropic axis along the longitudinal direction indicates greater continuity in the longitudinal direction is present in the experimental semivariogram of $E_{LWD\text{-}Z3}$, moisture content (w), and dry unit weight (γ_d) measured in dense gridded test locations in project MI I-96. Therefore, the univariate statistical analysis should be analyzed to assist in correctly describing spatial variability of pavement foundation properties and identifying possible trends.

Comparison of three theoretical semivariogram models reveals that no obviously best fitted model of the three models (i.e., spherical, exponential, Whittle or Matern with k=1) are found to describe the experimental semivariogram of dense gridded measurements of pavement foundation properties as the spatial variation at distances smaller than the smallest sampling distance were not determined. A nested model with an anisotropy ratio helps in estimating the data at unsampled locations with consideration of the correlation of data sampled at different locations. However, in most cases for this study on a small test area, the isotropic or omnidirectional semivariogram model works as well as an anisotropic semivariogram model. Correctly calculating an experimental semivariogram is more important than fitting different models. The MSPE from cross-validation on $E_{LWD\text{-}Z3}$ in MI I-96 TS1 decreased from 46.28 with angle tolerance of 45° to 33.3 with 25°.

Further study on spatial variability of pavement foundation properties is suggested with measurements at test locations in different spacing and across the pavement width. A smaller

spacing which is less than 0.6 m is suggested for research on identifying the initial spatial correlation characteristics.

3.9. Acknowledgements

This study was sponsored by the Federal Highway Administration under agreement No. DTFH61-06-H-00011 and the Iowa Department of Transportation under Transportation Pooled Fund Program TPF-5(183).

3.10. Notation

The following symbols are used in this paper:

a	=	Range
a_{s1}	=	Range in first part of anisotropic semivariogram model
a_{s2}	=	Range in second part of anisotropic semivariogram model
a'	=	Effective range where 95% C_s reached
Â	=	Variable component of AIC
AIC	=	Akaike Information Criterion
C	=	Sill
C_0	=	Nugget effect
C_s	=	Partial sill that obtained in variogram model
C_{s1}	=	Partial sill in first part of anisotropic semivariogram model
C_{s2}	=	Partial sill in second part of anisotropic semivariogram model
COV	=	Coefficient of variation
D_0	=	measured deflection under the plate (mm)
DCPI	=	Dynamic cone penetration index (mm/blow)
E	=	elastic modulus (MPa)
$E_{LWD\text{-}Z3}$	=	Elastic modulus (Zorn LWD test with 300 mm dia. plate) (MPa)
F	=	Shape factor for LWD
G_s	=	Specific gravity
$\boldsymbol{h}$	=	Vector indicates distance and direction of two points apart

h_i	=	Average distance of all N_i point pairs separated by distance h's.
k	=	Smoothness parameter in the Matérn model
k	=	Stiffness estimated from a static plate load test
n	=	Number of points on the experimental variogram
N	=	Number of tests
N_i	=	Number of point pairs that separated at distance h
p	=	Number of model parameters
P	=	Applied load at surface
r	=	Range number obtained in R program
r	=	radius of the plate (mm)
s	=	Spatial location
s^2	=	Sample variance
SSErr	=	Sum of squares of error or residuals
w_j	=	Weight in weighted least squares fit
w	=	Moisture content
w_{opt}	=	Optimum moisture content
γ_d	=	Dry unit weight
γ_{dmax}	=	Maximum dry unit weight
γ_{dmin}	=	Minimum dry unit weight
$\gamma(h)$	=	experimental semivariogram at distance h
$\hat{\gamma}(h)$	=	fitted theoretical semivariogram at distance h
δ	=	major anisotropy direction
η	=	Poisson's ratio (0.4)
θ	=	semivariogram direction (azimuth angle)
λ	=	anisotropy ratio
σ	=	standard deviation
σ_0	=	applied stress
$\Delta\theta$	=	angular tolerance
ϕ	=	angular tolerance direction

CHAPTER 4. CHARACTERIZATION OF VARIABILITY IN PAVEMENT FOUNDATION PROPERTIES

A paper submitted to *International Journal of Pavement Engineering*

Jia Li, David J. White, and Pavana Vennapusa

4.1. Abstract

This study investigates variability of pavement foundation properties (e.g., E_{LWD-Z3}, γ_d, and *w*) that were determined from four major in-situ tests (i.e., FWD, LWD, NG, and DCP) over 18 test sections of 6 project sites. Change in variation of in-situ measured properties is studied in relationship to the number of compaction passes. Univariate statistics of pavement foundation properties is documented to provide references to pavement engineers and researchers to know the range of variability that in-situ measured properties can vary. In addition to univariate statistics, spatial analysis is performed on selected sites that contain relatively large data sets. The difference in spatial variation can be expected in longitudinal and transverse directions. The correlation length of 2 m to 3 m in the minor or less uniform direction is quantified for spatial variability of dense gridded data on the base layer. The spatial variability of in-situ measured properties along the longitudinal direction can be expected to be 15 m to 23 m in the CTB layer. This study on spatial variability indicates that the correlation length can be different in different pavement foundation layers and materials.

4.2. Introduction

Pavement foundation structures are constructed to provide uniform support for upper pavement layers and traffic load. However, material properties of existing pavement foundation structures are generally non-homogeneous. Non-uniform pavement foundation structures may cause stress concentration and then reduce pavement service life according to White et al.

(2004). To achieve a reliable pavement design, variability of engineering properties should be properly quantified. Phoon and Kulhawy (1999) suggested estimating the variability of soil parameters to develop and apply reliability-based design. Otake and Honjo (2013) suggested to evaluating the effects of spatial variability of material properties on pavement structures. However, pavement design assumes that uniform layers are achieved and uses a single modulus of subgrade reaction to represent the whole layer.

Pavement foundation properties with less variability indicate better quality of construction. Factors that may affect this variability include the sampling pattern, distance between sampling locations, area of test section, and quantity of tests over the test sections where the variability is measured. It is likely that the decrease in variability of processes can be attributed to one or more of the following: contractor quality control, specifications that require a measurement of variability, improved industrial technology, and improved test methods (Hughes 1996).

Variability has been identified in constructed pavement foundations. Allen and Graves (1994) obtained falling weight deflectometer (FWD) and Road Rater deflection measurements data at 25 foot intervals along a 500 ft long test section and observed a 75% coefficient of variation in subgrade moduli within the section. Yoder (1975) reported a range in standard deviations of layer thickness from 0.6 to 0.72 with 9749 tests on cement treated base, 0.72 to 0.84 with 7046 on aggregate base, and 0.96 to 1.44 with 10758 tests on aggregate subbase. Yoder reported that a typical range for the standard deviation of percent compaction on embankment/subgrade varied from 2.0 to 7.0 percent and on subbase/base varied from 2.0 to 3.5 percent. Siddharthan et al. (1992) studied layer moduli that were determined from back calculation of FWD tests perfomed on asphalt concrete pavement and they reported the layer moduli has coefficient of variation in a range of 5 to 65 percent.

Dilip and Babu (2014) studied the effect of the variance and correlation length on pavement responses to loading. The variation in the correlation length was found to have a marginal effect on the mean values of the critical strains and a noticeable effect on the standard deviation which decreases with decreases in correlation length. The pavement performance is adversely affected by the presence of spatially varying layers. The study also confirmed that the higher the variability in the pavement layer moduli, introduced through a higher value of coefficient of variation (COV), the higher the variability in the pavement response. The study concludes that ignoring spatial variability by modeling the pavement layers as homogeneous with very short correlation lengths can result in the underestimation of the critical strains and thus an inaccurate assessment of the pavement performance.

Although variation of in-situ properties in pavement construction has been noticed, there is no documentation of variability in pavement foundation properties so that people have an idea of how variable the pavement foundation properties could be. Selective sampling by the inspector, often as ordered by the engineer, has played an important part in the failure to recognize the magnitude of the actual variations occurring in embankment and base construction.

This study will focus on documenting the variability on 18 test sections over 6 projects on either the base/subbase layer or subgrade layer to provide a reference for pavement engineers or researchers to know how variable some pavement foundation properties can be within a small distance of the test section compared to the single design value that is used to represent the properties of a whole pavement foundation layer across the project. The variability of pavement foundation properties is also studied in relation to the number of roller compaction passes to see how the variability of pavement foundation properties could be reduced with the number of passes. Spatial variability of pavement foundation properties is a growing interest for more

researchers, but cost and time restraints limited the quality of data that can be used for spatial analysis. This study also investigates the spatial variability of pavement foundation properties in both longitudinal and transverse directions for identifying the difference in spatial variation as related to pavement geometry.

4.3. Background

4.3.1. Project information

The variability of pavement foundation properties is studied by statistical analysis on the in-situ test data that were collected on base, subbase, or subgrade layers from six project sites cross five states (Figure 4.1).

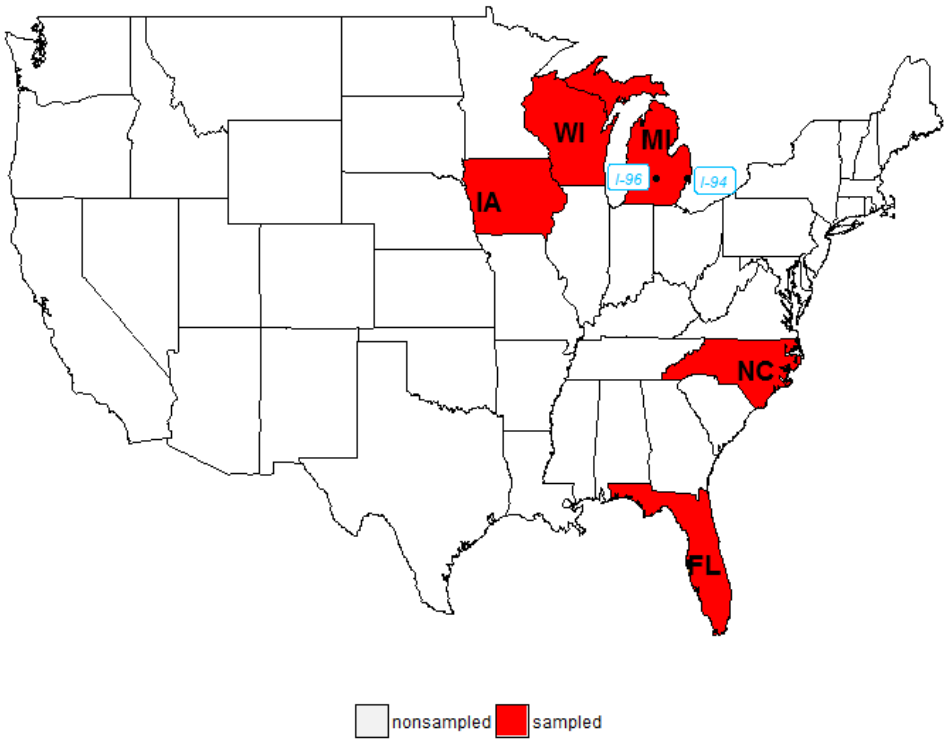

Figure 4.1. Test sites map

The MI I-96 reconstruction project used 65% of the existing sand subbase layer and about 35% of newly constructed sand subbase layer. In situ testing data were obtained from two test

sections (TS). TS1 involved tests performed on the sand subbase and TS2 involved tests performed on the cement treated base (CTB) that was constructed with recycled portland cement concrete (RPCC). The pavement structure was reconstructed with a twenty-year design life jointed PCC pavement that was composed of a 292 mm (11.5 in.) thick PCC pavement at 4.3 m (14 ft) joint spacing, a 127 mm (5 in.) cement treated base (CTB) layer with recycled PCC (RPCC) material and a 279 mm (11 in.) existing or new sand subbase with a geotextile separator at the CTB/subbase interface.

The MI I-94 reconstruction project used a 20-year design life jointed PCC pavement that was composed of a 280 mm (11 in.) thick jointed PCC pavement, and undercutting the existing foundation layers to a depth of about 686 mm (27 in.) for placement of a layer of open-graded drainage course (OGDC) that was composed of recycled steel slag over the subgrade with a geotextile separation layer at the subgrade/OGDC layer interface. Field testing was conducted on TS1 and TS3 that were the newly constructed ODGC base layer.

The IA US-30 reconstruction project used a pavement that was composed of a nominal 254 mm (10 in.) thick JPCP pavement surface and a 152 mm (6 in.) thick RPCC underlain by a 254 mm (10 in.) thick mixture of RPCC/RAP modified subbase layer over the existing subgrade.

The WI US-10 new construction project used a pavement that was composed of a 254 mm (10 in.) thick plain PCC with dowels surface, underlain by a 152 mm (6 in.) thick dense aggregate base layer that was on top of a 610 mm (24 in.) thick Grade 1 granular subbase layer over the subgrade.

The NC Hwy-218 and FL I-10 projects studied the correlation of roller-integrated compaction monitoring measurements with in-situ testing methods measured pavement foundation properties. The NC Hwy-218 project tests were performed on base and subgrade

layers after construction of 102 mm (4 in.) of granular base material and 203 mm (8 in.) of subgrade materials. The FL I-10 project tests were performed on base and subgrade layers after construction of 152 mm (6 in.) of granular base material and 305 mm (12 in.) of stabilized subgrade materials or natural subgrade materials.

In-situ test sampling plans are different in all test sections, the major sampling patterns that were used for collecting data in this study are shown in Figure 4.2 to Figure 4.5. Only test sections with more than 70 data values collected with small spacing (<1 m) will be considered as dense gridded sampling sites. The dense gridded data will be used for spatial variability analysis. The other test sections are all said to be sparse sampling sites, but the test sections with more than 30 data values collected in one direction may be used for studying the large spacing spatial variability behavior.

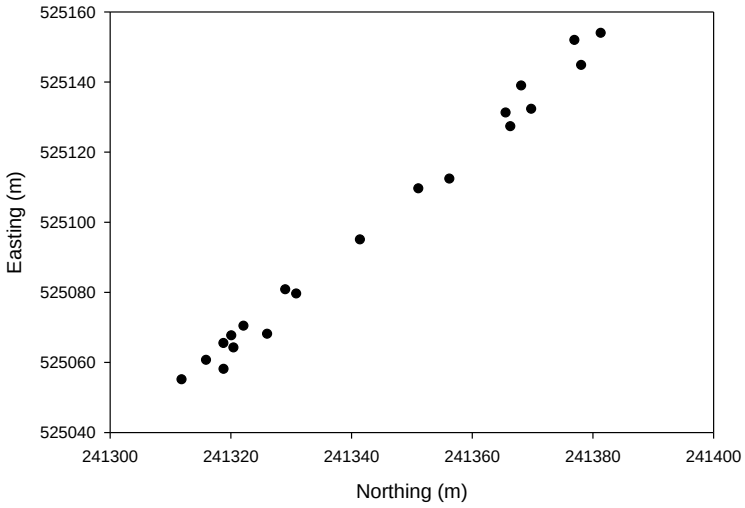

Figure 4.2. Sparse random linear test sampling on NC Hwy-218 TS3b

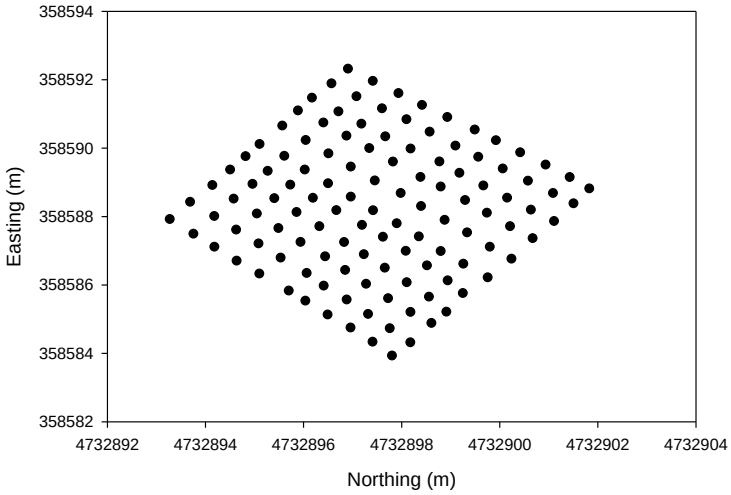

Figure 4.3. Dense square test sampling on MI I94 TS1b

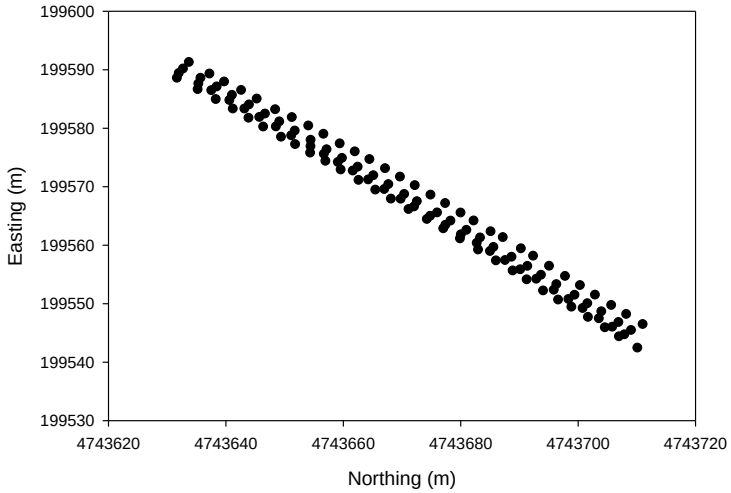

Figure 4.4. Sparse systematic linear test sampling on MI I96 TS2

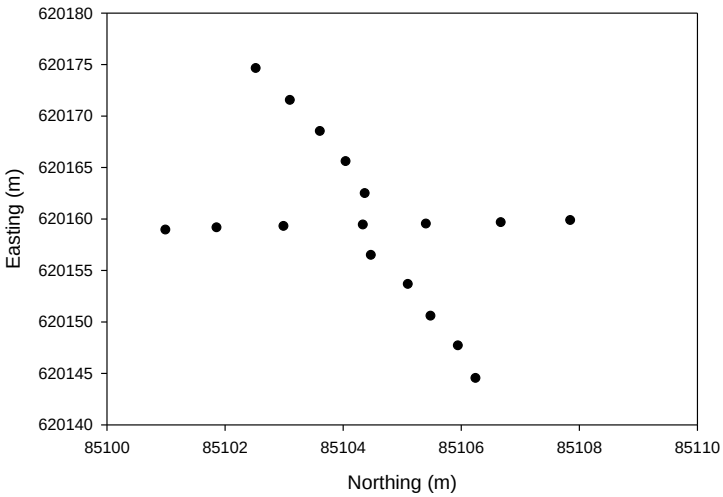

Figure 4.5. Sparse linear cross test sampling on WI US-10 TS1

The soil index properties of the layer that in-situ tests were performed on are summarized in Table 4.1 with approximate sampling rate calculated as the number of in-situ tests that were performed per unit length in the longitudinal direction of the pavement. The approximate sampling rate is calculated with the maximum number of tests over the maximum longitudinal distance of the test section, but it could be lower for certain types of tests that were not performed at certain points.

Two dense sampling sites, MI I-94 TS1b and MI I96 TS1, are used for quantifying the spatial variability of pavement foundation properties using geostatistical methods (Chapter 2). Sparse data does not allow correct quantification of the correlation length, but some features of anisotropic behavior that different spatial variability could be expect in the sparse data collected in both transverse and longitudinal directions with more than 40 points were collected in each direction. Oliver and Webster (2015) suggest a target of 150 data values and a minimum of 100 data values should be collected for spatial analysis on a variable that has isotropic variation while more than 150 data values should be collected for identifying anisotropic variation. However, limited data can be studied to characterize the spatial variability and to explore the number of data values that should be collected to properly study the spatial variability of pavement foundation properties.

Moreover, univariate statistics are used to relate the change of studied pavement foundation properties with the number of passes of roller compaction using the data from NC Hwy-218 and FL I-10 projects. However, these data were collected from the calibration test area are not presented for studying the overall variability of pavement foundation properties, only data collected in the production area will be used.

Table 4.1. Soil index properties and sampling rate summary

Site	Test Section (TS)	Layer	Soil index properties and classification						Sampling rate			
			γ_{dmax} (kN/m^3)[a]	γ_{dmin} (kN/m^3)[b]	γ_{dmax} (kN/m^3)[c]	w_{opt} (%)[c]	AASHTO	USCS	Sample grid	Max Length (m)	N of Tests	N/ unit length (N/m)
MI I-94	TS1a	Base	16.23	4.05	—	—	A-1-a	GP	Sparse	274.3	54	0.20
	TS1b	Base	16.23	4.05	—	—	A-1-a	GP	Dense	6.3	121	19.12
	TS3	Base	16.23	4.05	—	—	A-1-a	GP	Sparse	807.9	162	0.20
MI I-96	TS1	Sand subbase	20.06	14.98	19.96	7.9	A-1-b	SP-SM	Dense	7.9	73	9.22
	TS2	CTB	13.61	12.26	—	—	A-1-a	GP	Sparse	90.7	119	1.31
	TS3	Sand subbase	20.06	14.98	19.96	7.9	A-1-b	SP-SM	Sparse	320.5	26	0.08
WI US-10	TS1	Sandy Subbase	18.19	15.07	17.37	11.8	A-3	SP	Sparse	65.4	80	1.22
	TS2	Subgrade	—	—	18.67	12	A-6(8)	CL	Sparse	6.9	17	2.46
NC Hwy-218	TS1	Subgrade	—	—			A-2-4	SM	Sparse	160.5	19	0.12
	TS2	Subgrade	—	—			A-2-4	SM	Sparse	142.9	45	0.31
	TS3a	Base	—	—			A-1-a	SP-SM	Sparse	78.8	6	0.08
	TS3b	Base	—	—			A-1-a	SP-SM	Sparse	110.4	20	0.18
FL I-10	TS1	Base1	—	—	122	10	A-1-b	SM	Sparse	184.5	27	0.15
	TS2	Base2	—	—	121	11	A-1-b	SM	Sparse	78.3	15	0.19
	TS5	Subgrade	—	—	111	11	A-3	A-3	Sparse	266.2	40	0.15
	TS6	Stablized Subgrade	—	—	111	11	SM	SM	Sparse	262.0	27	0.10
IA US-30	TS1	RPCC modified Subbase	—	—	19.3	10.3	A-1-a	GP-GM	Sparse	106.7	20	0.19
	TS2	RPCC modified Subbase	—	—	19.3	10.3	A-1-a	GP-GM	Sparse	104.3	52	0.50

Note: [a]ASTM D4253-00; [b]ASTM D4253-00; [c]ASTM D698-07 (AASHTO T180 for FL I-10); [d]ASTM D3282-09; [e]ASTM D2487-00.

4.3.2. In Situ Testing Methods

The following in situ tests were conducted on 18 test sections of 6 project sites with real-time kinematic global positioning system (RTK-GPS) for positioning each test point to evaluate the variability in properties of pavement foundation systems (Table 4.2): Zorn light weight deflectometer (LWD); Kuab falling weight deflectometer (FWD); dynamic cone penetrometer (DCP); and Humboldt nuclear gauge (NG).

Table 4.2. In-situ tests summary

Field site	TS	Tests performed on	In-situ tests performed			
			FWD ($E_{FWD\text{-}k3}$)	LWD ($E_{LWD\text{-}Z3}$)	NG (γ_d and w)	DCP (DCPI)
MI I-94	TS1a	Base	N	Y	Y	Y
	TS1b	Base	N	Y	Y	Y
	TS3	Base	Y	Y	Y	Y
MI I-96	TS1	Sand subbase	N	Y	Y	Y
	TS2	CTB	Y	N	Y	Y
	TS3	Sand subbase	N	Y	Y	Y
WI US-10	TS1	Subbase	Y	N	Y	Y
	TS2	Subgrade	Y	N	Y	Y
NC Hwy-218	TS1	Subgrade	N	Y	Y	N
	TS2	Subgrade	N	Y	Y	Y
	TS3a	Base	N	Y	Y	Y
	TS3b	Base	N	N	N	Y
FL I-10	TS1	Base1	N	Y	Y	Y
	TS2	Base2	N	Y	Y	N
	TS5	Subgrade	N	Y	Y	N
	TS6	Stabilized Subgrade	N	Y	Y	N
IA US-30	TS1	RPCC modified Subbase	N	N	N	Y
	TS2	RPCC modified Subbase	N	Y	N	N

Note: Y = test was performed on all test locations; N = test was not performed.

Real-Time Kinematic Global Positioning System

An RTK GPS system was used to obtain global spatial coordinates (i.e., northing, easting, and elevation) of in situ test locations and tested pavement layers. The local spatial coordinates (x, y, and z) were determined for all tested sections from their global coordinates. A Trimble SPS 851 was established on site to provide base station correction for a Trimble SPS 851 receiver. This system has manufactured accuracies of < 10 mm in horizontal direction and < 20 mm in vertical direction.

Zorn Light Weight Deflectometer

Zorn LWD tests were performed according to manufacturer's recommendations (Zorn G. 2003) on base and subbase layers to determine elastic modulus. These LWD tests were set up with a 300 mm diameter plate and a 71 cm drop height. Elastic modulus ($E_{LWD\text{-}Z3}$) from LWD results was determined using Eq. 4.1:

$$E = \frac{(1-\eta^2)\sigma_0 r}{D_0} \times F \tag{4.1}$$

where: E = elastic modulus (MPa);

D_0 = measured deflection under the plate (mm);

η = Poisson's ratio (0.4);

σ_0 = applied stress (MPa);

r = radius of the plate (mm); and

F = shape factor = 8/3 per Vennapusa and White (2009).

Kuab Falling Weight Deflectometer

Kuab FWD tests were conducted by applying one seating drop using a nominal force of 24.5 kN (5500 lb) followed by test drops. The number of test drops and nominal forces varied for

each project. In every test, a load cell recorded actual applied forces, and deflections were recorded using seismometers mounted on the device according to ASTM D4694-09 (2009). A 300 mm diameter loading plate and 7 deflection sensors were set up. All deflection measurements were normalized to 40 kN to compare deflection values at different test locations. Composite modulus values (E_{FWD-K3}) were calculated using Eq. 4.1 with the measured deflection at the center of the plate and corresponding applied contact force. However, the plate used in Kuab FWD tests is a four-segmented plate that, according to the FWD manufacturer results in a uniform stress distribution. Therefore, a shape factor F = 2 was used in Eq. 4.1 instead of 8/3 according to Vennapusa and White (2009).

Nuclear gauge

A nuclear moisture-density gauge (NG) device was calibrated and used to measure in situ soil dry unit weights (γ_d) and moisture content (w) in the base and subbase materials. Tests were performed according to ASTM D6938-10 (2010) at each test location. The average values of γ_d and w are reported for spatial analysis.

Dynamic Cone Penetrometer

DCP tests were performed following ASTM D6951-03 (2003) to evaluate the in situ strength of compacted base, subbase, and subgrade materials, and to determine the dynamic penetration index (DCPI) and penetration depth at each test point. Weighted average DCPI is calculated for each layer to evaluate variability of the in-situ strength at different pavement foundation layers. The calibrated California bearing ratio (CBR), back calculated from DCPI is also studied.

Several test sampling grids were studied to characterize the spatial variability of pavement foundation properties, and the fundamental assumption of this spatial analysis is that sample population of the variable values has an approximate normal distribution. Histograms, box with

whiskers plots, and normal quantile plots of the sampled values are analyzed to verify the normal distribution assumption. If the values are normally distributed, the values will be used for semivariogram analysis. However, if the values are not normally distributed and highly skewed in their distribution, an appropriate transformation will be made based on format of the original distribution.

4.3.3. Statistical analysis on variability

Univariate statistics are used in this study to quantify the variability of pavement foundation properties as determined using limited in-situ tests. Spatial variability analysis is performed with the statistical program R (Bivand et al. 2013; Pebesma 2001) to characterize and quantify the spatial variability of pavement foundation properties in longitudinal and transverse directions.

Univariate statistics

The box plot is an efficient graphical method for displaying the distribution of the data (Figure 4.6) and will be used to present variation of pavement foundation properties determined from different test sections.

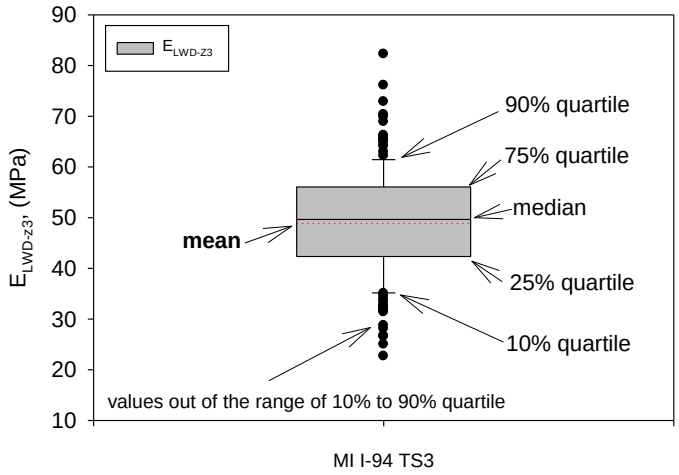

Figure 4.6. Illustration of box plot of $E_{LWD\text{-}Z3}$ measured in MI I-94 TS3

The coefficient of variation (COV) will be used as the primary way of quantifying the variability with respect to the mean of the sample. The ratio of standard deviation (σ) to mean (μ) in Eq. 4.2 is the COV where σ is calculated as Eq. 4.3 where n is the number of data values, x.

$$\mathrm{COV}=\frac{\sigma}{\mu} \tag{4.2}$$

$$\sigma=\sqrt{\frac{\sum(x-\mu)^2}{n-1}} \quad \text{and} \quad \mu=\frac{\sum x}{n} \tag{4.3}$$

Spatial variability analysis

Semivariogram γ(h) is a tool in geostatistical studies to describe and quantify spatial variability of studied variables. Semivariogram γ(h) measures the average dissimilarity of paired data separated by a vector ***h*** (Goovaerts 1997). The semivariogram γ(h) is defined as half of the average squared differences between number of pairs N(h) data values separated at a distance h as calculated in Eq. 4.4 (Isaaks and Srivastava 1989).

$$\gamma(\mathrm{h})=\frac{1}{2\mathrm{N(h)}}\sum_{(\mathrm{i,j})|\mathrm{h_{ij}}\approx\mathrm{h}}\left(\mathrm{Z}(\mathbf{s}_\mathrm{i})-\mathrm{Z}(\mathbf{s}_\mathrm{j})\right)^2 \tag{4.4}$$

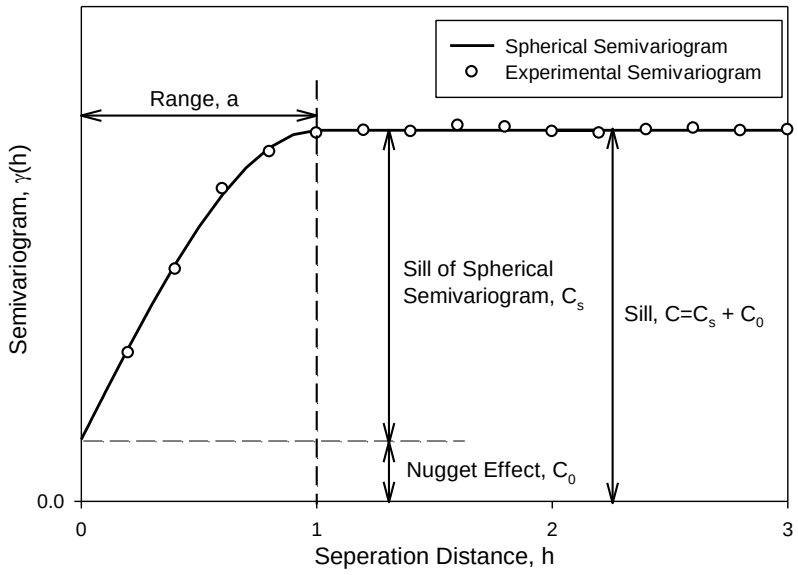

Figure 4.7. Typical semivariogram graph

A semivariogram plot is composed of a sill (C) that includes a nugget effect (C_0) and partial sill (C_s), and a range (a) or effective range (a'). Figure 4.7 shows a typical spherical semivariogram model fitted to the experimental semivariogram values.

Three major semivariogram parameters are nugget the effect (C_0), the sill ($C=C_0+C_s$), and the Range (a). A brief description of each parameter is summarized below using information from geostatistical books (Goovaerts 1997; Isaaks and Srivastava 1989).

The nugget effect (C_0) is the sudden increase of the semivariogram value as the separation distance goes from 0 m at the origin to an extremely small distance. This nugget effect can be the result of sampling error or short scale variability. The nugget effect can be determined by fitting a straight line though first few semivariogram values to intercept with the vertical axis. The relative nugget effect tends to increase with the lag (h) tolerance and data sparsity. Data sparsity or measurement errors may lead to a semivariogram with noisy values and can only be represented with a pure nugget effect. In general, the nugget effect is modelled as an isotropic component, but it can be modeled as an anisotropic spatial structure when the range value is smaller than the shortest sampling distance.

The sill ($C=C_0+C_s$) is the value of the semivariogram when the average squared difference between pairs of values no longer increases with increasing separation distance, that is the semivariogram reaches a plateau. The sill of the semivariogram may not be equal to the sample variance (Barnes 1991; Goovaerts 1997) and so forcing the sill to be equal to the sample variance (s^2) is a questionable practice.

The range (a) is the distance at which the semivariogram reaches the sill plateau. In most models, the effective range (a') is determined as the distance at which the semivariogram reaches

95% of the sill plateau. More and better data tends to produce a longer range for the experimental semivariogram.

The discrepancies in semivariogram values reflect experimental fluctuations that result from the small number of data pairs available for each lag. Generally, the minimum of 30 and preferred 50 or more data pairs is desired within each bin (Journel and Huijbregts 1978). Erratic behaviors can be found in experimental semivariograms for data that are skewed or have extremely high or low values (outliers). If the sampled data is highly skewed (skewness is out the range of -1 to 1), the data may be transformed before performing spatial analysis. If the experimental semivariogram keeps increasing with increasing separation distance between data pairs, there could be a trend in the sampled data that should be removed before spatial analysis (Gringarten and Deutsch 2001). If a significant trend is identified this violates the assumption for spatial analysis that the mean is constant.

Three theoretical semivariogram models (Table 4.3) are used in this study to describe the experimental semivariogram values and the best fitted model is chose using statistical criteria.

Table 4.3. Semivariogram models

Model	R code	Equation	Parameter note
Nugget	Nug	$\hat{\gamma}(h)=\begin{cases}0 & h=0\\ C_0 & h\neq 0\end{cases}$	
Spherical	Sph	$\hat{\gamma}(h)=\begin{cases}C_s\left(\frac{3}{2}\frac{h}{r}-\frac{1}{2}\left(\frac{h}{r}\right)^3\right) & 0\le h\le r\\ C_s & h>r\end{cases}$	a = *r* (range reaches 100% of C_s)
Exponential (Matérn, *k*=0.5)	Exp	$\hat{\gamma}(h)=\begin{cases}0 & h=0\\ C_s\left(1-e^{-\frac{h}{r}}\right) & h>0\end{cases}$	a′ = 3*r* (effective range reaches 95% of C_s)
Whittles (Matérn, *k*=1)	Bes	$\hat{\gamma}(h)=\begin{cases}0 & h=0\\ C_s\left(1-\left(\frac{h}{r}\right)K_1\left(\frac{h}{r}\right)\right) & h>0\end{cases}$	a′ = 4*r* (effective range reaches 95% of C_s)

Note: $K_1(h/r)$ is modified Bessel function of the second kind with order *k*=1, *r* is the range parameter obtained in R program.

In this study, model is fit to the The calculated experimental semivariogram using a weighted least squares method as Cressie (1985) suggested. The weight calculation method is presented in Eq. 4.5 where N_i is the number of data pairs that are an average distance, h_i, apart.

$$w_i = \frac{N_i}{h_i^2} \tag{4.5}$$

The sum of square errors (SSErr) is calculated for each fitted theoretical semivariogram to describe how well the model fits the experimental semivariogram. SSErr is calculated using Eq. 4.6 where $\hat{\gamma}(h_j)$ is the predicted semivariogram value using the fitted theoretical model and $\gamma(h_i)$ is the average experimental semivariogram value at a lag distance h_i.

$$SSErr = \sum_{i=1}^{n} w_i \left[\hat{\gamma}(h_i) - \gamma(h_i)\right]^2 \tag{4.6}$$

4.4. Results and Discussion

Variability of pavement foundation properties are studied in three sections, the first is to investigate how the variability changes with the number of roller compaction passes, second is to summarize the univariate statistical analysis of different in-situ tests measurements, and third is to introduce the spatial variability analysis.

4.4.1. Variation of pavement foundation properties to number of compaction passes

The relationship between in-situ measured pavement foundation properties and the number of compaction roller passes is studied on NC Hwy-218 with 21 tests performed after every target number of passes. The results are presented in box plots and COVs are calculated to see how variation changes with the number of passes for two subgrade and two base sections as Figure 4.8 to Figure 4.11 show.

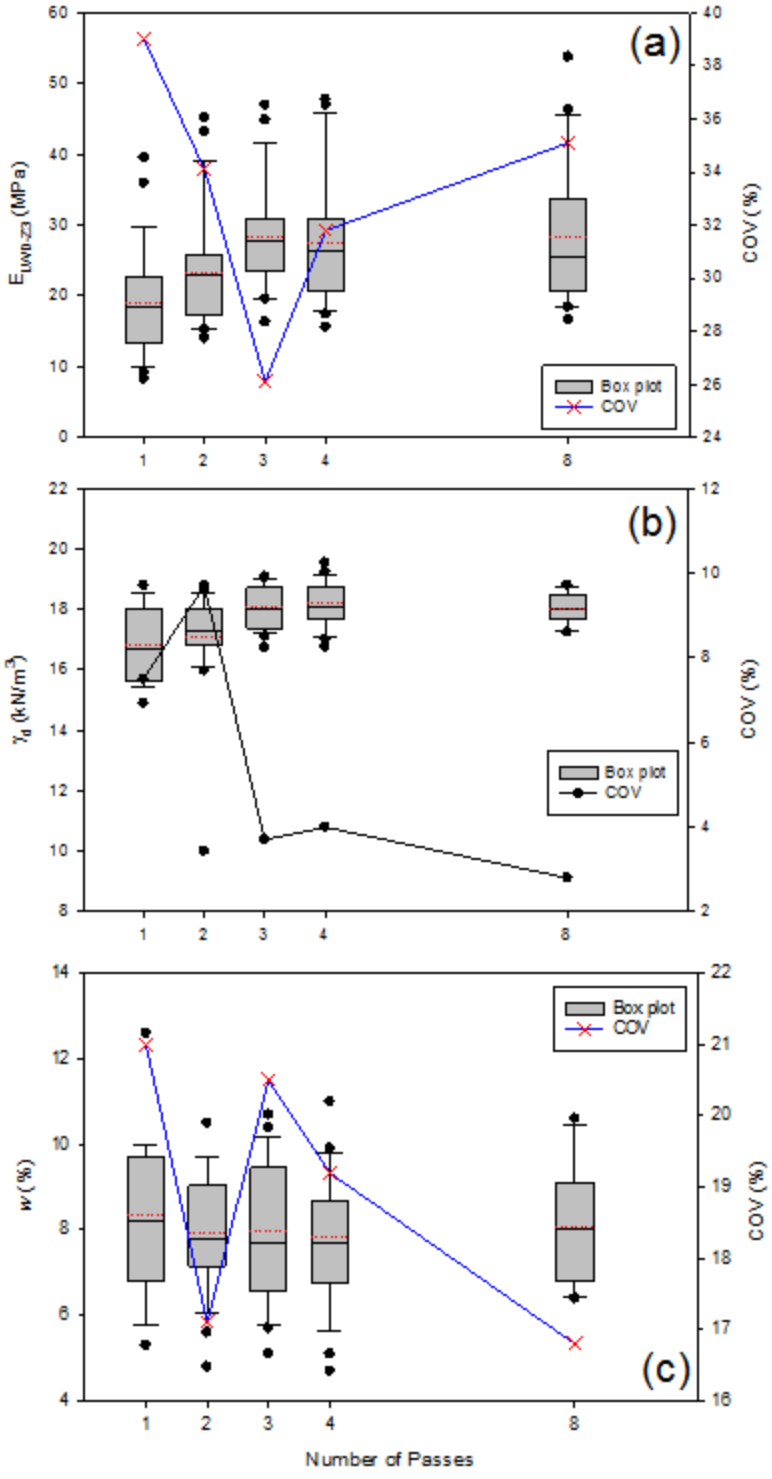

Figure 4.8. Variation of pavement foundation properties with number of compaction pass (NC Hwy-218 TS1 subgrade)

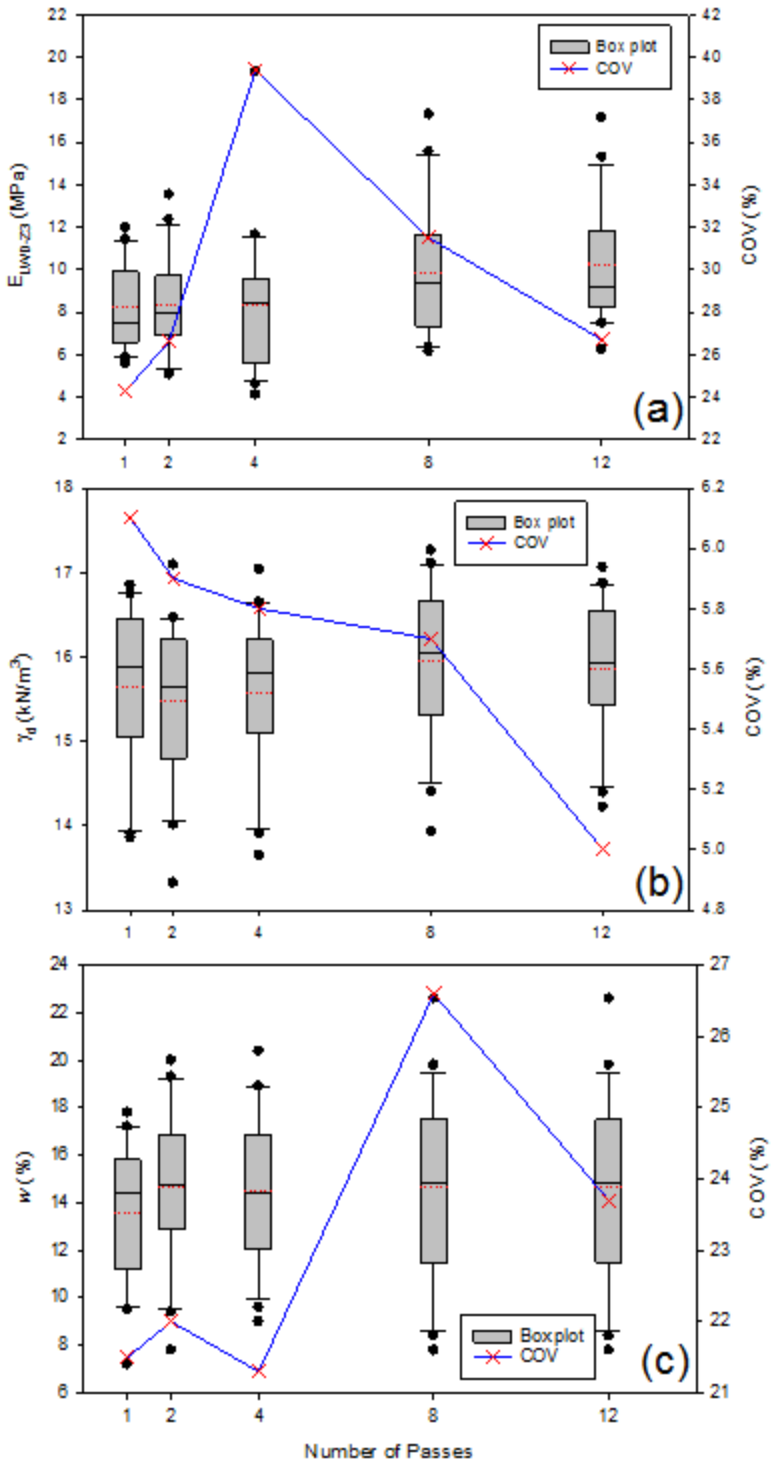

Figure 4.9. Variation of pavement foundation properties with number of compaction pass (NC Hwy-218 TS2 subgrade)

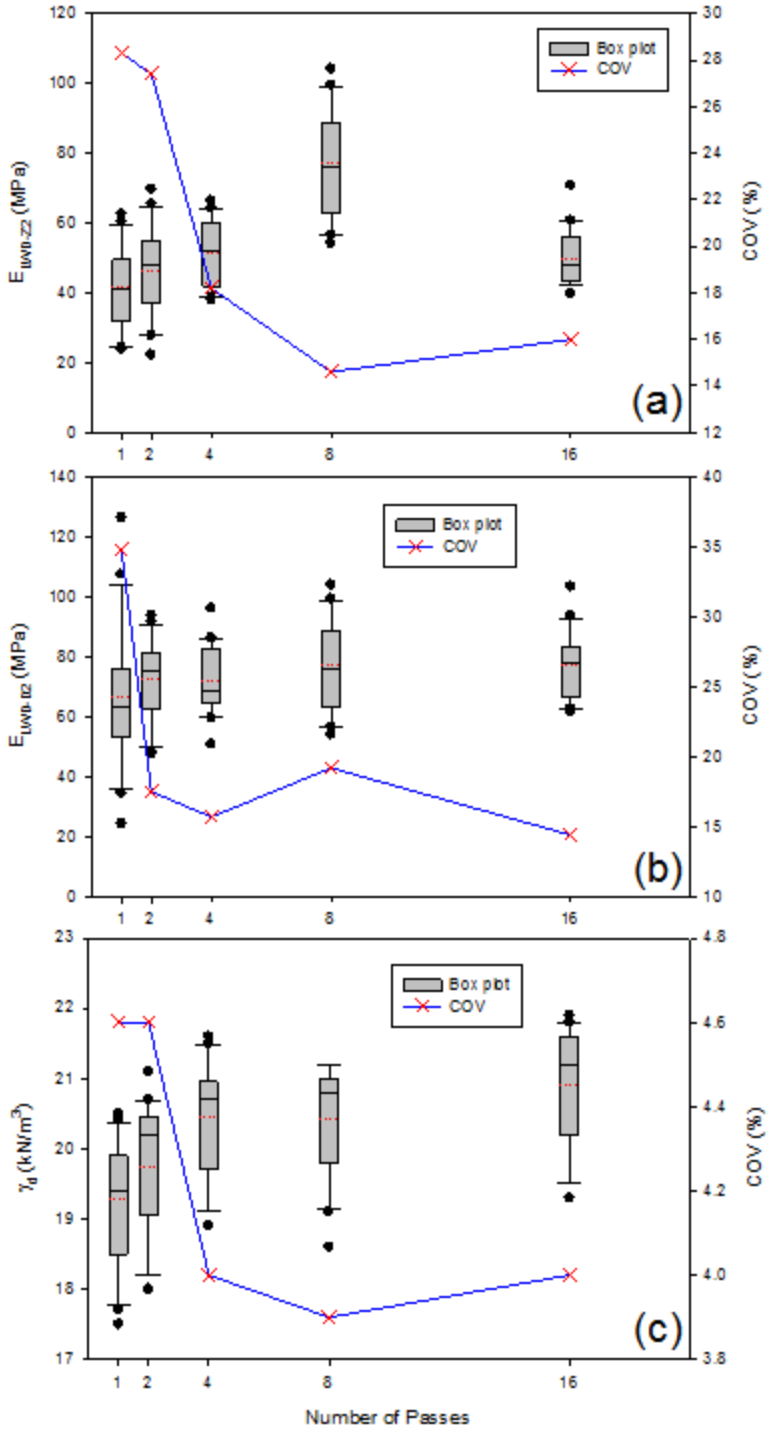

Figure 4.10. Variation of pavement foundation properties with number of compaction pass (NC Hwy-218 TS3a base)

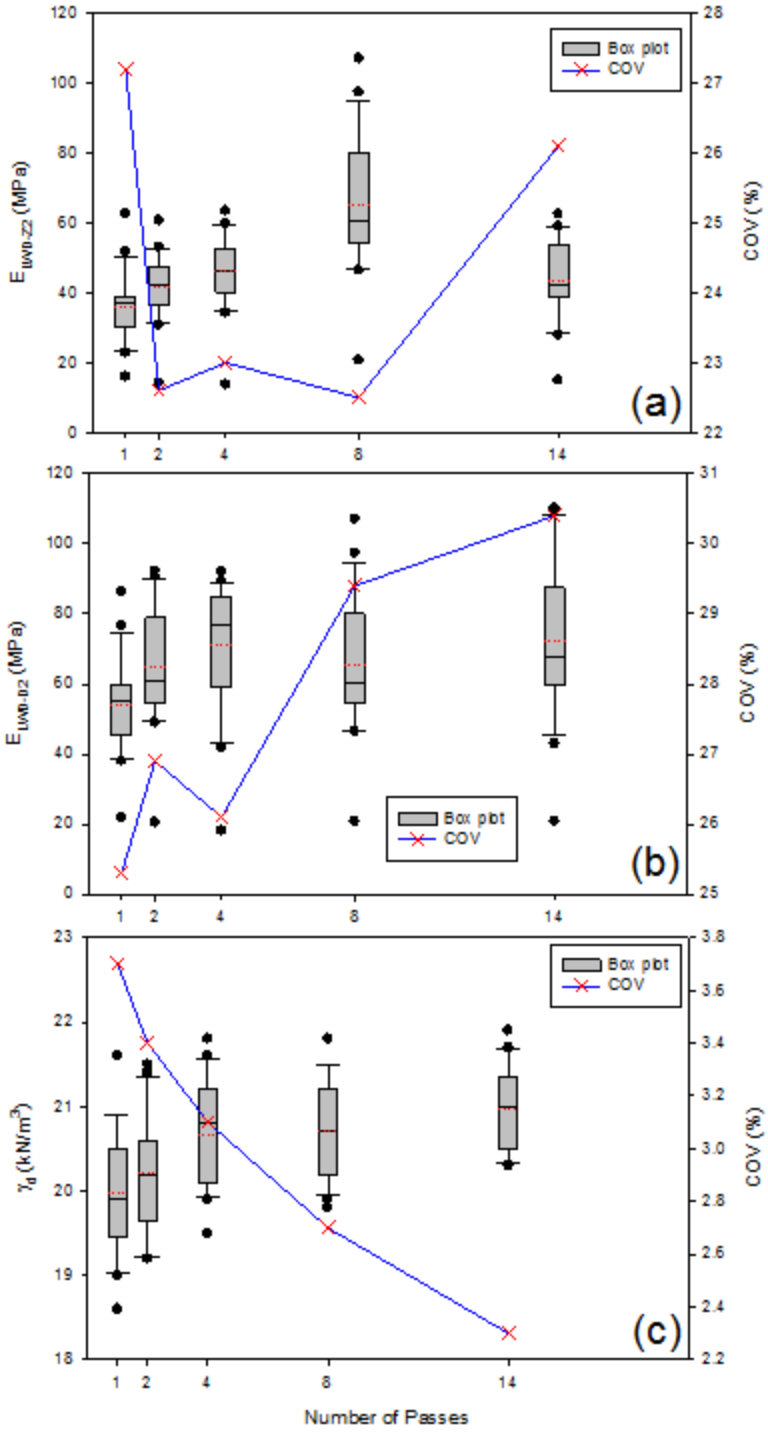

Figure 4.11. Variation of pavement foundation properties with number of compaction pass (NC Hwy-218 TS3b base)

Figure 4.8 shows the LWD test and NG test results with number of passes. The mean value of both E_{LWD-Z3} and γ_d increase to a relative constant value after three passes while there is no

obvious change in the mean value of moisture content. The COV of both $E_{LWD\text{-}Z3}$ and γ_d reaches the lowest value at the third pass, but increases in COV values for $E_{LWD\text{-}Z3}$ are observed with more compaction passes. Figure 4.10 shows relative lower COV value at the first two passes than after more passes in $E_{LWD\text{-}Z3}$ and *w* while the constant decreasing COV value is observed in the collected γ_d values.

The overall mean value of $E_{LWD\text{-}Z2}$ significantly decreases after more passes compaction after 8 passes on TB3a and 4 passes on TB3b (Figure 4.10 and Figure 4.11).

Figure 4.10 shows variation of two stiffness measurements and dry unit weight decreases with increasing number of passes. Figure 4.11 shows variation of $E_{LWD\text{-}Z2}$ and $E_{LWD\text{-}D2}$ initially decreases with up to 4 passes, but variation increases about 4% with more passes after 8 and 4 passes for $E_{LWD\text{-}Z2}$ and $E_{LWD\text{-}D2}$ respectively. The mean value of γ_d increases and COV decreases with number of passes.

The relationship between in-situ measured pavement foundation properties and the number of compaction roller passes is studied on FL I-10 with 20 tests on two base sections and 10 tests on two subgrade sections after every target number of passes. The results are presented in box plots and COVs are calculated to see variation change with number of passes for two subgrade and two base sections as Figure 4.12 to Figure 4.16 show.

Figure 4.12 shows increasing $E_{LWD\text{-}Z3}$ with increasing number of passes and COV decreasing from about 15.5% with passes to 10% after 8 passes. Increasing average γ_d values were observed with more passes of compaction while there is a slight decrease in w is observed. The variation of both γ_d and *w* is relatively small and does not change a lot with increasing number of compaction passes. The similar observation has been found in compaction on second base layer in FL I-10 TS2 (Figure 4.14).

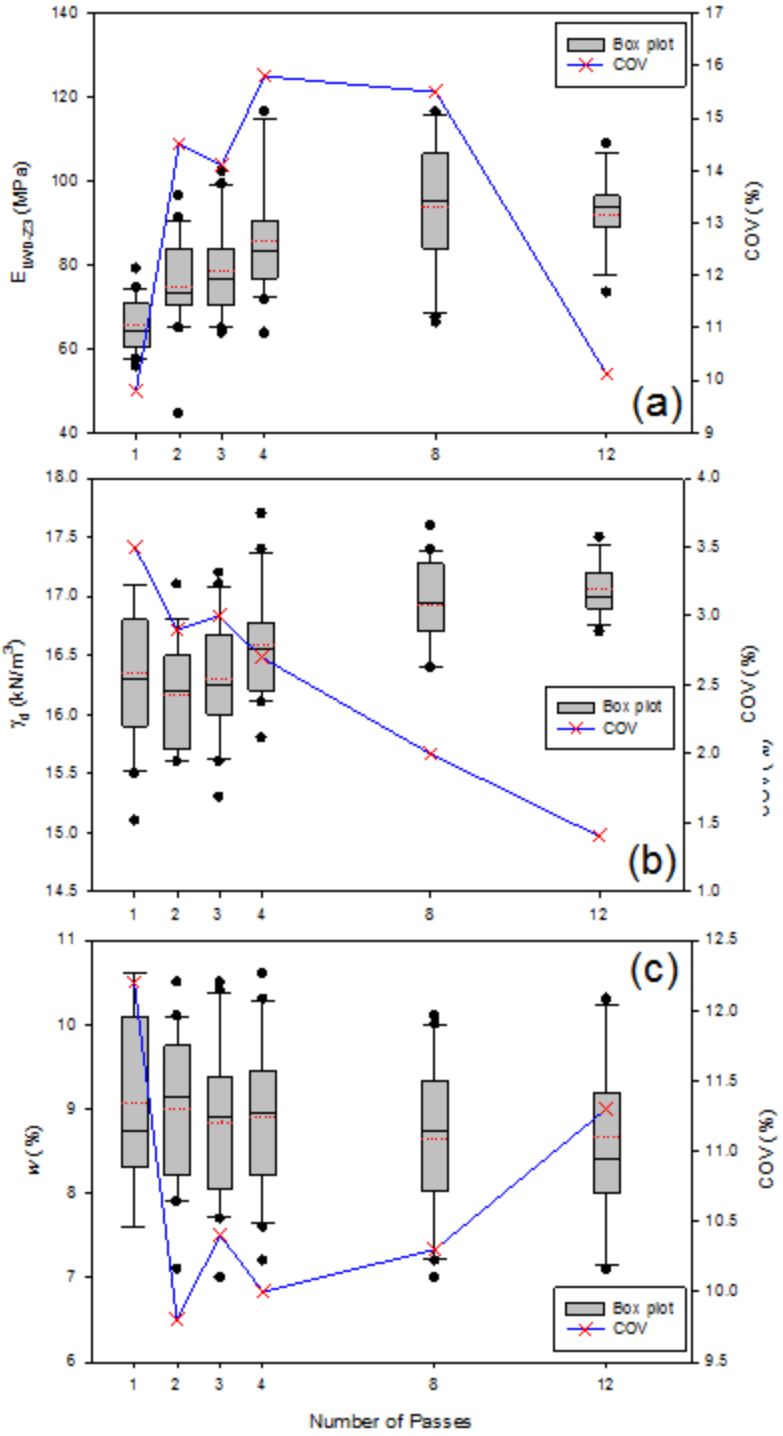

Figure 4.12. Variation of pavement foundation properties with number of compaction pass (FL I-10 TS1 Base)

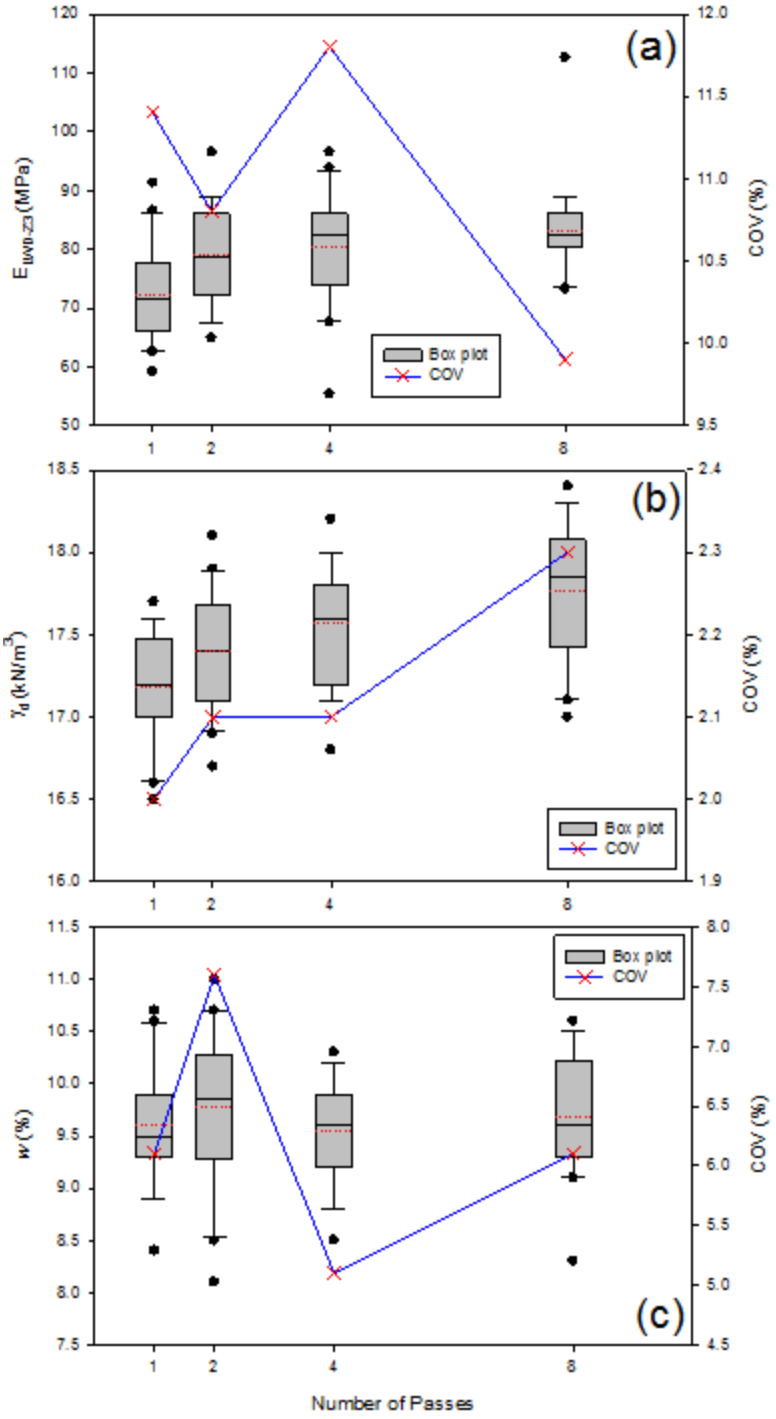

Figure 4.13. Variation of pavement foundation properties with number of compaction pass (FL I-10 TS2 Base)

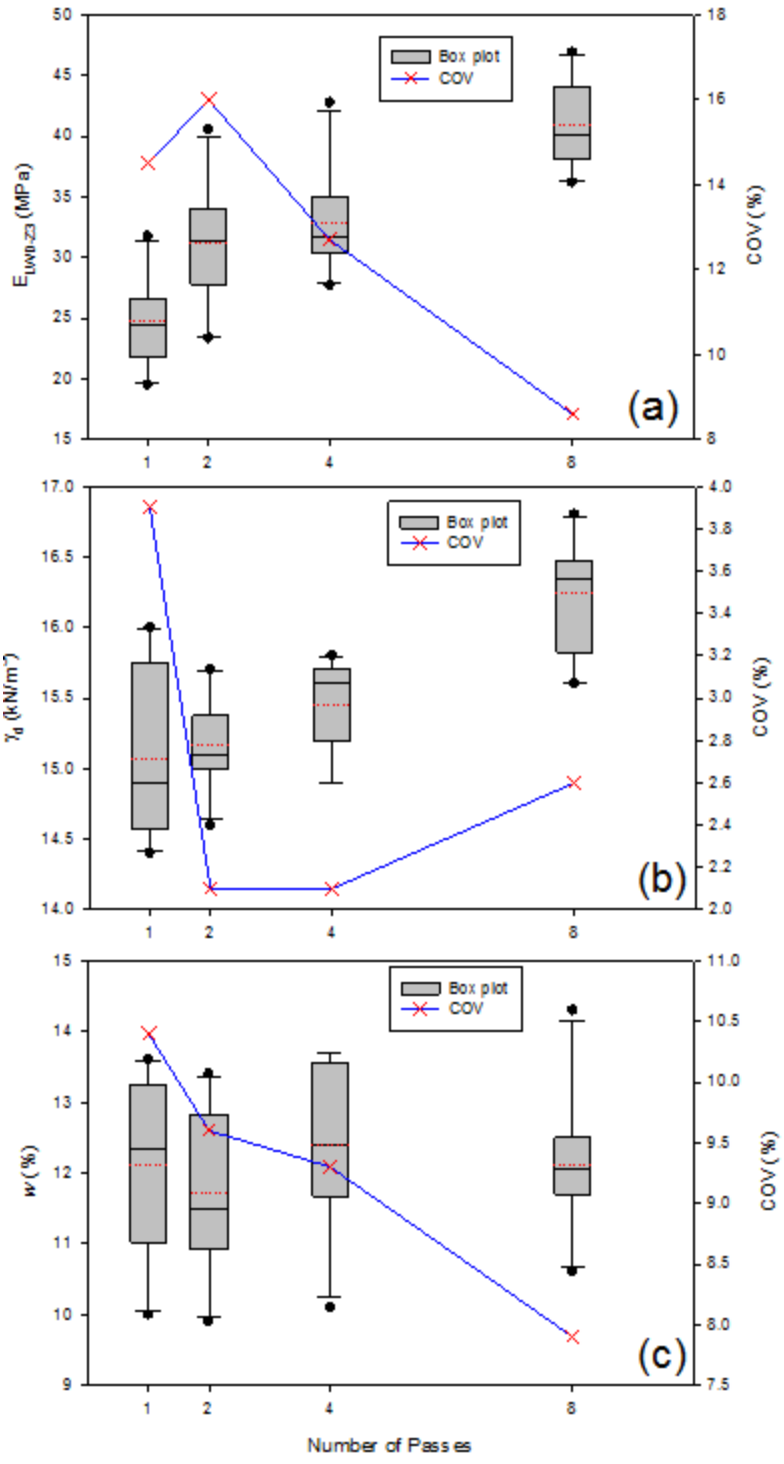

Figure 4.14. Variation of pavement foundation properties with number of compaction pass (FL I-10 TS5 subgrade)

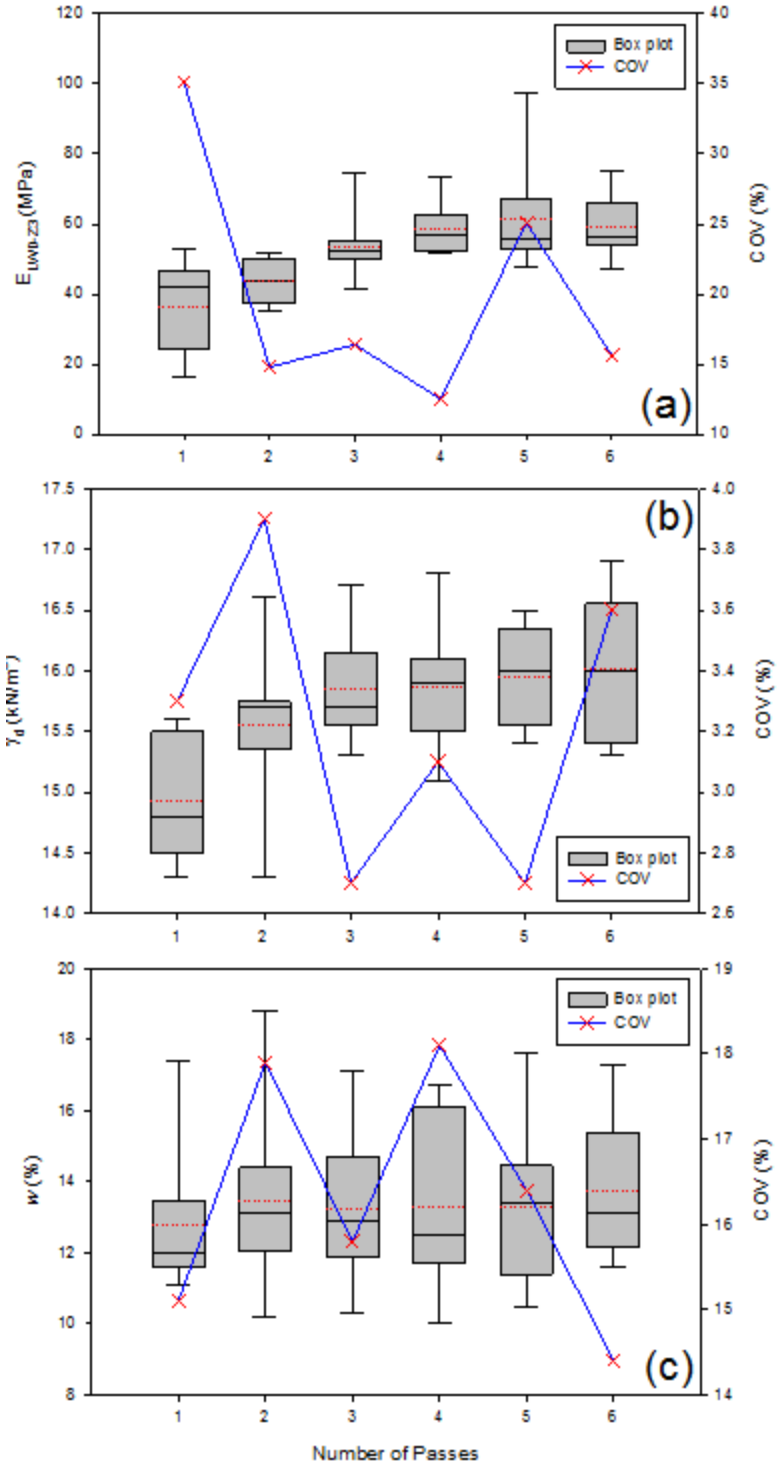

Figure 4.15. Variation of pavement foundation properties with number of compaction pass (FL I-10 TS6 Stabilized subgrade)

Figure 4.14 shows that the mean $E_{LWD\text{-}Z3}$ value increases from 25 MPa to 40 MPa with COV decreases from 16% to 8.5% after 8 compaction passes on the subgrade. The increase in mean γ_d

value has been observed with increasing number of compaction passes while moisture content remains nearly the same. The variations in γ_d and *w* are small in comparison with variation of $E_{LWD\text{-}Z3}$. Figure 4.15 shows consistent increase in the mean value of $E_{LWD\text{-}Z3}$ and γ_d with first three passes and then levels off while moisture content remains nearly unchanged. Decrease of variation in $E_{LWD\text{-}Z3}$ has been observed with increasing number of compaction passes while no clear relationship between COV and number of passes observed in γ_d and *w* measurements on FL I-10 TS6 stabilized subgrade.

4.4.2. Univariate variability

Univariate statistics are calculated for data measured on each test section on all 6 projects. The LWD test determined $E_{LWD\text{-}Z3}$ and NG test determined γ_d and *w* are measured on all test sections, so the univariate statistics of each of these three pavement foundation properties are summarized in a single table (Table 4.4, Table 4.5, and Table 4.6). The rest of the in-situ test results for pavement foundation properties are summarized in Table 4.7.

According to the variability study on LWD tests measurements (Table 4.4), the average (μ) $E_{LWD\text{-}Z3}$ on base/subbase layer is generally varying in a range from 12.6 MPa to 98.7 MPa and at maximum of 214.8 MPa on CTB and on subgrade layer is varying from 18.9 MPa to 34.9 MPa in general and the maximum 83.6 MPa is the average measurements on stabilized subgrade. The coefficient of variation (COV) of $E_{LWD\text{-}Z3}$ varies from 11% to 39% on 11 base/subbase layers and from 17% to 89% on 5 subgrade layers. The largest COV of 89% is obtained at the NC Hwy-218 TS1 which has the lowest mean value of $E_{LWD\text{-}Z3}$, and possible soft area could be expected according to the measured $E_{LWD\text{-}Z3}$ cross the study area that shown in Figure 4.16. Higher COV will be expected in stiffness measurements as the stiffness is measured as a composite layer property that not a value measured for a point whining a layer as NG does.

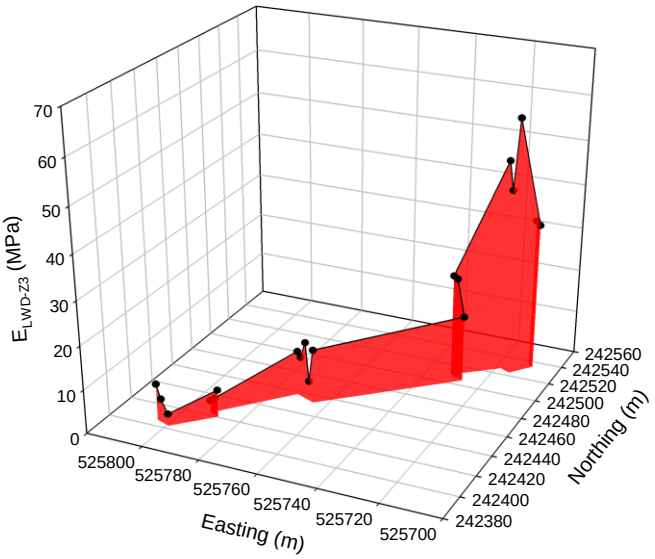

Figure 4.16. Variation of E_{LWD-Z3} in NC Hwy-218 TS1

Table 4.4. Univariate statistics summary of E_{LWD-Z3} (MPa)

Field site	TS	Layer	Univariate Statistics						
			Mean (μ)	Median	Variance (s^2)	Std Dev (σ)	COV	N	Skewness
MI I-94	TS1a	Base	73.3	73.7	206.0	14.4	20	54	0.27
	TS1b	Base	58.5	58.6	50.5	7.1	12	121	0.43
	TS3	Base	49.0	49.6	109.8	10.5	21	162	0.06
MI I-96	TS1	Sand subbase	30.9	31.3	124.1	11.1	36	73	-0.20
	TS2	CTB	214.8	216.9	7152.4	84.57	39	119	0.29
	TS3	Sand subbase	33.2	35.8	108.7	10.4	31	26	-0.57
WI US-10	TS1	Sandy Subbase	12.6	12.6	10.3	3.2	25	17	0.00
	TS2	Subgrade	30.7	30.4	28.3	5.3	17	80	0.62
NC Hwy -218	TS1	Subgrde	18.9	12.4	285.8	16.9	89	19	1.10
	TS2	Subgrade	29.2	26.1	349.8	18.7	64	45	2.06
	TS3a	Base	39.7	40.4	28.7	5.4	13	6	-0.05
FL I-10	TS1	Base1	98.7	93.8	379.6	19.5	20	27	0.98
	TS2	Base2	83.2	84.4	87.8	9.4	11	15	0.39
	TS5	Subgrade	34.9	33.6	194.6	14.0	40	40	1.38
	TS6	Stablized Subgrade	83.6	82.4	263.4	16.2	19	27	0.20
IA US-30	TS2	RPCC modified Subbase	56.6	57.5	120.6	11.0	19	40	-0.81

Dry unit weight (γ_d) was measured with NG tests on 15 test sections for 5 of the project sites. The summarized univariate statistics (Table 4.5) shows that the mean γ_d of 10 base/subbase layers varies from 14.6 kN/m^3 to 20.3 kN/m^3 with the COV varies from 2% to 6%. The mean γ_d of 5 subgrade layers varies from 15.7 kN/m^3 to 19.84 kN/m^3 with the COV varies from 2% to 6%. A lower COV should be expected according to the density control method used in pavement foundation construction. The test area should be evaluated for identifying possible weak area when COV of higher than 10% was obtained.

Table 4.5. Univariate statistics summary of γ_d (kN/m^3)

Field site	TS	Layer	Univariate Statistics						
			Mean (μ)	Median	Variance (s^2)	Std Dev (σ)	COV	N	Skewness
MI I-94	TS1a	Base	20.08	20.07	0.43	0.66	3	54	-0.37
	TS1b	Base	20.00	20.00	0.38	0.61	3	121	-0.13
	TS3	Base	19.21	19.25	0.77	0.88	5	162	-0.02
MI I-96	TS1	Sand subbase	20.16	20.15	0.34	0.59	3	73	-0.03
	TS2	CTB	14.56	14.59	0.66	0.81	6	119	-0.3
	TS3	Sand subbase	20.01	19.89	0.26	0.51	3	26	0.30
WI US-10	TS1	Sandy Subbase	16.15	16.07	0.12	0.35	2	17	-0.3
	TS2	Subgrade	19.84	19.84	0.15	0.38	2	79	0.1
NC Hwy-218	TS1	Subgrde	18.00	18.21	0.83	0.91	5	18	-0.27
	TS2	Subgrade	16.98	16.71	1.08	1.04	6	44	0.47
	TS3a	Base	20.25	20.35	0.30	0.55	3	6	-1.12
FL I-10	TS1	Base1	17.78	17.80	0.29	0.54	3	26	-0.56
	TS2	Base2	17.79	17.80	0.09	0.30	2	15	-0.26
	TS5	Subgrade	16.27	16.25	0.20	0.45	3	40	0.30
	TS6	Stabilized Subgrade	15.70	15.7	0.11	0.34	2	23	-0.43

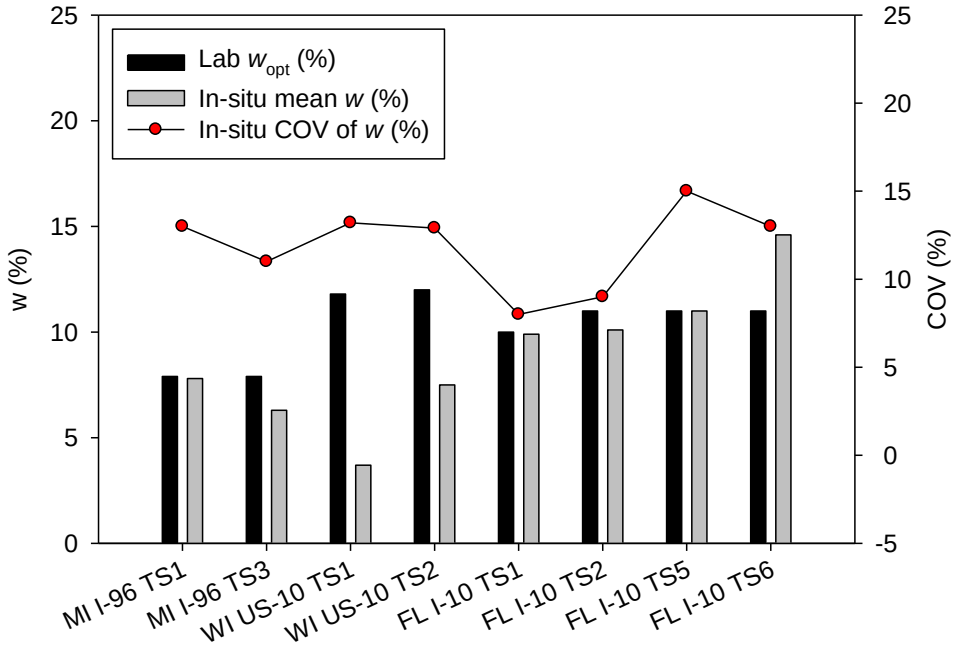

Figure 4.17. Variation of in-situ measured *w* compared to laboratory determined w_{opt}.

Moisture content (*w*) was measured with NG tests on 14 test sections over the 5 project sites. The summarized univariate statistics (Table 4.6) shows that the mean value of *w* varies from 1.3% to 10.1% over 9 test sections on base/subbase and varies from 7.5% to 14.6% over 5 test sections on subgrade. The large range of *w* variation could be the result of the length of time after construction that NG tests were performed and the difference in target moisture content which is in a range of w_{opt} determined with laboratory tests. The mean value of in-situ measured *w* was compared to laboratory determined w_{opt} on selected test sections that laboratory tests were performed in determining the compaction curve (Figure 4.17). There is no definite trend of COV with w_{opt} or difference between in-situ measured *w* and w_{opt}.

Table 4.6. Univariate statistics summary of *w* (%)

Field site	TS	Layer	Univariate Statistics						
			Mean (μ)	Median	Variance (s^2)	Std Dev (σ)	COV	N	Skewness
MI I-94	TS1a	Base	1.8	1.8	0.1	0.4	22	54	0.42
	TS1b	Base	2.3	2.3	0.1	0.3	14	121	-0.70
	TS3	Base	1.3	1.3	0.1	0.3	25	162	0.44
MI I-96	TS1	Sand subbase	7.8	7.7	1.0	1.0	13	73	0.47
	TS2	CTB	7.3	7.2	1.0	1.0	13.9	119.0	1.4
	TS3	Sand subbase	6.3	6.3	0.5	0.7	11	26	0.44
WI US10	TS1	Sandy Subbase	3.7	3.7	0.2	0.5	13.2	17.0	-0.9
	TS2	Subgrade	7.5	7.4	0.9	1.0	12.9	79.0	1.0
NC Hwy218	TS1	Subgrde	10.2	8.1	16.0	4.0	39	18	0.85
	TS2	Subgrade	12.1	11.6	13.0	3.6	30	44	0.50
FL I-10	TS1	Base1	9.9	10.1	0.7	0.8	8	26	-0.99
	TS2	Base2	10.1	10.5	0.9	0.9	9	15	-0.42
	TS5	Subgrade	11.0	10.8	2.5	1.6	15	40	0.19
	TS6	Stablized Subgrade	14.6	13.7	3.5	1.9	13	23	0.76

The in-situ tests in addition to LWD and NG tests were performed on selected test sections and the univariate statistics of variation of DCPI and CBR determined from DCP tests and $E_{FWD\text{-}K3}$ determined from FWD tests are summarized in Table 4.7. The average DCPI of base or subbase layer varies from 7 mm/blow to 19 mm/blow with COV varied from 8% to 53% over 8 tests sections of three projects. The high COV value might be expected due to the calculation of DCPI that is the weighted average value across the data analyst identified layer thickness. California bearing ratio (CBR) was calculated from the DCP tests and is not a direct measurements. The mean value of CBR of tests performed on base/subbase layer over 4 test sections of three project sites varies from 11% to 67% with COV varies from 19% to 35%.

Table 4.7. Univariate statistics summary of other pavement foundation properties

Field site	TS	Layer	Properties	Univariate Statistics						
				Mean (μ)	Median	Variance (s^2)	Std Dev (σ)	COV	N	Skewness
MI I-94	TS1a	Base	DCPI	6	6	3.0	1.7	27	54	1.87
	TS1b	Base	DCPI	7	7	1.3	1.1	17	120	0.48
	TS3	Base	E_{FWD-k3}	44.7	44.4	195.0	14.0	31	50	0.83
			DCPI	8	8	3.8	2.0	23	162	0.69
MI I-96	TS1	Sand subbase	DCPI	19	19	20.7	4.5	24	57	0.37
	TS3	Sand subbase	DCPI	16	16	25.0	5.0	30	26	0.45
WI US10	TS1	Sandy Subbase	CBR	5.6	5.7	1.4	1.2	21.5	17	-1.1
	TS2	Subgrade	CBR	15.4	14.5	24.8	5.0	32.2	79	1.2
NC Hwy218	TS2	Subgrade	DCPI	13	11	57.6	7.6	59	25	1.36
	TS3a	Base	DCPI	12	12	0.9	0.9	8	6	2.37
	TS3b	Base	DCPI	14	11	57.8	7.6	53	20	0.97
FL I-10	TS1	Base1	DCPI	7	7	1.9	1.4	19	27	0.90
			CBR	32.9	33.8	39.1	6.2	19.0	27	-0.29
IA US30	TS1	RPCC Subbase	CBR	11.0	9.6	14.9	3.9	35	20	1.08
		RPCC/RAP Subbase	CBR	67.0	70.6	330.8	18.2	27	20	-0.37
		Subgrade	CBR	12.9	12.1	15.6	3.9	31	20	1.25

Note: DCPI unit is mm/blow; E_{FWD-K3} unit is MPa; CBR unit is %.

4.4.3. Directional spatial variability

Spatial variability of pavement foundation properties is studied in longitudinal and transverse directions with respect to pavement structure geometry as many researchers have indicated a possible anisotropic spatial variability in pavement structure. Two sections of the total 18 test sections over the 6 project sites are densely gridded samples appropriate for spatial variability analysis study on pavement foundation properties. The detailed procedures of spatial are discussed chapter 3 and will not be provided in this section. Only the directional experimental semivariogram with fitted theoretical semivariogram models are presented for characterizing the

directional spatial variability of pavement foundation properties and these are compared with directional spatial variability of those properties measured in long sparse sampled test sections. Although the in-situ measurements are much more than the required number in pavement construction quality control and quality assurance programs, the amount of data in several test sections is inadequate for spatial variability analysis.

The first dense gridded test section MI I-94 TS1b is inside of the long sparse sampled test section MI I-94 TS1a as shown in Figure 4.18.

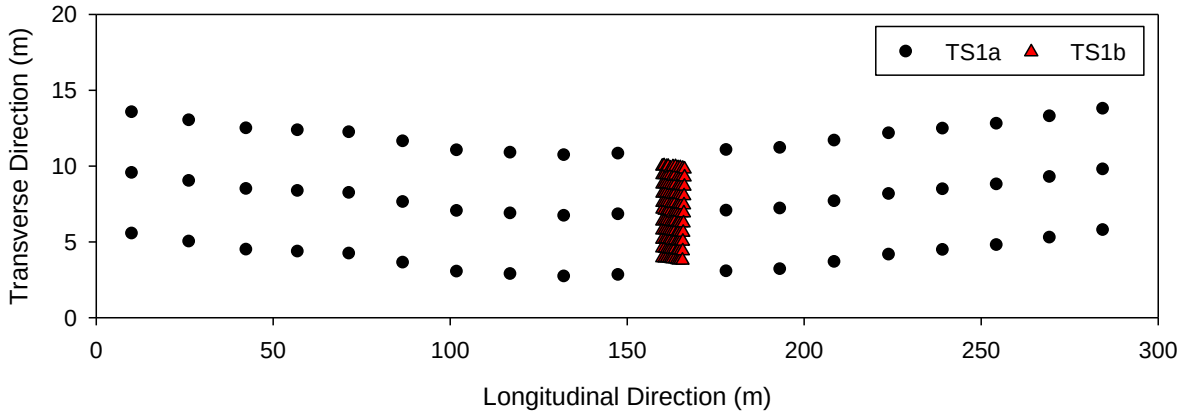

Figure 4.18. Test plan for TS1a and TS1b test sections of MI I94

Semivariograms for directional spatial variability are presented for $E_{LWD\text{-}Z3}$, γ_d, and $DCPI_{subbase}$ in Figure 4.19, Figure 4.20, and Figure 4.21, respectively. The semivariogram in the transverse direction for $E_{LWD\text{-}Z3}$ tend to reach the sample variance in larger range distance >4 m while the semivariogram in longitudinal direction shows a shorter range <4 m. In the longitudinal direction the sill is larger than the sample variance. The transverse $\gamma(h)$ of γ_d shows a range of about 2 m while the longitudinal $\gamma(h)$ shows a possible trend. The $\gamma(h)$ of $DCPI_{subbase}$ in both transverse and longitudinal directions show clear sill values with similar range length which may imply isotropic $\gamma(h)$ of $DCPI_{subbase}$. Semivariograms based on the long sparse data from MI I94 TS1a (Figure 4.22, Figure 4.23, and Figure 4.24), show erratic behavior as

separated distance increases beyond 45 m. There is clear relationship between γ(h) and separation distance can be identified, so the theoretical model was controlled with sample variation as partial sill (C_s) to fit to the experimental γ(h). With the controlled sill, the range value are expected to be in a range of 25 m to 40 m that may not be true with no data pairs was obtained within a separation distance of 15 m. According to the spatial analysis on the same test site, the minimum spacing should be about 0.5 m to catch the initial part of the semivariogram from the origin to describe the directional semivariogram with more confidence. If only large spacing data are collected with a limited number of tests, the data may not be useful for spatial variability analysis.

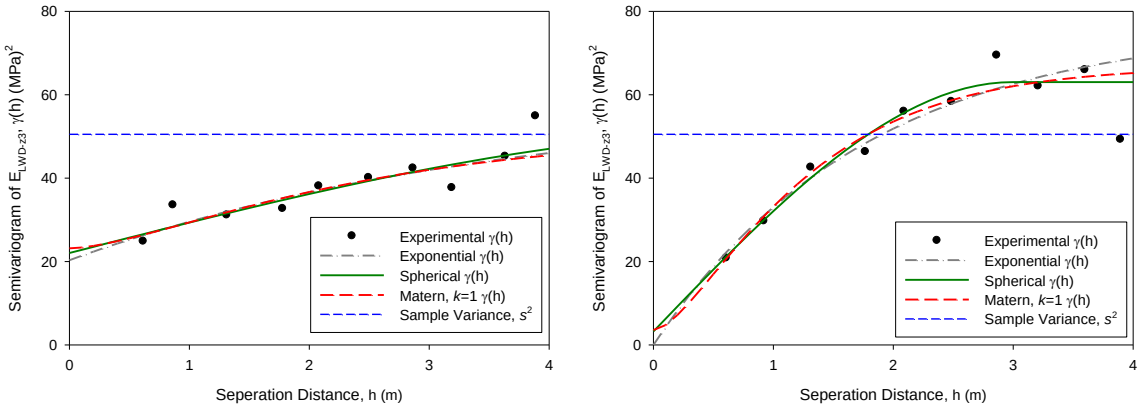

Figure 4.19. Experimental γ(h) of E_{LWD-Z3} on MI I-94 TS1b in transverse direction (left) and longitudinal direction (right)

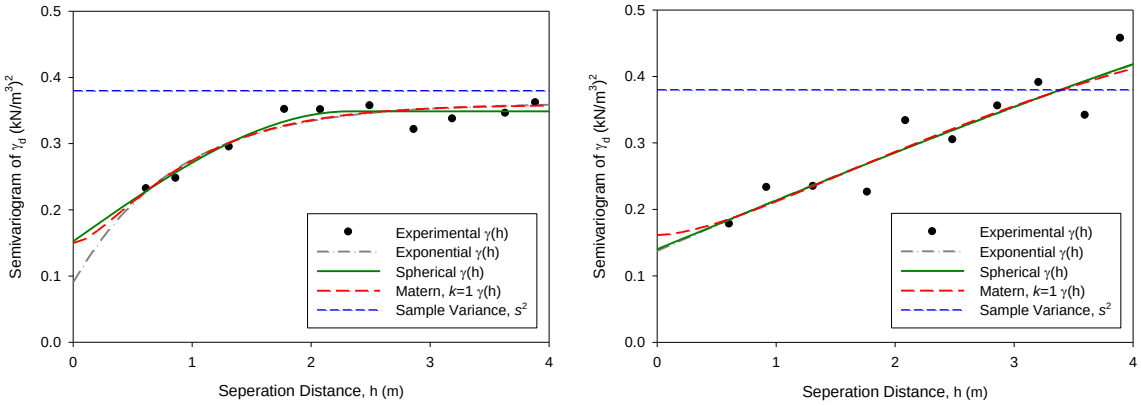

Figure 4.20. Experimental γ(h) of γ_d on MI I-94 TS1b in transverse direction (left) and longitudinal direction (right)

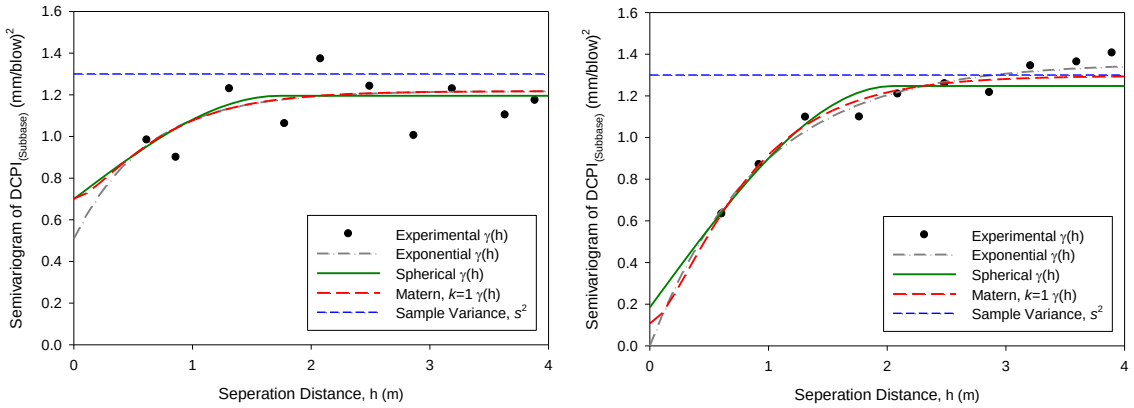

Figure 4.21. Experimental γ(h) of $DCPI_{subbase}$ on MI I-94 TS1b in transverse direction (left) and longitudinal direction (right)

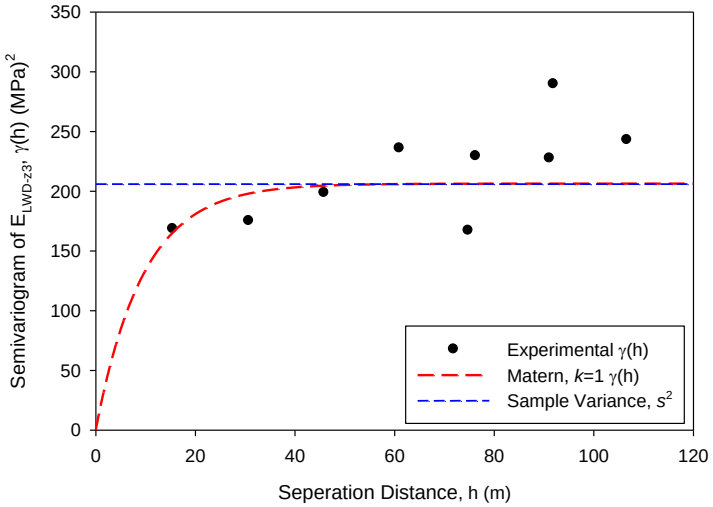

Figure 4.22. Experimental γ(h) of $E_{LWD\text{-}Z3}$ on MI I-94 TS1a in longitudinal direction

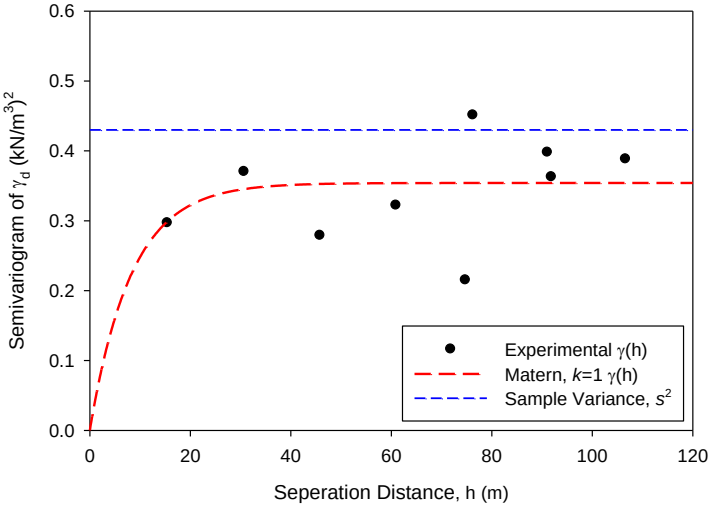

Figure 4.23. Experimental γ(h) of γ_d on MI I-94 TS1a in longitudinal direction

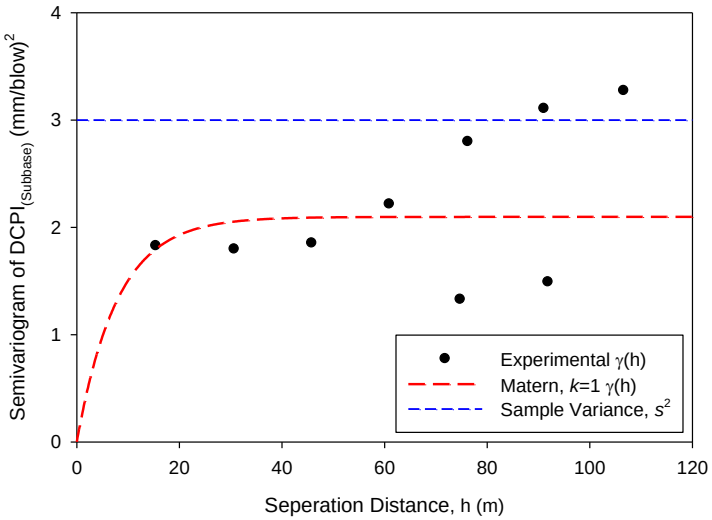

Figure 4.24. Experimental γ(h) of $DCPI_{subbase}$ on MI I-94 TS1a in longitudinal direction

Directional spatial variability analysis was performed on the dense gridded data collected on MI I-96 TS1. According to the spatial analysis on E_{LWD-Z3}, γ_d, and *w* (Figure 4.25, Figure 4.26, and Figure 4.27) shows higher variation within smaller correlation lengths in the transverse direction compared to the longitudinal direction. This indicates more uniform pavement foundation properties (E_{LWD-Z3}, γ_d, and *w*) would be expected in the longitudinal direction than the transverse direction. However, the spatial analysis on $DCPI_{subbse}$ and $DCPI_{subgrade}$ does not show the same trends as described for E_{LWD-Z3}, γ_d, and *w*. Figure 4.28 shows that higher spatial variation of $DCPI_{subbase}$ will be expected in both transverse and longitudinal directions at a correlation distance longer than 4 m. Figure 4.29 shows $DCPI_{subgrade}$ is possibly more uniform in the longitudinal direction than the transverse direction with small correlation length <2 m..

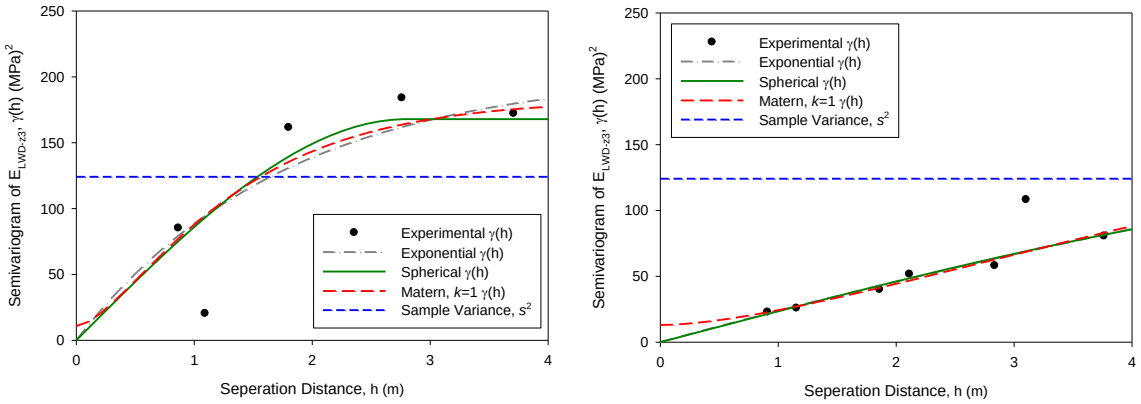

Figure 4.25. Experimental γ(h) of E_{LWD-Z3} on MI I-96 TS1 in transverse direction (left) and longitudinal direction (right)

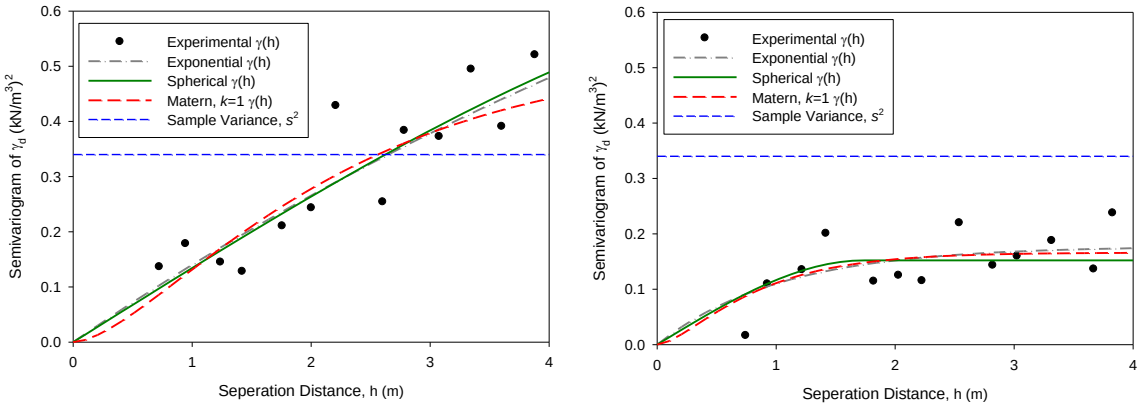

Figure 4.26. Experimental γ(h) of γ_d on MI I-96 TS1 in transverse direction (left) and longitudinal direction (right)

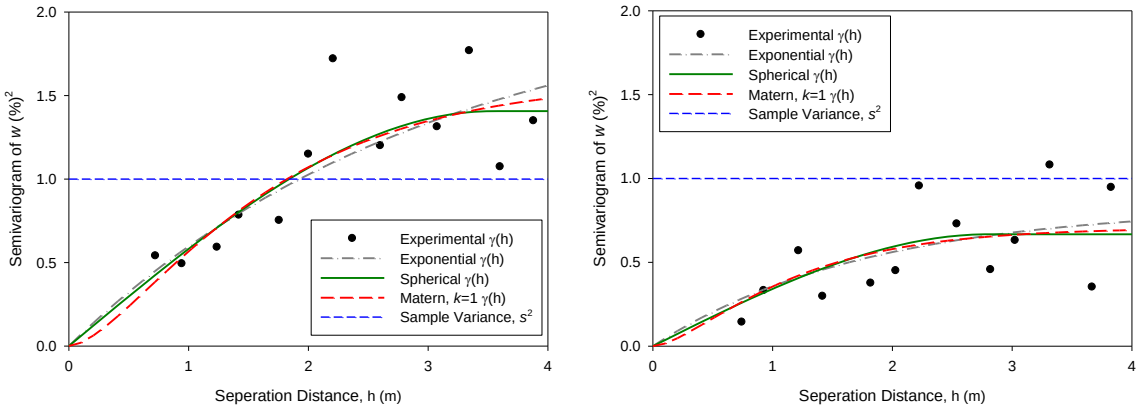

Figure 4.27. Experimental γ(h) of *w* on MI I-96 TS1 in transverse direction (left) and longitudinal direction (right)

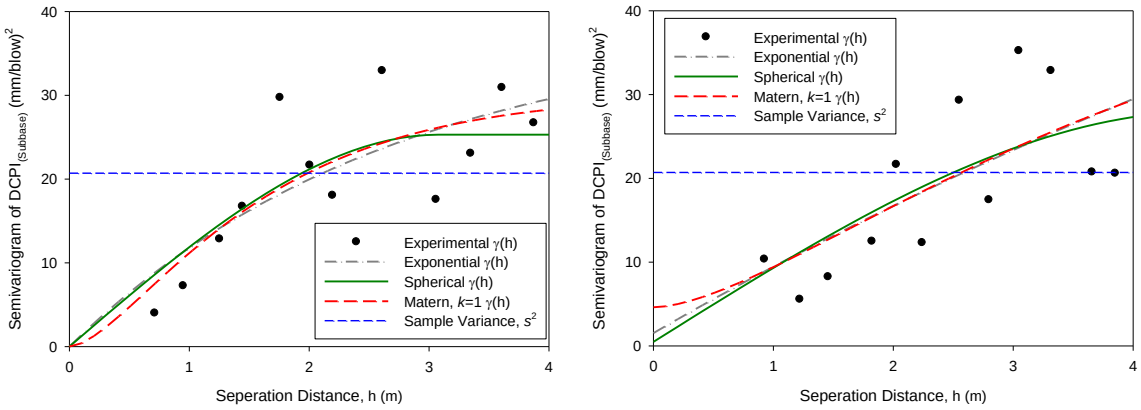

Figure 4.28. Experimental γ(h) of $DCPI_{subbase}$ on MI I-96 TS1 in transverse direction (left) and longitudinal direction (right)

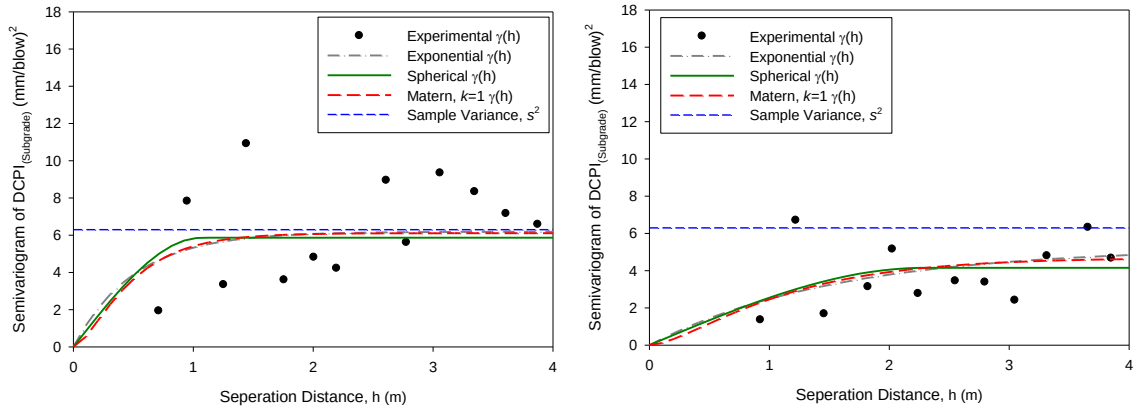

Figure 4.29. Experimental γ(h) of $DCPI_{subgrade}$ on MI I-96 TS1 in transverse direction (left) and longitudinal direction (right)

With 121 of each FWD and NG test performed on cement treated base on MI I-96 TS2, the spatial analysis is performed to characterize and quantify the spatial variability only in the longitudinal direction as only 4 tests were performed along the transverse direction. Although the data spacing is larger than 2 m which may not be able to use for sampling MI I94 TS1 above to study spatial variability, the higher correlation of $E_{LWD\text{-}Z3}$, γ_d, and *w* (Figure 4.30, Figure 4.31, and Figure 4.32) allows spatial variability on this CTB layer. A clear relationship between γ(h) and separation distance helps with fitting the theoretical semivariogram model to quantify the spatial variability of $E_{LWD\text{-}Z3}$, γ_d, and *w* that are summarized in Table 4.8.

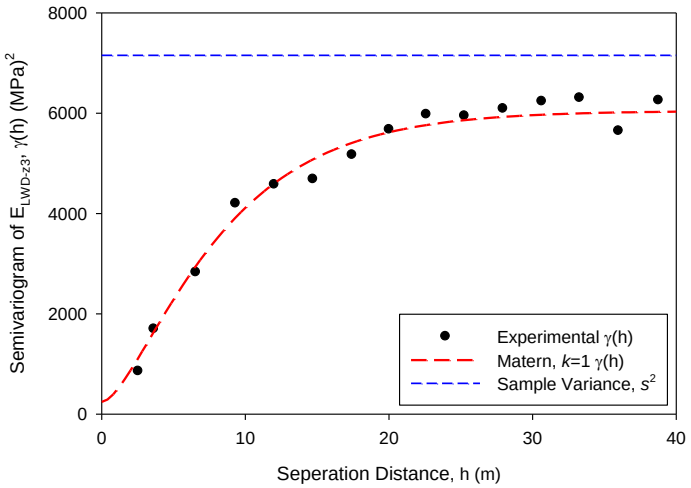

Figure 4.30. Experimental γ(h) of E_{LWD-Z3} on MI I-96 TS2 in longitudinal direction

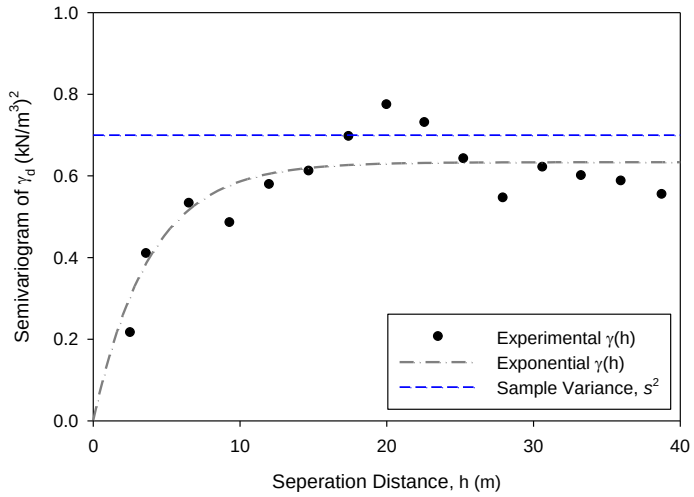

Figure 4.31. Experimental γ(h) of γ_d on MI I-96 TS2 in longitudinal direction

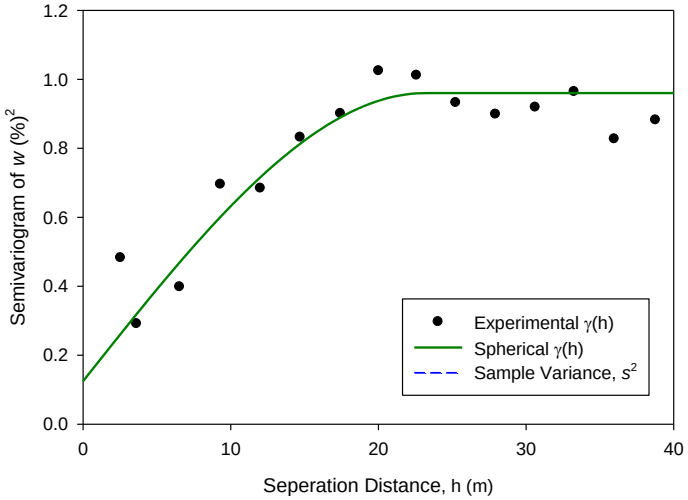

Figure 4.32. Experimental γ(h) of *w* on MI I-96 TS2 in longitudinal direction

Table 4.8. Directional spatial variability characteristics summary on four test sections

Properties	Sampling type	Small Dense		Long Sparse		Small Dense		Long Sparse	
Properties	Direction	MI I-94 TS1b		MI I-94 TS1a		MI I-96 TS1		MI I-96 TB2	
		Sill ($C+C_0$)	Range (a or a'), m	Sill ($C+C_0$)	Range (a or a'), m	Sill ($C+C_0$)	Range (a or a'), m	Sill ($C+C_0$)	Range (a or a'), m
E_{LWD-Z3} (MPa)	Transverse	59.08	11.022			165.301	2.624		
	Longitudinal	63.019	2.993	206.3599	38.288	203.5	8.284		
E_{FWD-K3} (MPa)	Transverse								
	Longitudinal							6046.3	22.452
γ_d (kN/m^3)	Transverse	0.3488	2.328			0.674	7.482		
	Longitudinal	0.6244	9.86	0.3541	33.172	0.1661	2.232	0.633619	15.444
w (%)	Transverse					1.406	3.531		
	Longitudinal			0.157294	27.048	0.8321	5.355	0.9601	23.16
$DCPI_{subbase}$ (mm/blow)	Transverse	1.1952	1.732			30.21	4.288		
	Longitudinal	1.2961	2.1792	288.2	45.4	27.9924	4.603		
$DCPI_{subgrade}$ (mm/blow)	Transverse					5.865	1.068		
	Longitudinal			2.097	31.712	4.152	2.289		

The summarized spatial variability characteristics (Table 4.8) show that the correlation length of around 2 m to 11 m could be expected in small dense gridded area while the long sparse sampling with about 16 m spacing in longitudinal direction does not tell the true estimation of spatial variability. However, with more data collected with about 5 m spacing in longitudinal direction on CTB layer can clearly tell the correlation length of about 22 m for E_{FWD-K3} and *w* and about 15 m for γ_d. for spatial analysis and is expected to have an erratic experimental semivariogram.

4.5. Conclusions

This study investigates variability of pavement foundation properties that were determined from four major in-situ tests (FWD, LWD, NG, and DCP) over 18 test sections of 6 project sites. Studying the variability of $E_{LWD\text{-}Z3}$, γ_d, and w revealed that 4 passes of compaction could result in a production as good as are compacted with more passes and reduced coefficient of variation could be expected at larger number of passes.

Univariate statistics of in-situ measured data show that the highest variation could be expected in stiffness measurements (e.g.,, $E_{LWD\text{-}Z3}$, $E_{FWD\text{-}K3}$, and CBR), the reason could be that the stiffness is measured for the whole pavement foundation while the other can be measured at certain depth of pavement structure. The COV of $E_{LWD\text{-}Z3}$ varies from 11% to 39% on studied base/subbase layer and 19% to 89% on subgrade layer that COV of 89% in subgrade stiffness could be questioned for testing weak area. In addition, the lowest COV will be expected as 2% to 6% in dry unit weight of base/subbase or subgrade layer while the moisture content shows high variation. A test section might have a weak spot with γ_d varying with COV more than 10%.

Spatial variability analysis on a dense gridded test section suggests that different anisotropic major directions can be expected in different test areas. The dense gridded MI I-94 TS1b shows the transverse direction is more uniform than the longitudinal direction, but the dense gridded MI I-96 TS1 shows the longitudinal direction is more uniform than the transverse direction. The two dense gridded sites suggest that the correlation length is about 2 m to 3 m in the minor direction (less uniform) and the correlation length in the major direction is about 3 to 4 times that of the minor direction. In addition, the longitudinal direction spatial variability of $E_{FWD\text{-}K3}$, γ_d, and w on the CTB layer suggests a 15 m to 23 m correlation length. The spatial variability of pavement foundation properties could be different for different pavement structures and are recommended

with more number of tests (>150 points) with smaller spacing (<0.7 m spacing in 100 m^2 area and <2 m in large study area).

4.6. Acknowledgements

This study was sponsored by the Federal Highway Administration under agreement No. DTFH61-06-H-00011 and the Iowa Department of Transportation under Transportation Pooled Fund Program TPF-5(183).

4.7. Notation

The following symbols are used in this paper:

a	=	Range
a'	=	Effective range where 95% C_s reached
C	=	Sill
C_0	=	Nugget effect
C_s	=	Partial sill that obtained in variogram model
COV	=	Coefficient of variation
D_0	=	measured deflection under the plate (mm)
DCPI	=	Dynamic cone penetration index
E	=	elastic modulus (MPa)
E_{LWD-Z3}	=	Elastic modulus (Zorn LWD test with 300 mm dia. plate)
E_{FWD-K3}	=	Elastic modulus (Kuab FWD test with 300 mm dia. plate)
F	=	Shape factor for LWD
G_s	=	Specific gravity
$\boldsymbol{h}$	=	Vector indicates distance and direction of two points apart
k	=	Smoothness parameter in the Matérn model
k	=	Stiffness estimated from a static plate load test
n	=	Number of points on the experimental variogram
N	=	Number of tests
P	=	Applied load at surface

r	=	Range number obtained in R program
r	=	radius of the plate (mm)
s^2	=	Sample variance
SSErr	=	Sum of squares of error or residuals
w_j	=	Weight in weighted least squares fit
w	=	Moisture content
w_{opt}	=	Optimum moisture content
γ_d	=	Dry unit weight
γ_{dmax}	=	Maximum dry unit weight
γ_{dmin}	=	Minimum dry unit weight
$\gamma(h)$	=	experimental semivariogram at distance h

CHAPTER 5. CONCLUSIONS AND RECOMMENDATIONS

This research is composed of three major topics, assessing laboratory determination of M_r values as design input for pavement design, introducing the detailed geostatistical method for characterizing and quantifying spatial variability of pavement foundation properties, and documenting the univariate and spatial variability of in-situ measured pavement foundation properties. The results should be of use to people who want to have knowledge on assessing the variability of pavement foundations for improving the construction of pavement foundation support to extend the pavement service life.

Errors related to stress measurements were characterized by identifying the difference between in situ and laboratory stress pulse shape and duration, studying the effects of sampling rates, and P and I signal values. A comparison of randomly selected raw data of a AASHTO T307 test with the required theoretical haversine-shaped stress pulse and in situ stress pulses revealed inadequate modeling of in situ stress pulse shapes and fast stress pulse durations in laboratory tests. The haversine-shaped stress pulse does not model the actual slow stress initialization and dissipation that an in situ stress pulse experienced. A modified Gaussian model with 5 parameters can better model in situ stress pulses. Stress pulse duration of 0.1 s is too fast compared to the observed in situ stress pulse duration of 0.14 s at 304.8 mm beneath the pavement surface and base layer when the test vehicle was driving at 96.6 km/h. In addition, a 0.1 s stress pulse duration might be obtained at the same position when the test vehicle is driving at 128 km/h. Although M_r values varied with different stress pulse durations, three laboratory tests are not sufficient to conclude effects of stress pulse duration on M_r values. Therefore, the effects of the inadequate modeling of M_r values needs to be studied further to determine if a revision is needed for the laboratory tests. Further, the specified 200 Hz sampling rate for

laboratory tests is insufficient to fully characterize the true shape of stress pulses, especially the applied peak stresses. After tests with different sampling rates, rates of 500 Hz or greater can capture applied peak stresses better than the 200 Hz rate and result in less variation in M_r values. However, the different M_r test appliance may perform better or worse with the same sampling rate. Different sampling rates during the loading and rest period might be used with capable software to save computer storage and time for processing data. Initial adjustments of P and I signal values and automatic adaptation with time within the PC sequence is good when applying the target load in the PC sequence but not for achieving target loads for subsequent sequences where different stress levels are required. Therefore, careful adjustments of P and I signal values in each load sequence might be suggested when M_r test equipment with a PID controller is used.

The differences between deformation measurements of two LVDTs were studied. In some cases, large differences were observed perhaps because top surfaces of the test specimens were not perfectly flat and the unit weights of the specimens were not uniform. In some cases, large differences in two LVDTs measurements were not observed in the PC sequence but in other load sequences. The larger the difference in two LVDTs measurements, the lower the accuracy in M_r values. Therefore, quality control and quality assurance (QC/QA) are needed to determine the reliability of the M_r tests results. SNR values of loads, the AASHTO T307 required displacement ratio R_v in the PC sequence, a proposed resilient strain ratio $R_{\varepsilon r}$ of LVDT1 to LVDT2, and c_v of the last five M_r values in each load sequence were studied for QC/QA. Most of the SNR values met the requirement except for the first load sequence. The first load sequence has most SNR values less than 10, the minimum criteria. A possible reason for this is particle rearrangement in the specimen. Values of R_v in the PC sequence are not representative of R_v values for all load sequences, so R_v values should be checked for all load sequences. The highest $R_{\varepsilon r}$ values were

obtained in the first load sequence not the PC sequence this suggests a possible particle rearrangement might have occurred in that load sequence. Therefore, $R_{\varepsilon r}$ should be studied to check the uniformity of the specimen response. However, two LVDTs may not be sufficient for checking the uniformity of the specimen response and more LVDTs are suggested. In addition, c_v was calculated for the last five load cycles of selected M_r tests and all the values met the requirement. However, this only shows that variations within the last five load cycles were acceptable and that the average of the last five M_r values is used to represent the M_r at the given stress for the tested material.

However, M_r values varied in different ways than the average of the last five M_r values, they could be higher than the maximum or lower than the minimum M_r values. This suggests steady M_r values were not obtained at the end of the 100 load cycles. According to the statistical analysis on all 36 M_r tests on three granular materials, variations among the average of the last five M_r values, the average of the maximum and adjacent four M_r values, and the average of the minimum and adjacent four M_r values are statistically different. In addition, crushed limestone specimens had higher average M_r than RAP and RPCC/RAP specimens, and material type is a statistically significant factor affecting M_r values. Although increasing use of recycled materials can help environmental sustainability and reduce costs, careful investigation of the properties of the recycled materials should be conducted. Moreover, regression coefficient k_3 is not necessary for granular materials because the effects of shear stress that k_3 interprets in the universal model can be negative or positive.

Spatial variability analysis on dense gridded test section suggests that different anisotropic major directions could be expected in different test areas. The dense gridded MI I-94 TS1b shows the transverse direction is more uniform than the longitudinal direction, but the dense

gridded MI I-96 TS1 shows the longitudinal direction is more uniform than the transverse direction. The two dense gridded sites suggest that the correlation length is about 2 m to 3 m in the minor direction (less uniform) and the correlation length in the major direction is about 3 to 4 times as the minor direction. In addition, the longitudinal direction spatial variability of $E_{FWD\text{-}K3}$, γ_d, and w on CTB layer suggests a 15 m to 23 m correlation length.

Preliminary study on anisotropy of spatial variability of pavement foundation properties is allowed with the dense gridded measurements, but different anisotropic behavior was identified in two test sections that may only represent the local sample area. More data in the longitudinal direction should be provided for further anisotropy analysis.

Experimental semivariogram of layer averaged DCPI values are nearly isotropic with possible anisotropic behavior in horizontal directions (parallel to pavement surface) with study on both subbase and subgrade layers. Zonal anisotropy with major anisotropic axis along the longitudinal direction which means greater continuity in the longitudinal direction are presented in experimental semivariograms of $E_{LWD\text{-}Z3}$, moisture content (w), and dry unit weight (γ_d) measured in dense gridded test locations in project MI I-96. Therefore, the univariate statistical analysis should be analyzed to assist in correctly describing spatial variability of pavement foundation properties and identifying possible trends.

Comparison of three theoretical semivariogram models reveals that no obviously best fitted model of the three models (i.e., spherical, exponential, Whittle or Matern with k=1) are found to describe the experimental semivariogram of dense gridded measurements of pavement foundation properties as the spatial variation at distances smaller than the smallest sampling distance were not determined. A nested model with an anisotropy ratio helps in estimating the values at unsampled locations with consideration of the correlation of data sampled at different

locations. However, in most cases for this study on a small test area, the isotropic or omnidirectional semivariogram model can work as well as an anisotropic semivariogram model. Correctly calculated the experimental semivariogram is more important than fitting different models. For example, the MSPE from cross-validation on $E_{LWD\text{-}Z3}$ in MI I-96 TS1 decreased from 46.28 with an angle tolerance of 45° to 33.3 with 25° angle tolerance.

Studying the variability of $E_{LWD\text{-}Z3}$, r_d, and w revealed that 4 passes of compaction could result in a production as good as are compacted with more passes and a reduced coefficient of variation could be expected at larger number of passes.

Univariate statistics of in-situ measured data shows that the highest variation could be expected in stiffness measurements (e.g.,, $E_{LWD\text{-}Z3}$, $E_{FWD\text{-}K3}$, and CBR), the reason could be that the stiffness is measured for the whole pavement foundation while the other can be measured at certain depth of pavement structure. The COV of $E_{LWD\text{-}Z3}$ varies from 11% to 39% on studied base/subbase layer and 19% to 89% on subgrade layer that COV of 89% in subgrade stiffness could be questioned for testing weak area. In addition, the lowest COV will be expected as 2% to 6% in dry unit weight of base/subbase or subgrade layer while the moisture content shows high variation. A test section might have a weak spot varying with γ_d varied with COV more than 10%.

5.1. Recommendations

There are several ideas for future research related to studying variability of pavement foundation properties.

- The laboratory determined M_r values are always higher than the in-situ measured stiffness, the correlation between laboratory tests and in-situ measurement could be

constructed by testing the composite specimens with variation of combination of soil index properties to simulate the variation of in-situ dry unit weight and moisture content.

- Further study on spatial variability of pavement foundation properties is suggested with measurements at test locations with different spacing and across the pavement width. A smaller spacing which is less than 0.5 m is suggested for research studying for identifying the initial spatial correlation characteristics.
- The spatial variability of pavement foundation properties could be different for different pavement structures and are recommended with a greater number of tests (>150 points) with smaller spacing (<0.7 m spacing in 100 m^2 area and <2 m in large study area).

BIBLIOGRAPHY

AASHTO (2007). "Standard Method of Test for Determining the Resilient Modulus of Soils and Aggregate Materials." *T307-99*, AASHTO.

AASHTO (2015). "AASHTOWare-Pavement." *AASHTOWare*, http://www.aashtoware.org/Pavement/Pages/default.aspx. (July 11, 2015).

Allen, D. L., and Graves, R. C. (1994). "Variability in measurement of in-situ material properties." *Proc., 4th International Conference, Bearing Capacity of Roads and Airfields*, 989-1005.

Allen, J. J., and Thompson, M. R. (1974). "Resilient Response of Granular Materials Subjected to Time-Dependent Lateral Stresses." *Transportation Research Record*, 510, 1-13.

ASTM (2003). "Standard Test Method for Use of the Dynamic Cone Penetrometer in Shallow Pavement Applications." *D6951 - 03*, ASTM International, West Conshohocken, PA.

ASTM (2007). "ASTM D422 - 63(2007)e1 Standard Test Method for Particle Size Analysis of Soils." American Standards for Testing Methods.

ASTM (2009). "Standard Test Method for Deflections with a Falling-Weight-Type Impulse Load Device." *D4694 - 09*, ASTM International, West Conshohocken, PA.

ASTM (2010). "ASTM D2216 - 10 Standard Test Methods for Laboratory Determination of Water (Moisture) Content of Soil and Rock by Mass." American Standards for Testing Methods.

ASTM (2010). "Standard Test Method for In-Place Density and Water Content of Soil and Soil-Aggregate by Nuclear Methods (Shallow Depth)." *D6938-10*, ASTM International, West Conshohocken, PA.

Bachmaier, M., and Backes, M. (2011). "Variogram or Semivariogram? Variance or Semivariance? Allan Variance or Introducing a New Term?" *Mathematical Geosciences*, 43(6), 735-740.

Barksdale, R. D. (1971). "Compressive Stress Pulse Times in Flexible Pavements for Use in Dynamic Testing." *Highway Research Record*, 345, 32-44.

Barnes, R. J. (1991). "The variogram sill and the sample variance." *Mathematical Geology*, 23(4), 673-678.

Bivand, R. S., Pebesma, E., and Gómez-Rubio, V. (2013). *Applied Spatial Data Analysis with R*, Springer New York.

Boyce, J. R., Brown, S. F., and Pell, P. S. (1976). "The Resilient Behaviour of a Granular Material under Repeated Loading." *Proc., 8th Australian Road Research Board Conference*, 1-12.

Bozyurt, O., Tinjum, J., Son, Y., Edil, T., and Benson, C. (2012). "Resilient Modulus of Recycled Asphalt Pavement and Recycled Concrete Aggregate." *Proc., GeoCongress 2012*, American Society of Civil Engineers, 3901-3910.

Brown, S. F. (1973). "Determination of Young's Modulus for Bituminous Materials in Pavement Design." *Highway Research Record*, 431, 38-49.

Camargo, F., Benson, C., and Edil, T. (2012). "An Assessment of Resilient Modulus Testing: Internal and External Deflection Measurements." *Geotechnical Testing Journal*, 35(6), 1-8.

Clark, I., and Harper, W. V. (2002). *Practical Geostatistics 2000*, Ecosse North America Llc, Columbus, Ohio.

Cressie, N. (1985). "Fitting variogram models by weighted least squares." *Journal of the International Association for Mathematical Geology*, 17(5), 563-586.
Cressie, N. A. C. (1993). *Statistics for spatial data / Noel A.C. Cressie*, New York : J. Wiley, New York.
Deutsch, C. V., and Journel, A. G. (1998). *GSLIB: Geostatistical Software Library and User's Guide*, Oxford University Press.
Dilip, D. M., and Babu, G. L. S. (2014). "Influence of Spatial Variability on Pavement Responses Using Latin Hypercube Sampling on Two-Dimensional Random Fields." *Journal of Materials in Civil Engineering*, 26(11).
Elliott, R. P., and Thornton, S. I. (1988). "Simplification of subgrade resilient modulus testing." *Transportation Research Record*, 1192, 1-7.
Eriksson, M., and Siska, P. P. (2000). "Understanding Anisotropy Computations." *Mathematical Geology*, 32(6), 683-700.
Facas, N. W., Mooney, M. A., and Furrer, R. (2010). "Anisotropy in the Spatial Distribution of Roller-Measured Soil Stiffness." *International Journal of Geomechanics*, 10(4), 129-135.
Goovaerts, P. (1997). *Geostatistics for Natural Resources Evaluation*, Oxford University Press.
Gringarten, E., and Deutsch, C. V. (2001). "Teacher's Aide Variogram Interpretation and Modeling." *Mathematical Geology*, 33(4), 507-534.
Groeger, J. L., Rada, G. R., and Lopez, A. (2003). "AASHTO T307-Background and Discussion." *Resilient Modulus Testing for Pavement Components*, G. N. Durham, W. A. Marr, and W. L. DeGroff, eds., ASTM International, West Conshohocken, PA, 16-29.
Hallenbeck, M. E., Selezneva, O. I., and Quinley, R. (2014). "Verification, Refinement, and Applicability of Long-Term Pavement Performance Vehicle Classification Rules." Office of Infrastructure Research & Development, Federal Highway Administration, 1200 New Jersey Avenue, SE, Washington, D.C.
Hicks, R. G., and Monismith, C. L. (1971). "Factors Influencing the Resilient Response of Granular Materials." *Highway Research Record*, 345, 15-31.
Hughes, C. S. (1996). *Variability in highway pavement construction*, National Academy Press, Washington, D.C.
Irwin, L. H. (2009). "The Resilient Modulus Test." http://www.resilientmodulus.com/index.php?q=system/files/Lynne_Irwin.pdf.
Isaaks, E. H., and Srivastava, R. M. (1989). "An Introduction to Applied Geostatistics." Oxford University Press.
Jian, X., Olea, R. A., and Yu, Y.-S. (1996). "Semivariogram modeling by weighted least squares." *Computers & Geosciences*, 22(4), 387-397.
Journel, A. G., and Huijbregts, C. J. (1978). *Mining geostatistics*, Academic Press.
Kim, W., Labuz, J., and Dai, S. (2007). "Resilient Modulus of Base Course Containing Recycled Asphalt Pavement." *Transportation Research Record: Journal of the Transportation Research Board*, 2005, 27-35.
Kim, W., and Labuz, J. F. (2007). "Resilient modulus and strength of base course with recycled bituminous material." Minnesota Department of Transportation.
Lea, J. D., and Harvey, J. T. (2015a). "A spatial analysis of pavement variability." *Int. J. Pavement Eng.*, 16(3), 256-267.
Lea, J. D., and Harvey, J. T. (2015b). "Using spatial statistics to characterise pavement properties." *Int. J. Pavement Eng.*, 16(3), 239-255.

Marr, W. A., Hankour, R., and Werden, S. K. (2003). "A Fully Automated Computer Controlled Resilient Modulus Testing System." *The Symposium on Resilient Modulus Testing for Pavement Components*, G. N. Durham, W. A. Marr, and W. L. DeGroff, eds., ASTM International, West Conshohocken, PA, 141-151.

Moore, W. M., Britton, S. C., and Scrivner, F. H. (1970). "A Laboratory Study of the Relation of Stress to Strain for A Crushed Limestone Base Material." *Research Report 99-5F*, Texas Transportation Institute.

Morgan, J. R. (1966). "The Response of Granular Materials to Repeated Loading." *Proc., 3rd Conf., Australian Road Research Board*, 1179-1192.

NCHRP (2004). "Guide for the Design of New and Rehabilitated Pavement Structures." *NCHRP Report 01-37A*, Transportation Research Board, Washington, D.C.

Olea, R. (2006). "A six-step practical approach to semivariogram modeling." *Stochastic Environmental Research and Risk Assessment*, 20(5), 307-318.

Oliver, M. A., and Webster, R. (2015). *Basic Steps in Geostatistics: The Variogram and Kriging*, Springer International Publishing.

Otake, Y., and Honjo, Y. (2013). "A simplified reliability analysis of spatial variability employing local average of geotechnical parameters." *Proc., 11th International Conference on Structural Safety and Reliability, ICOSSAR 2013*, Taylor & Francis - Balkema, 1995-2002.

Pebesma, E. J. (2001). "Gstat user's manual." *gstat 2.5.1*, Dept. of Physical Geography, Utrecht University, Utrecht, The Netherlands.

Phoon, K.-K., and Kulhawy, F. H. (1999). "Evaluation of geotechnical property variability." *Canadian Geotechnical Journal*, 36(4), 625-639.

Ping, W. V., Xiong, W., and Yang, Z. (2003). "Implementing resilient modulus test for design of pavement structures in Florida." Florida Department of Transportation, Tallahassee, FL.

Roesler, J. R., Chavan, H., King, D., and Brand, A. S. (2016). "Concrete slab analyses with field-assigned non-uniform support conditions." *International Journal of Pavement Engineering*, 17(7), 578-589.

Seed, H. B., Mitry, F. G., Monismith, C. L., and Chan, C. K. (1967). "Prediction of flexible pavement deflections from laboratory repeated-load tests." *NCHRP Report No. 35*, National Cooperative Highway Research Program.

Siddharthan, R., Sebaaly, P. E., and Javaregowda, M. (1992). "Influence of statistical variation in falling weight deflectometers on pavement analysis." *Transportation research record*.(1377).

Titi, H., Faheem, A., Tabatabai, H., and Tutumluer, E. (2014). "Influence of Aggregate Base Layer Variability on Pavement Performance." *Transp. Res. Record*, 3(2457), 58-71.

Vennapusa, P. K. R. (2004). "Determination of the optimum base characteristics for pavements." Iowa State University.

Vennapusa, P. K. R., and White, D. J. (2009). "Comparison of Light Weight Deflectometer Measurements for Pavement Foundation Materials." *Geotechnical Testing Journal*, 32(3), 239-251.

Vennapusa, P. K. R., White, D. J., and Morris, M. D. (2010). "Geostatistical Analysis for Spatially Referenced Roller-Integrated Compaction Measurements." *http://dx.doi.org/10.1061/(ASCE)GT.1943-5606.0000285*.

Wackernagel, H. (2003). *Multivariate geostatistics : an introduction with applications / Hans Wackernagel*, Springer-Verlag Berlin Heidelberg, Berlin ; New York.

Webster, R., and Oliver, M. A. (2007). *Geostatistics for environmental scientists*, Wiley, Chichester; Hoboken, NJ.

White, D. J., Rupnow, T. D., and Ceylan, H. (2004). "Influence of Subgrade/Subbase Non-Uniformity on PCC Pavement Performance." *Proc., GeoTrans 2004*, American Society of Civil Engineers.

White, D. J., Vennapusa, P. K. R., Becker, P., and White, C. (2013). "Subgrade Stabilization Using Geosynthetics."

Witczak, M. W. (2004). "Laboratory Determination of Resilient Modulus for Flexible Pavement Design." *Research Results Digest 285*, National Cooperative Highway Research Program.

Yoder, E. J. (1975). *Principles of pavement design / E. J. Yoder, M. W. Witczak*, New York : Wiley, New York.

Zorn G. (2003). *Operating manual: Light drop-weight tester ZFG2000*, Zorn Stendal, Germany.

APPENDIX A. R PROGRAM CODE FOR SPATIAL SEMIVARIOGRAM ANALYSIS

```
# Data format: Excel.csv   id-x-y-variables (no blank cells allowed)
#              x=longitudinal direction and y= transverse direction
#              Units of coordinates is "m", modulus is "MPa", and DCPI is
"mm/blow"
# analyze each variable separately (be aware of state and test bed that
data was collected in data analysis report)
# data is the general name for the studied data file
data<- read.csv(file.choose(), as.is=T)

# Print variable name to make sure that the name of the analyzed variable
is right in coding.
head(data)
data[1,]

# Plot test locations
plot(data$x, data$y,xlab='longitudinal direction (m)',ylab='transverse
direction (m)')
# Specify axis options within plot()
# plot(x, y, main="title", sub="subtitle",
#     xlab="x-axis label", ylab="y-axis label",
#     xlim=c(xmin, xmax), ylim=c(ymin, ymax))


# Univariate statistics analysis

summary(data)
library(pastecs)
options(scipen=100)
options(digits=4)
stat.desc(data, basic=F)
hist(data$ELWD)
hist(data$rd)
hist(data$w)
hist(data$DCPI_subbase_w.o.1st)
hist(data$DCPI_subgrade)


# Spatial variance analysis
library(sp)
library(gstat)
data.sp<- data
coordinates(data.sp)<- c('x','y')
plot(coordinates(data.sp))


bubble(data.sp,'ELWD', maxsize = 2.5,
scales=list(draw=T),xlab="Longitudinal direction (m)",ylab="Transverse
direction (m)")
bubble(data.sp,'rd', maxsize = 2.5,scales=list(draw=T),xlab="Longitudinal
direction (m)",ylab="Transverse direction (m)")
bubble(data.sp,'w', maxsize = 2.5,scales=list(draw=T),xlab="Longitudinal
direction (m)",ylab="Transverse direction (m)")
```

```
bubble(data.sp,'DCPI_subbase_w.o.1st', maxsize =
2.5,scales=list(draw=T),xlab="Longitudinal direction (m)",ylab="Transverse
direction (m)")
bubble(data.sp,'DCPI_subgrade', maxsize =
2.5,scales=list(draw=T),xlab="Longitudinal direction (m)",ylab="Transverse
direction (m)")


# define the grid number and size for kriging, can define or adjust later
after obtain the semivariogram model
xrange = bbox(data.sp)[1,]
yrange = bbox(data.sp)[2,]
data.grid <- expand.grid(
  x=seq(xrange[1], xrange[2], length=100),
  y=seq(yrange[1], yrange[2], length=100) )
plot(data.grid,main='Specified data grid',xlab='longitudinal direction
(m)',ylab='transverse direction (m)')
coordinates(data.grid) <- c('x','y')   # quick way to convert to sp object
gridded(data.grid) <- T                # and flag as a grid
plot(data.grid, xlab='longitudinal direction(m)',ylab='transverse
direction(m)') #view the defined grid


# variogram estimation
# vgm(), show.vgms( par.strip.text=list(cex=0.7) )
# variogram, define alpha is to define the direction of the variogram,
# tol.hor is the tolerance in xy-plane, the default value is =90
degree/number of the alpha defined in the same variogram.

#-----------------------------------
#-----------------------------------
# omni-directional variogram
data.vc <- variogram(ELWD~1, data.sp, cloud=T)
plot(data.vc, main='ELWD', xlab='Seperation Distance (m)',
ylab='Semivariance (MPa^2)')
# data.vc is the experimental semivariogram cloud, the default maximum
cutoff distance is 1/3 of the maximum distance tha two test location
seperated
data.v <- variogram(ELWD~1, data.sp, cutoff=4)
# calculate experimental semi-variogram, assuming constant mean
plot(data.v,main='ELWD')
# the output object from variogram() has three variables of interest:
#   dist: average distance for that bin
#   gamma: empirical semivariance for that bin
#   np: number of points in that bin

#-----------------------------------
# fit theoretical model to experimental variogram calculated in omni-
direction
omni.vm <- variogram(ELWD~1, data.sp, cutoff=4)
plot(omni.vm,main='ELWD')
data.omni.vm1 <- fit.variogram(omni.vm, vgm(6, 'Sph', 4, 0)) #fit
spherical model
```

```
data.omni.vm2 <- fit.variogram(omni.vm, vgm(6, 'Exp', 2, 0)) #fit
exponential model
data.omni.vm3 <- fit.variogram(omni.vm, vgm(6, 'Mat', 1, 0, k=1)) #fit
matern model with k=1
plot(omni.vm, data.omni.vm1, main="ELWD omni-direction Sph")
data.omni.vm1
attr(data.omni.vm1, 'SSErr') #SSErr is sum of square errors in weighted
least square fitting the semivariogram
plot(omni.vm, data.omni.vm2, main="ELWD omni-direction Exp")
data.omni.vm2
attr(data.omni.vm2, 'SSErr')
plot(omni.vm, data.omni.vm3, main="ELWD omni-direction Mat k=1")
data.omni.vm3
attr(data.omni.vm3, 'SSErr')

with(omni.vm, plot(dist, gamma, xlim=c(0,4), ylim=c(0,200)))  # plot
experimental semivariogram with all three fitted models
lines(variogramLine(data.omni.vm1, maxdist=4), lwd=2)
lines(variogramLine(data.omni.vm2, maxdist=4), col=2, lwd=2)
lines(variogramLine(data.omni.vm3, maxdist=4), col=4, lwd=2)
legend('bottomright', bty='n', lty=1, col=c(1,2,4), lwd=2,
       legend=c('Spherical','Exponential','Matern, k=1') )
#-----
# if the plot need to be plotted in the other programs, the line value can
be extracted as following
omni.vm.fit1= variogramLine(data.omni.vm1, 4, 40)
omni.vm.fit2= variogramLine(data.omni.vm2, 4, 40)
omni.vm.fit3= variogramLine(data.omni.vm3, 4, 40)
library(xlsx)
library(dplyr)
omni.vmfit <- omni.vm.fit1 %>%
  left_join(omni.vm.fit2, by = "dist", suffix = c("Sph", "Exp")) %>%
  left_join(omni.vm.fit3, by = "dist") %>% glimpse
write.xlsx(omni.vmfit, "omni.vm.fit.xlsx", sheetName="Sheet1", col.names =
TRUE, row.names = TRUE, append = FALSE, showNA = TRUE)
#-----
# choose the suitable model as data.ovm (omni-direction vm)
data.ovm= data.omni.vm1
data.ovm


#-----------------------------------
#-----------------------------------
# analysis with anisotropy
# start to look at the directional variogram
# variogram map:
plot(variogram(ELWD~1, data.sp, map=T, cutoff=4, width=1), main='ELWD',
xlab='dx (Longitudinal)', ylab='dy (Transverse)')
# width is the bin size, dx=dy=width

# directional variograms
data.v4 <- variogram(ELWD~1, data.sp,
alpha=c(0,45,90,135),cutoff=4,tol.hor=25, width=0.5) #four major
directions
```

```
plot(data.v4,type='b', main='ELWD')
write.xlsx(data.v4, "directional_expr_vm_new.xlsx", sheetName="Sheet1",
col.names = TRUE, row.names = TRUE, append = FALSE, showNA = TRUE)
# save calculated directional semivariogram into Excel

# direction at alpha=0 along y or transverse direction
data.vT <- variogram(ELWD~1, data.sp, cutoff=4,alpha=c(0),tol.hor=25,
width=0.5)
# alpha=direction in plane (x,y), in positive degrees clockwise from
positive y (North)
plot(data.vT)
data.vmT1 <- fit.variogram(data.vT, vgm(100, 'Sph', 6, 0),
fit.sills=c(FALSE,TRUE))
# if fixed nugget value is desired, add fit.sills=c(FALSE, TRUE) to
fit.variogram
data.vmT2 <- fit.variogram(data.vT, vgm(100, 'Exp', 1.3, 0))
data.vmT3 <- fit.variogram(data.vT, vgm(100, 'Mat', 1, 0, k=1))
data.vmT1
attr(data.vmT1, 'SSErr')
data.vmT2
attr(data.vmT2, 'SSErr')
data.vmT3
attr(data.vmT3, 'SSErr')
with(data.vT, plot(dist, gamma, xlim=c(0,4), ylim=c(0,200),main='ELWD
along Y direction'))
lines(variogramLine(data.vmT1, maxdist=4), col=1, lwd=2)
lines(variogramLine(data.vmT2, maxdist=4), col=2, lwd=2)
lines(variogramLine(data.vmT3, maxdist=4), col=4, lwd=2)
legend('bottomright', bty='n', lty=1, col=c(1,2,4), lwd=2,
       legend=c('Spherical','Exponential','Whittle') )

# direction at alpha=90 along x or longitudinal direction
data.vL <- variogram(ELWD~1, data.sp, cutoff=4,alpha=c(90),tol.hor=25,
width=0.5)
plot(data.vL)
#     if fixed nugget value is desired, add fit.sills=c(FALSE, TRUE) to
fit.variogram
data.vmL1 <- fit.variogram(data.vL, vgm(50, 'Sph', 4,0),fit.sills=c(FALSE,
TRUE))
data.vmL2 <- fit.variogram(data.vL, vgm(50, 'Exp',
1.5,0),fit.sills=c(FALSE, TRUE))
data.vmL3 <- fit.variogram(data.vL, vgm(50, 'Mat', 2,0,
k=1),fit.sills=c(FALSE, TRUE))
data.vmL1
attr(data.vmL1, 'SSErr')
data.vmL2
attr(data.vmL2, 'SSErr')
data.vmL3
attr(data.vmL3, 'SSErr')
plot(data.vL, data.vmL3)
with(data.vL, plot(dist, gamma, xlim=c(0,4), ylim=c(0,20),main='ELWD along
X direction'))
lines(variogramLine(data.vmL1, maxdist=4), col=1, lwd=2)
lines(variogramLine(data.vmL2, maxdist=4), col=2, lwd=2)
```

```
lines(variogramLine(data.vmL3, maxdist=4), col=4, lwd=2)
legend('bottomright', bty='n', lty=1, col=c(1,2,4), lwd=2,
       legend=c('Spherical','Exponential','Whittle') )

# Identify major direction (lowest sill in zonal anisotropy or largest
range in geometric anisotropy),
#     this case is 90 degree (X direction)
# model geometric anisotropy first
v <- variogram(ELWD~1, data.sp, alpha=c(0,45,90,135),cutoff=4, tol.hor=45)
# use the coefficients from the autofitted vargioram values for the major
direction
vm1<- vgm(4.152, 'Sph',2.289,0, anis=c(90,0.8))
# the anisotropy factor =(range at minor direction reach sill,
smaller)/(range at major direction, larger)<1
vm1
plot(v, vm1, main = "geometric")
# if only geometric anisotropy exist, then just model geometric anisotropy
vm.final = vm1

# Then, model zonal anisotropy (difference between major and minor
directions)
zonal= vgm(1.713,'Sph',1e9, anis=c(90,1/9.36e8))
# partial sill=sill in the original minor direction-(nugget and partial
sill from geometric anis model)
# 1e9 is the range, effectively infinity in 90 direction that means model
zonal effect in 0 direction only
#     anisotropy ratio 9.36e8= 1e9/1.068 (3.105 is the range from 0
direction)
vm2<- vgm(4.152, 'Sph',2.289,0, add.to=zonal)
plot(v, vm2, main = "zonal")
vm2
vm.final=vm2
plot(v, vm.final)

# extract points' coordinates on the fitted anisotropic variogram
vfit1= variogramLine(vm.final, 4, 40,dir=c(0,1,0)) #in y-direction (0
degrees)
vfit2= variogramLine(vm.final, 4, 40,dir=c(sqrt(2)/2,sqrt(2)/2,0)) #in y-
direction (45 degrees)
vfit3= variogramLine(vm.final, 4, 40,dir=c(1,0,0)) #in x-direction (90
degrees)
vfit4= variogramLine(vm.final, 4, 40,dir=c(-sqrt(2)/2,sqrt(2)/2,0)) #in y-
direction (135 degrees)
library(dplyr)
vfit <- vfit1 %>%
  left_join(vfit2, by = "dist", suffix = c("0", "45")) %>%
  left_join(vfit3, by = "dist") %>%
  left_join(vfit4, by = "dist", suffix = c("90", "135")) %>% glimpse
write.xlsx(vfit, "fit.xlsx", sheetName="Sheet1", col.names = TRUE,
row.names = TRUE, append = FALSE, showNA = TRUE)
getwd()


#-----------------------------------
```

```
#-------------------------------------
# kriging

# need four things:
#     model for trend (could be just a mean)
#     data (sp PointsDataFrame object),
#     locations to predict at (sp Points or Pixels (for grid) object)
#     the semivariogram model (est. from empirical SV or specified)

# Keep originally setted data.grid or reset the suitable grid size and
estimation area
ts1b.grid <- expand.grid(x=seq(0,8.5,0.1), y=seq(0,8.5,0.1))
coordinates(ts1b.grid) <- c('x','y')
gridded(ts1b.grid) <- T

#--Omni-directional, without consideration in anisotropy
data.ovm=data.omni.vm3 #the one you chose from the three fitted models
data.ovm #double check if the correct one is chosen
data.k.omni <- krige(ELWD ~ 1, data.sp, ts1b.grid, data.ovm)
image(data.k.omni) #visualize the krigged plot
plot(data.k.omni, main="semivariogram_omni_Mat", xlab="distance",
ylab="semivaiance",axes=TRUE) #visualize the krigged plot in another way


#--Consider anisotropy, now, use vm.final
vm.final
data.k.final <- krige(ELWD ~ 1, data.sp, ts1b.grid, vm.final)
image(data.k.final)
plot(data.k.final, main="ELWD semivariogram_Anisotropy", axes=T,
xlim=c(0,8.5),ylim=c(0,8.5))

#-------------------------------------
#-------------------------------------
# cross validation

#--Omni-directional,
data.cv.omni <- krige.cv(ELWD ~ 1, data.sp, data.ovm)
names(data.cv.omni)
bubble(data.cv.omni, 'residual')
mean(data.cv.omni$residual) # average prediction error
mean(data.cv.omni$residual^2) # mean squared prediction error
plot(data.cv.omni$var1.pred,data.cv.omni$residual)
plot(data.cv.omni$var1.pred,data.cv.omni$observed)

#--Consider anisotropy,
data.cv.final <- krige.cv(ELWD ~ 1, data.sp, vm.final)
names(data.cv.final)
bubble(data.cv.final, 'residual')
mean(data.cv.final$residual) # average prediction error
mean(data.cv.final$residual^2) # mean squared prediction error
plot(data.cv.final$var1.pred,data.cv.final$residual)

#-------------------------------------
#--Save kriged map values into excel file
```

```
library(xlsx)
write.xlsx(data.k.omni, "yourfilenamepath_new_omni.xlsx",
sheetName="Sheet1", col.names = TRUE, row.names = TRUE, append = FALSE,
showNA = TRUE)
write.xlsx(data.k.final, "yourfilenamepath_new_anis.xlsx",
sheetName="Sheet1", col.names = TRUE, row.names = TRUE, append = FALSE,
showNA = TRUE)
# the file will be automatically saved into the working directory
# find the working directory to find the file
getwd()
# or we can set the working directory to the target folder that we want to
saved our files in.
setwd("..")
```

APPENDIX B. STATISTICAL ANALYSIS PLOTS FOR CHAPTER 2

B.1. MI I-94 TS1a

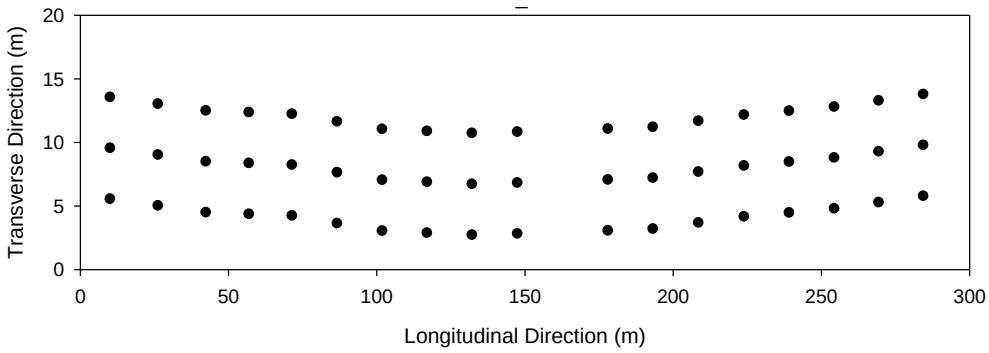

Figure B.1. Test plan for MI I-94 TS1a

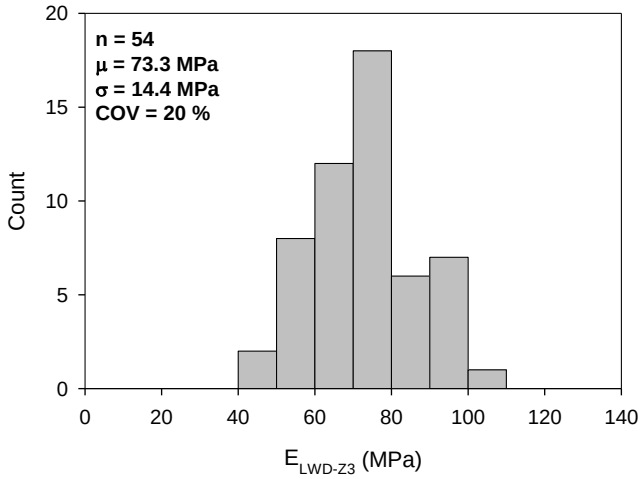

Figure B.2. Histogram of E_{LWD-Z3} for MI I-94 TS1a

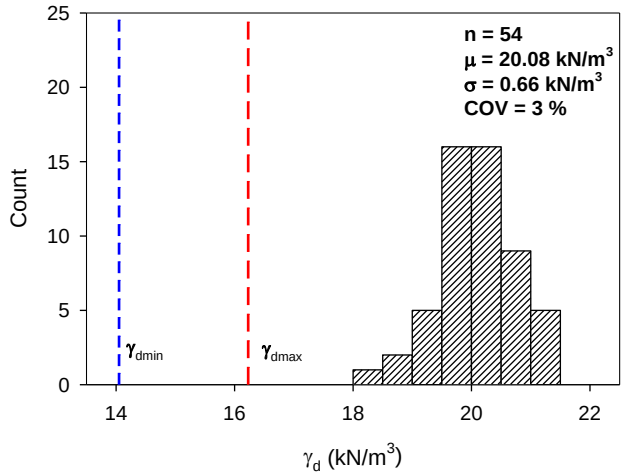

Figure B.3. Histogram of γ_d for MI I-94 TS1a

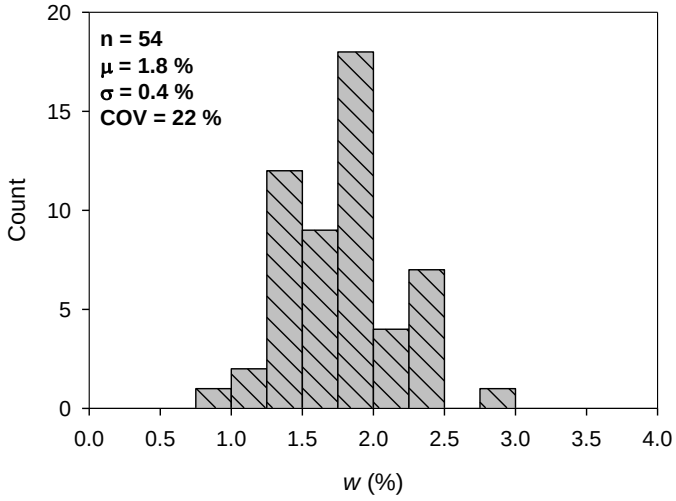

Figure B.4. Histogram of *w* for MI I-94 TS1a

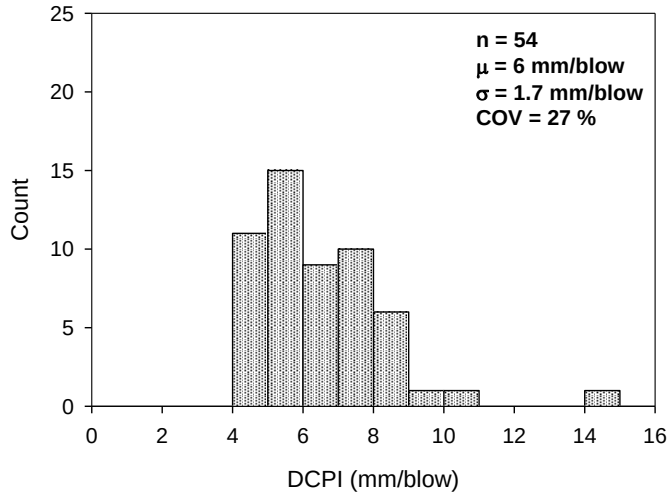

Figure B.5. Histogram of $DCPI_{subbase}$ for MI I-94 TS1a

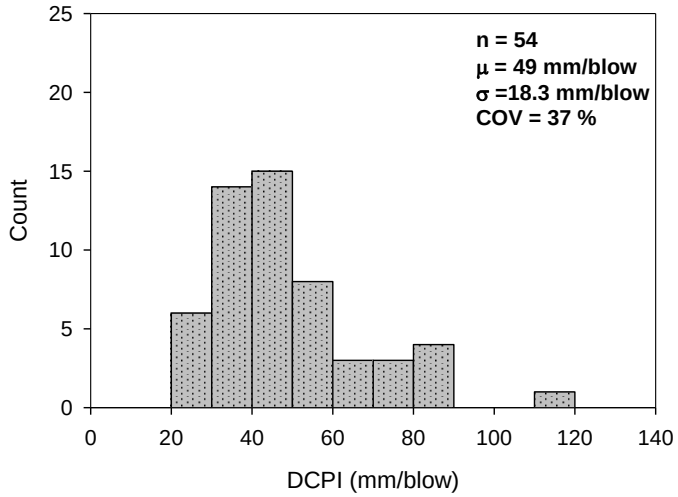

Figure B.6. Histogram of $DCPI_{subgrade}$ for MI I-94 TS1a

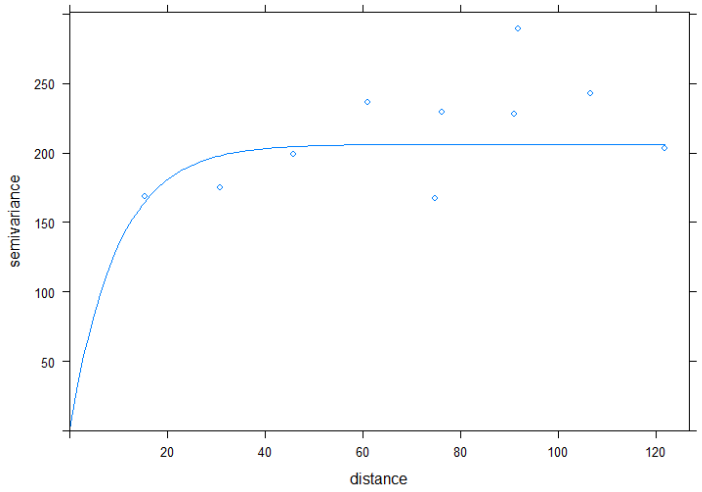

Figure B.7. Omnidirectional semivariogram of $E_{LWD\text{-}Z3}$ for MI I-94 TS1a

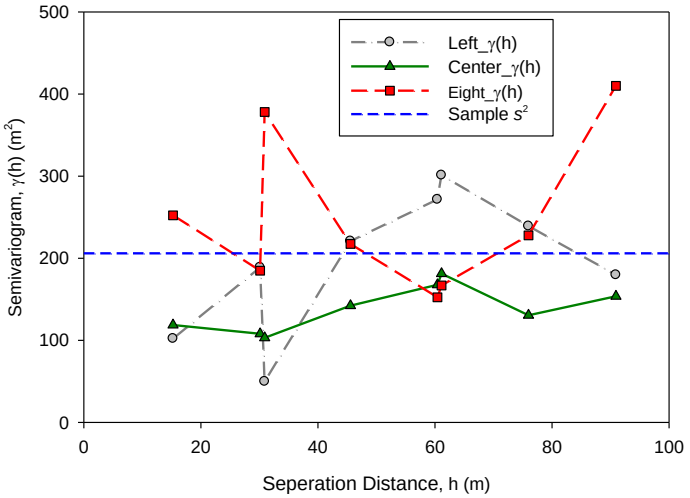

Figure B.8. Omnidirectional semivariogram of $E_{LWD\text{-}Z3}$ in three lanes for MI I-94 TS1a

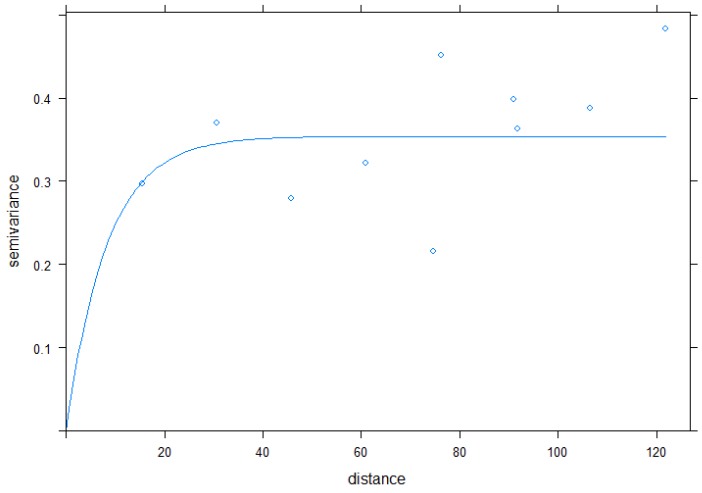

Figure B.9. Omnidirectional semivariogram of γ_d for MI I-94 TS1a

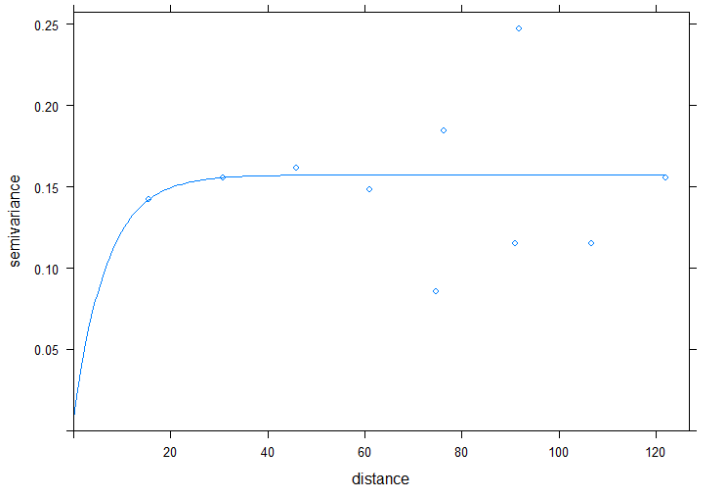

Figure B.10. Omnidirectional semivariogram of *w* for MI I-94 TS1a

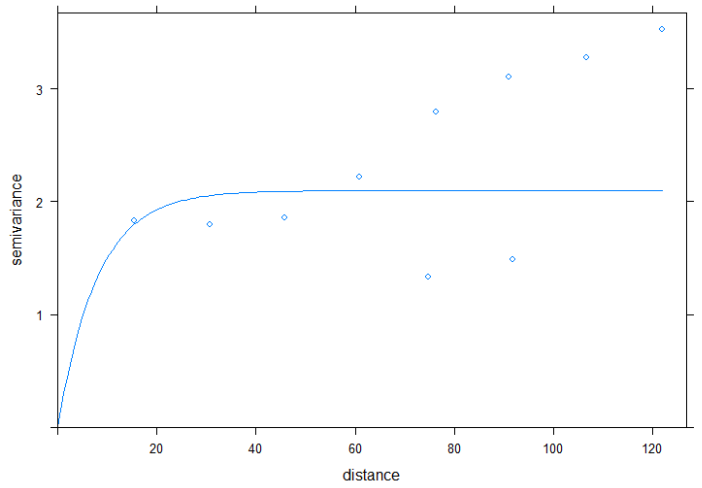

Figure B.11. Omnidirectional semivariogram of $DCPI_{subbase}$ for MI I-94 TS1a

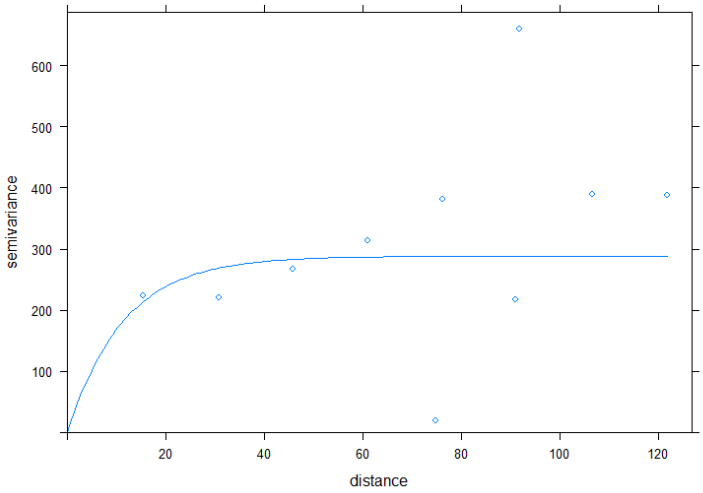

Figure B.12. Omnidirectional semivariogram of $DCPI_{subgrade}$ for MI I-94 TS1a

B.2. MI I-94 TS1b

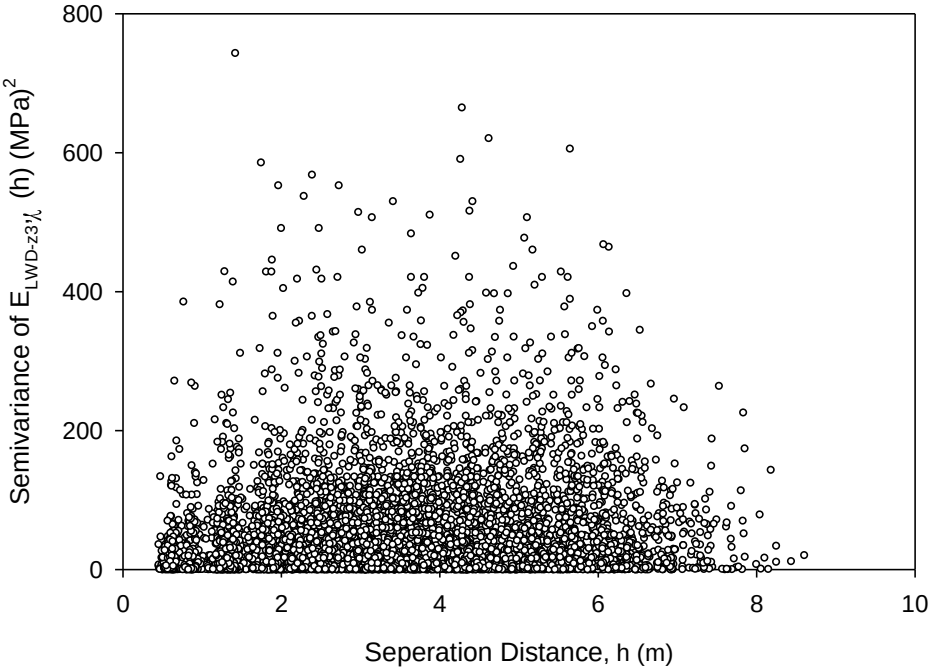

Figure B.13. Semivariogram cloud for $E_{LWD\text{-}Z3}$ in full test section length in MI I-94 TS1b

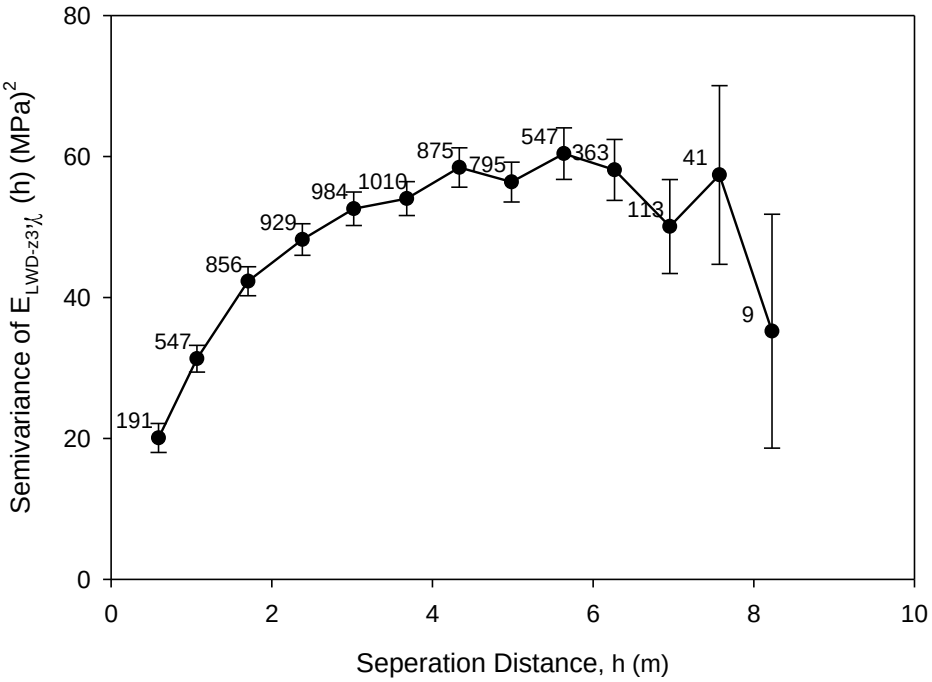

Figure B.14. Average semivariogram in each bin with number of data pairs for $E_{LWD\text{-}Z3}$ in full test section length in MI I-94 TS1b

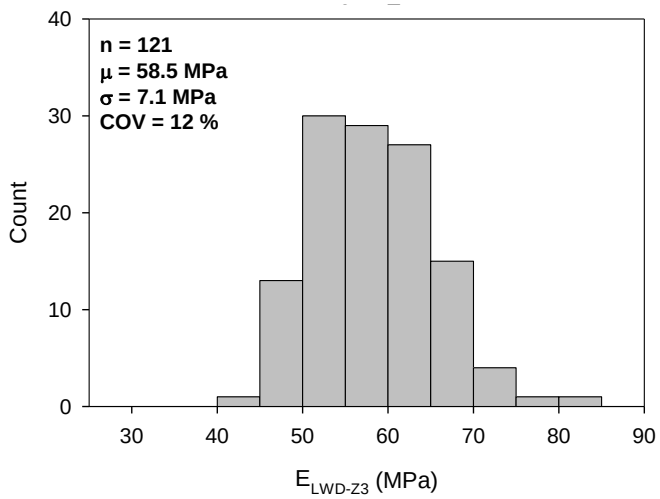

Figure B.15. Histogram of E_{LWD-Z3} for MI I-94 TS1b

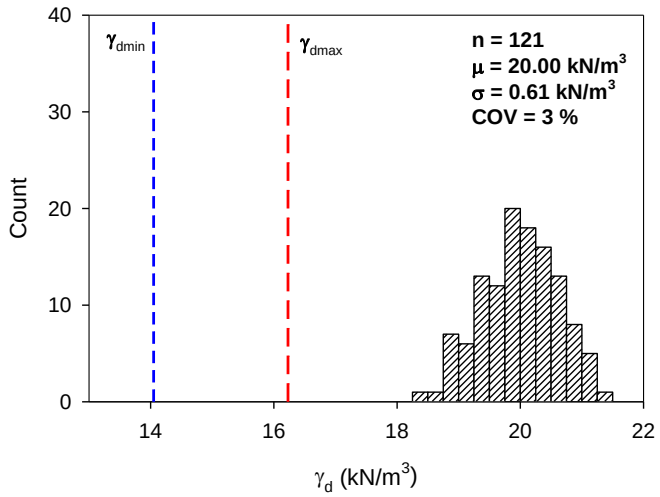

Figure B.16. Histogram of γ_d for MI I-94 TS1b

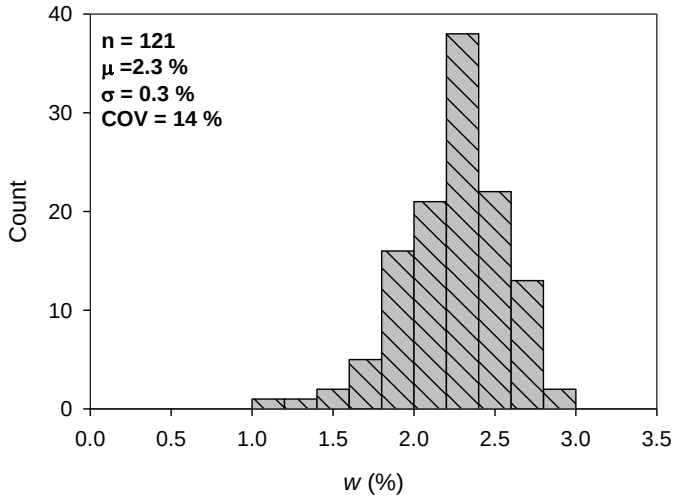

Figure B.17. Histogram of *w* for MI I-94 TS1b

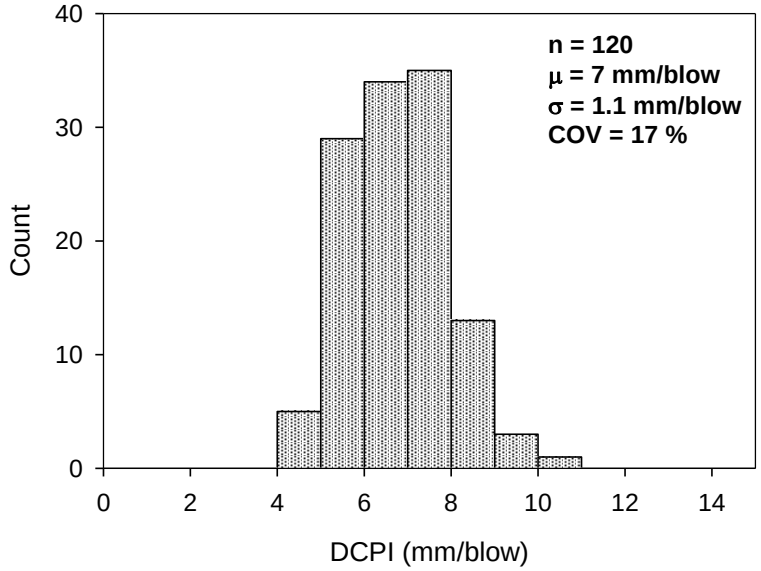

Figure B.18. Histogram of $DCPI_{subbase}$ (removed one outlier) for MI I-94 TS1b

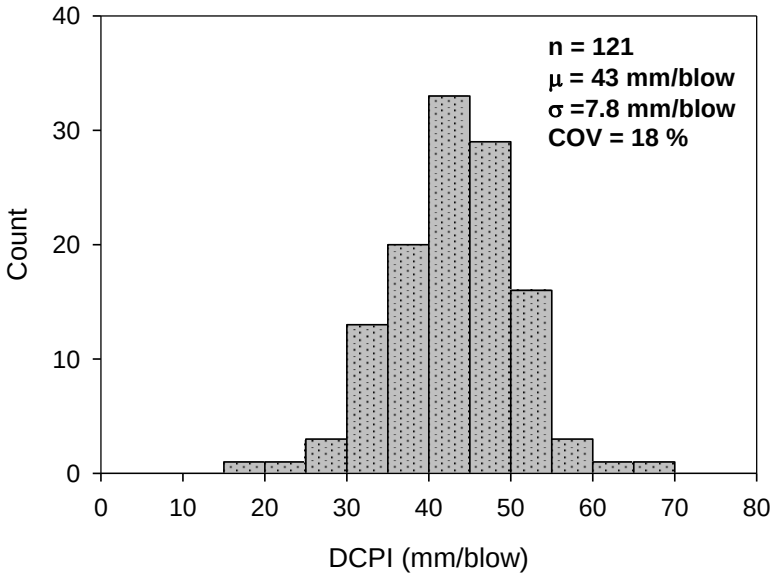

Figure B.19. Histogram of $DCPI_{subgrade}$ for MI I-94 TS1b

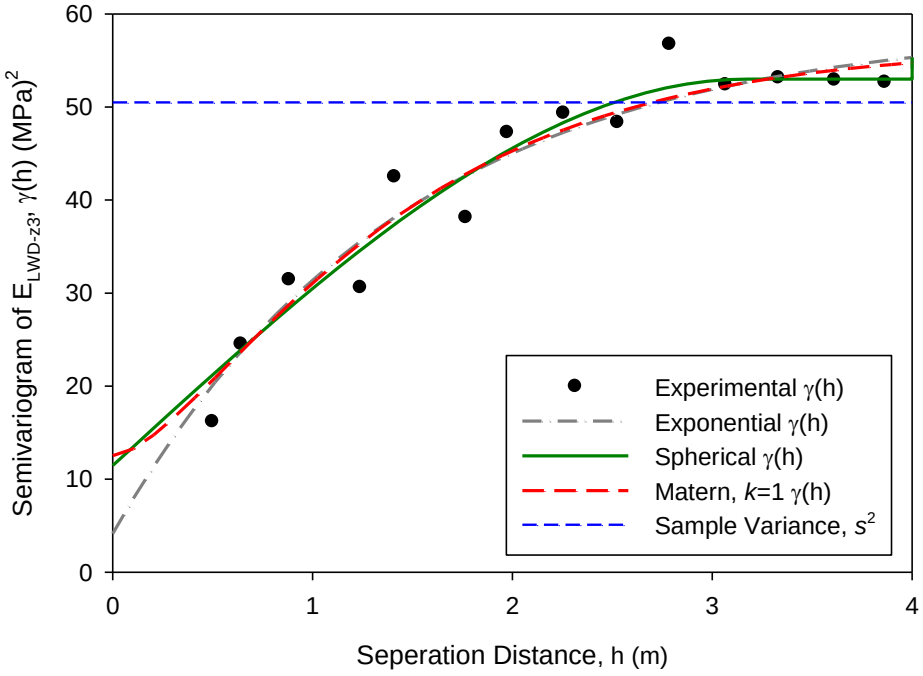

Figure B.20. Omnidirectional semivariogram of E_{LWD-Z3} for MI I-94 TS1b

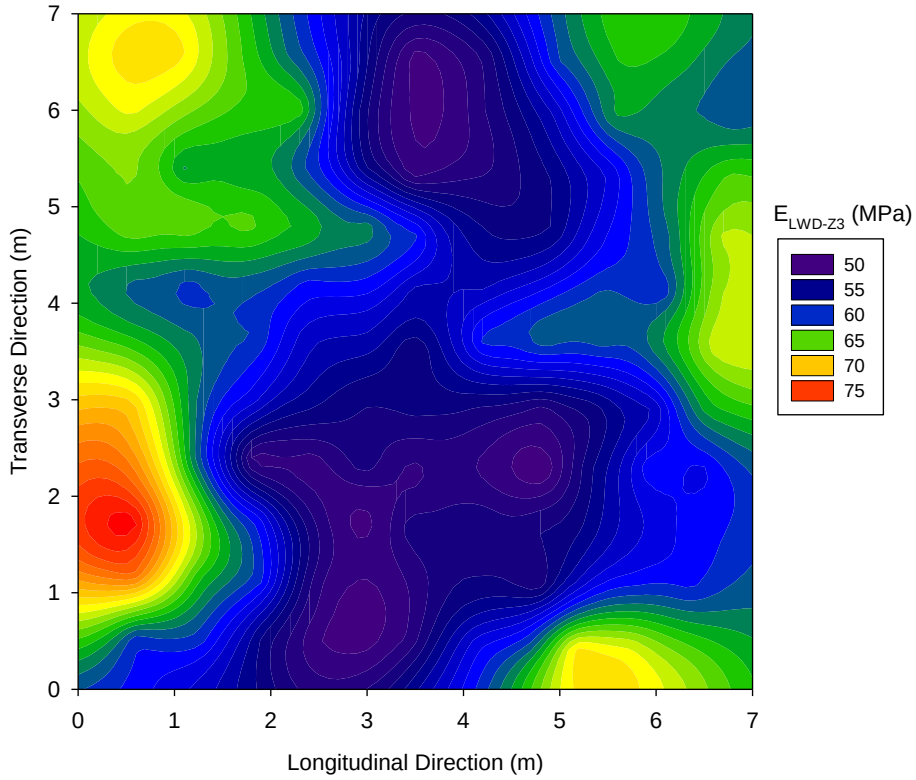

Figure B.21. Kriging contour map with spherical model of E_{LWD-Z3} for MI I-94 TS1b

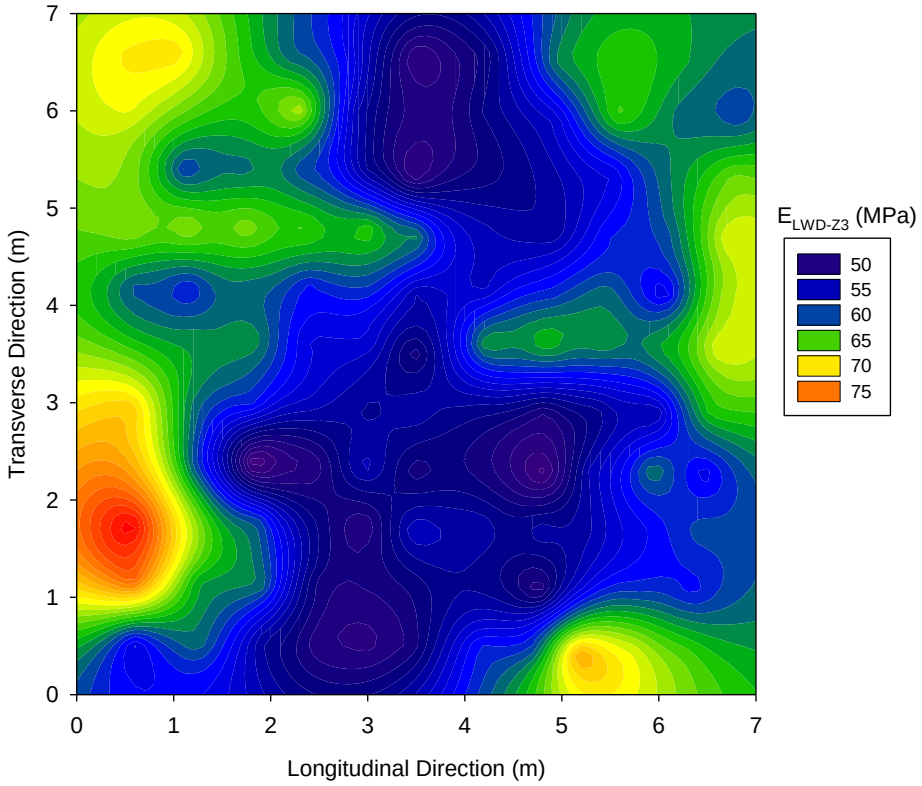

Figure B.22. Kriging contour map with exponential model of E_{LWD-Z3} for MI I-94 TS1b

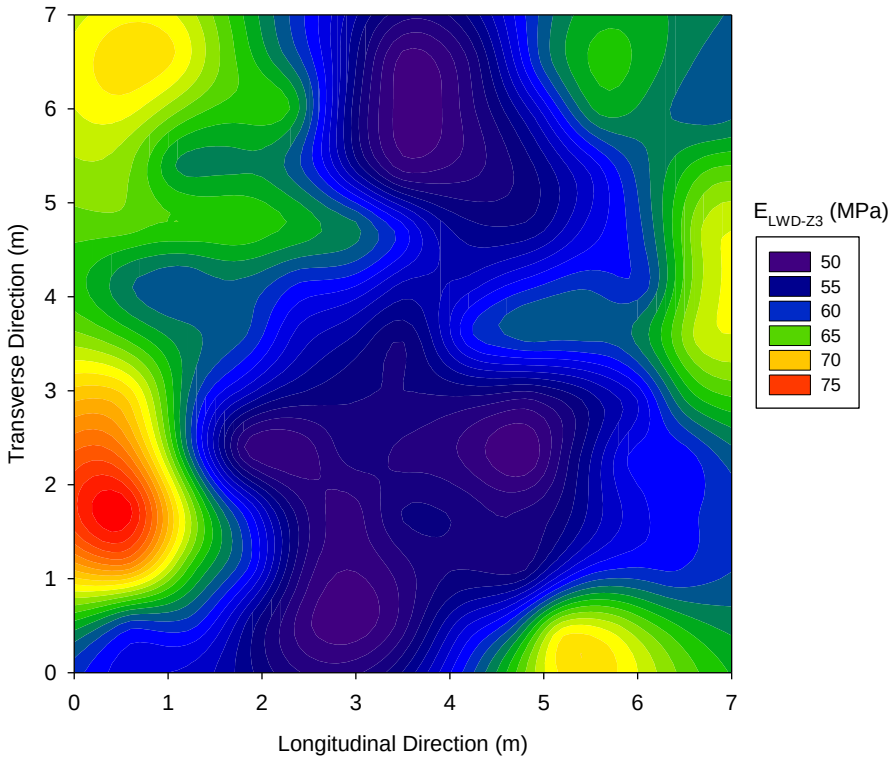

Figure B.23. Kriging contour map with Matérn (k=1) model of E_{LWD-Z3} for MI I-94 TS1b

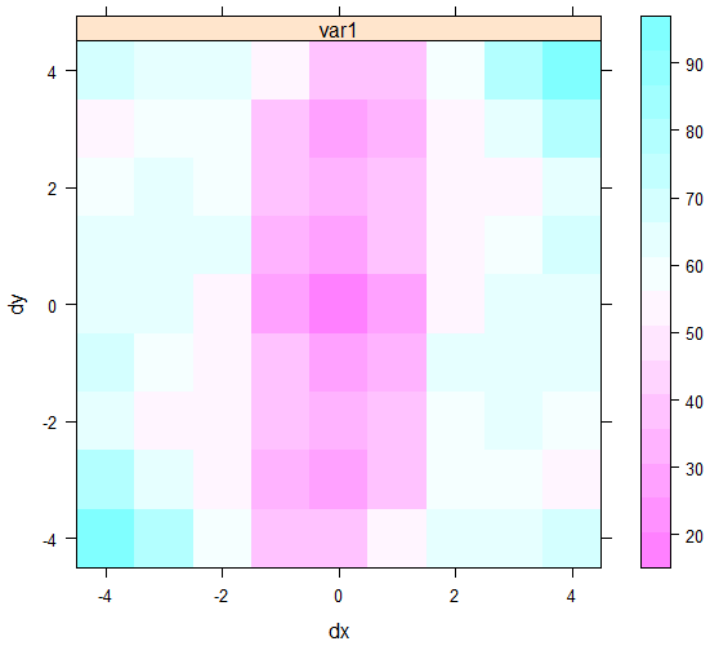

Figure B.24. Semivariogram map of $E_{LWD\text{-}Z3}$ for MI I-94 TS1b

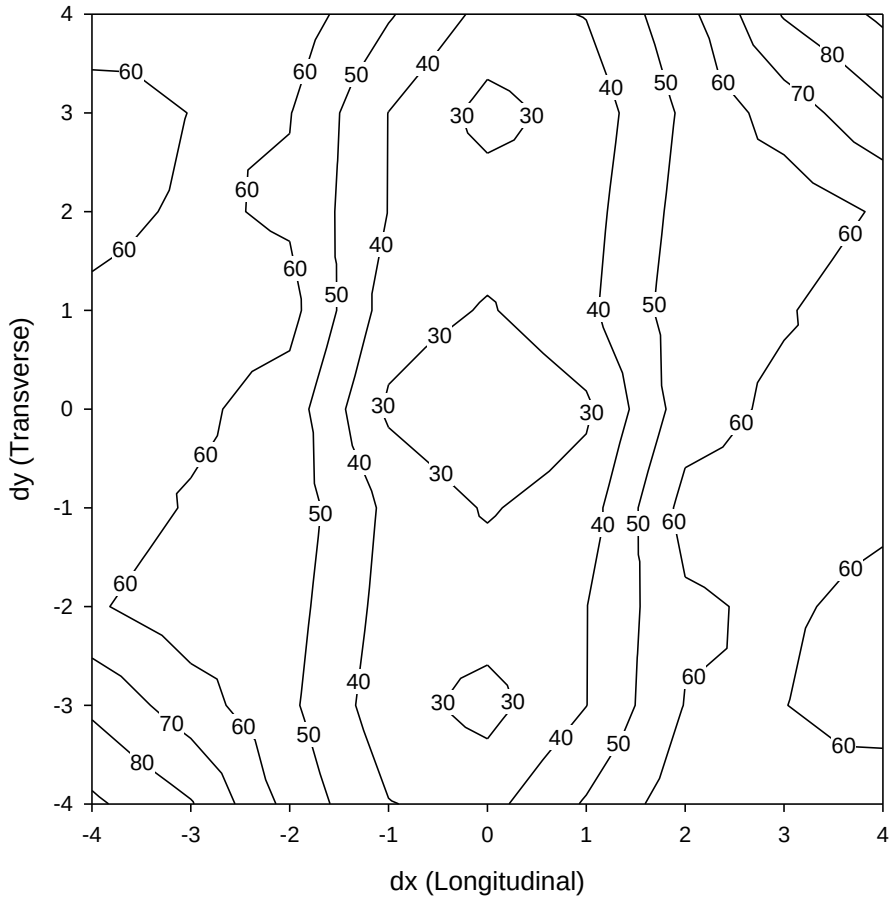

Figure B.25. Semivariogram contour plot of $E_{LWD\text{-}Z3}$ for MI I-94 TS1b

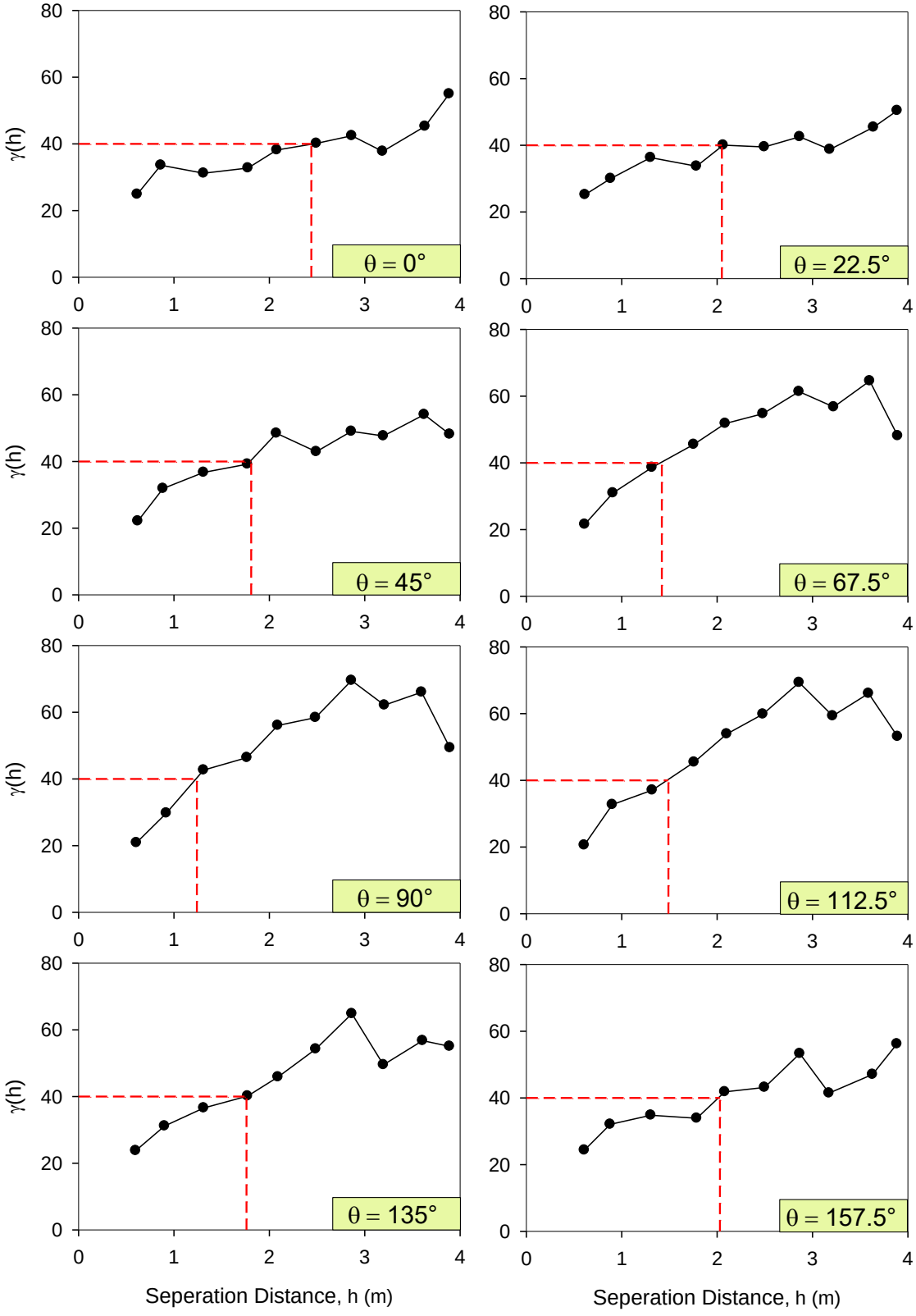

Figure B.26. Multiple directional semivariogram of $E_{LWD\text{-}Z3}$ for MI I-94 TS1b

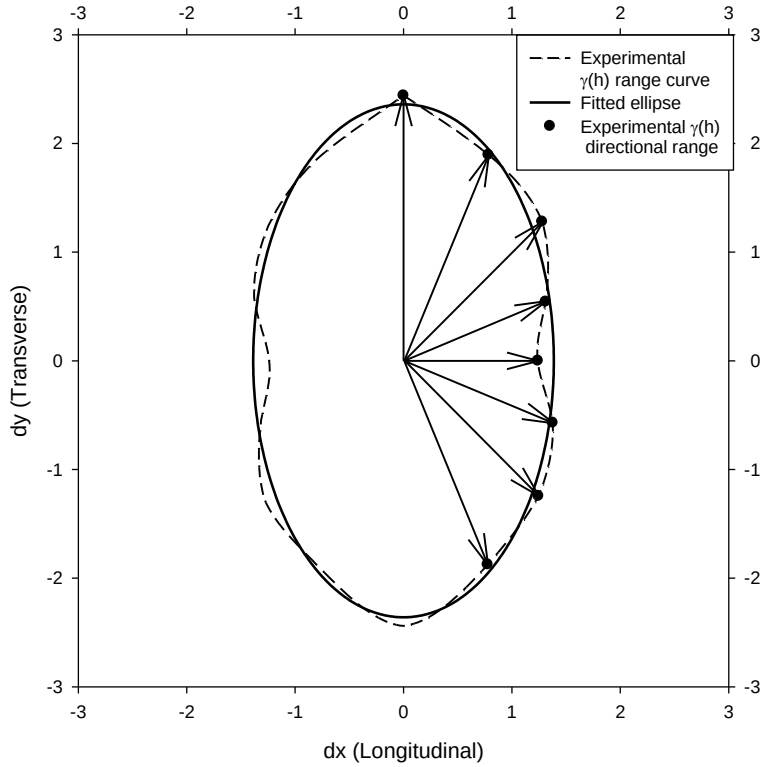

Figure B.27. Rose diagram of directional range values of $E_{LWD\text{-}Z3}$ for MI I-94 TS1b

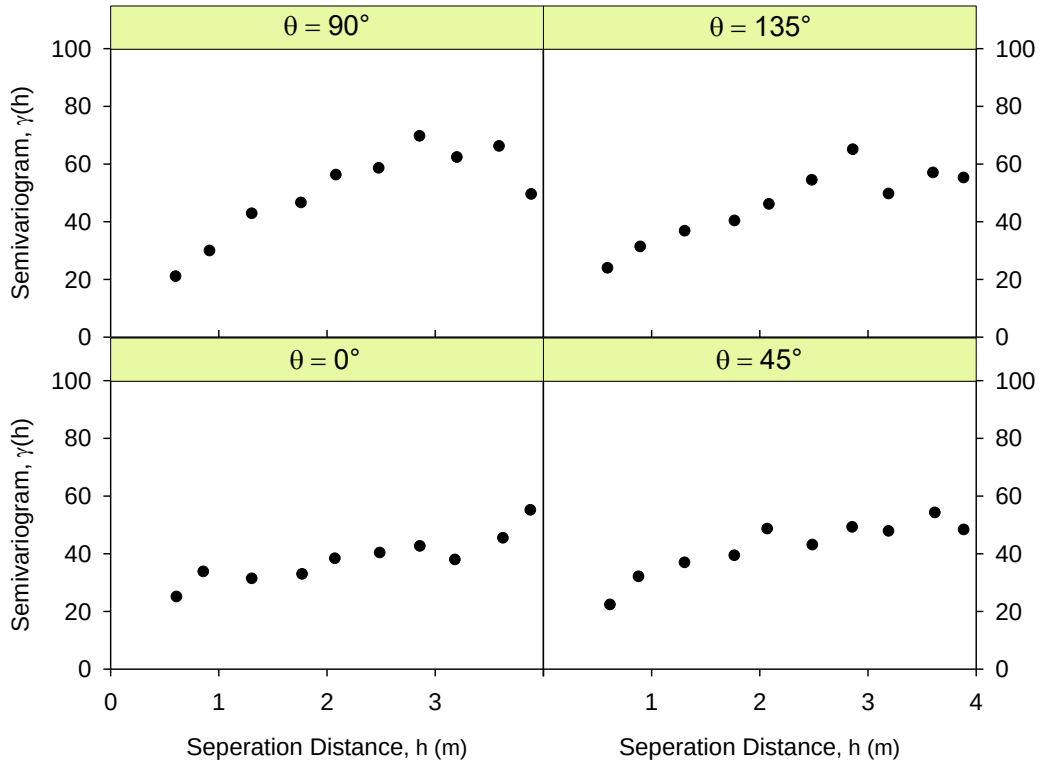

Figure B.28. Directional semivariogram of $E_{LWD\text{-}Z3}$ for MI I-94 TS1b

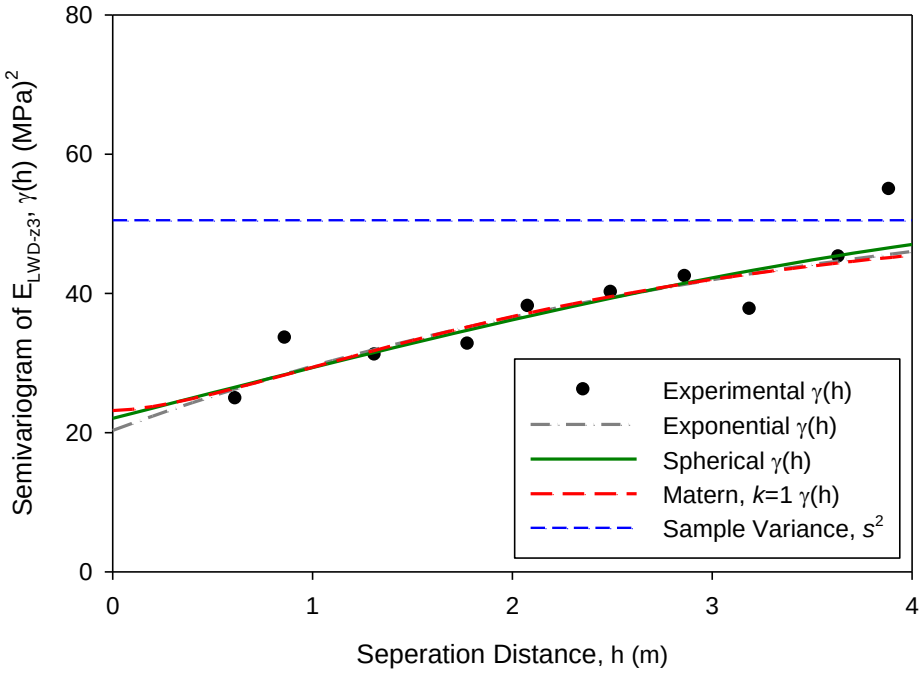

Figure B.29. Transverse direction semivariogram with model fitted of E_{LWD-Z3} for MI I-94 TS1b

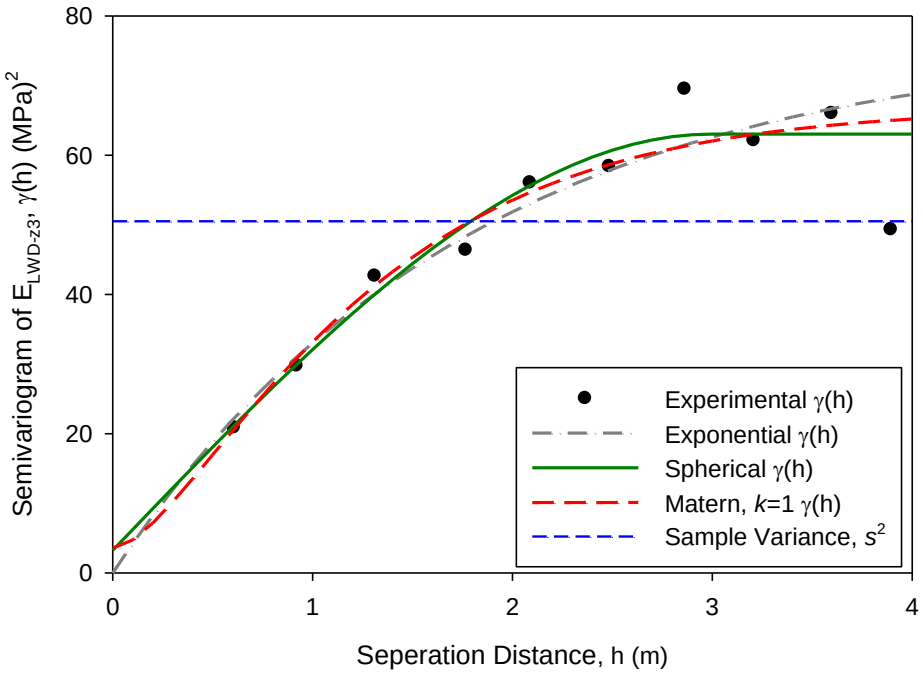

Figure B.30. Longitudinal direction semivariogram with model fitted of E_{LWD-Z3} for MI I-94 TS1b

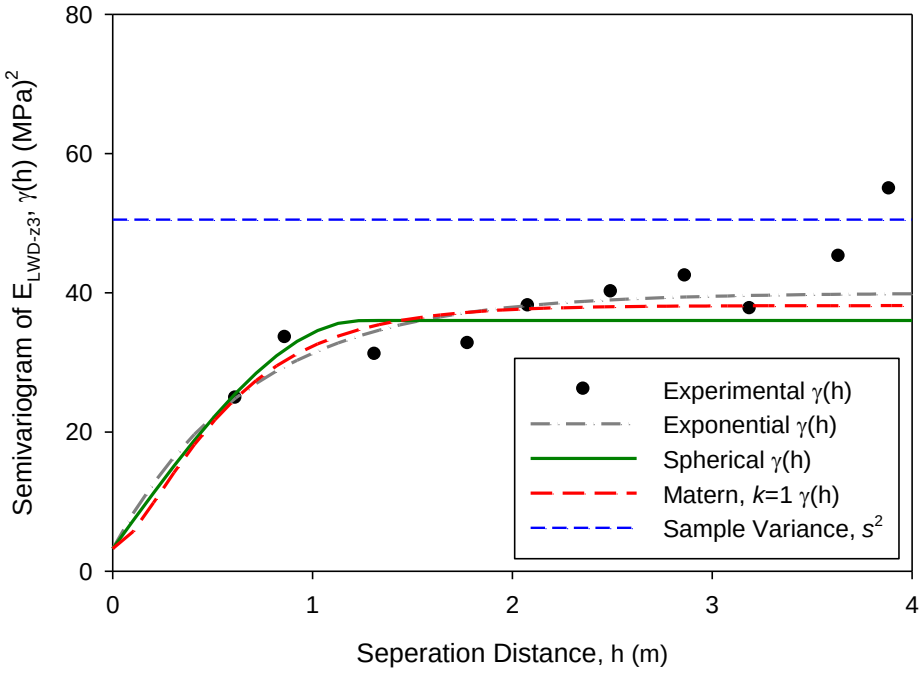

Figure B.31. Transverse direction semivariogram with model fitted and fixed C_0 =0 of E_{LWD-Z3} for MI I-94 TS1b

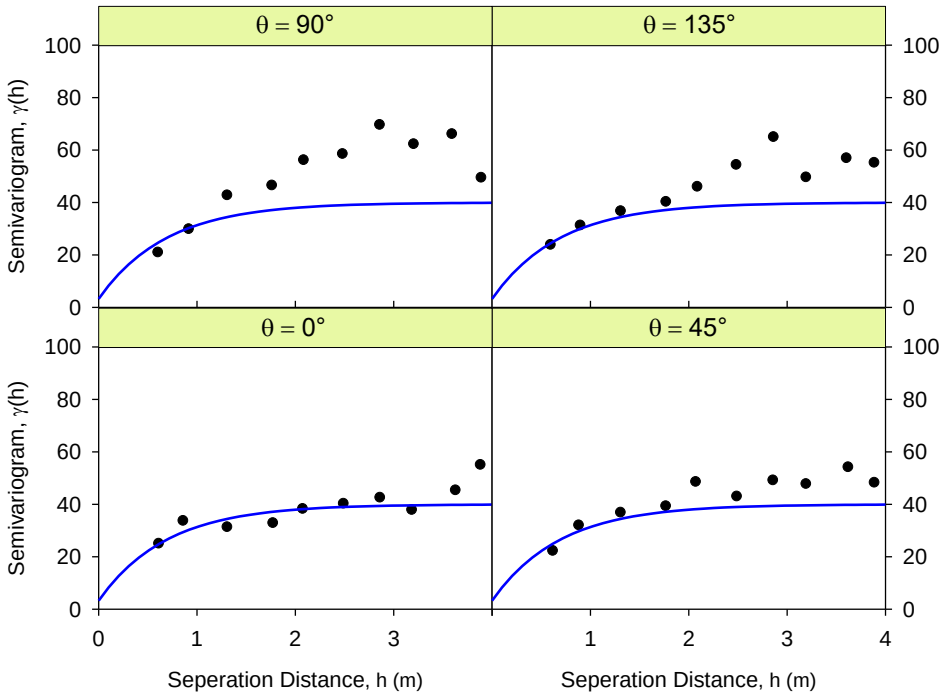

Figure B.32. First step of fitting semivariogram with zonal anisotropy of E_{LWD-Z3} for MI I-94 TS1b

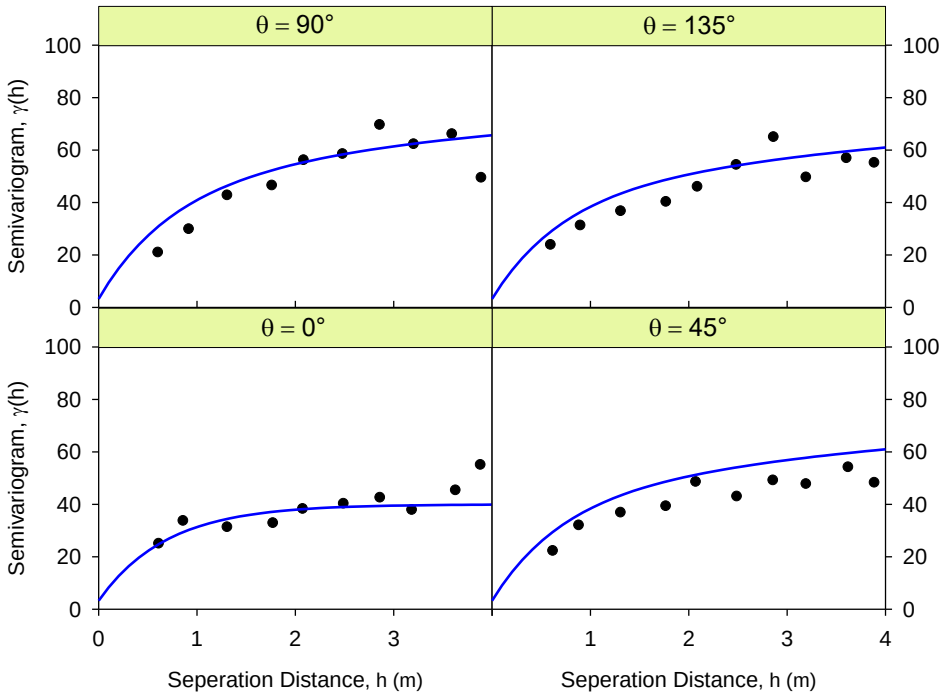

Figure B.33. Second step of fitting semivariogram with zonal anisotropy of E_{LWD-Z3} for MI I-94 TS1b

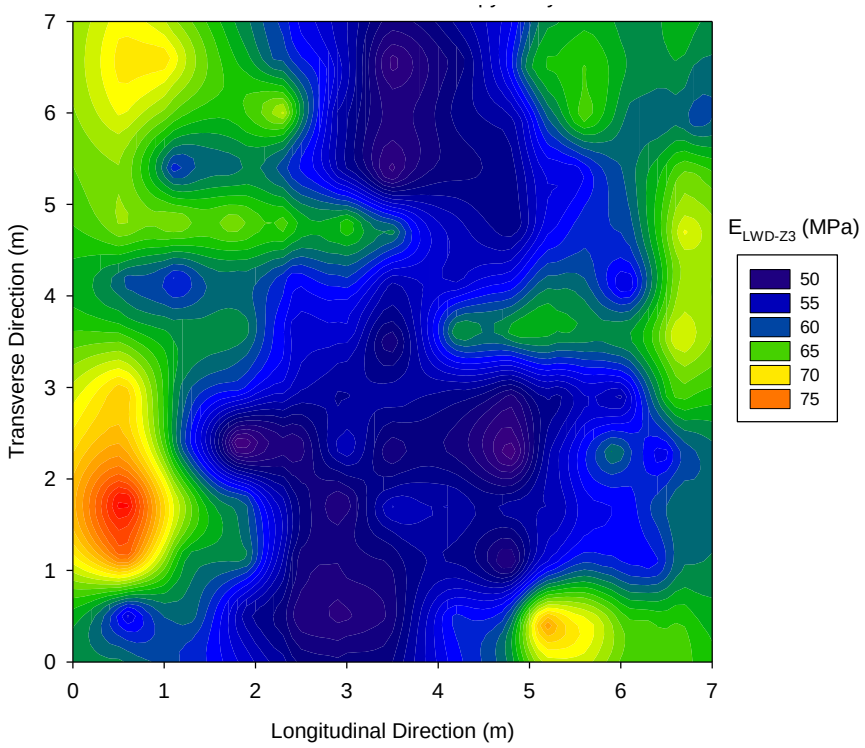

Figure B.34. Kriging contour plot with model considered zonal anisotropy of E_{LWD-Z3} for MI I-94 TS1b

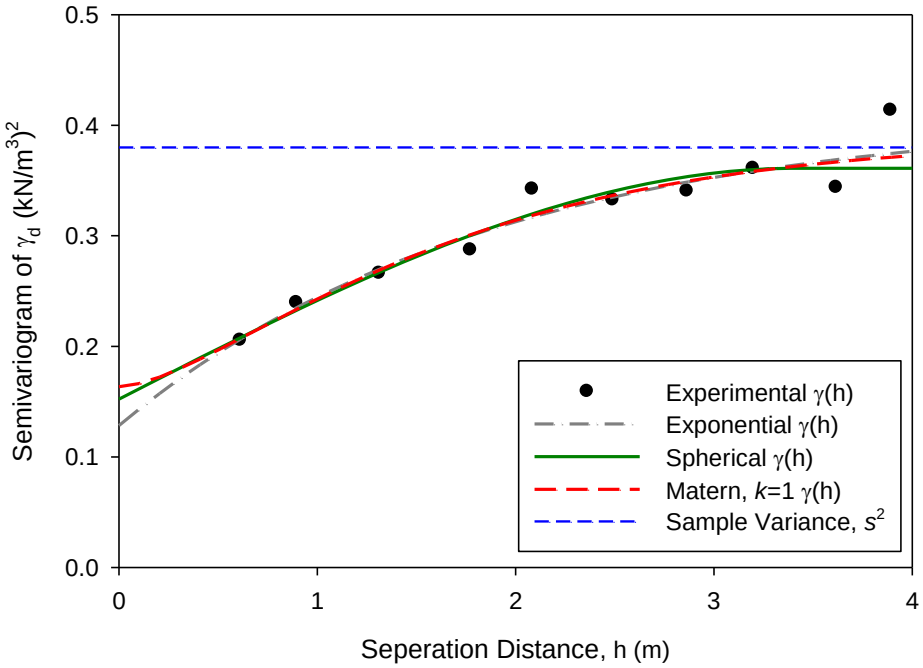

Figure B.35. Omnidirectional semivariogram with fitted model of γ_d for MI I-94 TS1b

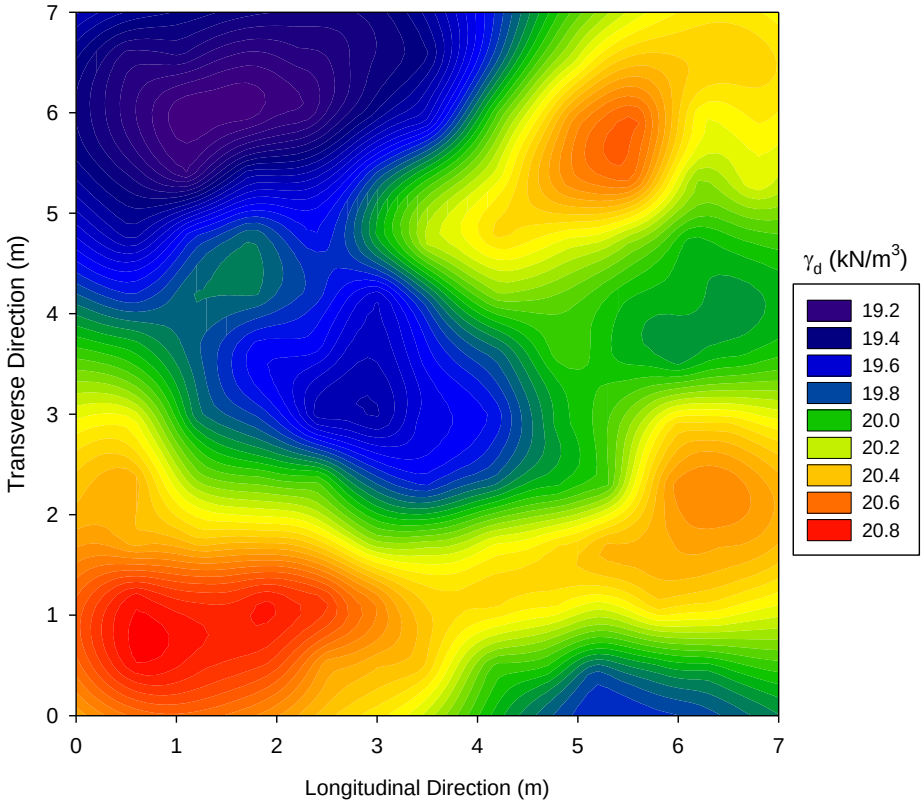

Figure B.36. Kriging contour plot with spherical model of γ_d for MI I-94 TS1b

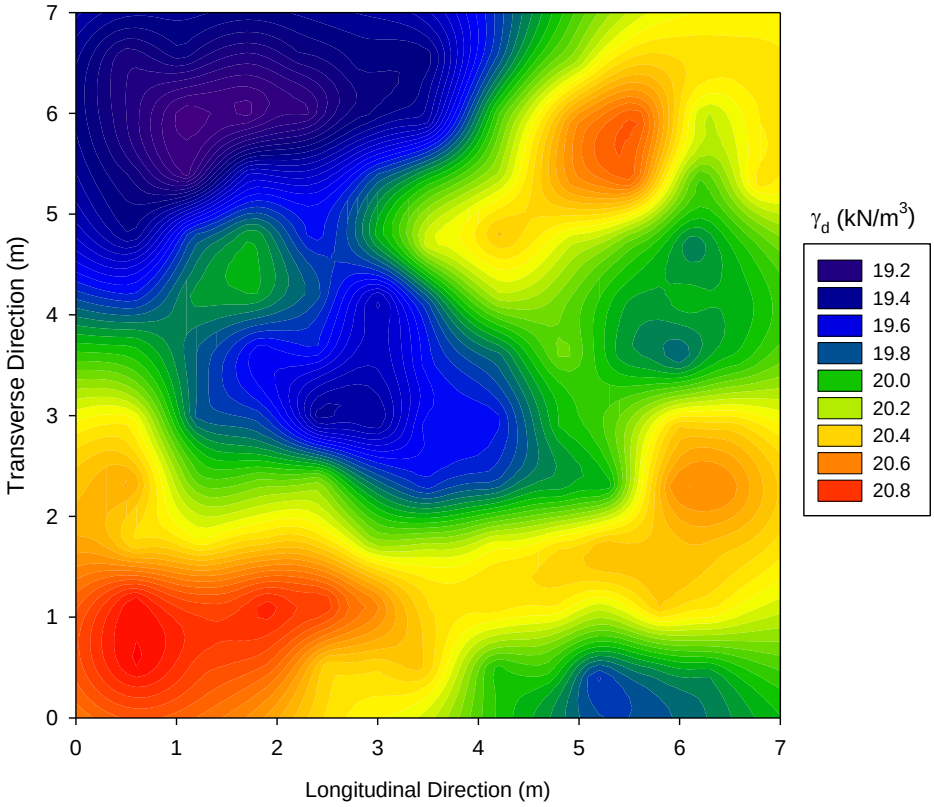

Figure B.37. Kriging contour plot with exponential model of γ_d for MI I-94 TS1b

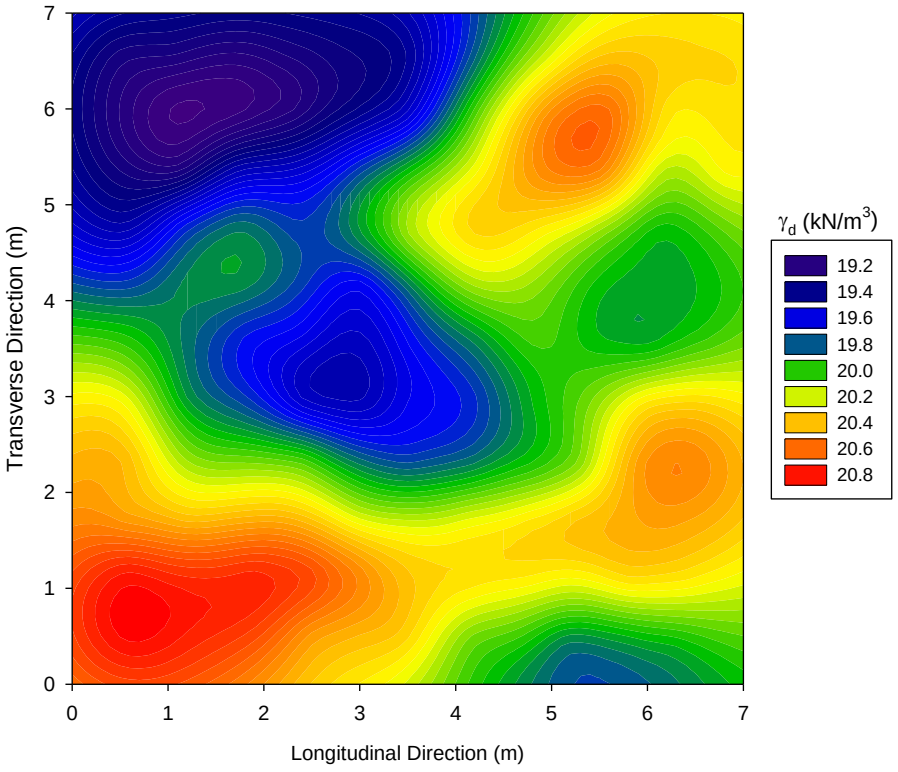

Figure B.38. Kriging contour plot with Matérn (k=1) model of γ_d for MI I-94 TS1b

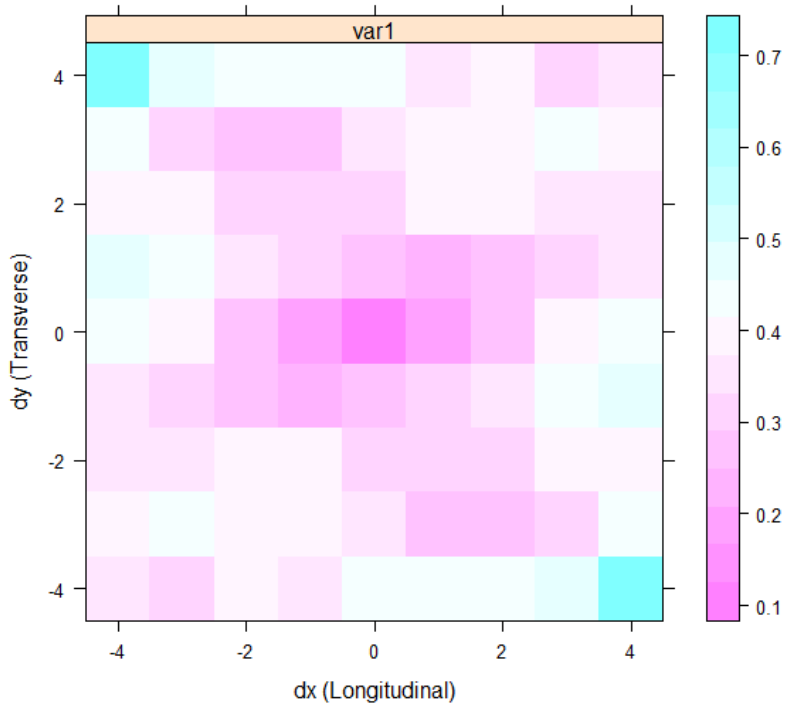

Figure B.39. Semivariogram map of γ_d for MI I-94 TS1b

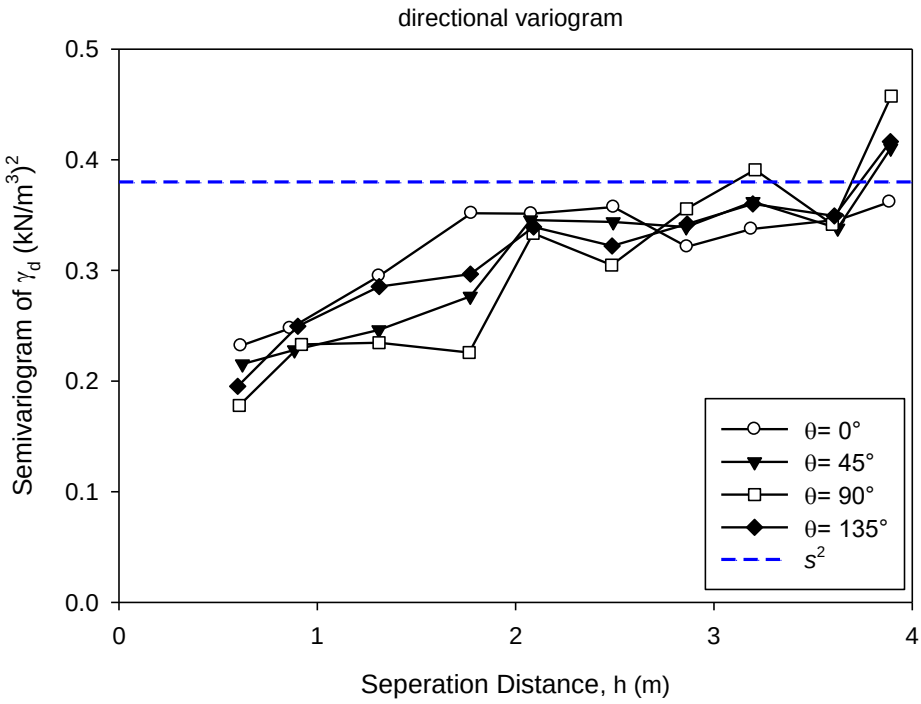

Figure B.40. Directional semivariogram of γ_d for MI I-94 TS1b

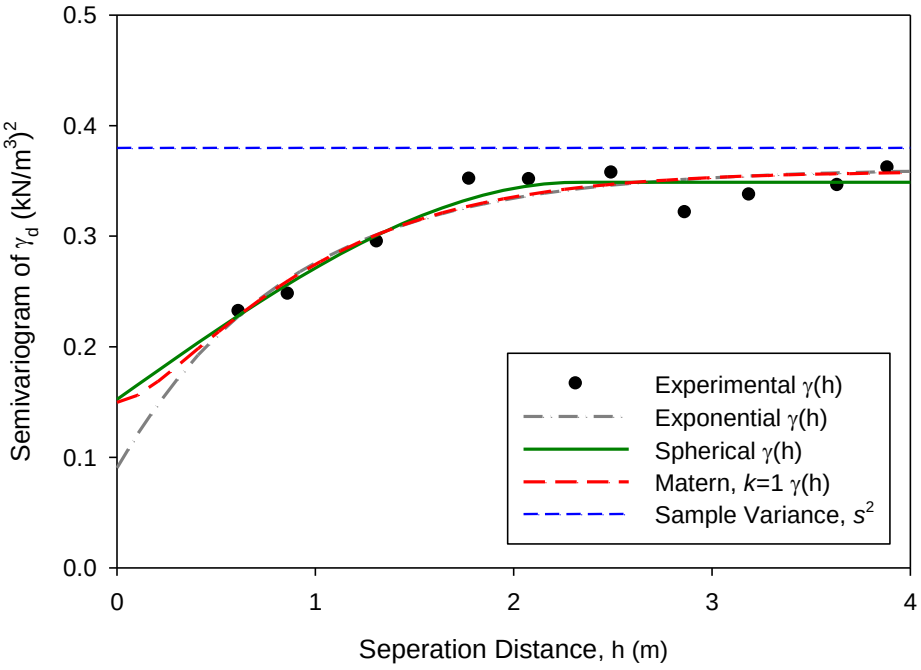

Figure B.41. Transverse direction semivariogram of γ_d for MI I-94 TS1b

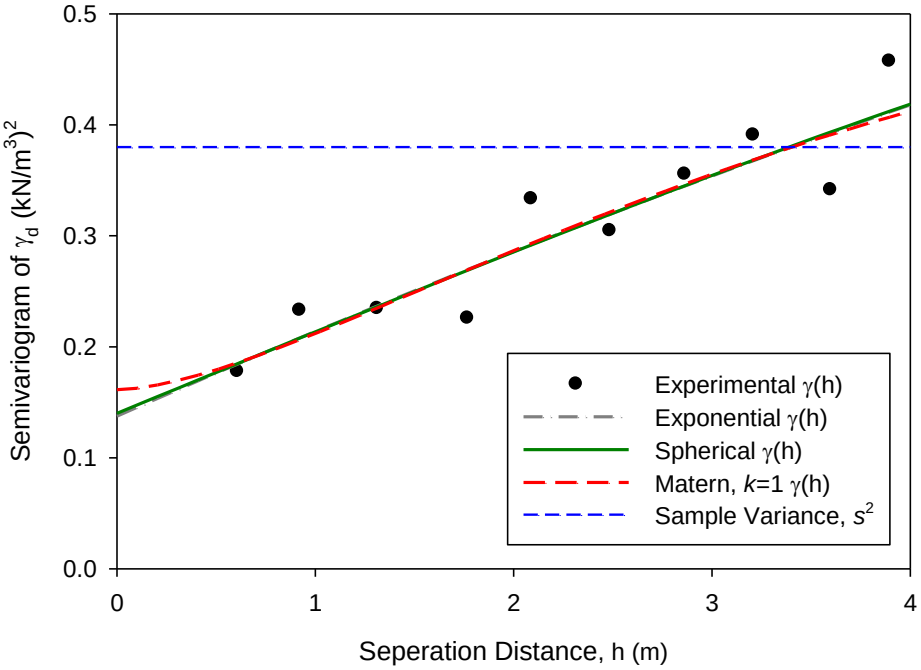

Figure B.42. Longitudinal direction semivariogram of γ_d for MI I-94 TS1b

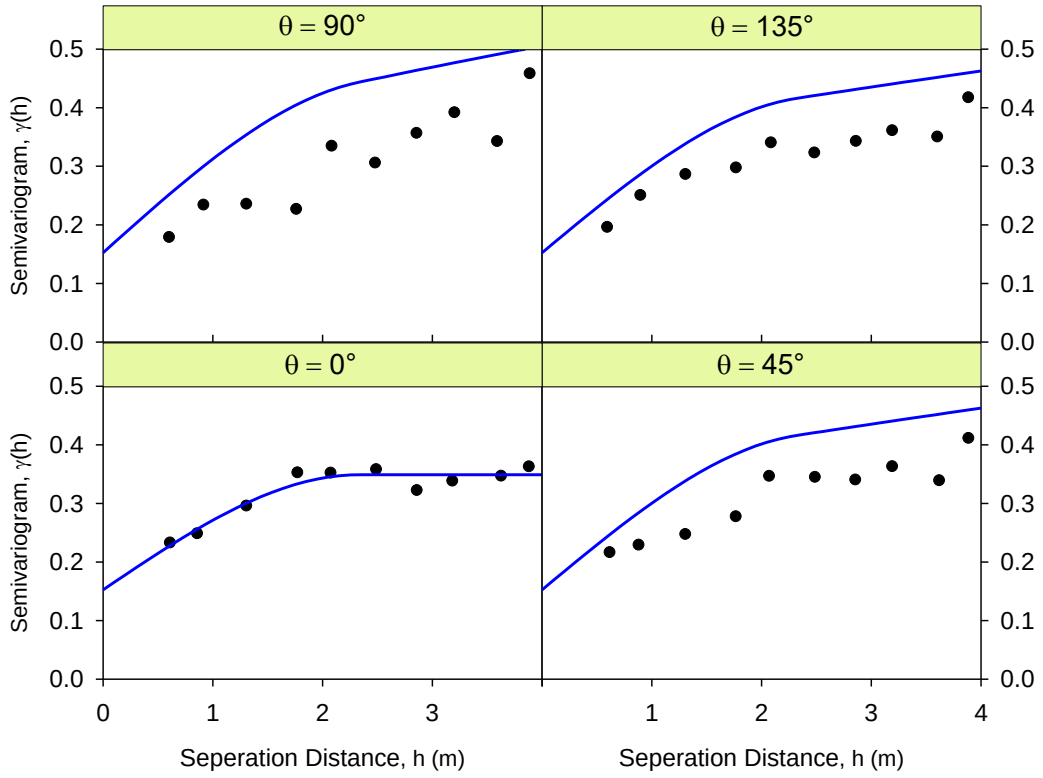

Figure B.43. Directional semivariogram with fitted zonal anisotropic model of γ_d for MI I-94 TS1b

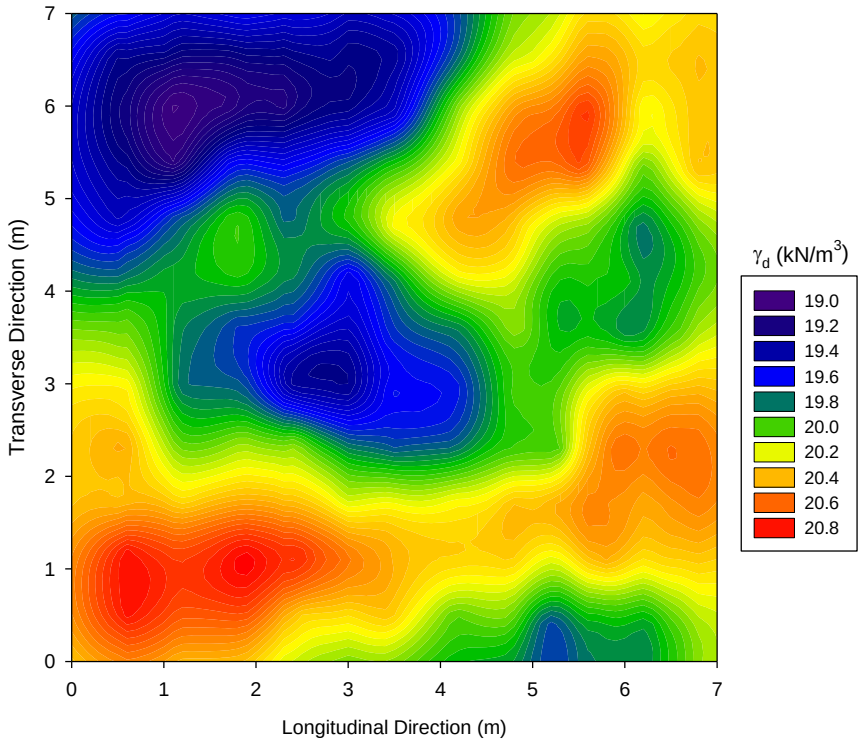

Figure B.44. Kriging contour plot with zonal anisotropic model of γ_d for MI I-94 TS1b

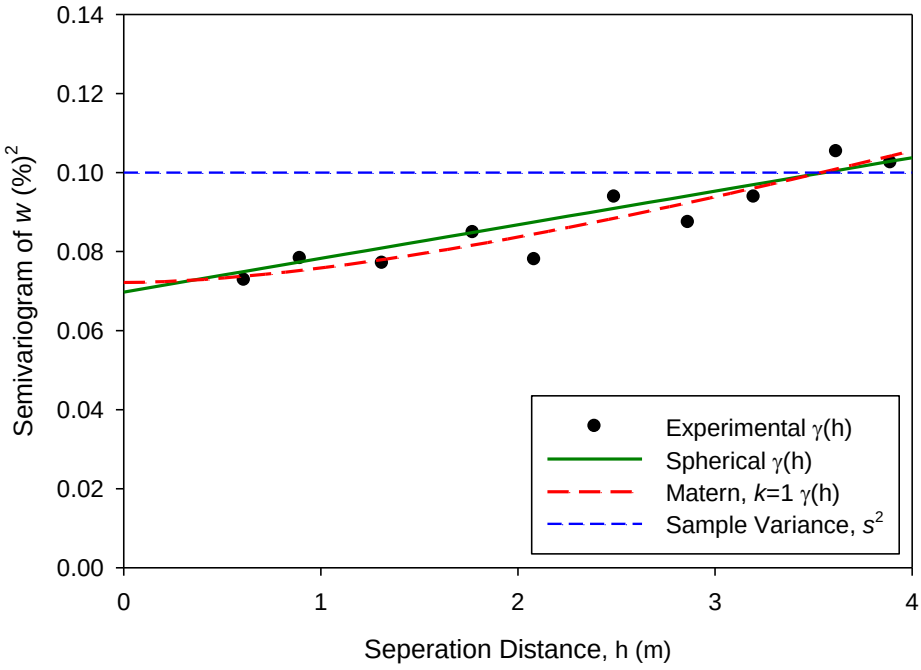

Figure B.45. Omnidirectional semivariogram with fitted model of *w* for MI I-94 TS1b

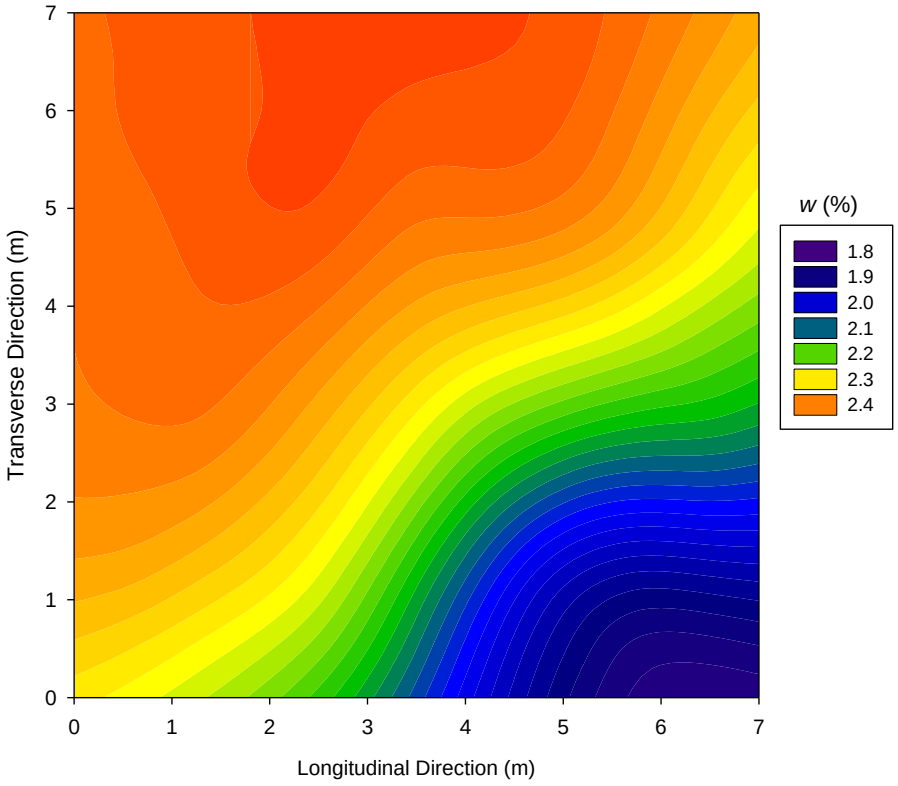

Figure B.46. Kriging contour plot with Matérn (*k*=1) model of *w* for MI I-94 TS1b

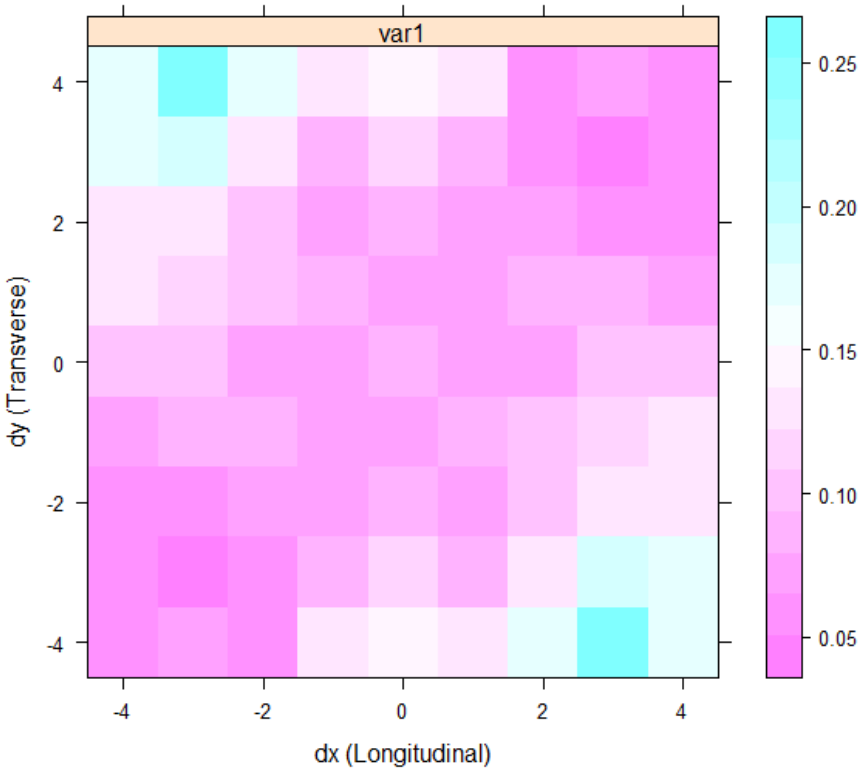

Figure B.47. Semivariogram map of *w* for MI I-94 TS1b

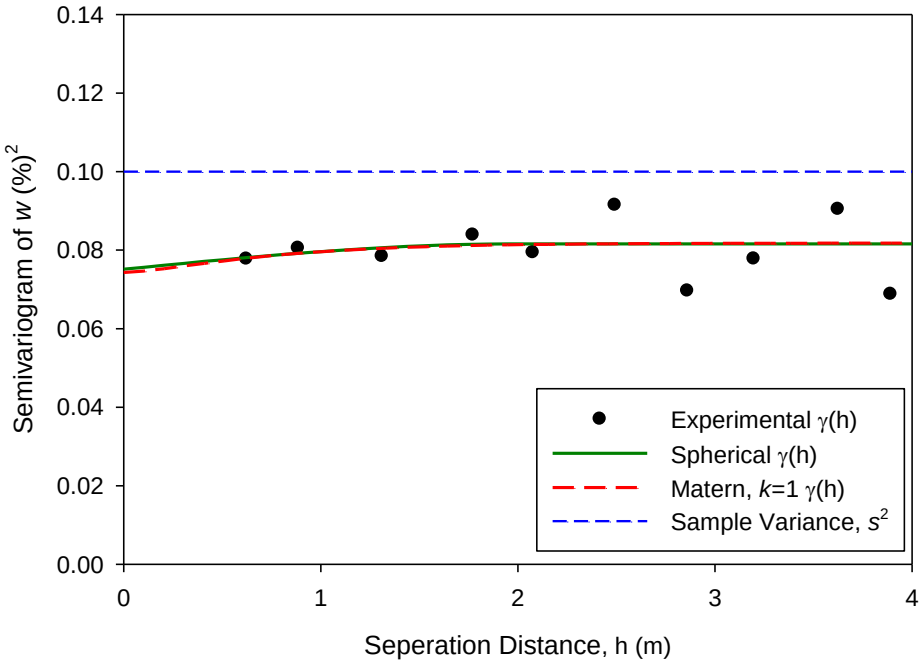

Figure B.48. Directional semivariogram with model fitted at θ=45° of *w* for MI I-94 TS1b

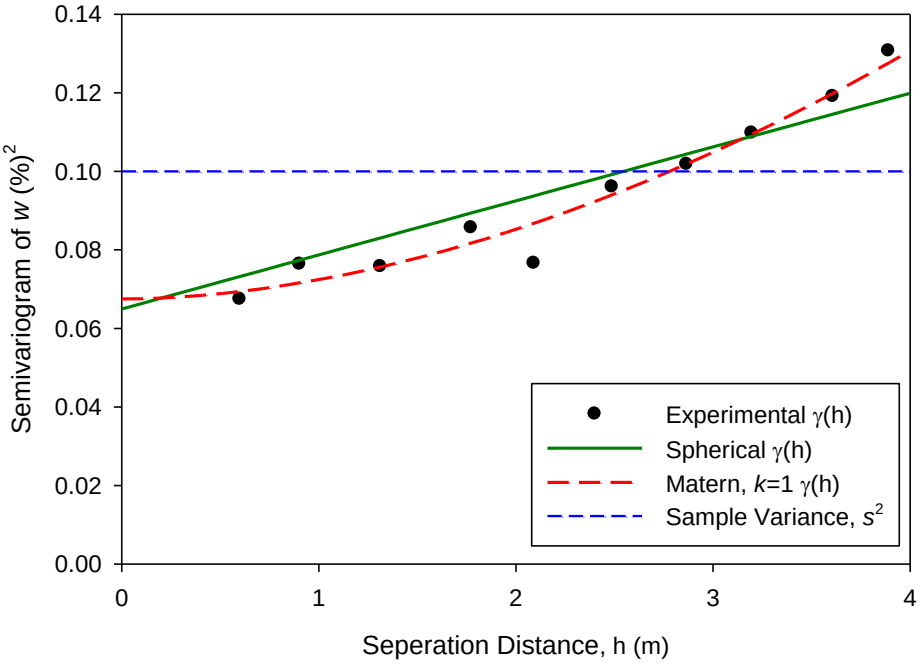

Figure B.49. Directional semivariogram with model fitted at θ=135° of *w* for MI I-94 TS1b

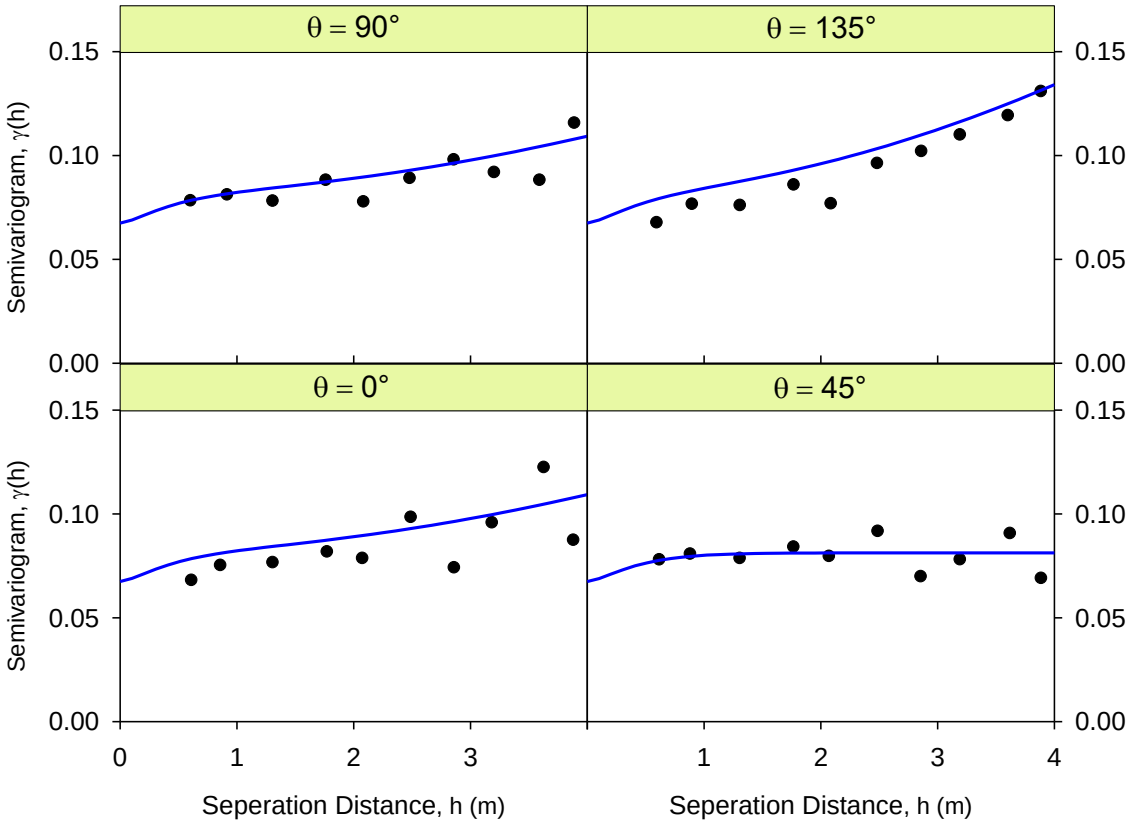

Figure B.50. Directional semivariogram with fitted zonal anisotropic model of *w* for MI I-94 TS1b

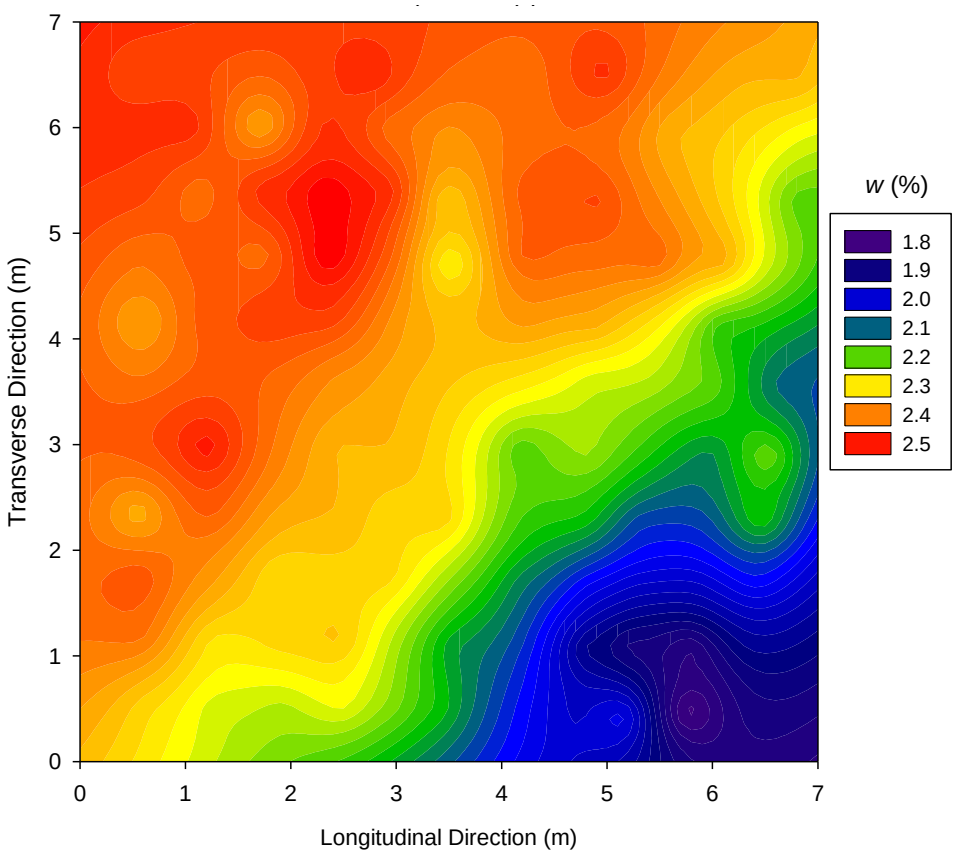

Figure B.51. Kriging contour plot with zonal anisotropic model of *w* for MI I-94 TS1b

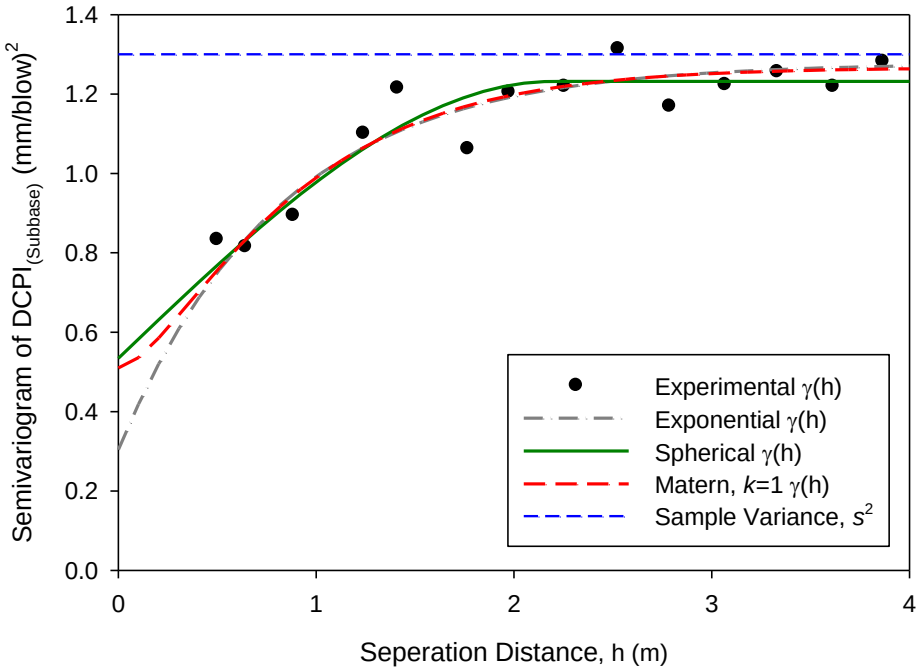

Figure B.52. Omnidirectional semivariogram with fitted model of $DCPI_{subbase}$ for MI I-94 TS1b

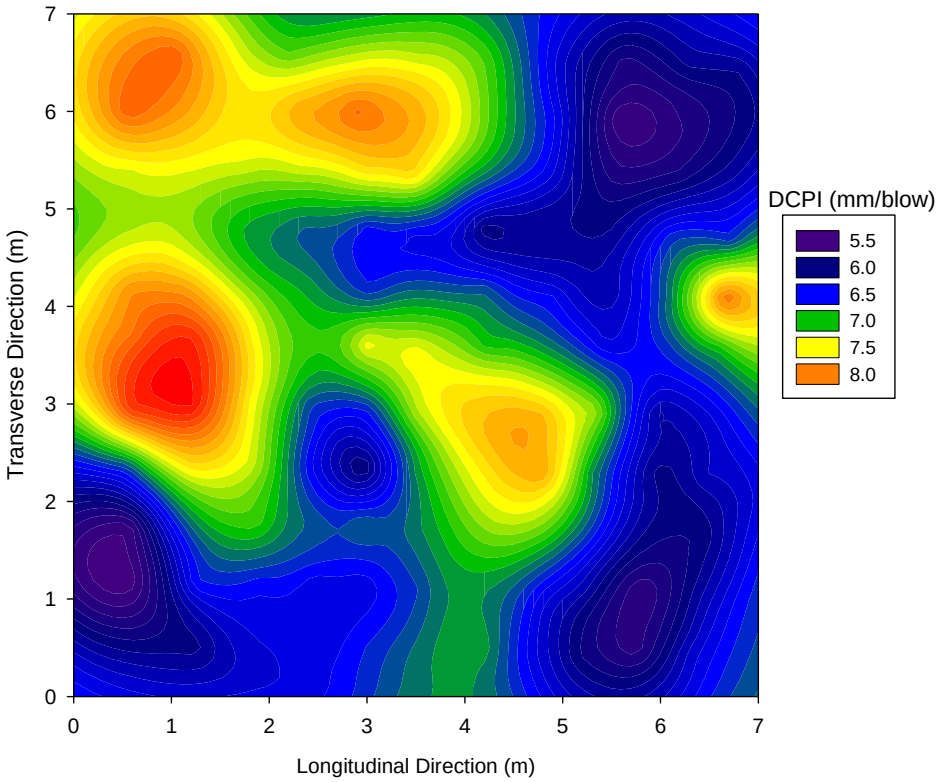

Figure B.53. Kriging contour plot with spherical model of $DCPI_{subbase}$ for MI I-94 TS1b

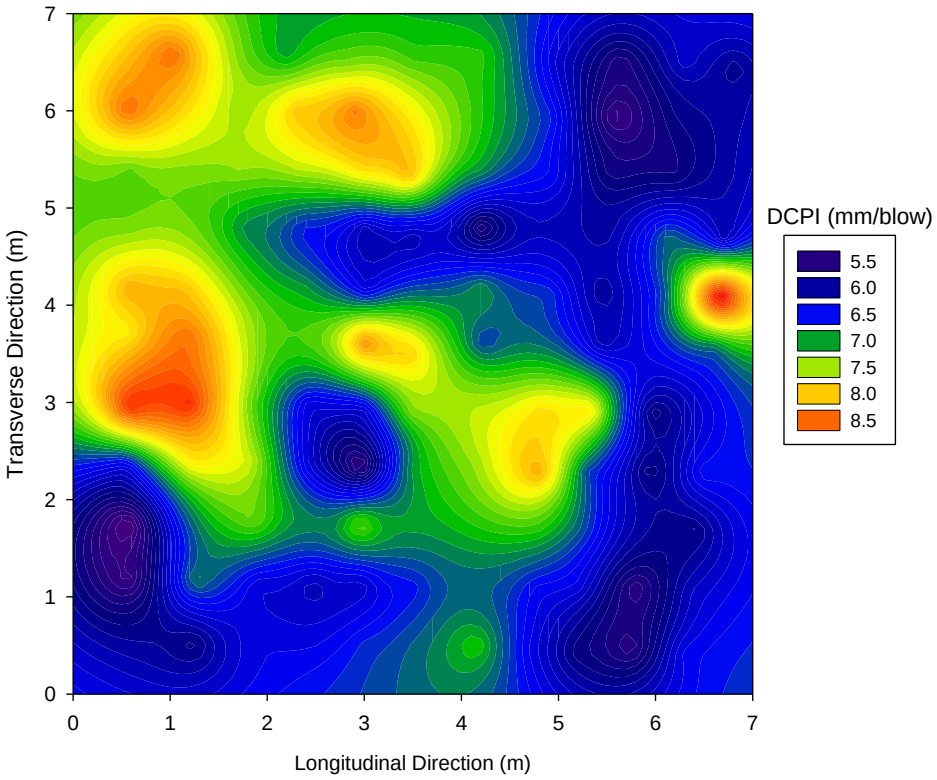

Figure B.54. Kriging contour plot with exponential model of $DCPI_{subbase}$ for MI I-94 TS1b

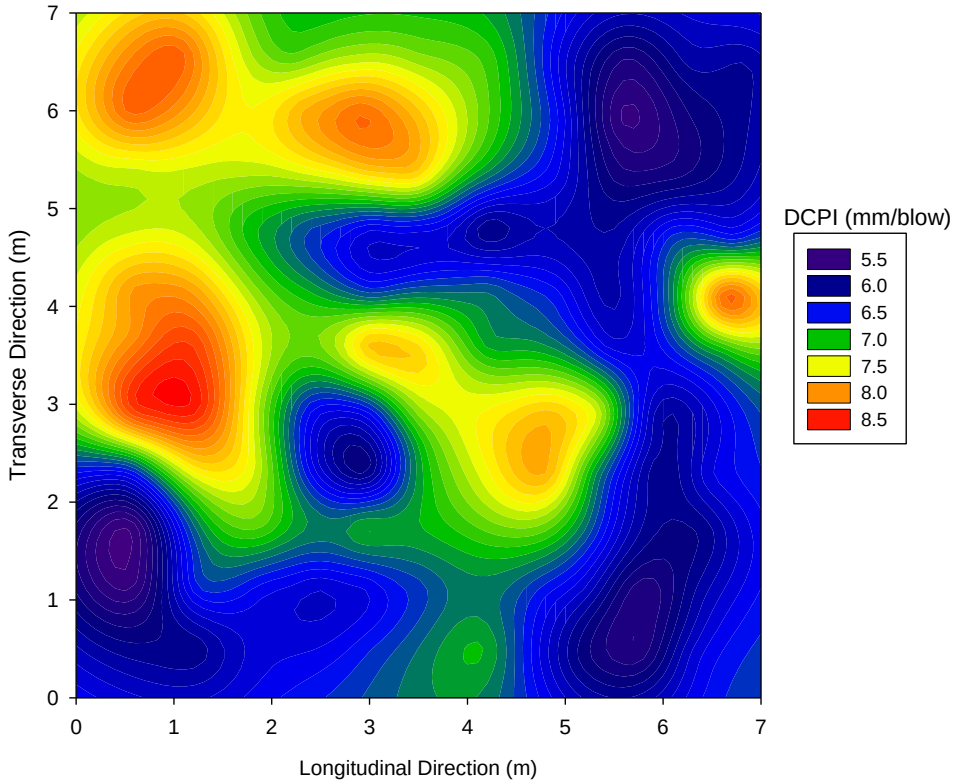

Figure B.55. Kriging contour plot with Matérn (k=1) model of $DCPI_{subbase}$ for MI I-94 TS1b

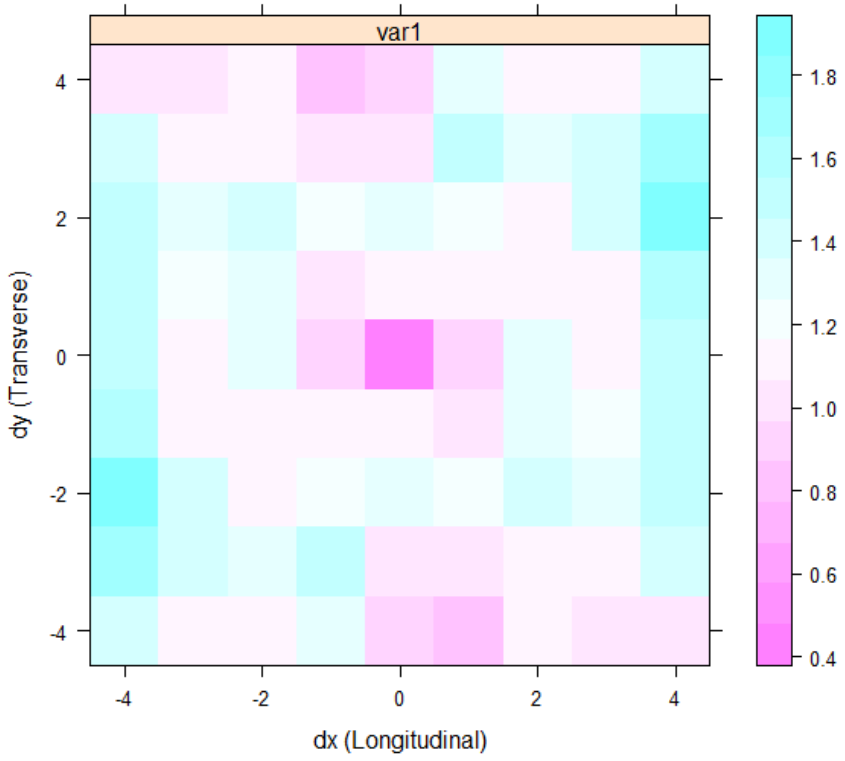

Figure B.56. Semivariogram map of $DCPI_{subbase}$ for MI I-94 TS1b

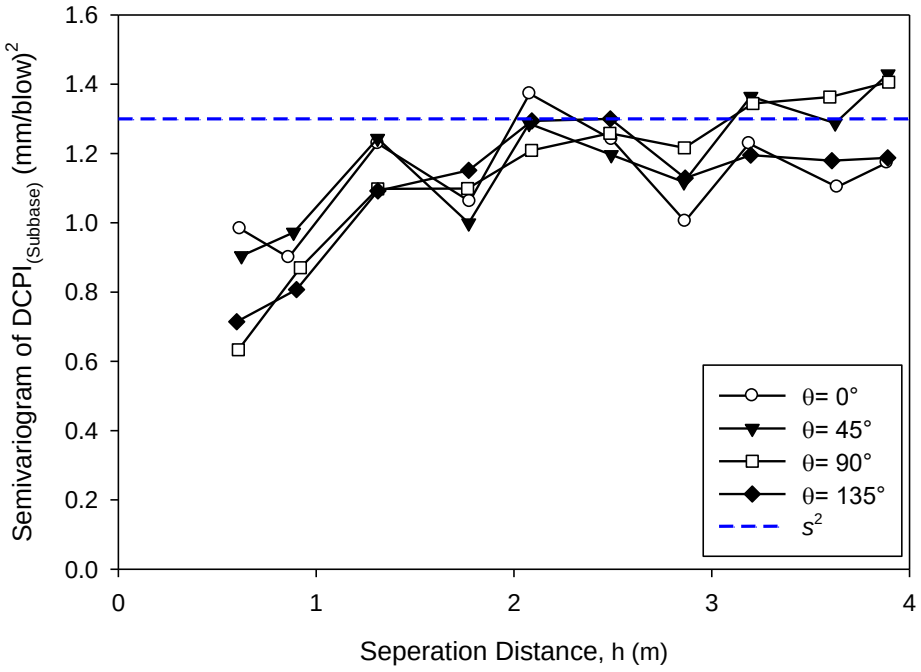

Figure B.57. Directional semivariogram of $DCPI_{subbase}$ for MI I-94 TS1b

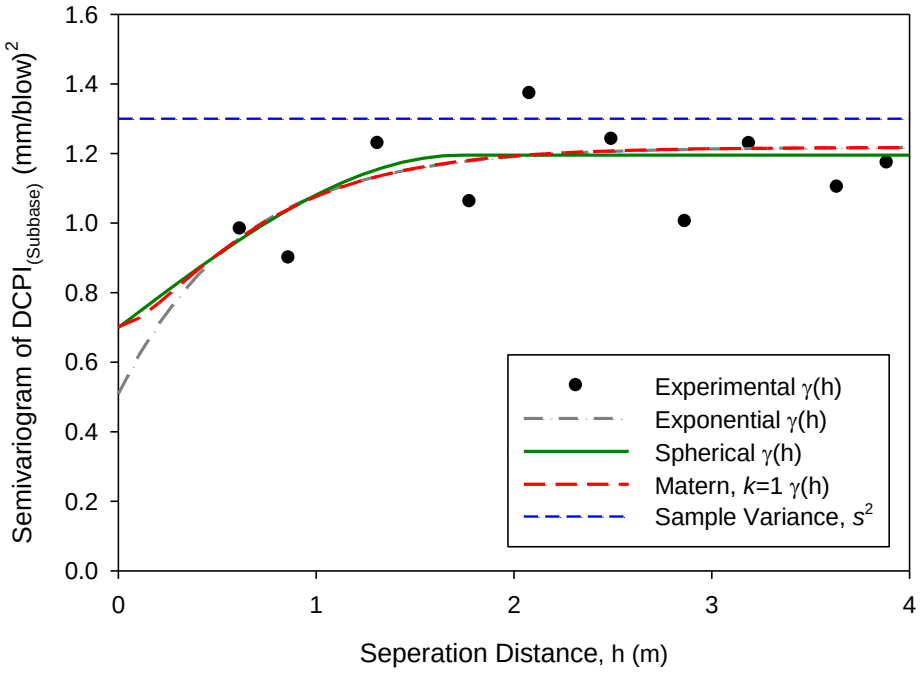

Figure B.58. Transverse direction semivariogram with fitted model of $DCPI_{subbase}$ for MI I-94 TS1b

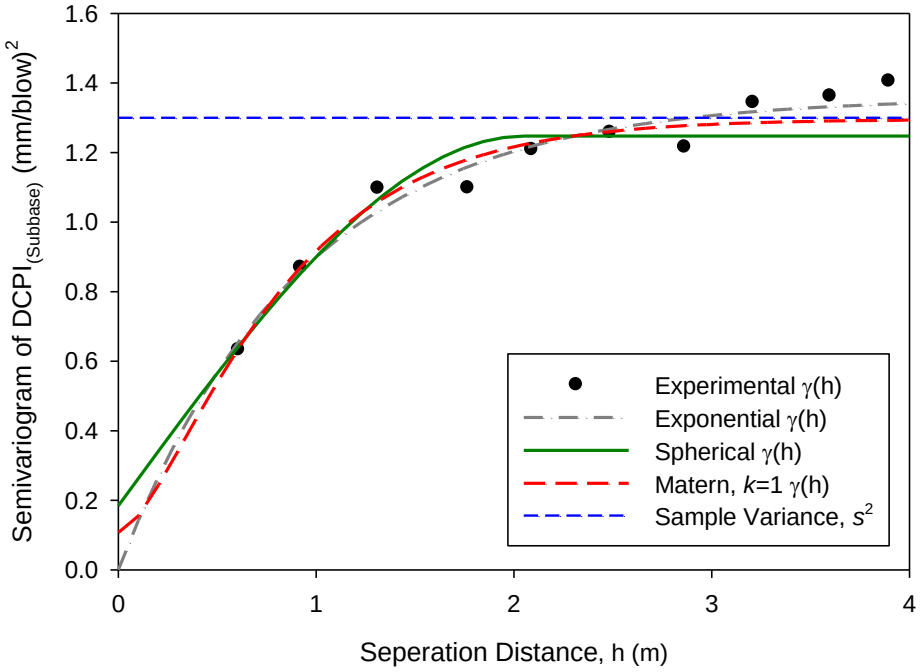

Figure B.59. Longitudinal direction semivariogram with fitted model of $DCPI_{subbase}$ for MI I-94 TS1b

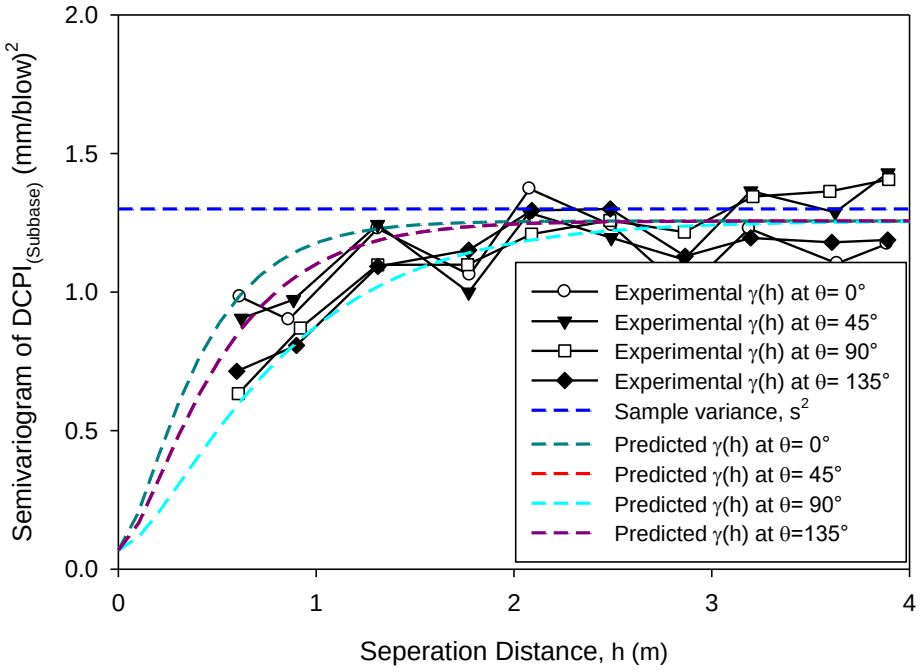

Figure B.60. Directional semivariogram with fitted model of $DCPI_{subbase}$ for MI I-94 TS1b

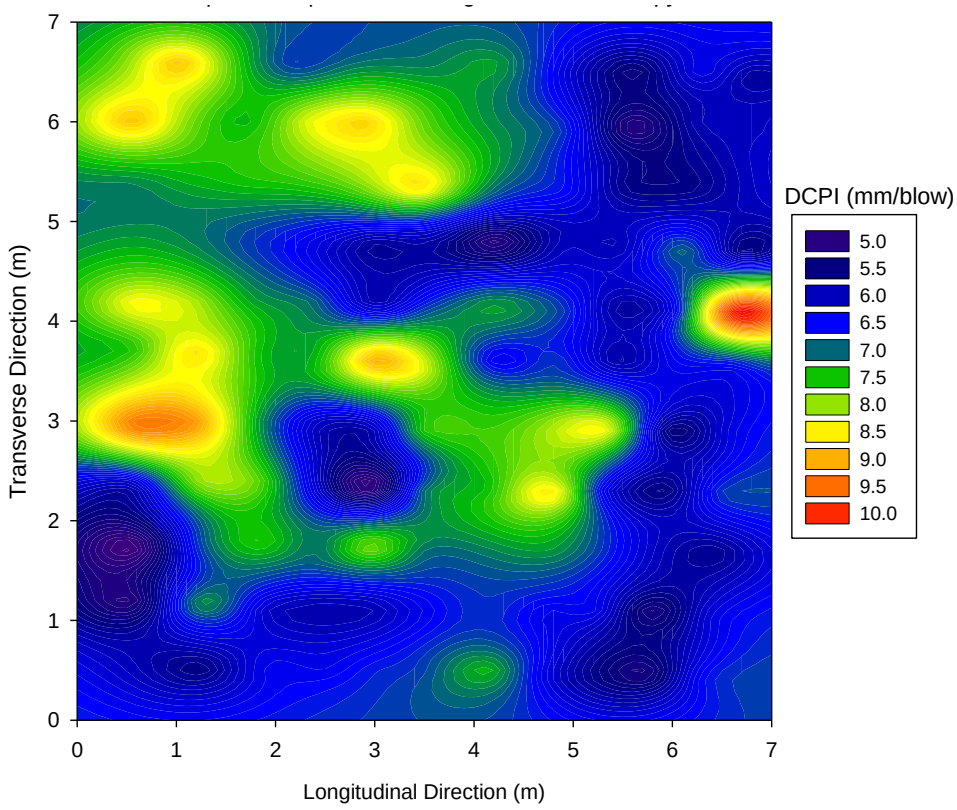

Figure B.61. Kriging contour plot with geometric anisotropic model of $DCPI_{subbase}$ for MI I-94 TS1b

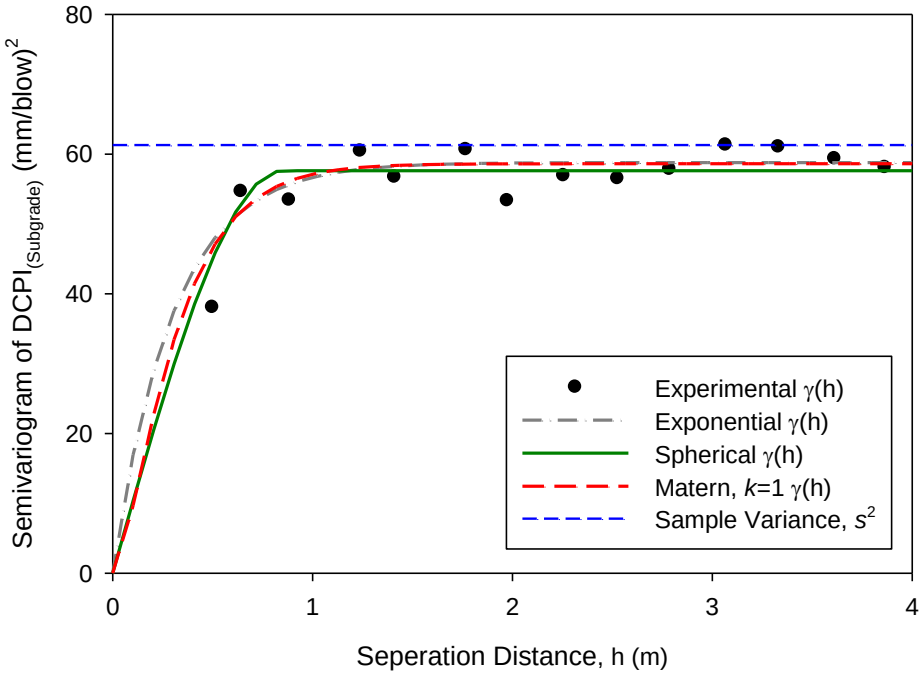

Figure B.62. Omnidirectional semivariogram with fitted model of $DCPI_{subgrade}$ for MI I-94 TS1b

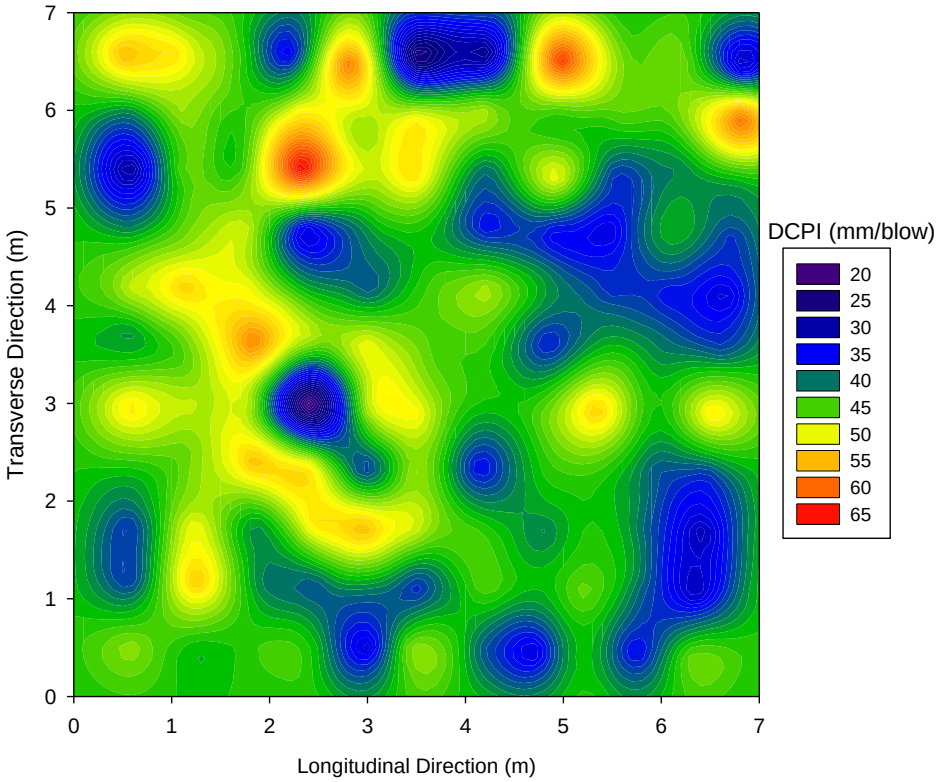

Figure B.63. Kriging contour plot with spherical model of $DCPI_{subgrade}$ for MI I-94 TS1b

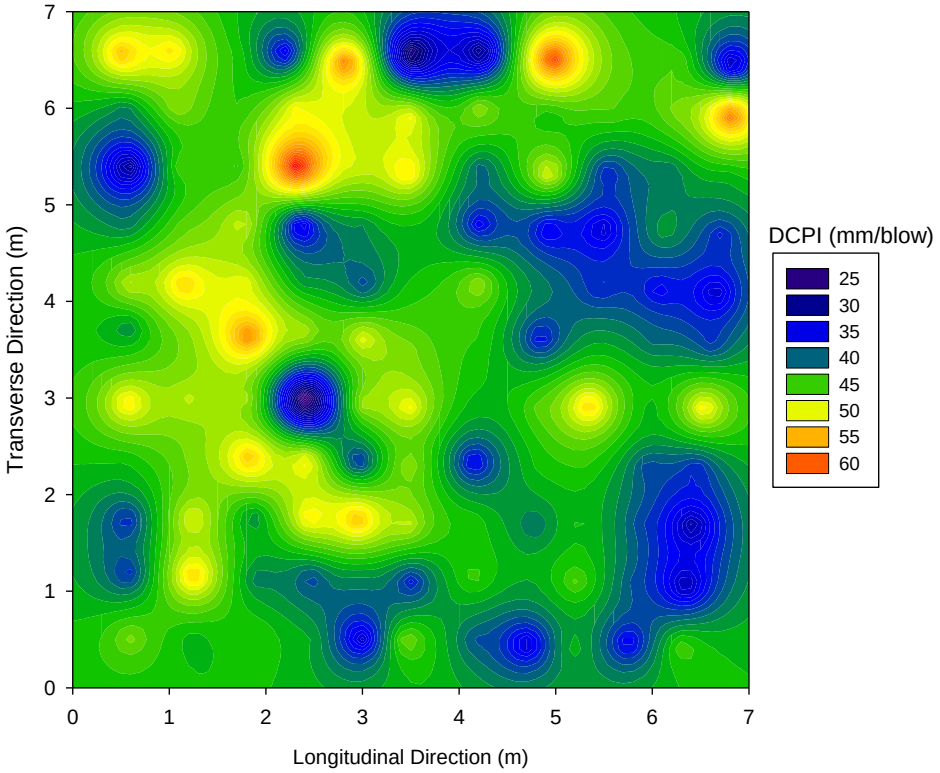

Figure B.64. Kriging contour plot with exponential model of $DCPI_{subgrade}$ for MI I-94 TS1b

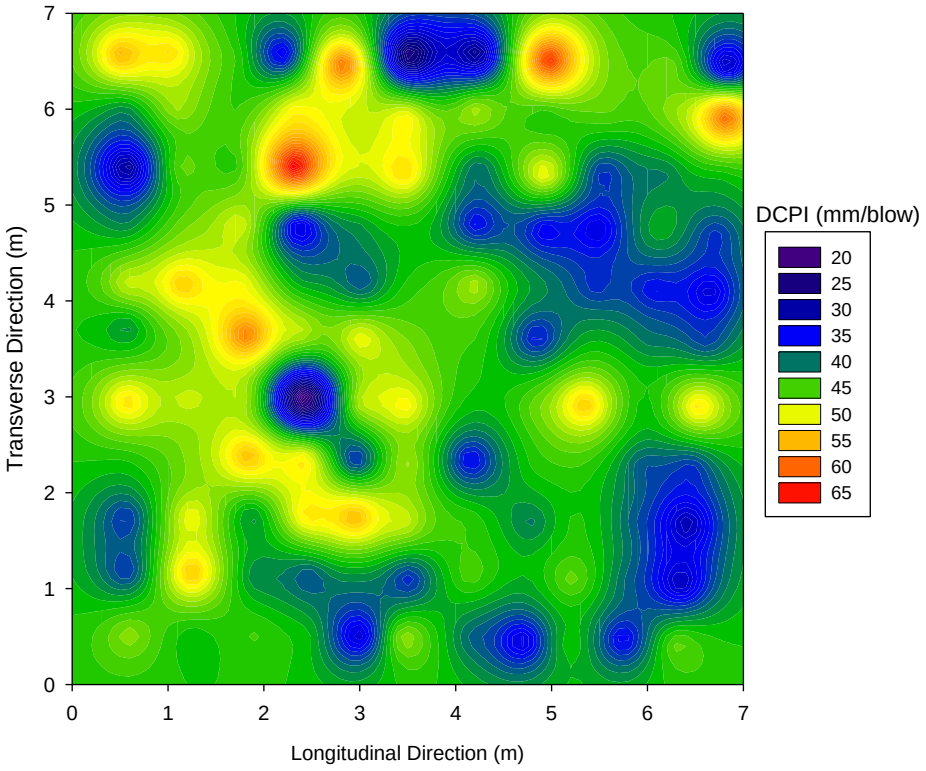

Figure B.65. Kriging contour plot with Matérn (k=1) model of $DCPI_{subgrade}$ for MI I-94 TS1b

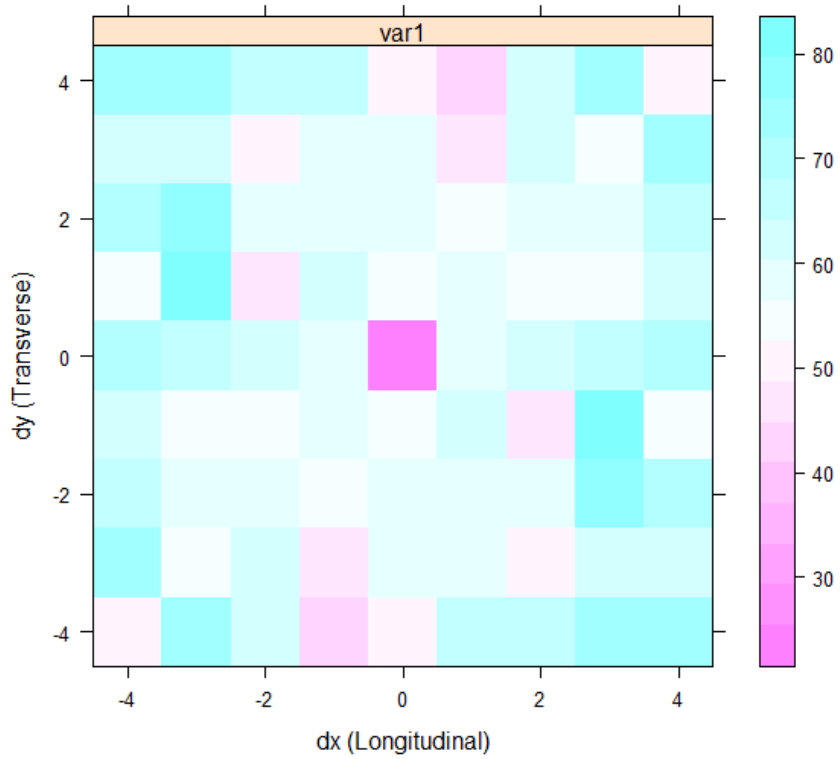

Figure B.66. Semivariogram map of $DCPI_{subgrade}$ with width =1 for MI I-94 TS1b

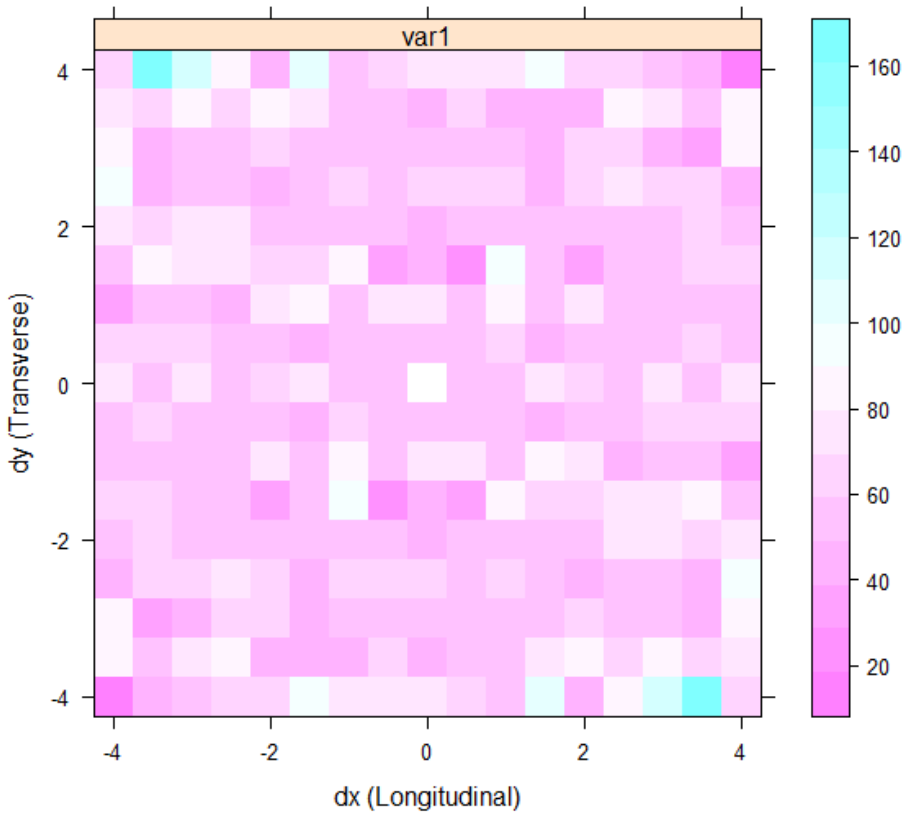

Figure B.67. Semivariogram map of $DCPI_{subgrade}$ with width =0.5 for MI I-94 TS1b

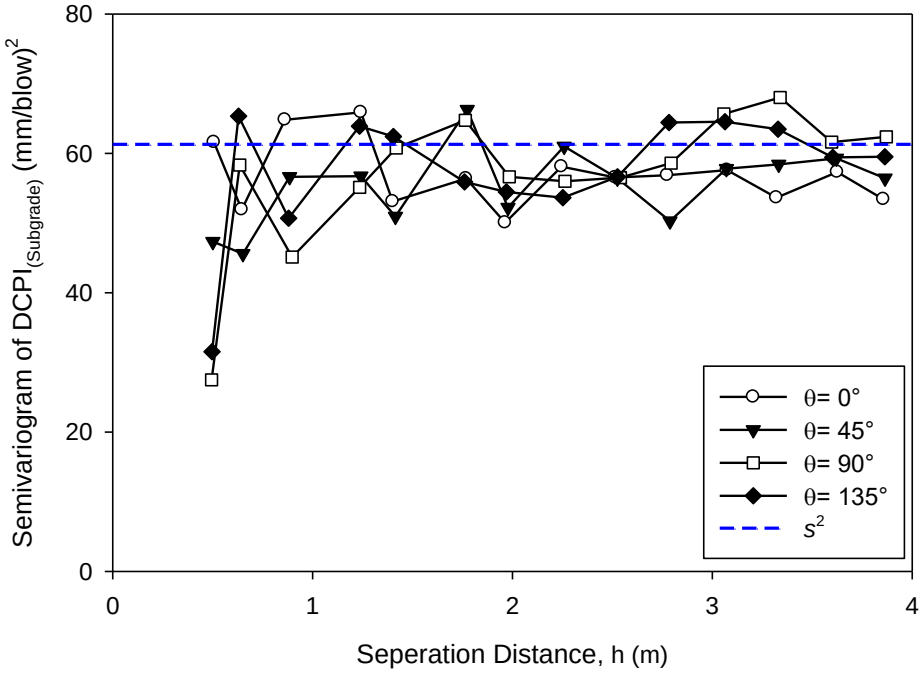

Figure B.68. Directional semivariogram of $DCPI_{subgrade}$ for MI I-94 TS1b

B.3. MI I-94 TS3

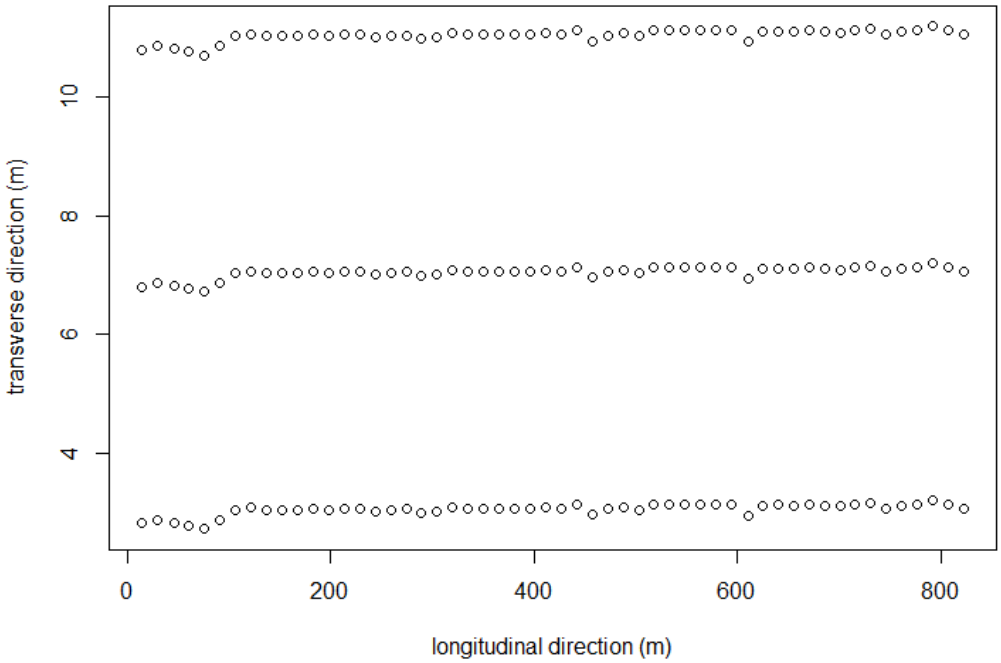

Figure B.69. Test plan for MI I-94 TS3

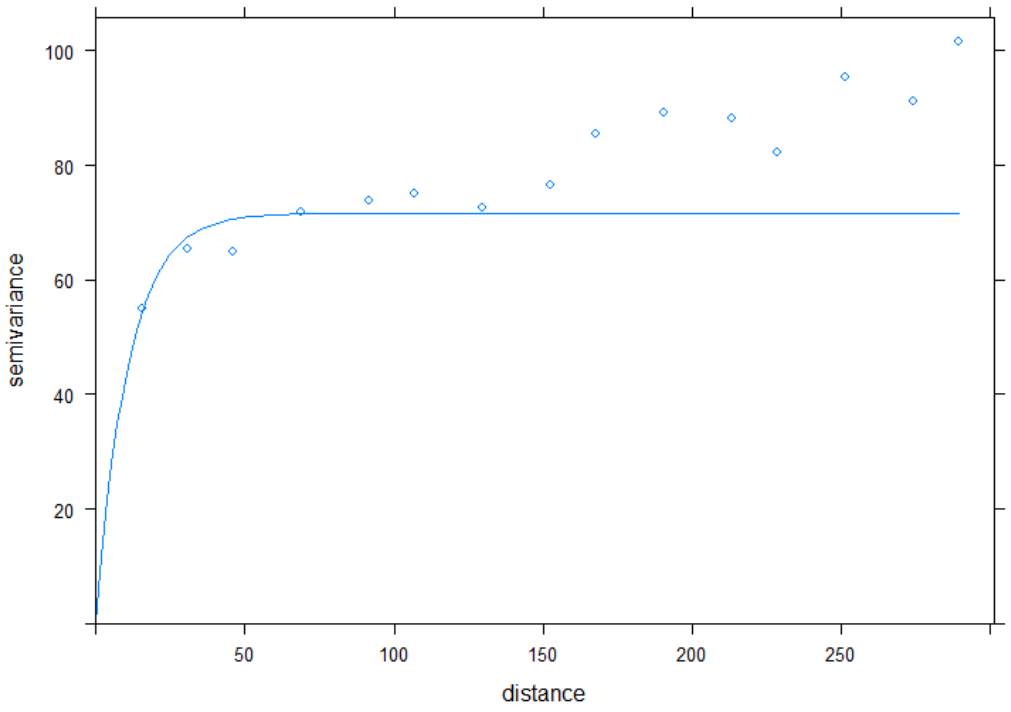

Figure B.70. Omnidirectional semivariogram of $E_{LWD\text{-}Z3}$ for MI I-94 TS3

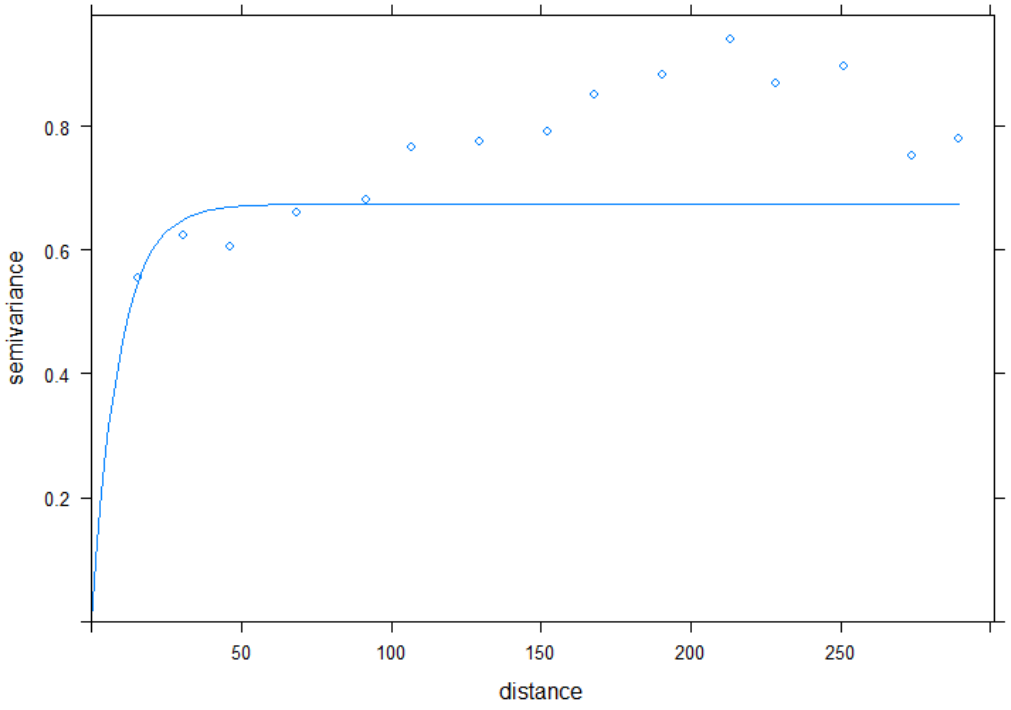

Figure B.71. Omnidirectional semivariogram of γ_d for MI I-94 TS3

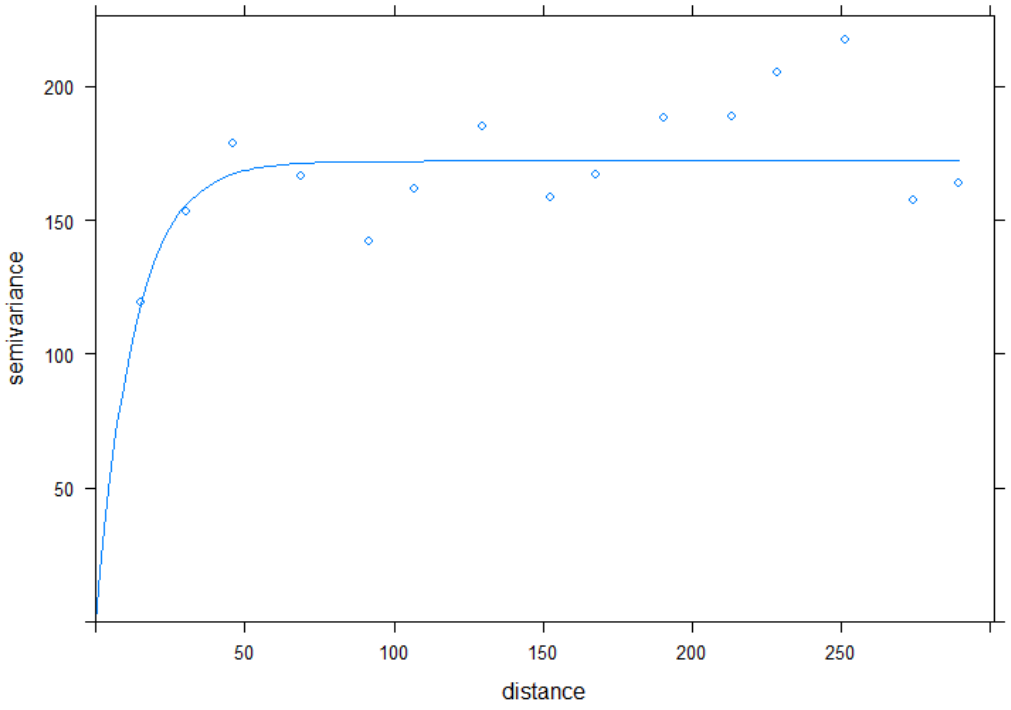

Figure B.72. Omnidirectional semivariogram of $E_{FWD\text{-}K3}$ for MI I-94 TS3

LWD Moduli (MPa)

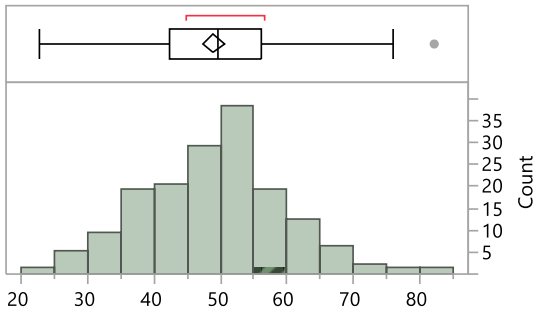

Quantiles		
100.0%	maximum	82.258065
99.5%		82.258065
97.5%		70.308692
90.0%		61.445783
75.0%	quartile	56.043956
50.0%	median	49.63533
25.0%	quartile	42.323651
10.0%		35.161082
2.5%		26.806391
0.5%		22.666667
0.0%	minimum	22.666667

Summary Statistics	
Mean	48.972388
Std Dev	10.477248
Std Err Mean	0.8231703
Upper 95% Mean	50.597992
Lower 95% Mean	47.346785
N	162
Variance	109.77272
Skewness	0.0576545
CV	21.394194
Median	49.63533

FWD Moduli (MPa)

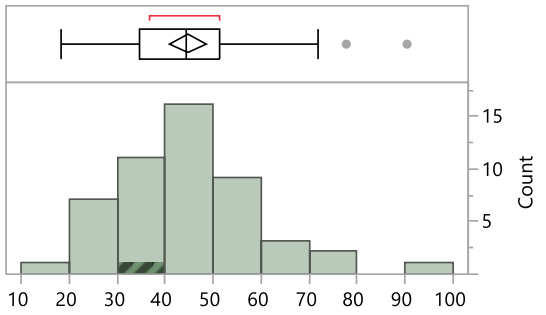

Quantiles		
100.0%	maximum	90.5216
99.5%		90.5216
97.5%		87.0305025
90.0%		61.61655
75.0%	quartile	51.3993
50.0%	median	44.38595
25.0%	quartile	34.427375
10.0%		27.79096
2.5%		19.73651
0.5%		18.2998
0.0%	minimum	18.2998

Summary Statistics	
Mean	44.709258
Std Dev	13.964046
Std Err Mean	1.9748143
Upper 95% Mean	48.677796
Lower 95% Mean	40.74072
N	50
Variance	194.99457
Skewness	0.8295161
CV	31.233007
Median	44.38595

Figure B.73. Univariate statistics summary of $E_{LWD\text{-}Z3}$ and $E_{FWD\text{-}K3}$ for MI I-94 TS3 (JMP)

rd(kN/m3)

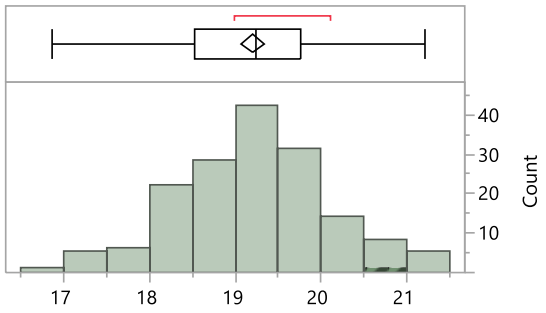

Quantiles		
100.0%	maximum	21.22076825
99.5%		21.22076825
97.5%		21.156760381
90.0%		20.316018987
75.0%	quartile	19.75997517
50.0%	median	19.249482965
25.0%	quartile	18.53479388
10.0%		18.104409683
2.5%		17.292334397
0.5%		16.85409647
0.0%	minimum	16.85409647

Summary Statistics	
Mean	19.205172
Std Dev	0.8771149
Std Err Mean	0.0689127
Upper 95% Mean	19.341262
Lower 95% Mean	19.069083
N	162
Variance	0.7693305
Skewness	-0.023743
CV	4.5670764
Median	19.249483

w%

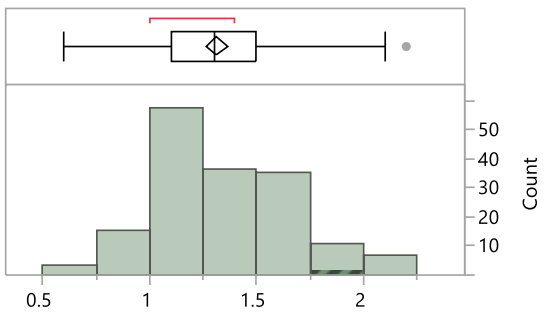

Quantiles		
100.0%	maximum	2.2
99.5%		2.2
97.5%		2.1
90.0%		1.77
75.0%	quartile	1.5
50.0%	median	1.3
25.0%	quartile	1.1
10.0%		0.9
2.5%		0.8
0.5%		0.6
0.0%	minimum	0.6

Summary Statistics	
Mean	1.3111728
Std Dev	0.323777
Std Err Mean	0.0254383
Upper 95% Mean	1.3614086
Lower 95% Mean	1.260937
N	162
Variance	0.1048315
Skewness	0.4410291
CV	24.693692
Median	1.3

Figure B.74. Univariate statistics summary of γ_d and w for MI I-94 TS3 (JMP)

DCPI base

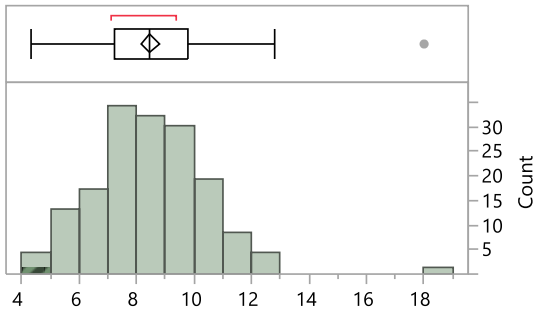

Quantiles		
100.0%	maximum	18.01471264
99.5%		18.01471264
97.5%		12.378659703
90.0%		10.783768039
75.0%	quartile	9.7914907333
50.0%	median	8.448603611
25.0%	quartile	7.2164129093
10.0%		5.8926885314
2.5%		4.8326790361
0.5%		4.309923664
0.0%	minimum	4.309923664

Summary Statistics	
Mean	8.4647156
Std Dev	1.9565762
Std Err Mean	0.1537231
Upper 95% Mean	8.7682893
Lower 95% Mean	8.1611419
N	162
Variance	3.8281903
Skewness	0.6871488
CV	23.114494
Median	8.4486036

DCPI subgrade

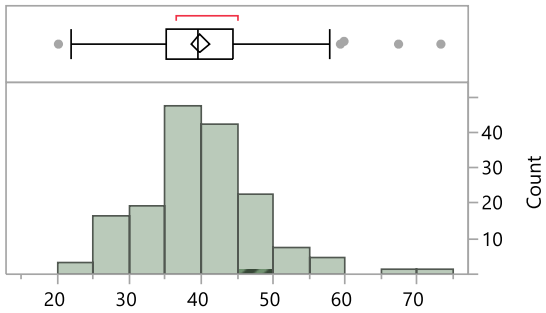

Quantiles		
100.0%	maximum	73.4
99.5%		73.4
97.5%		59.295
90.0%		48.38
75.0%	quartile	44.45
50.0%	median	39.65
25.0%	quartile	35.1
10.0%		29.26
2.5%		25.5075
0.5%		20.1
0.0%	minimum	20.1

Summary Statistics	
Mean	39.809877
Std Dev	8.1150746
Std Err Mean	0.6375805
Upper 95% Mean	41.068976
Lower 95% Mean	38.550777
N	162
Variance	65.854436
Skewness	0.6334507
CV	20.384576
Median	39.65

Figure B.75. Univariate statistics summary of $DCPI_{base}$ and $DCPI_{subgrade}$ for MI I-94 TS3 (JMP)

B.4. MI I-96 TS1

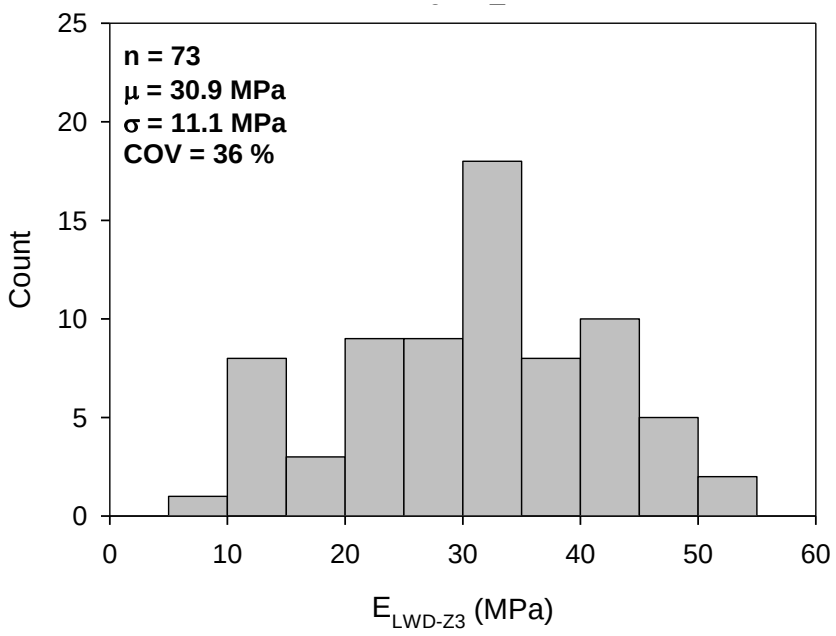

Figure B.76. Histogram of $E_{LWD\text{-}Z3}$ for MI I-96 TS1

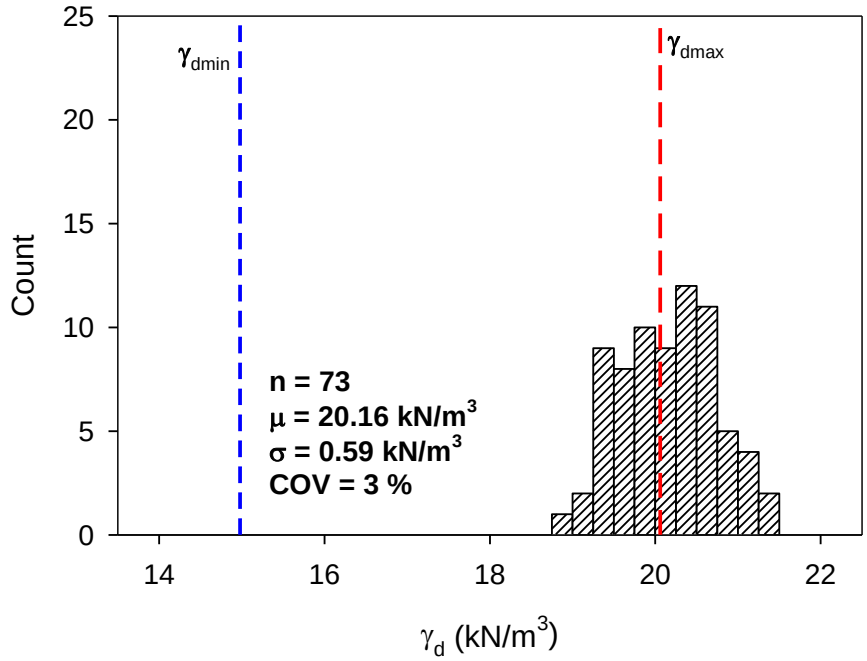

Figure B.77. Histogram of γ_d for MI I-96 TS1

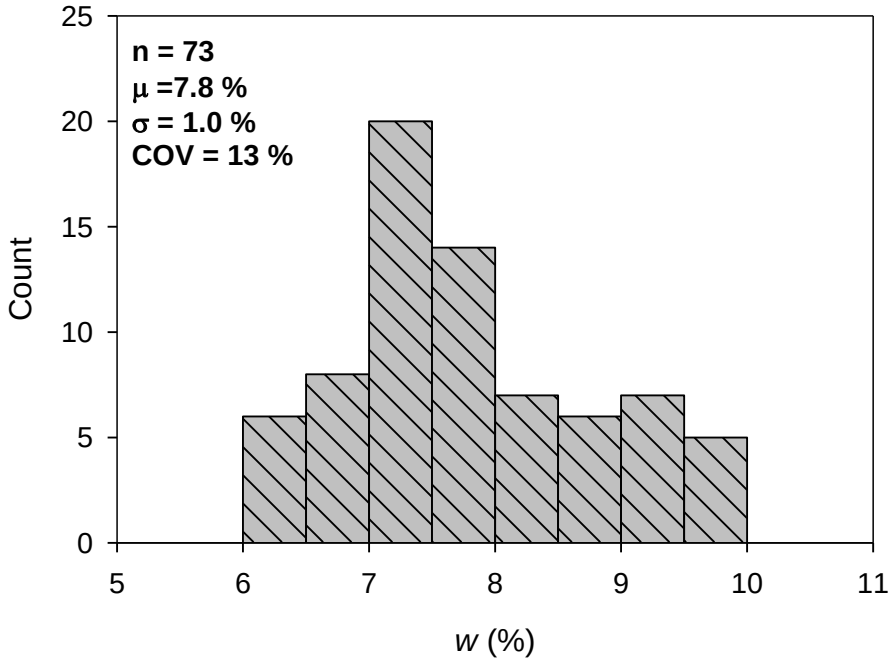

Figure B.78. Histogram of *w* for MI I-96 TS1

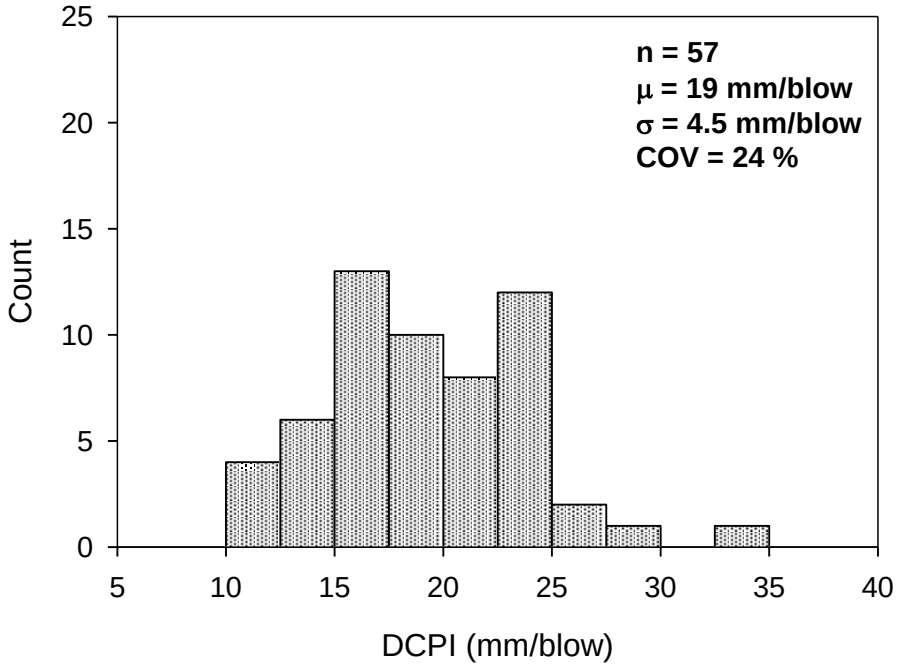

Figure B.79. Histogram of $DCPI_{subbase}$ for MI I-96 TS1

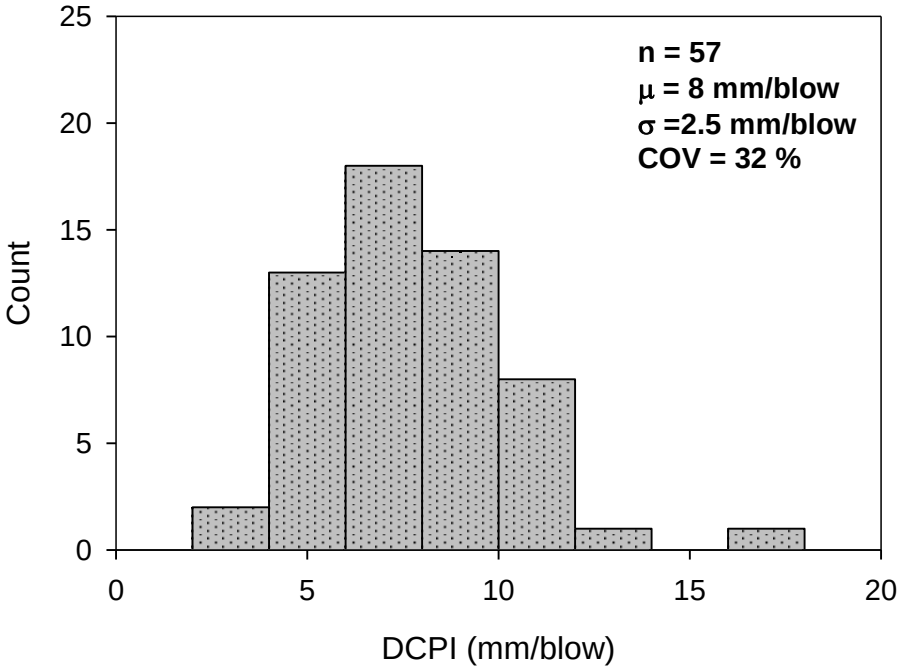

Figure B.80. Histogram of $DCPI_{subgrade}$ for MI I-96 TS1

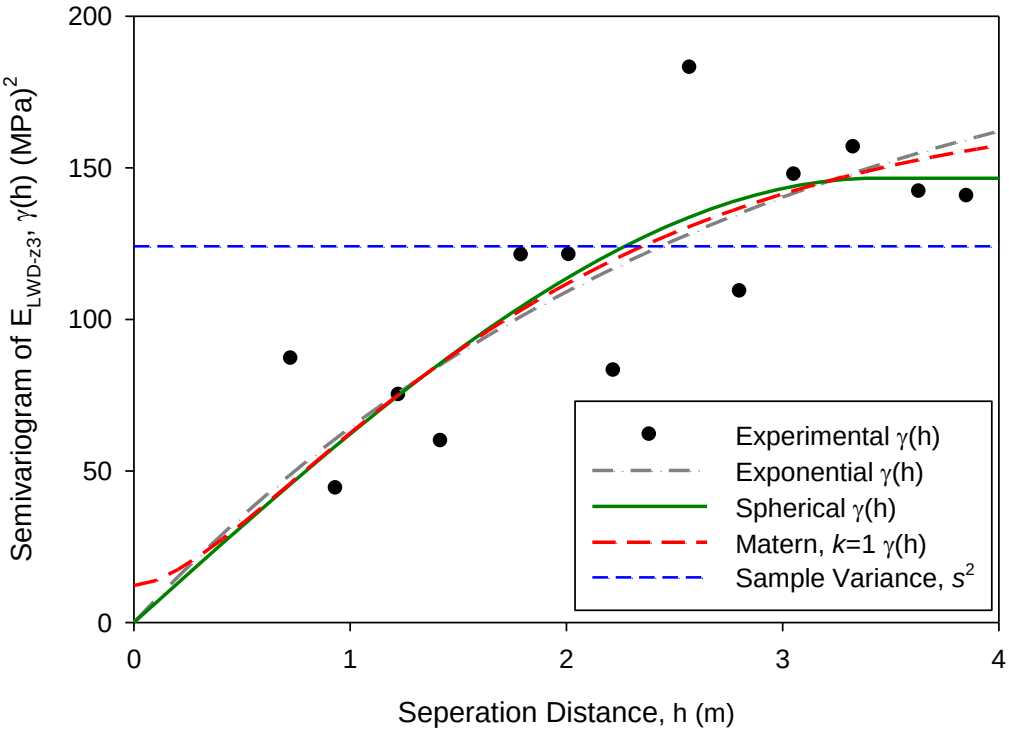

Figure B.81. Omnidirectional semivariogram of E_{LWD-Z3} for MI I-96 TS1

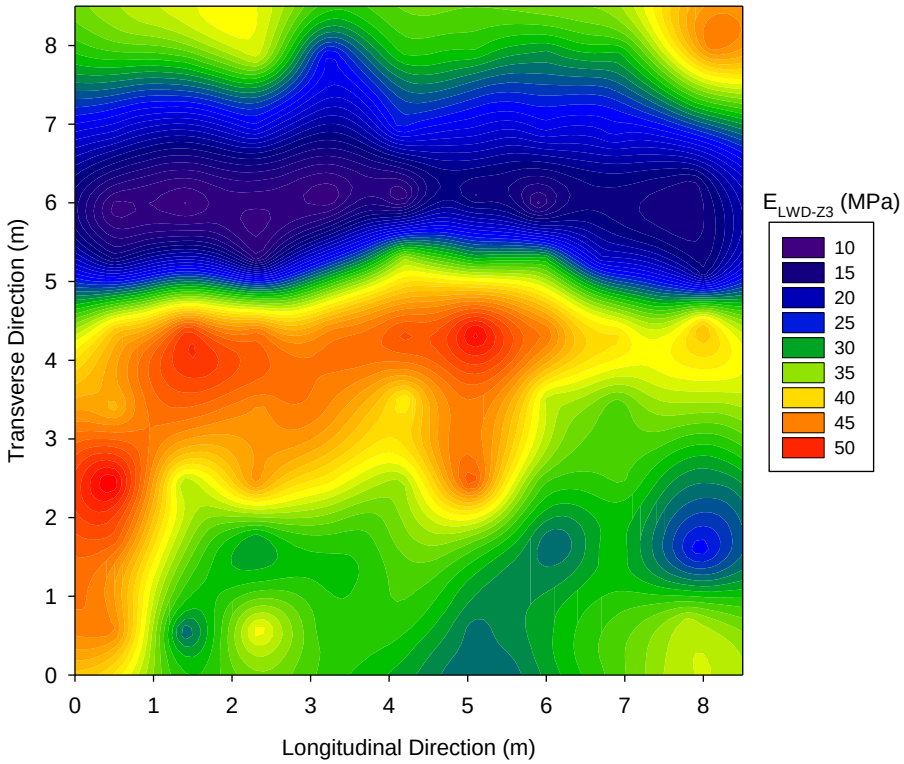

Figure B.82. Kriging contour map with spherical model of E_{LWD-Z3} for MI I-96 TS1

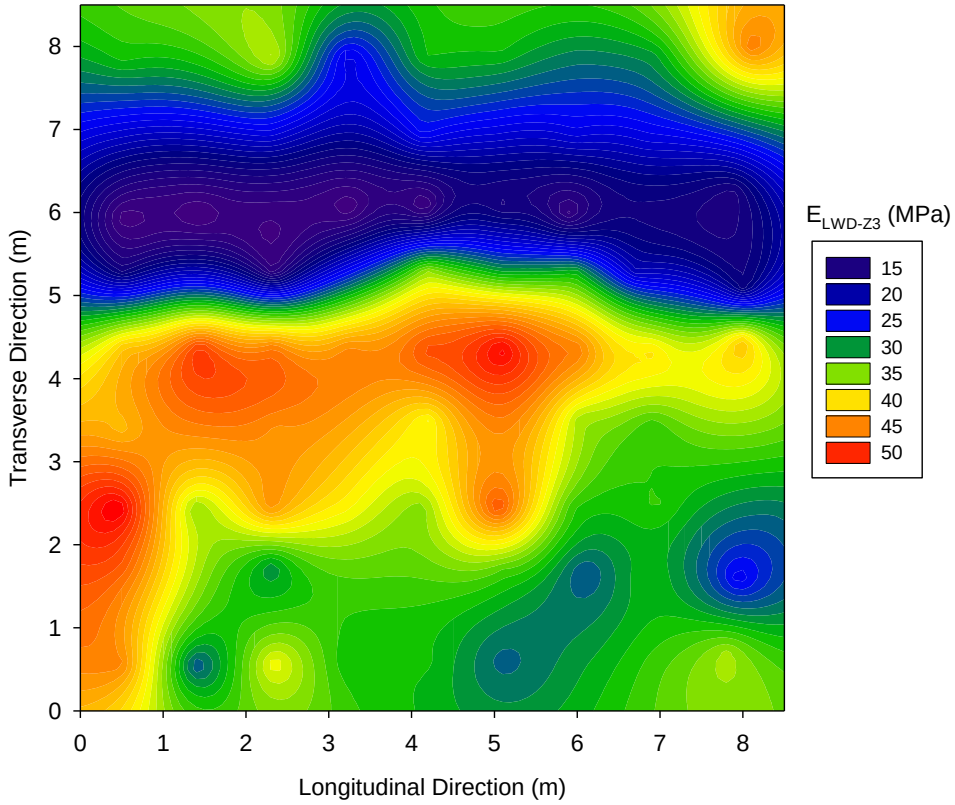

Figure B.83. Kriging contour map with exponential model of $E_{LWD\text{-}Z3}$ for MI I-96 TS1

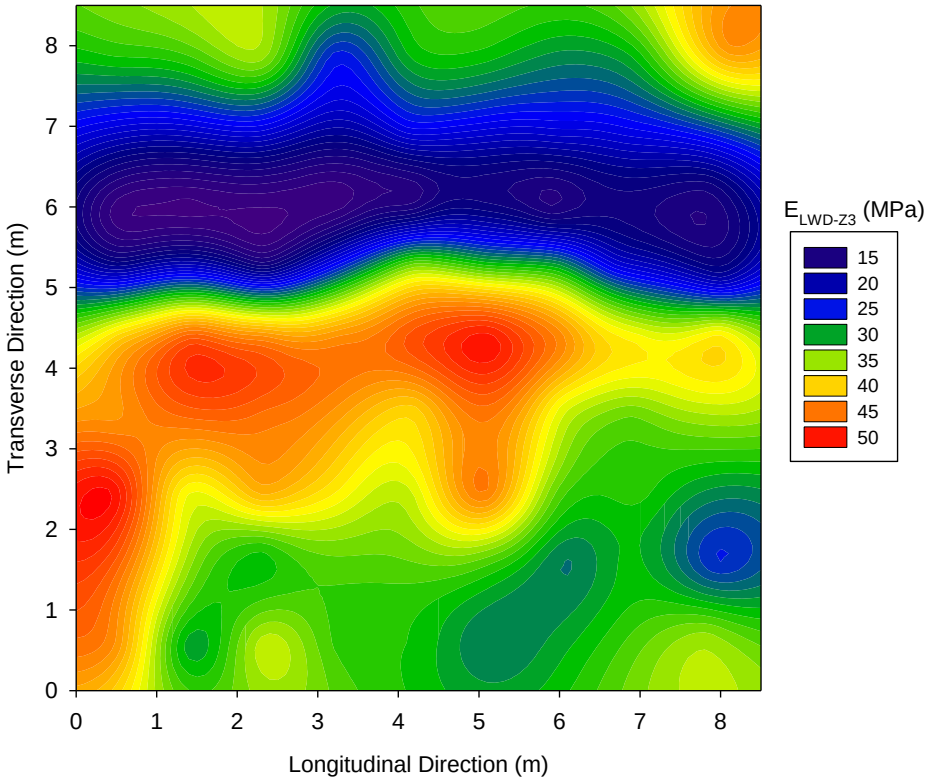

Figure B.84. Kriging contour map with Matérn (k=1) model of $E_{LWD\text{-}Z3}$ for MI I-96 TS1

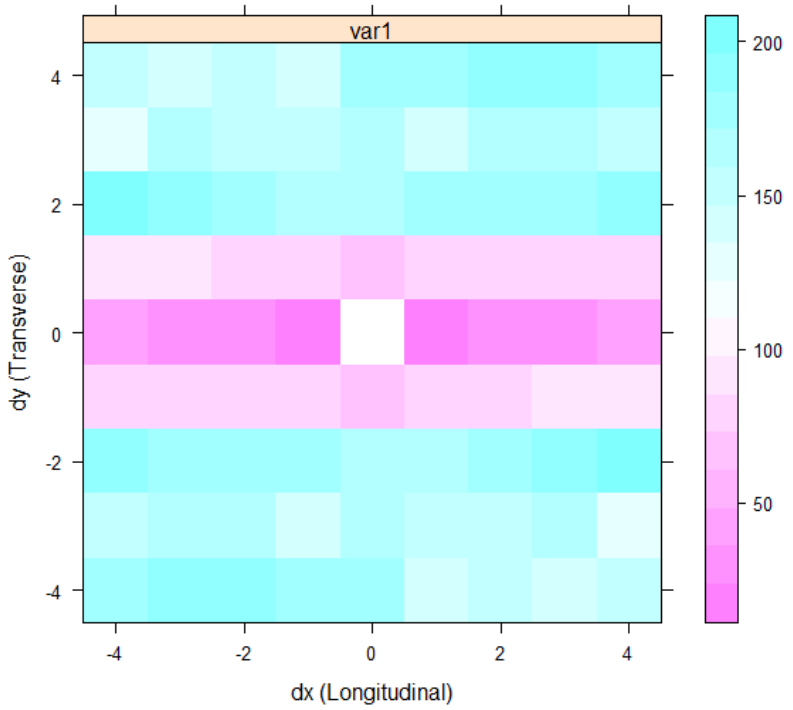

Figure B.85. Semivariogram map of $E_{LWD\text{-}Z3}$ for MI I-96 TS1

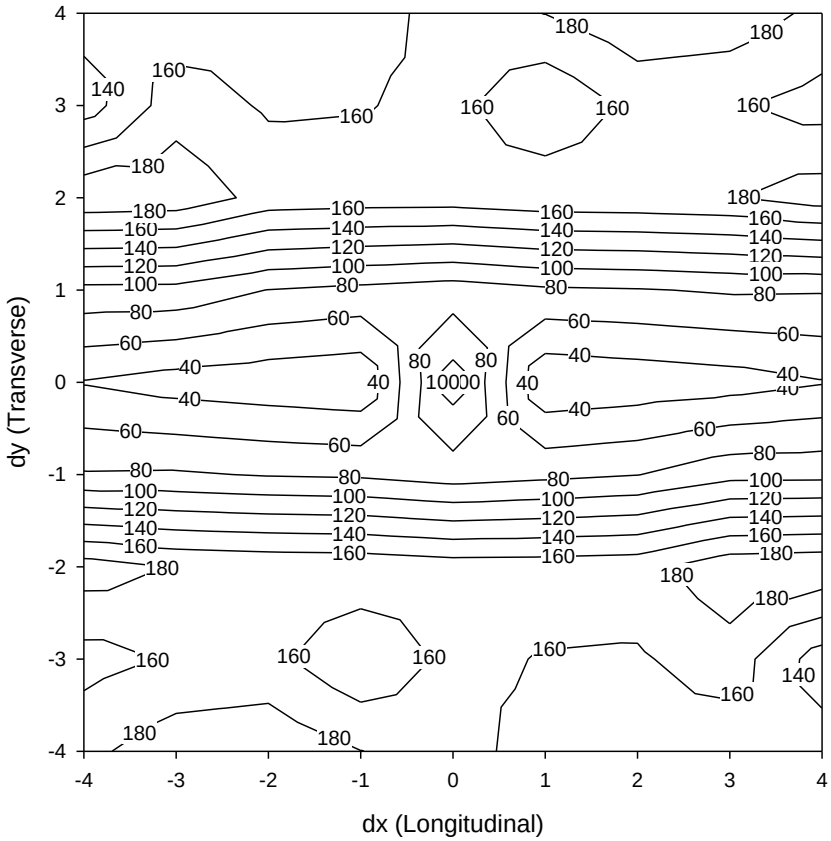

Figure B.86. Semivariogram contour plot of $E_{LWD\text{-}Z3}$ for MI I-96 TS1

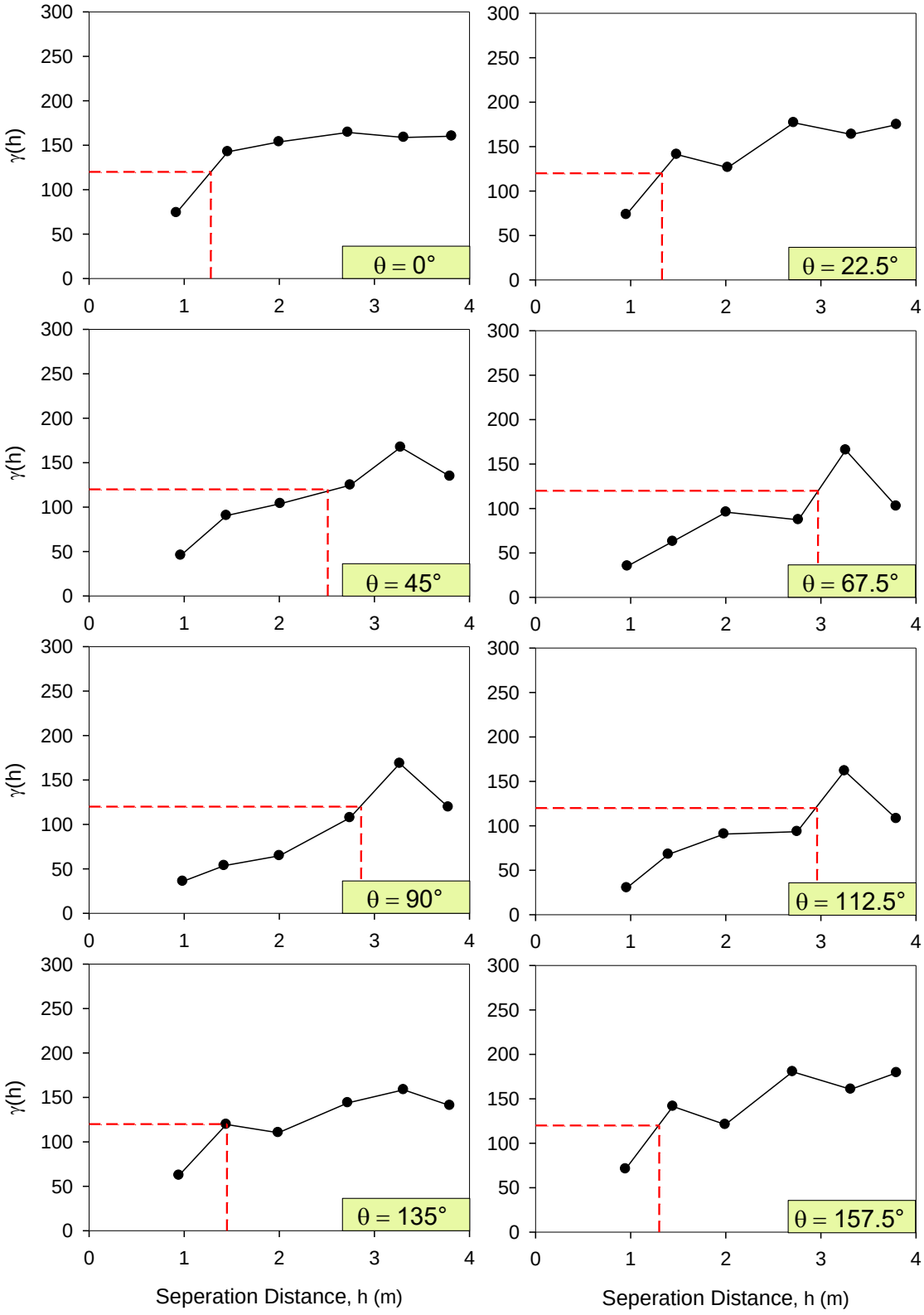

Figure B.87. Multiple directional semivariogram of $E_{LWD\text{-}Z3}$ for MI I-96 TS1

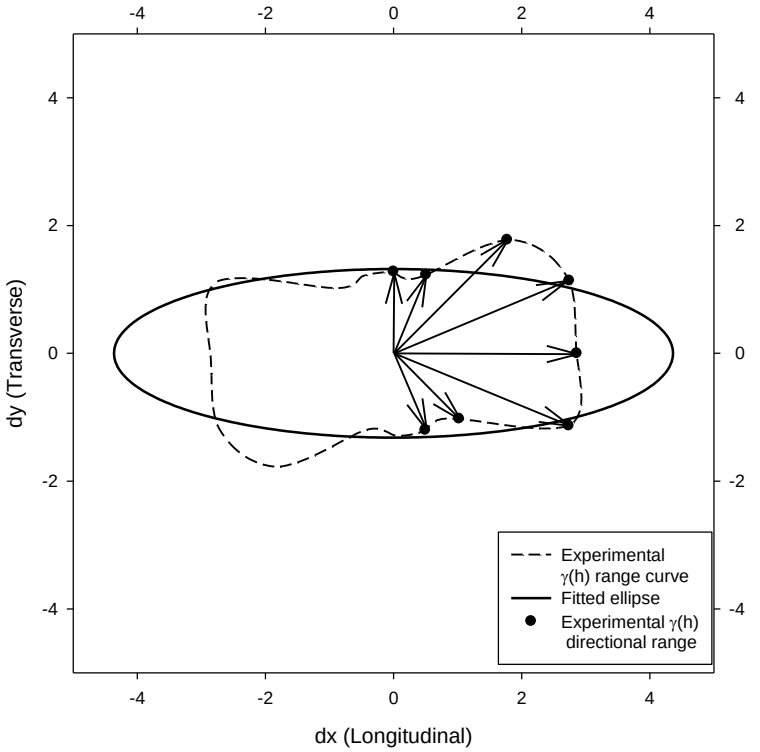

Figure B.88. Rose diagram of directional range values of $E_{LWD\text{-}Z3}$ for MI I-96 TS1

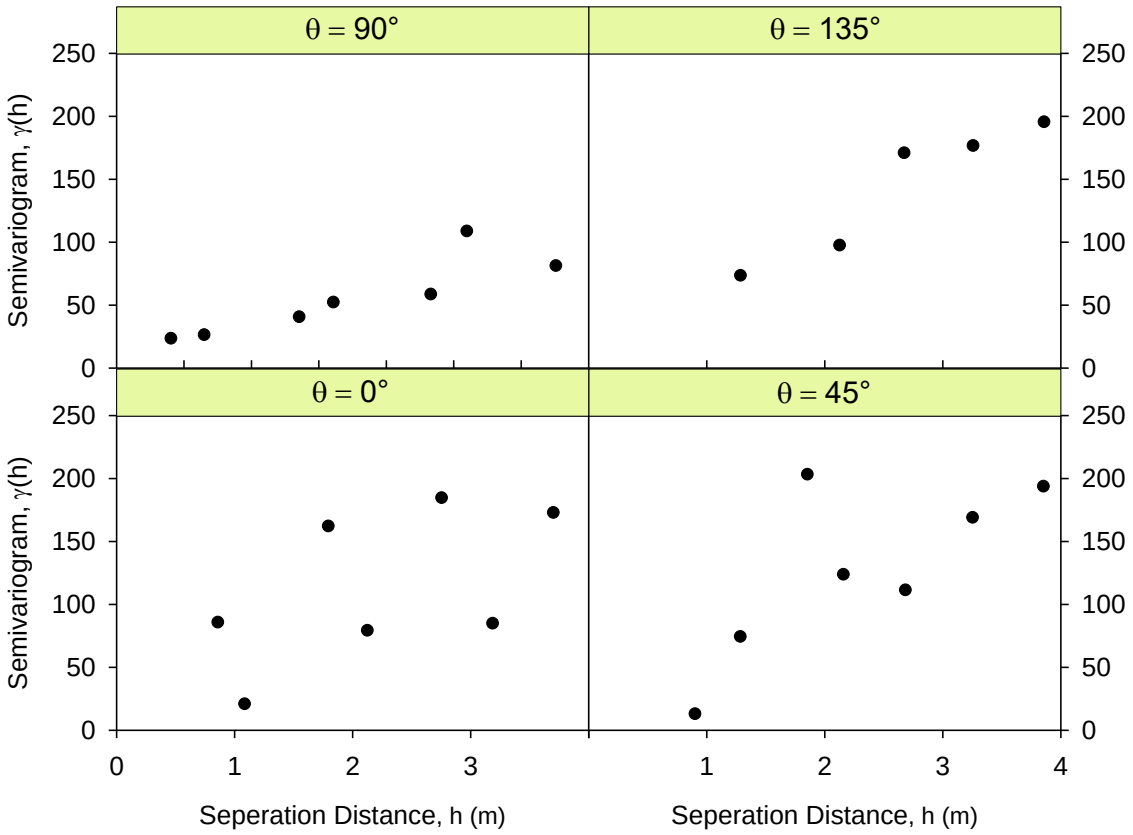

Figure B.89. Directional semivariogram of $E_{LWD\text{-}Z3}$ for MI I-96 TS1

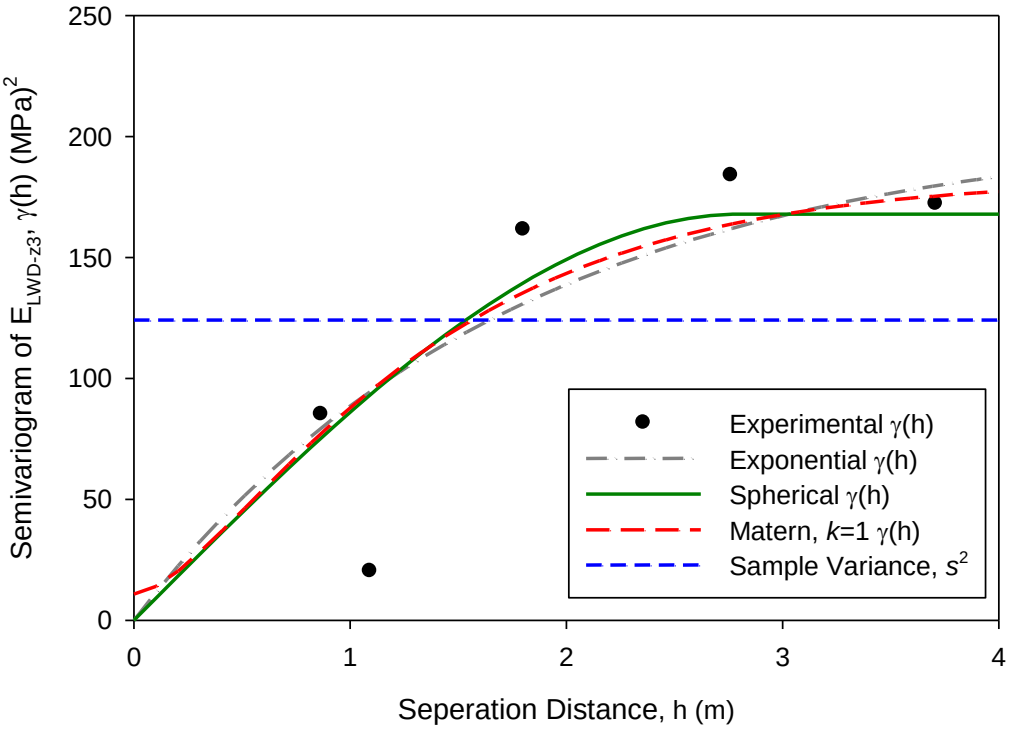

Figure B.90. Transverse direction semivariogram with model fitted of E_{LWD-Z3} for MI I-96 TS1

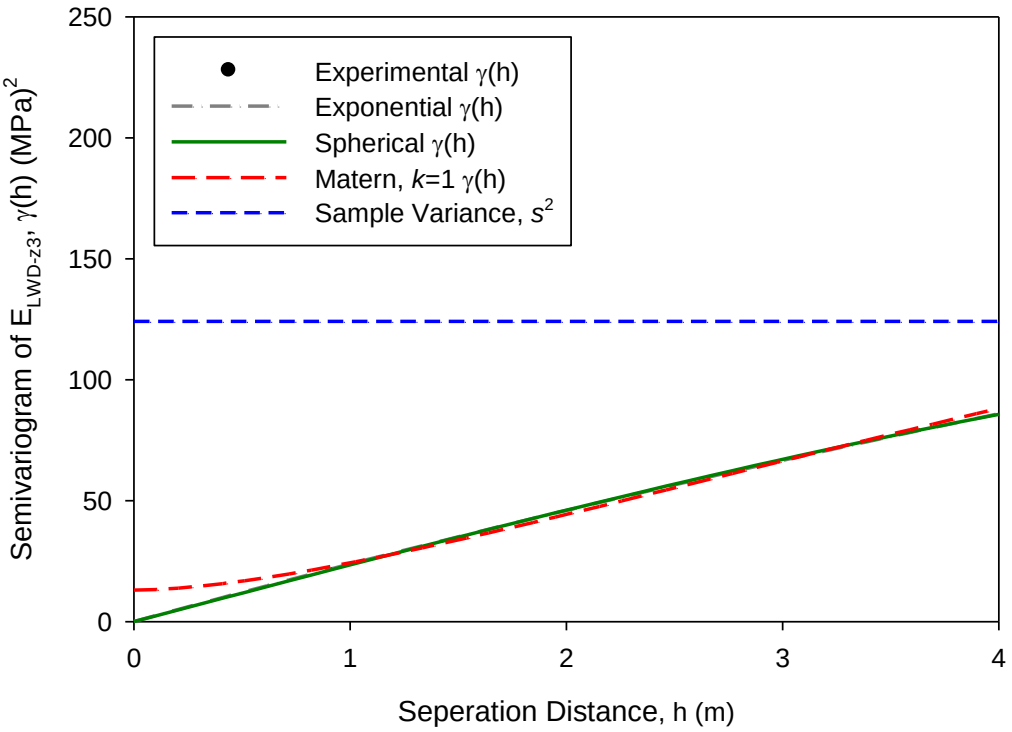

Figure B.91. Longitudinal direction semivariogram with model fitted of E_{LWD-Z3} for MI I-96 TS1

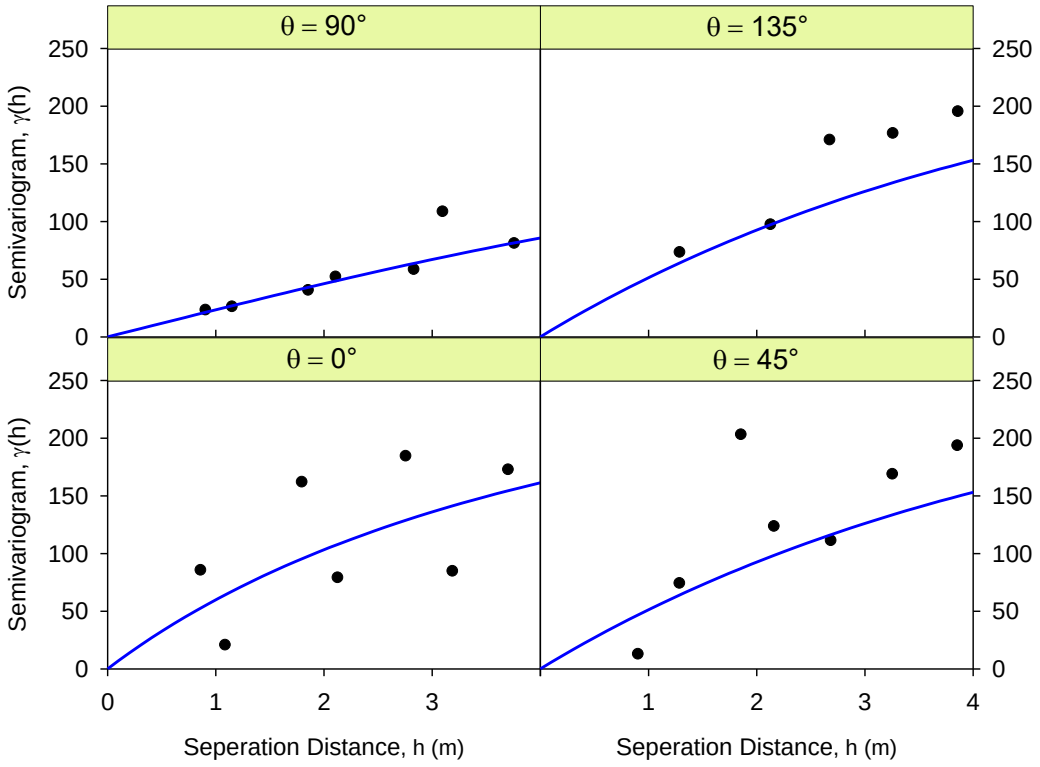

Figure B.92. Fitting semivariogram with zonal anisotropy of $E_{LWD\text{-}Z3}$ for MI I-96 TS1

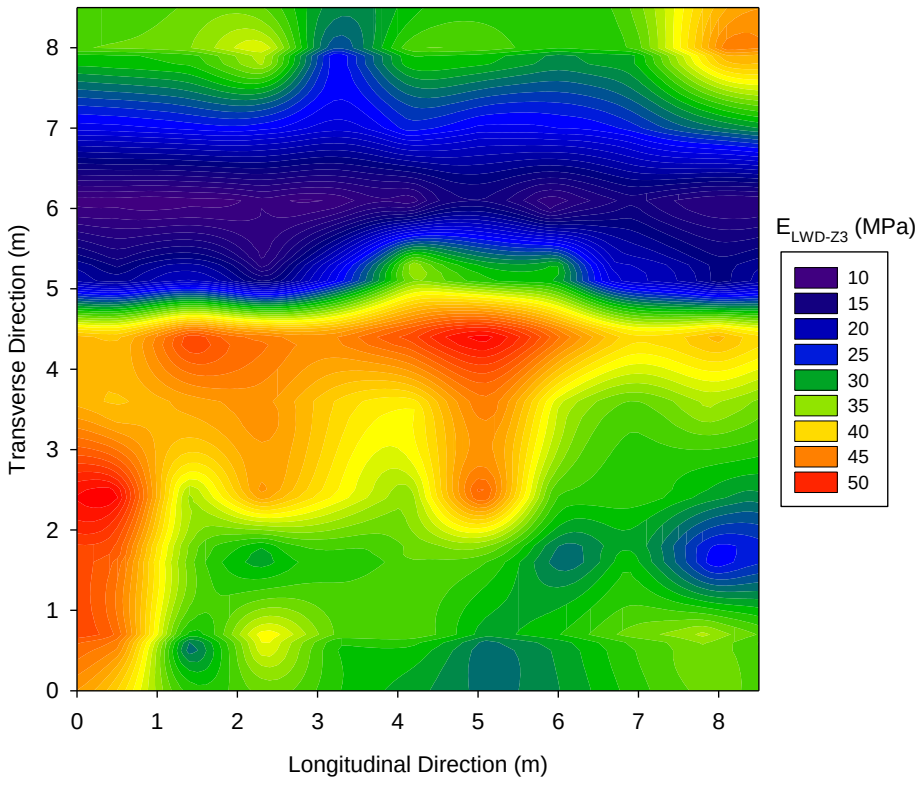

Figure B.93. Kriging contour plot with model considered zonal anisotropy of $E_{LWD\text{-}Z3}$ for MI I-96 TS1

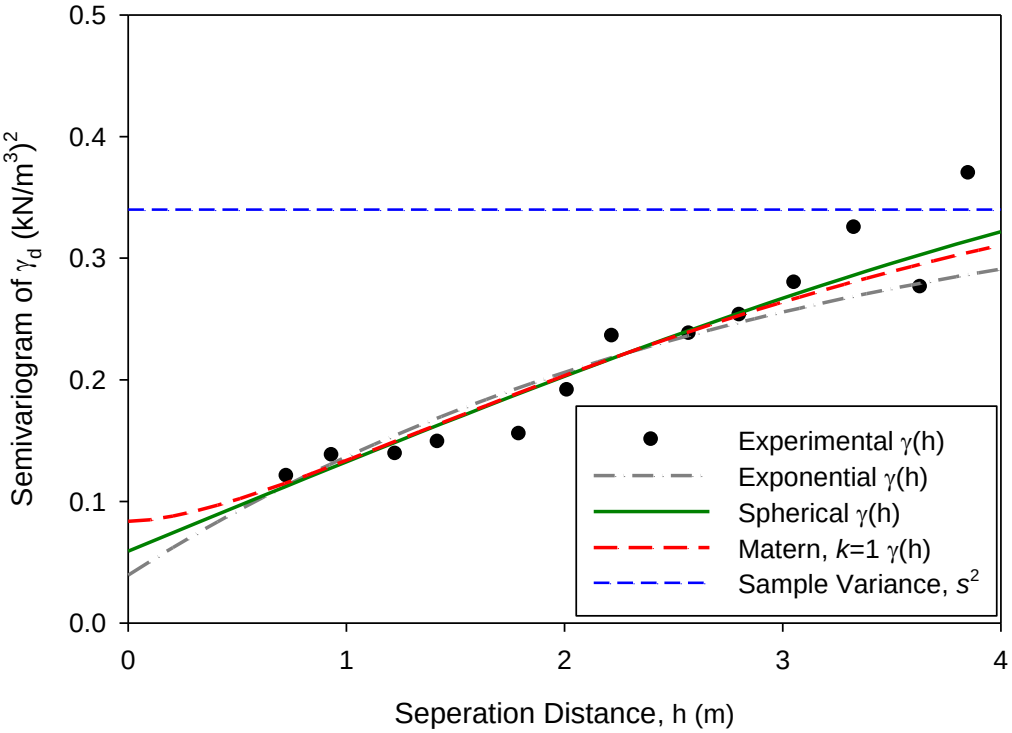

Figure B.94. Omnidirectional semivariogram with fitted model of γ_d for MI I-96 TS1

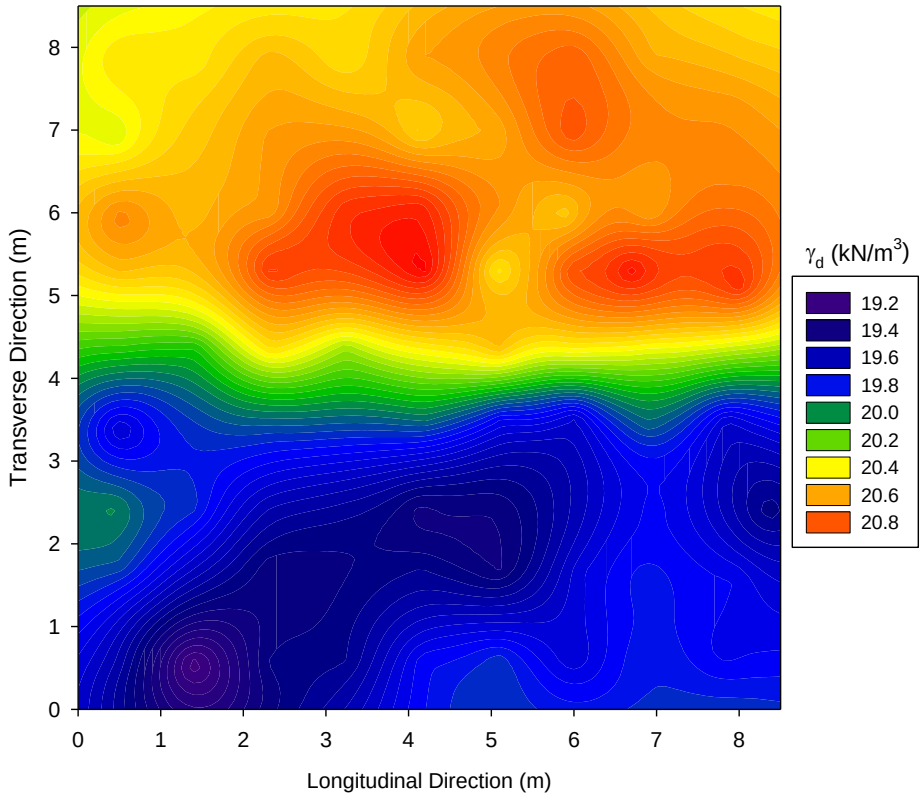

Figure B.95. Kriging contour plot with spherical model of γ_d for MI I-96 TS1

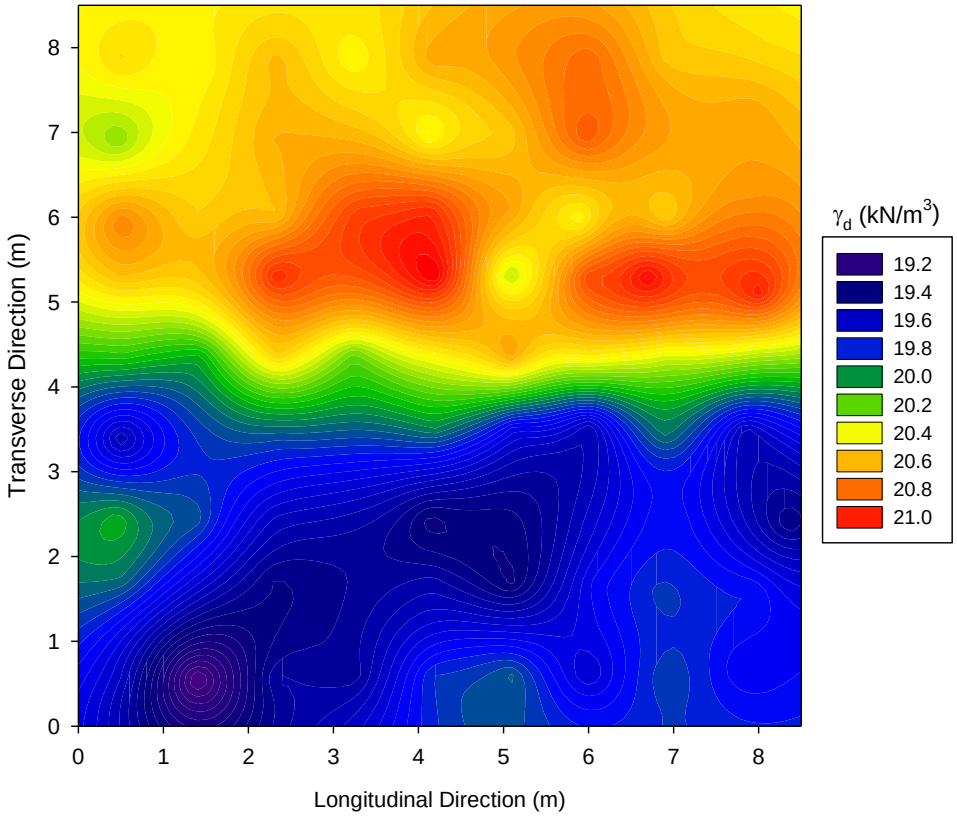

Figure B.96. Kriging contour plot with exponential model of γ_d for MI I-96 TS1

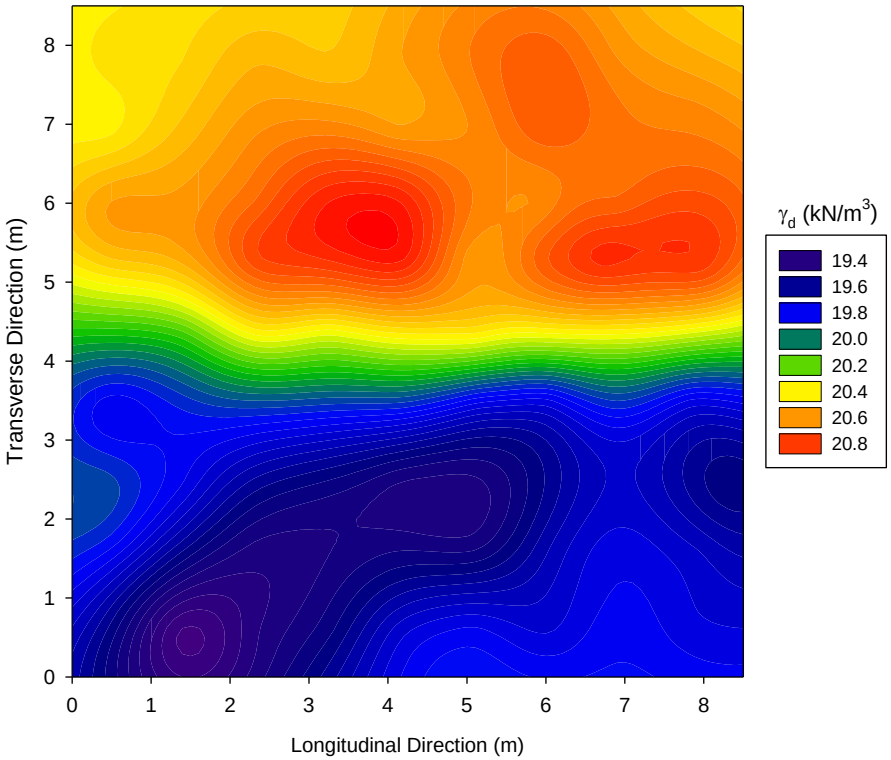

Figure B.97. Kriging contour plot with Matérn (k=1) model of γ_d for MI I-96 TS1

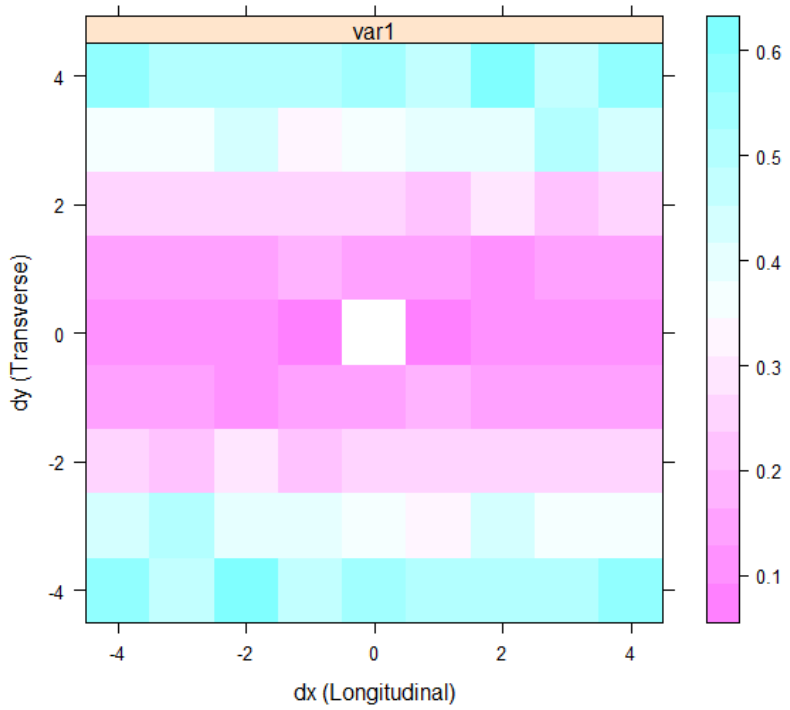

Figure B.98. Semivariogram map of γ_d for MI I-96 TS1

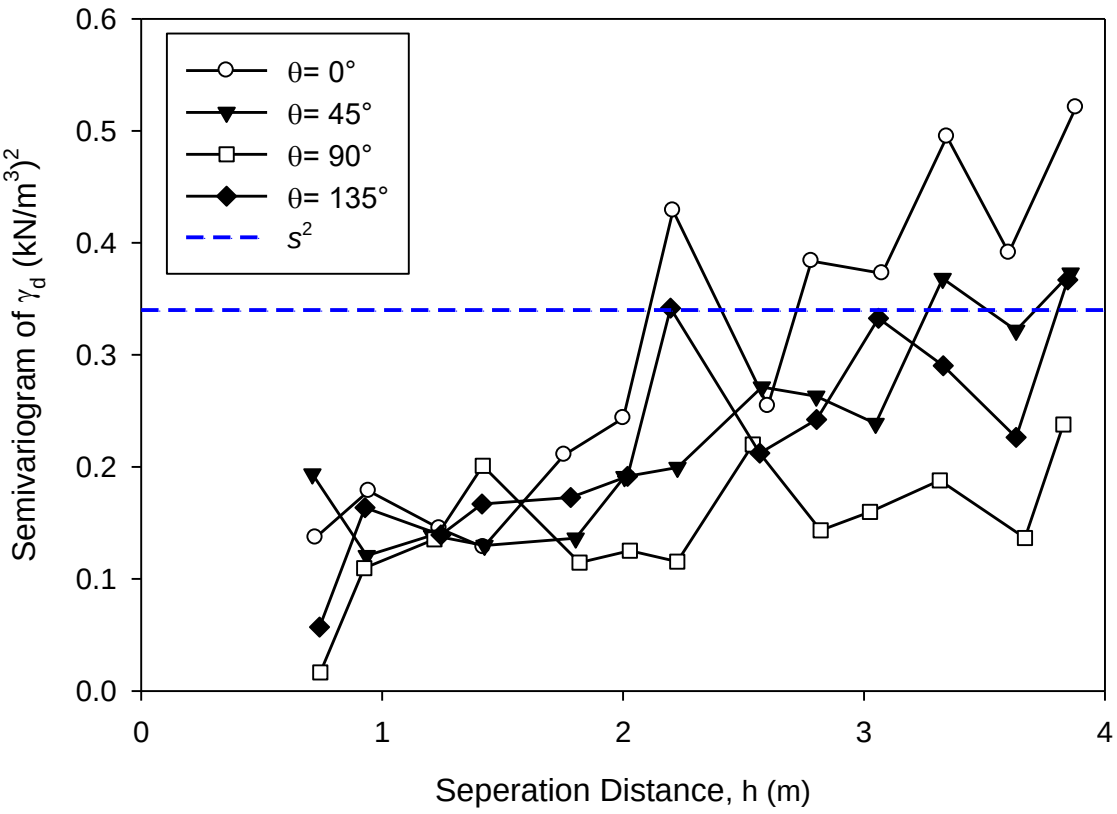

Figure B.99. Directional semivariogram of γ_d for MI I-96 TS1

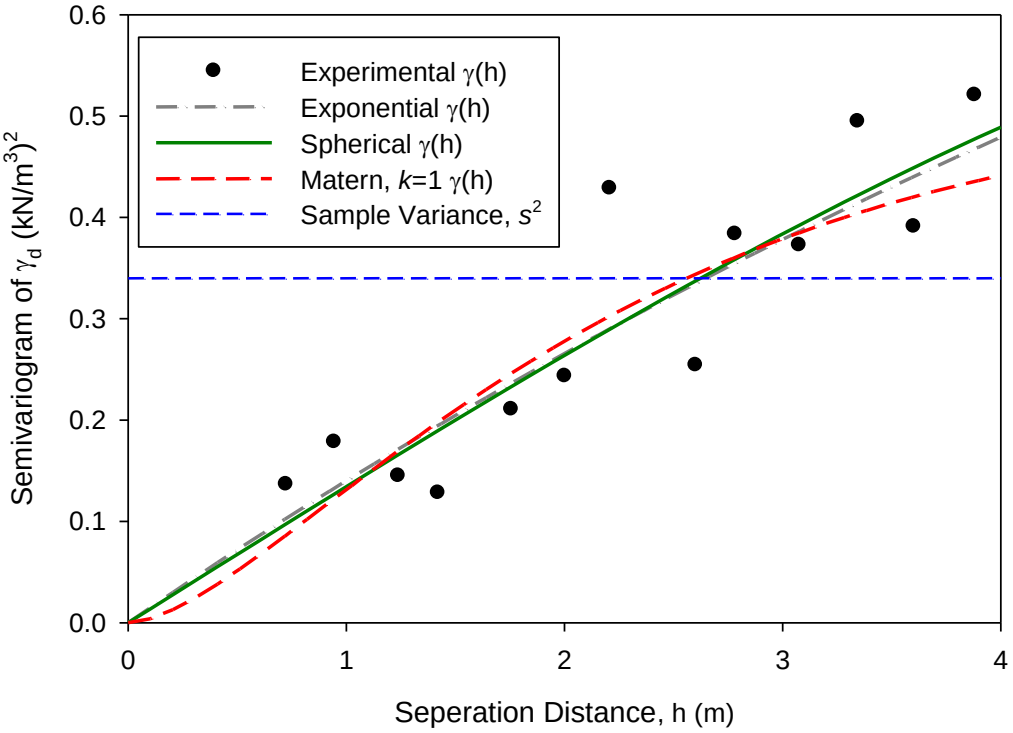

Figure B.100. Transverse direction semivariogram of γ_d for MI I-96 TS1

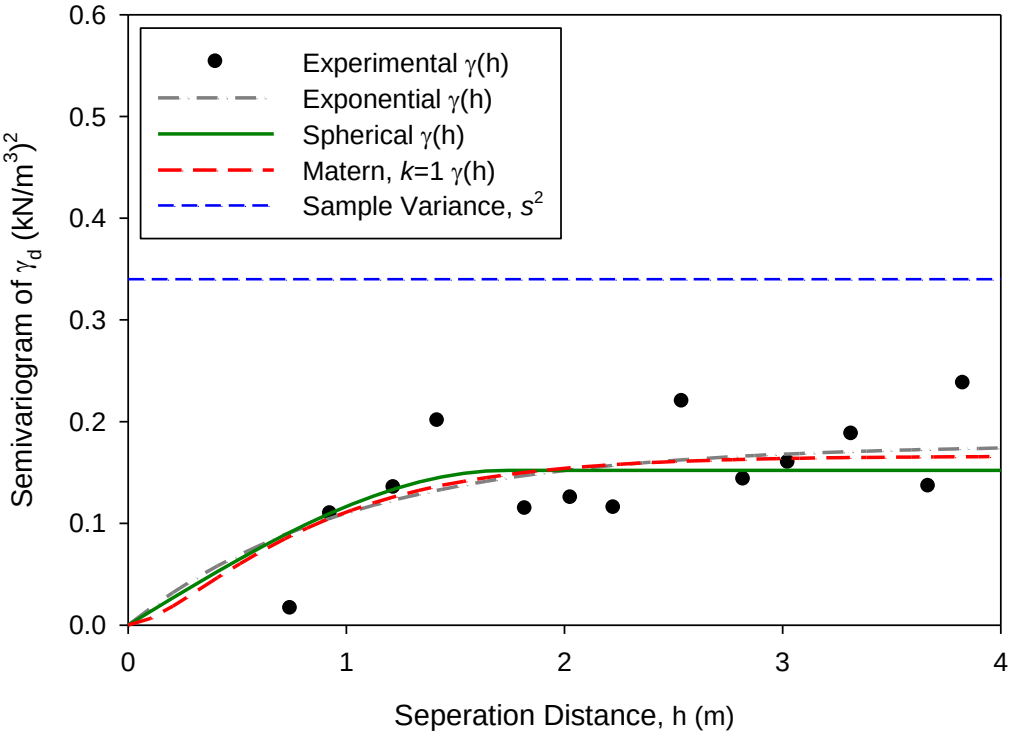

Figure B.101. Longitudinal direction semivariogram of γ_d for MI I-96 TS1

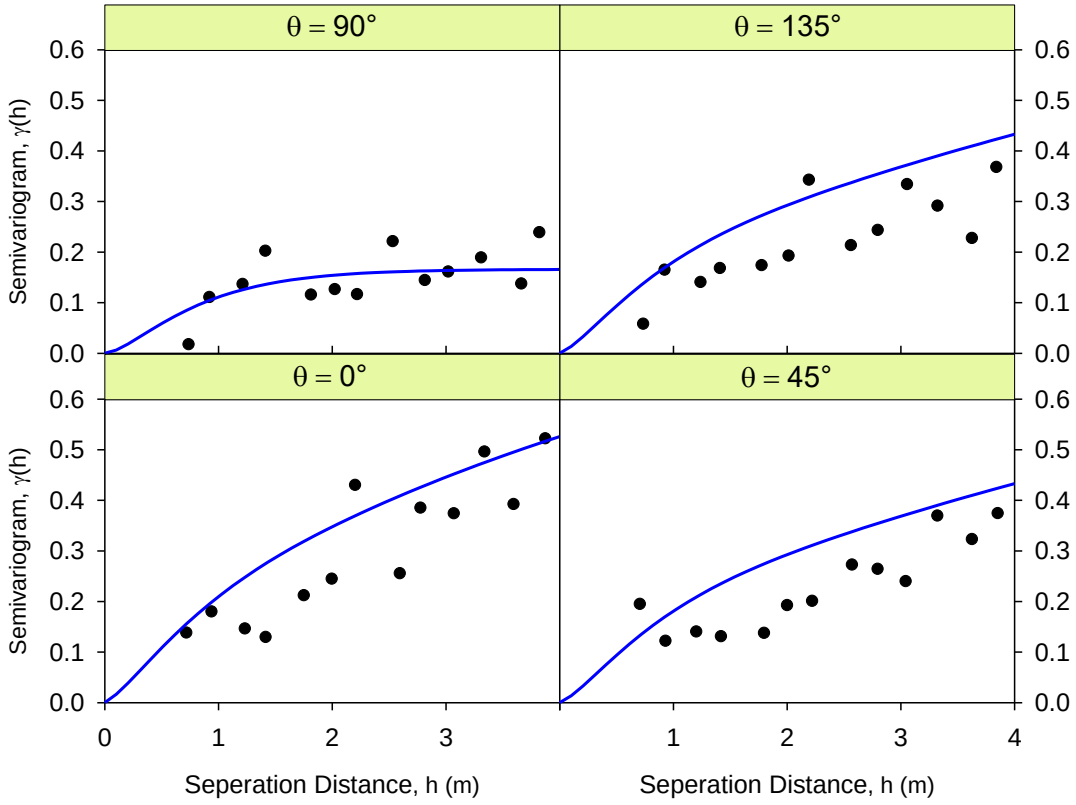

Figure B.102. Directional semivariogram with fitted zonal anisotropic model of γ_d for MI I-96 TS1

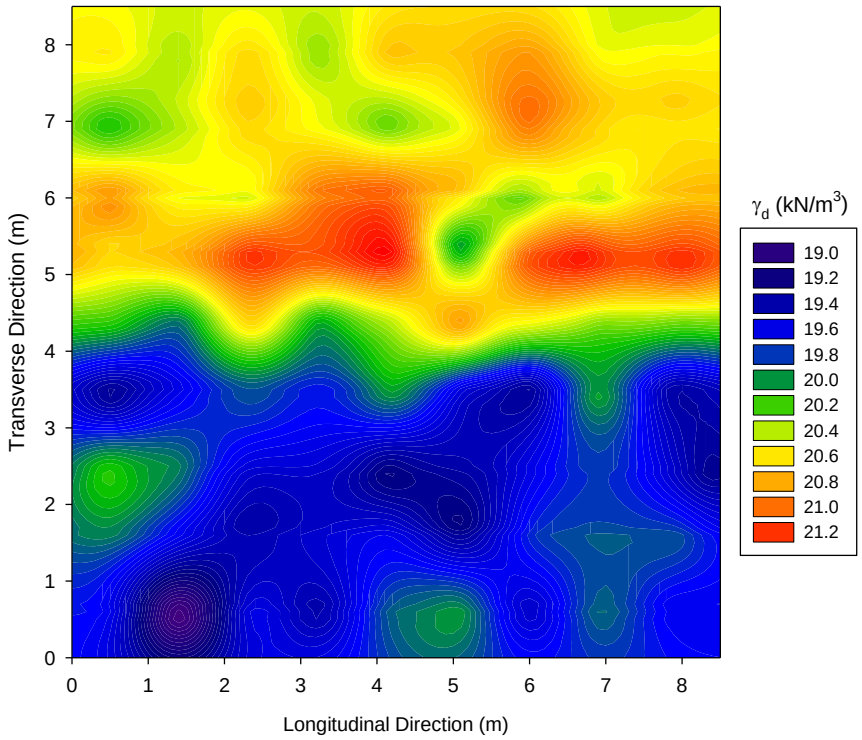

Figure B.103. Kriging contour plot with zonal anisotropic model of γ_d for MI I-96 TS1

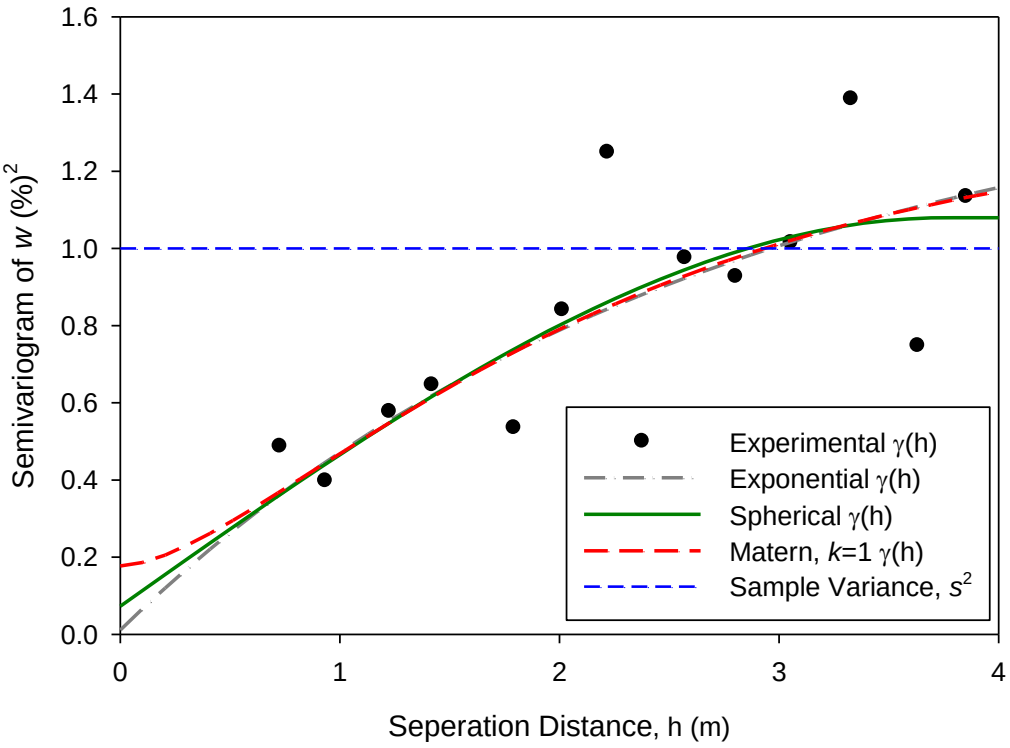

Figure B.104. Omnidirectional semivariogram with fitted model of *w* for MI I-96 TS1

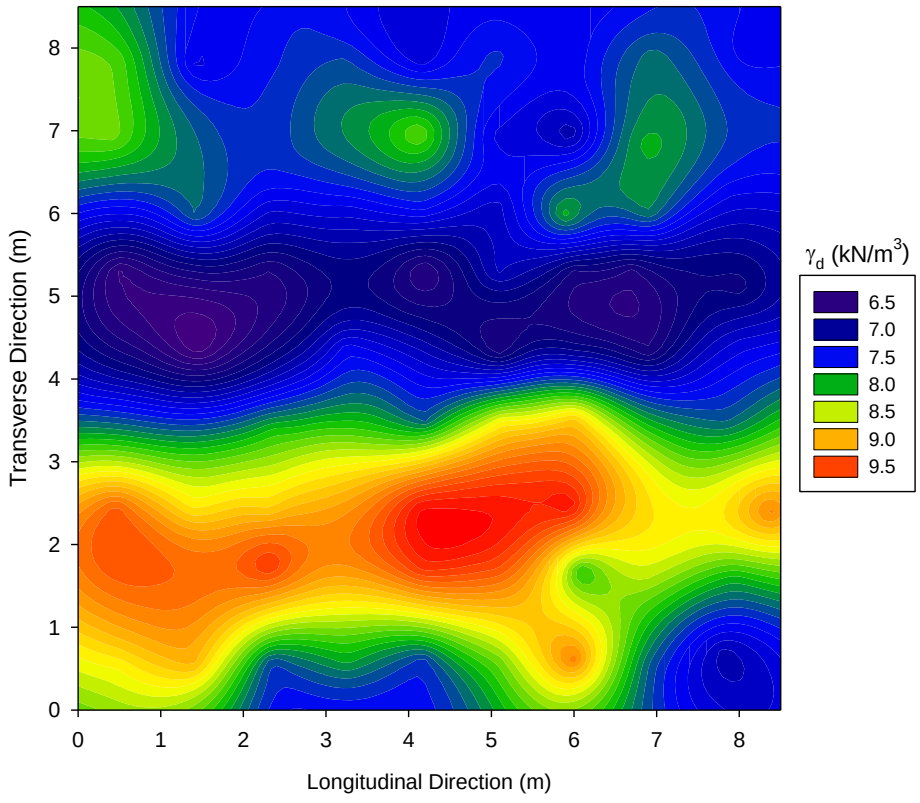

Figure B.105. Kriging contour plot with spherical model of *w* for MI I-96 TS1

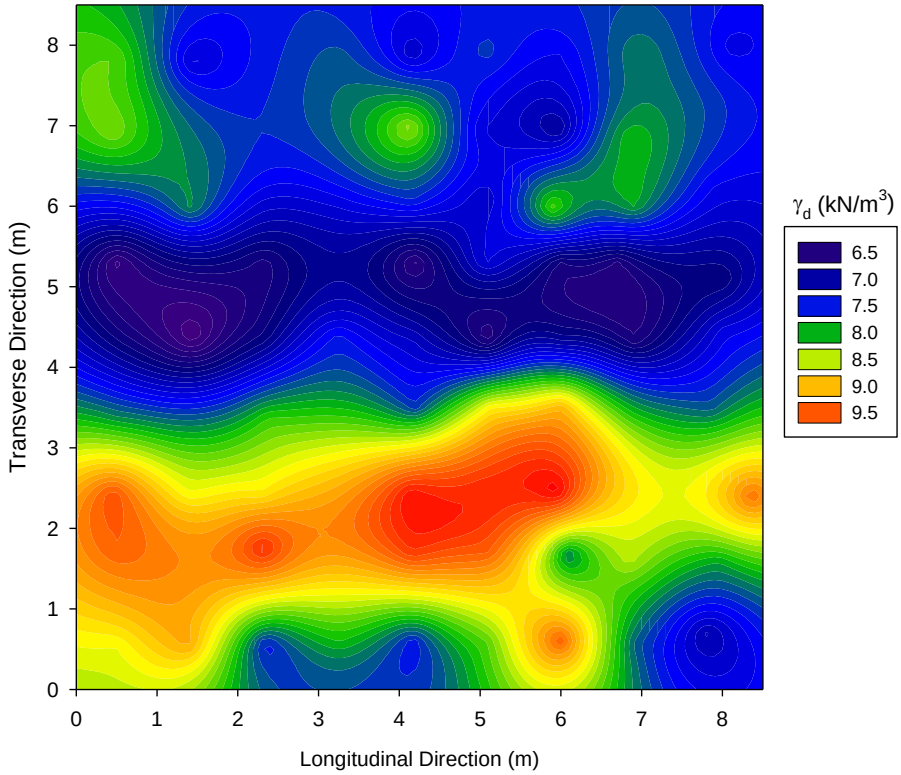

Figure B.106. Kriging contour plot with exponential model of *w* for MI I-96 TS1

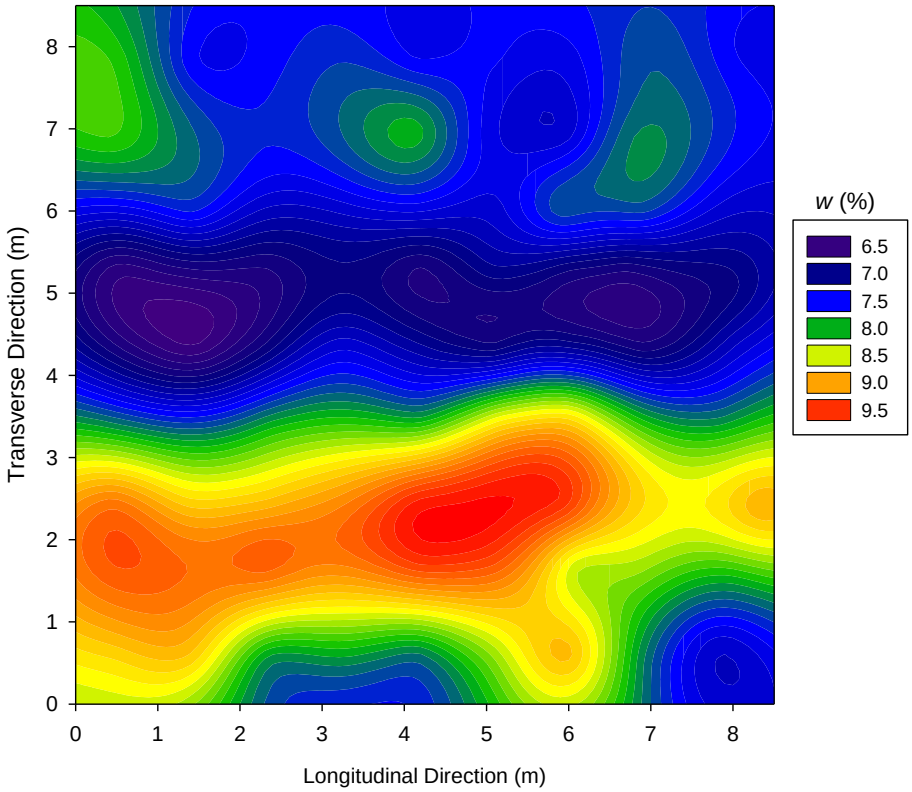

Figure B.107. Kriging contour plot with Matérn (*k*=1) model of *w* for MI I-96 TS1

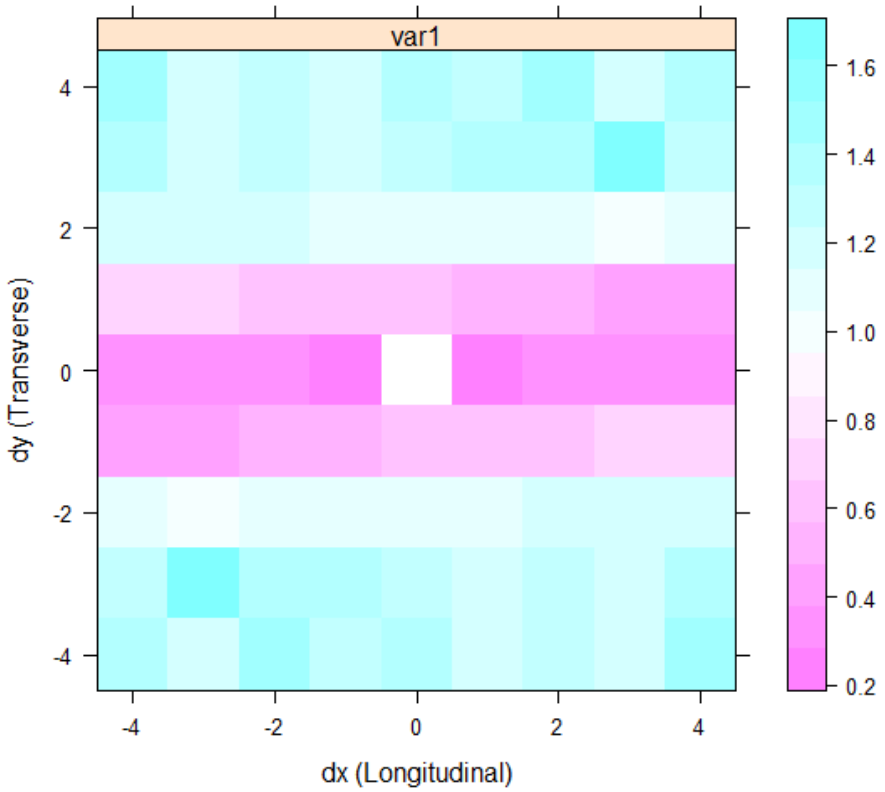

Figure B.108. Semivariogram map of *w* for MI I-96 TS1

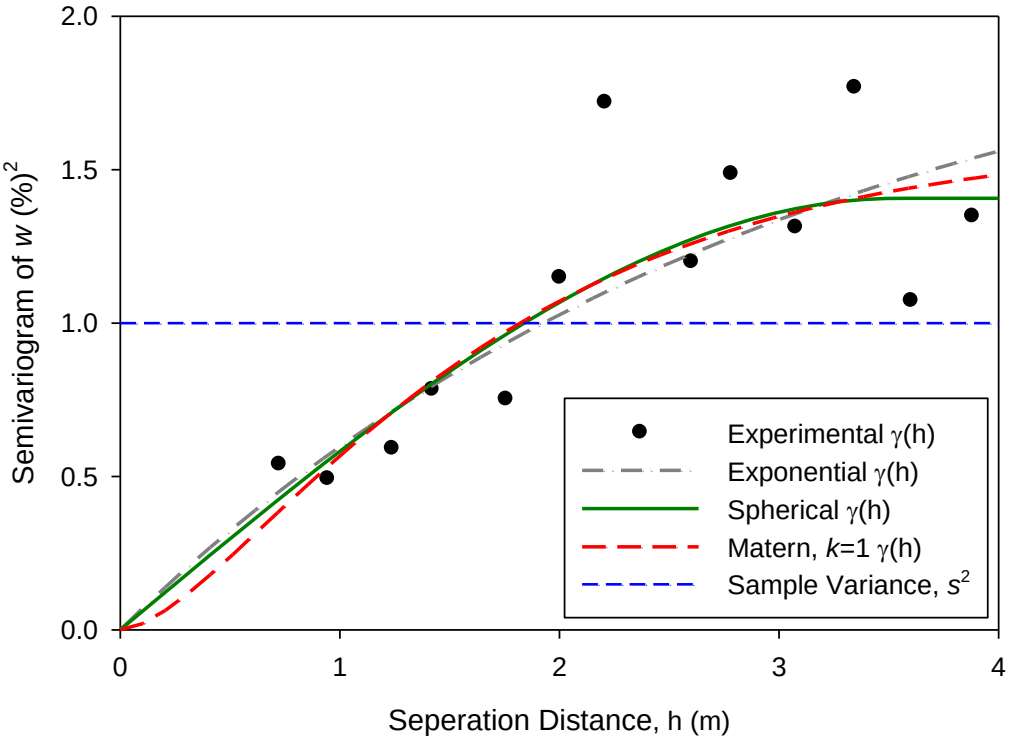

Figure B.109. Transverse direction semivariogram of *w* for MI I-96 TS1

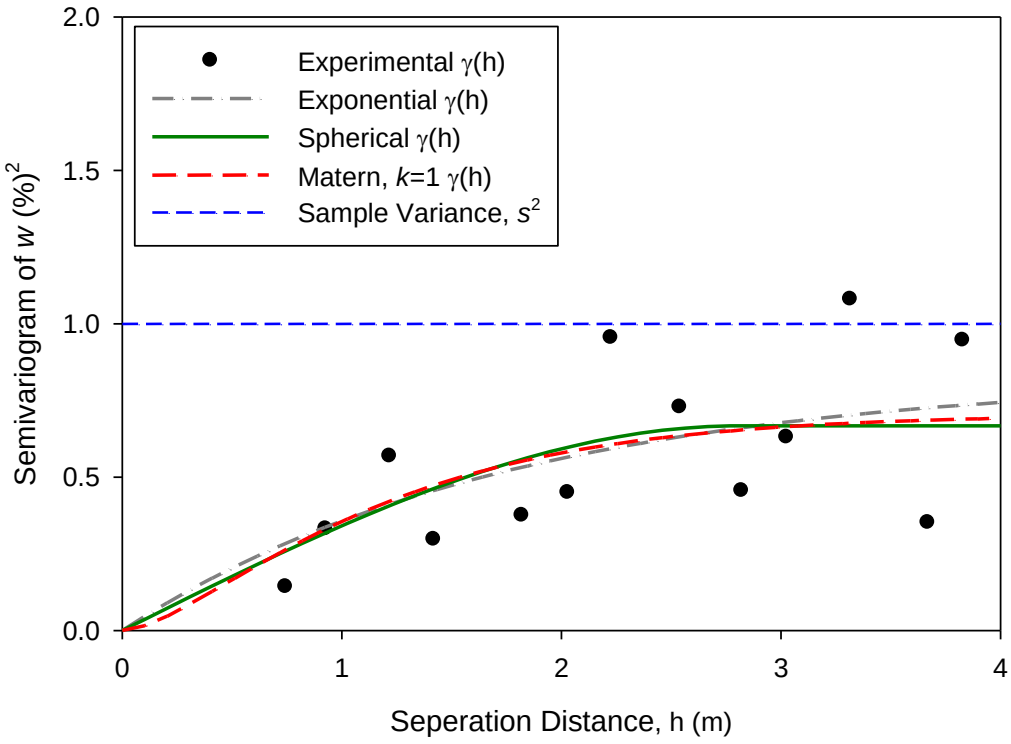

Figure B.110. Longitudinal direction semivariogram of *w* for MI I-96 TS1

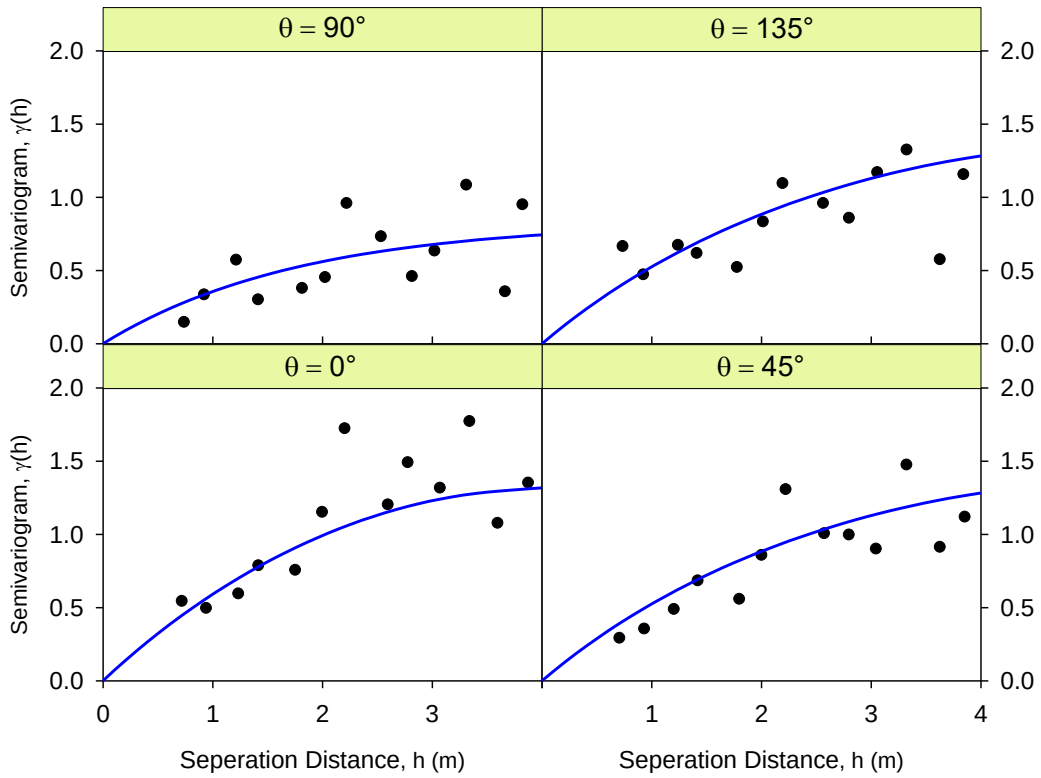

Figure B.111. Directional semivariogram with fitted zonal anisotropic model of *w* for MI I-96 TS1

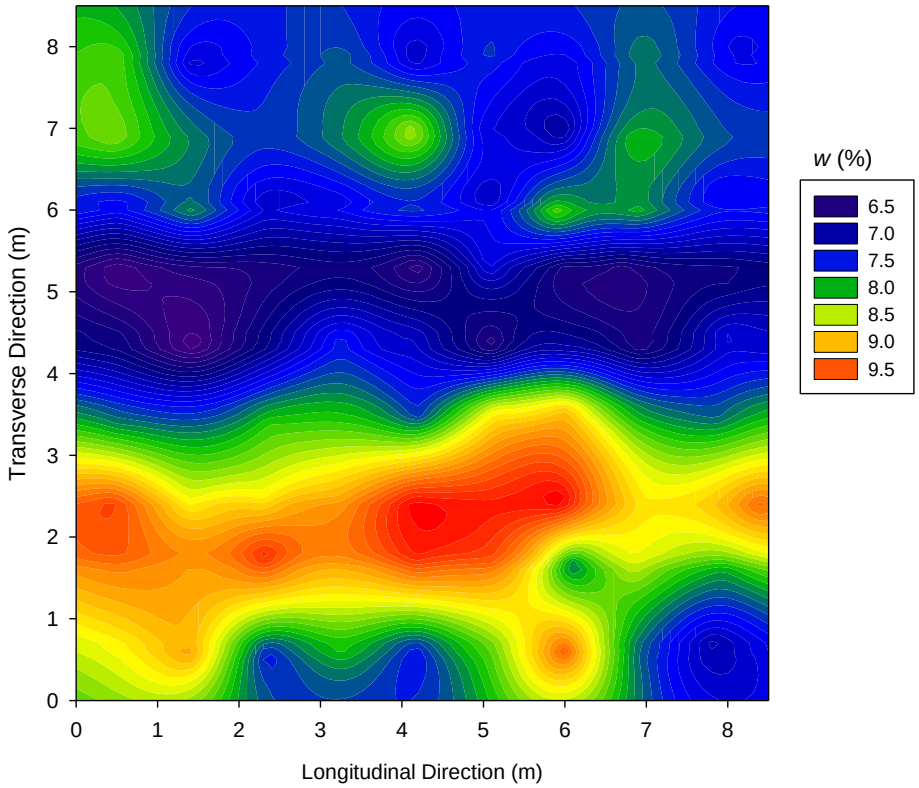

Figure B.112. Kriging contour plot with zonal anisotropic model of *w* for MI I-96 TS1

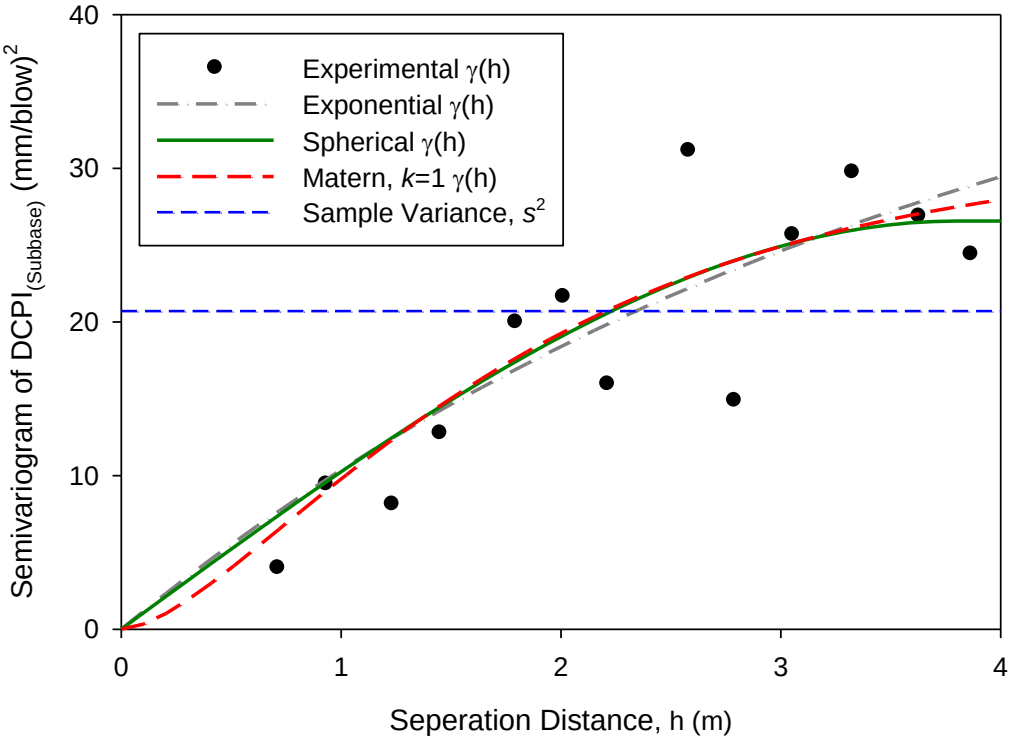

Figure B.113. Omnidirectional semivariogram with fitted model of $DCPI_{subbase}$ for MI I-96 TS1

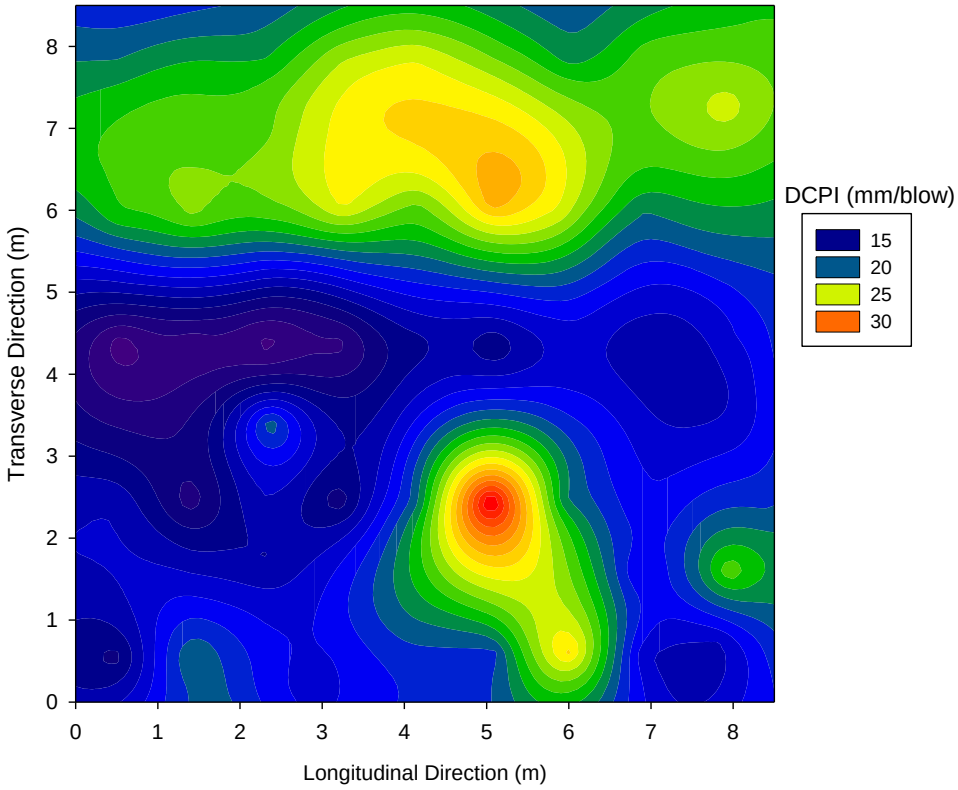

Figure B.114. Kriging contour plot with spherical model of $DCPI_{subbase}$ for MI I-96 TS1

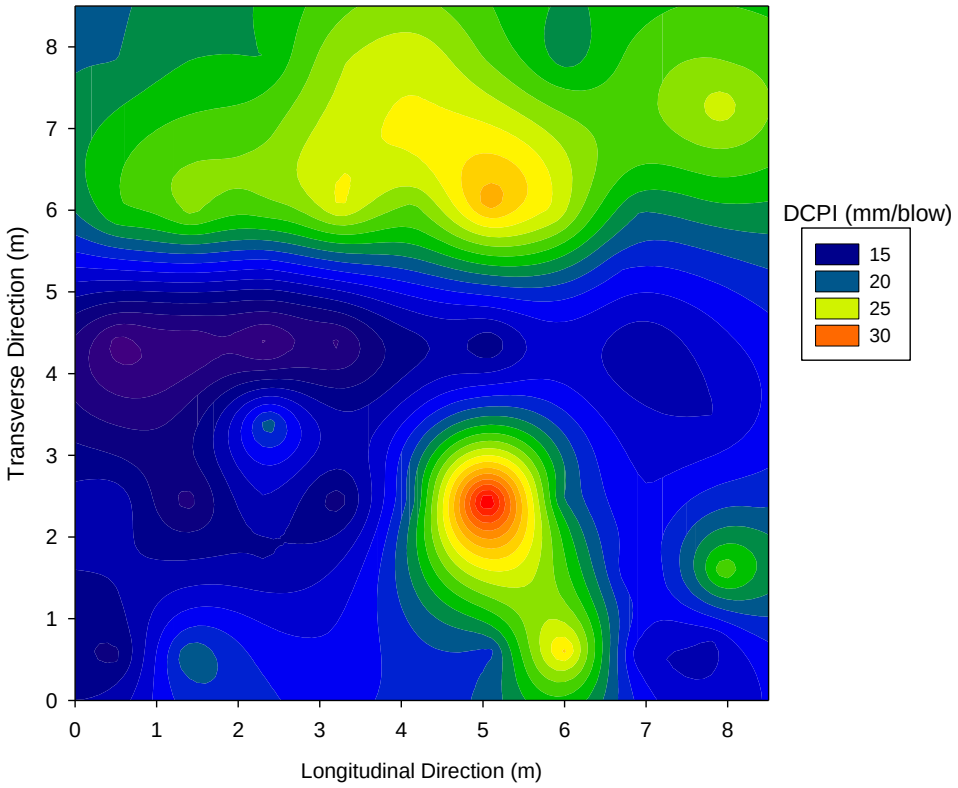

Figure B.115. Kriging contour plot with exponential model of $DCPI_{subbase}$ for MI I-96 TS1

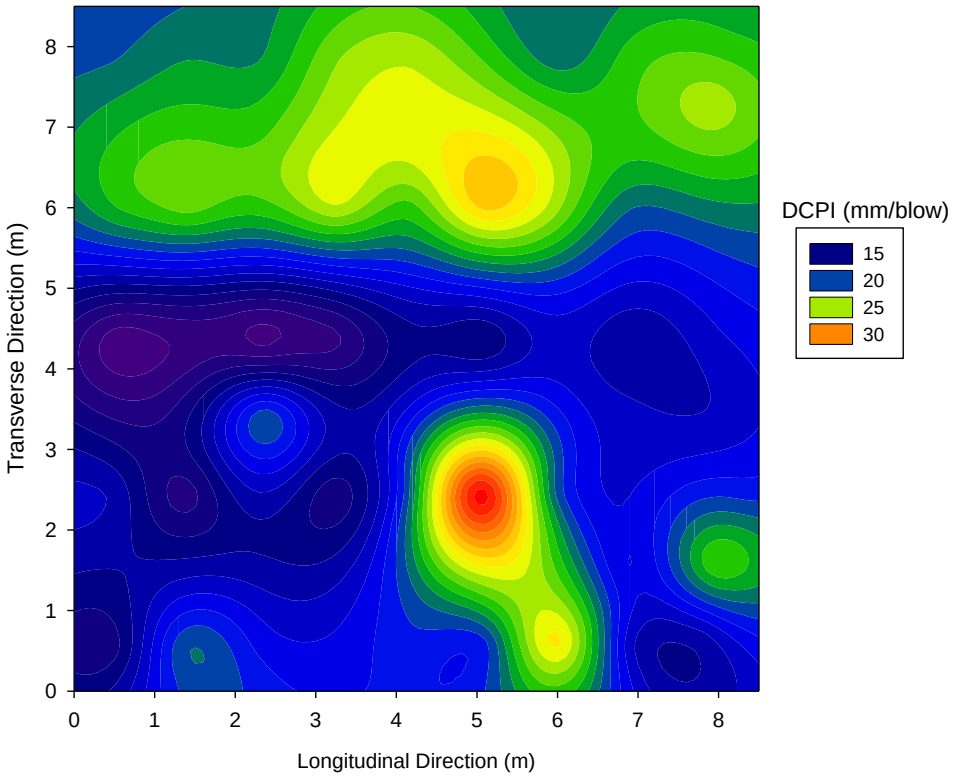

Figure B.116. Kriging contour plot with Matérn (k=1) model of $DCPI_{subbase}$ for MI I-96 TS1

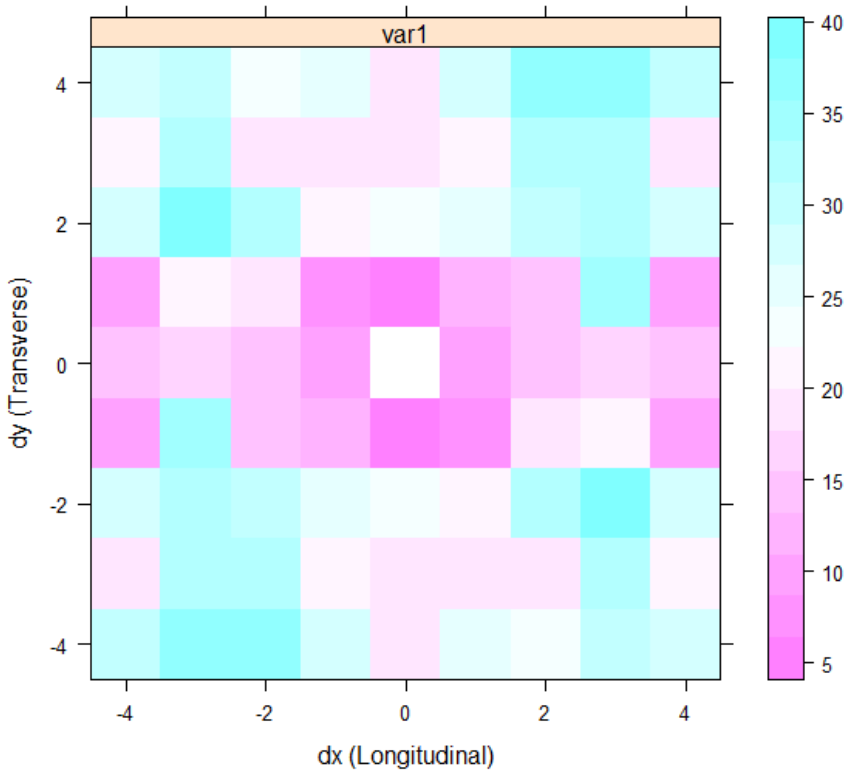

Figure B.117. Semivariogram map of $DCPI_{subbase}$ for MI I-96 TS1

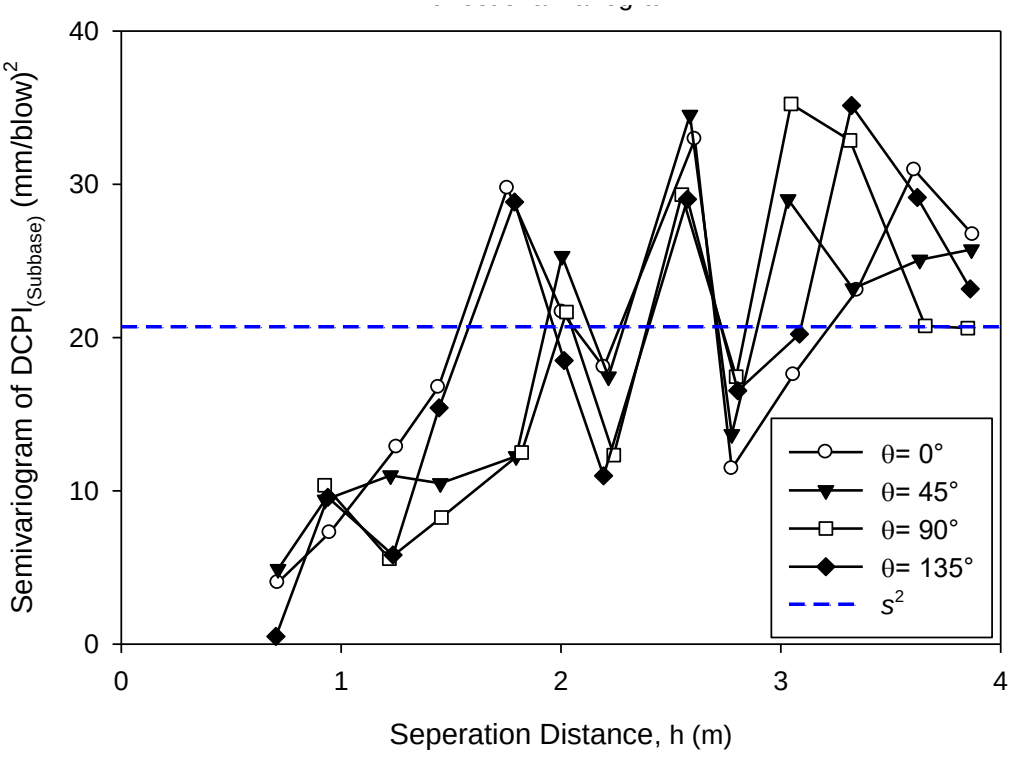

Figure B.118. Directional semivariogram of $DCPI_{subbase}$ for MI I-96 TS1

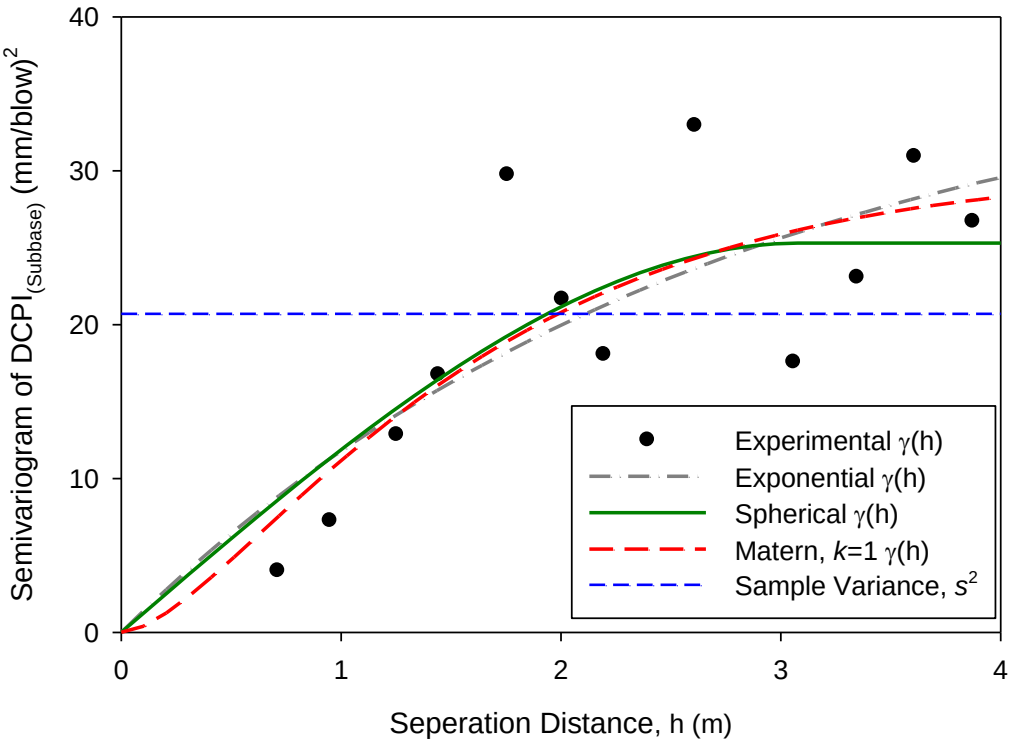

Figure B.119. Transverse direction semivariogram with fitted model of $DCPI_{subbase}$ for MI I-96 TS1

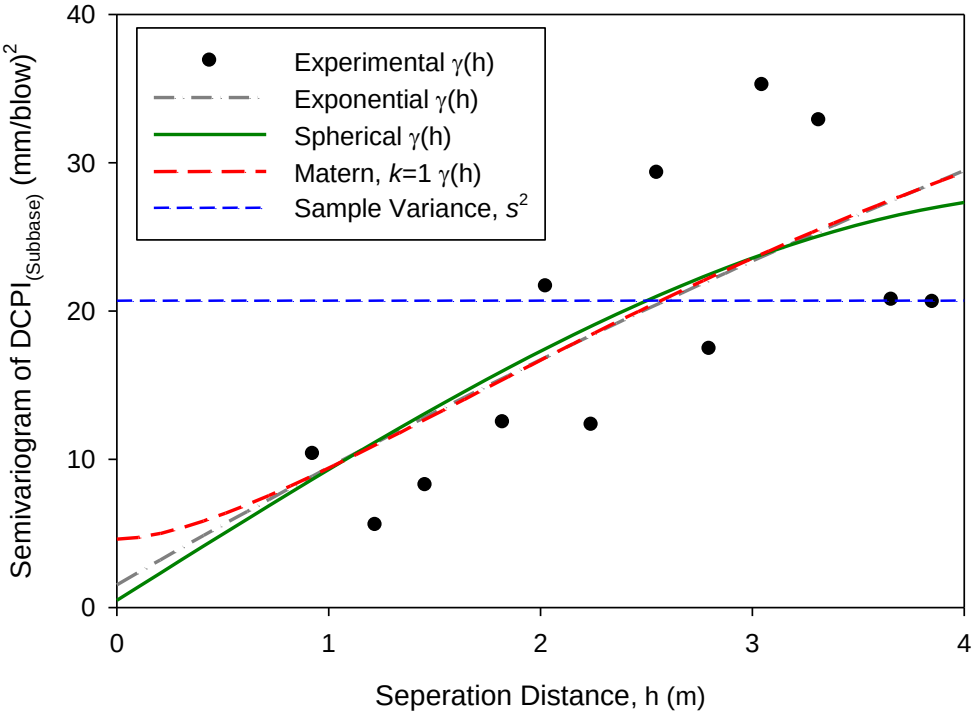

Figure B.120. Longitudinal direction semivariogram with fitted model of $DCPI_{subbase}$ for MI I-96 TS1

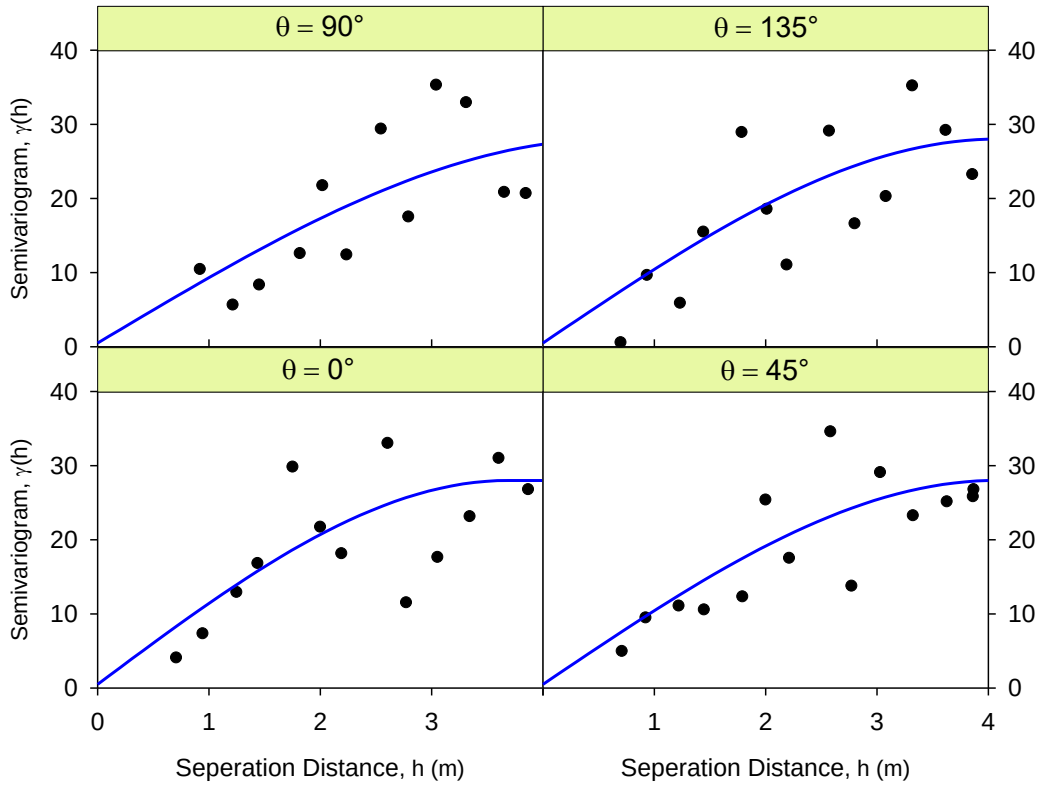

Figure B.121. Directional semivariogram with fitted geometric anisotropic model of $DCPI_{subbase}$ for MI I-96 TS1

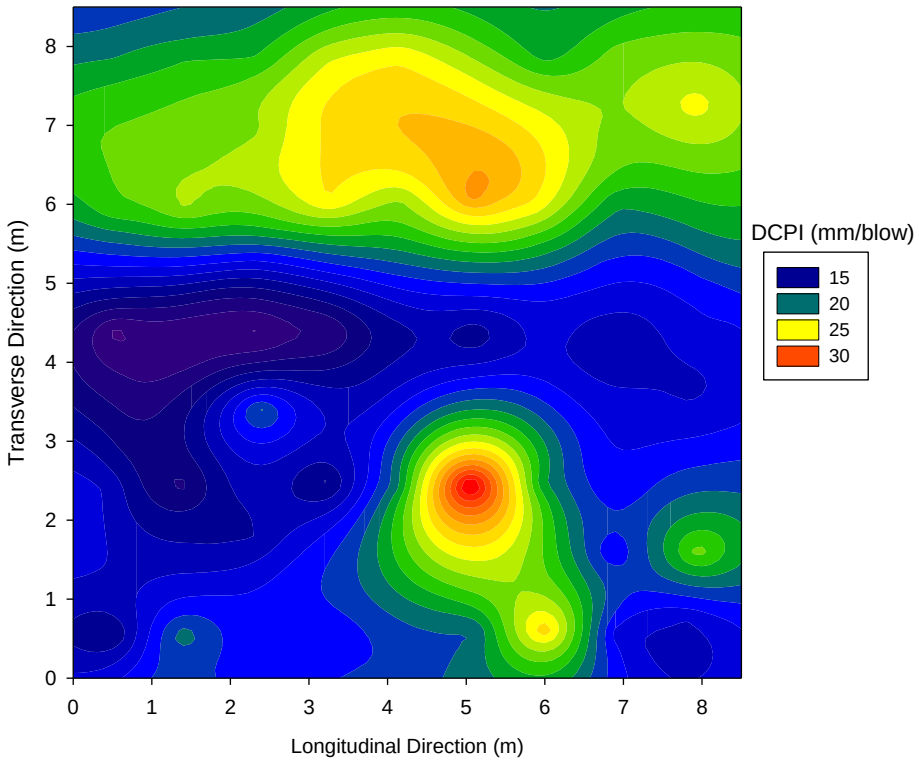

Figure B.122. Kriging contour plot with geometric anisotropic model of $DCPI_{subbase}$ for MI I-96 TS1

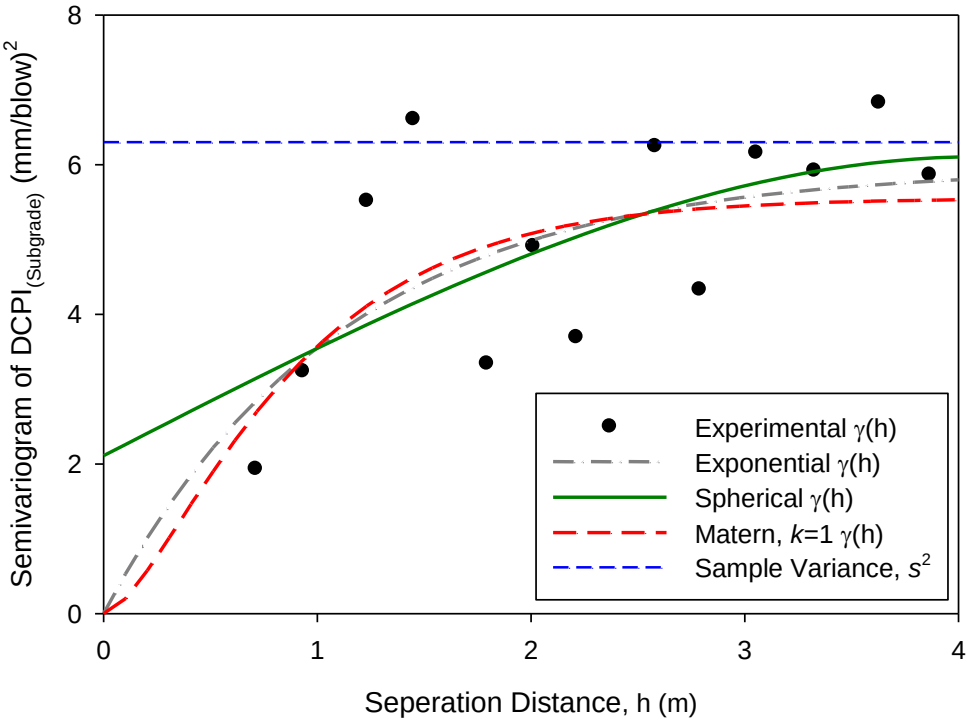

Figure B.123. Omnidirectional semivariogram with fitted model of $DCPI_{subgrade}$ for MI I-96 TS1

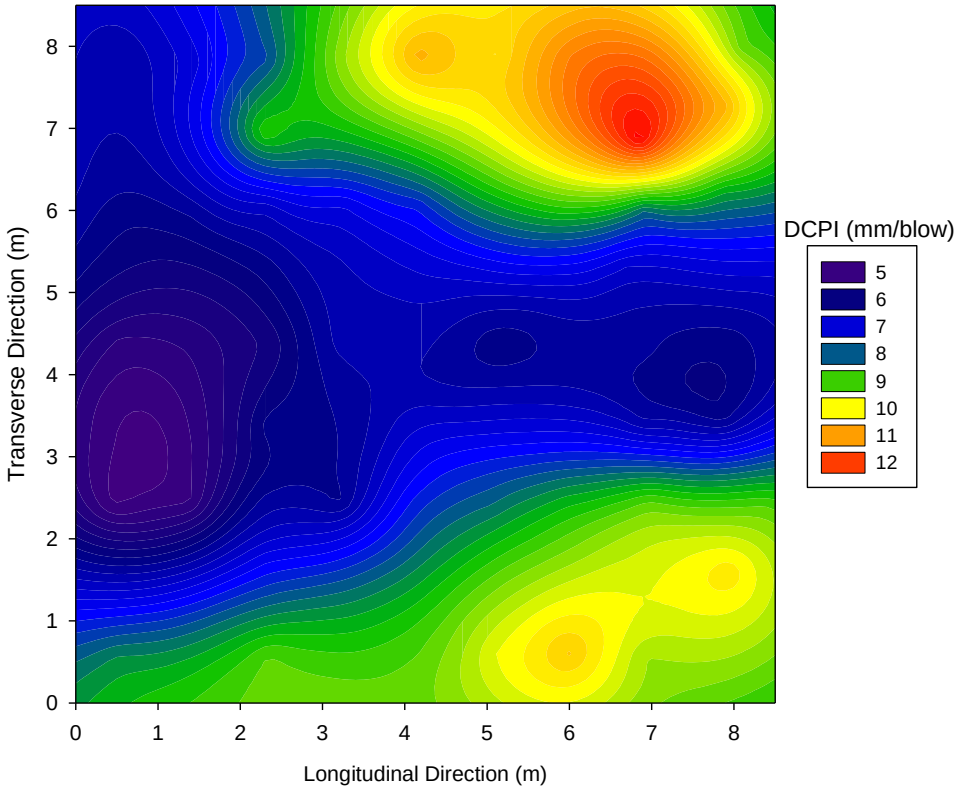

Figure B.124. Kriging contour plot with spherical model of $DCPI_{subgrade}$ for MI I-96 TS1

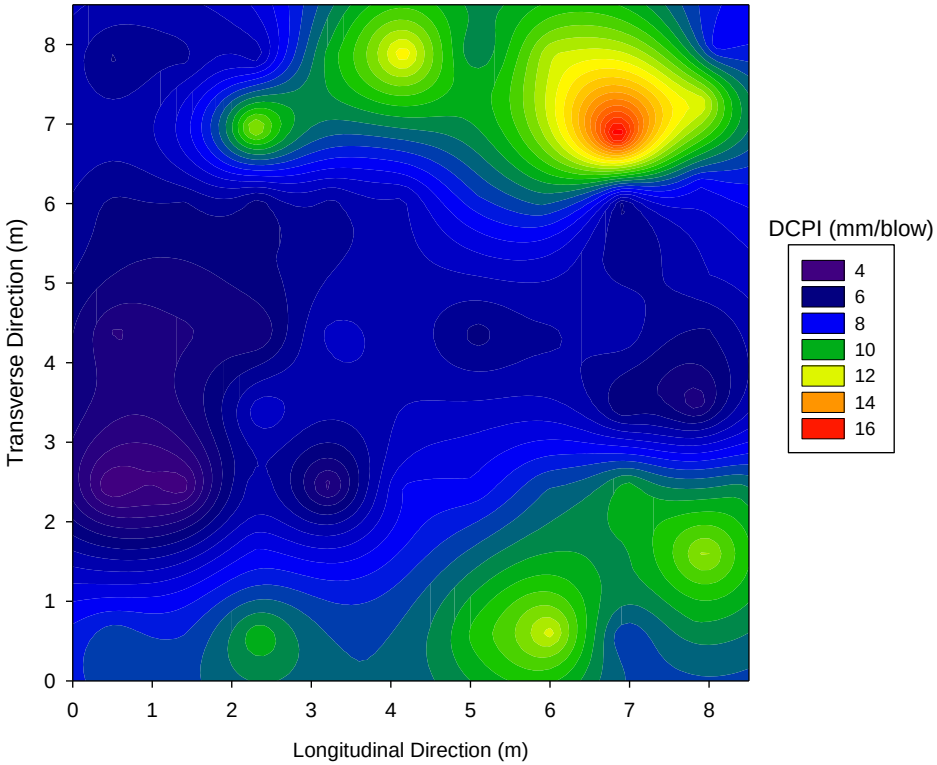

Figure B.125. Kriging contour plot with exponential model of $DCPI_{subgrade}$ for MI I-96 TS1

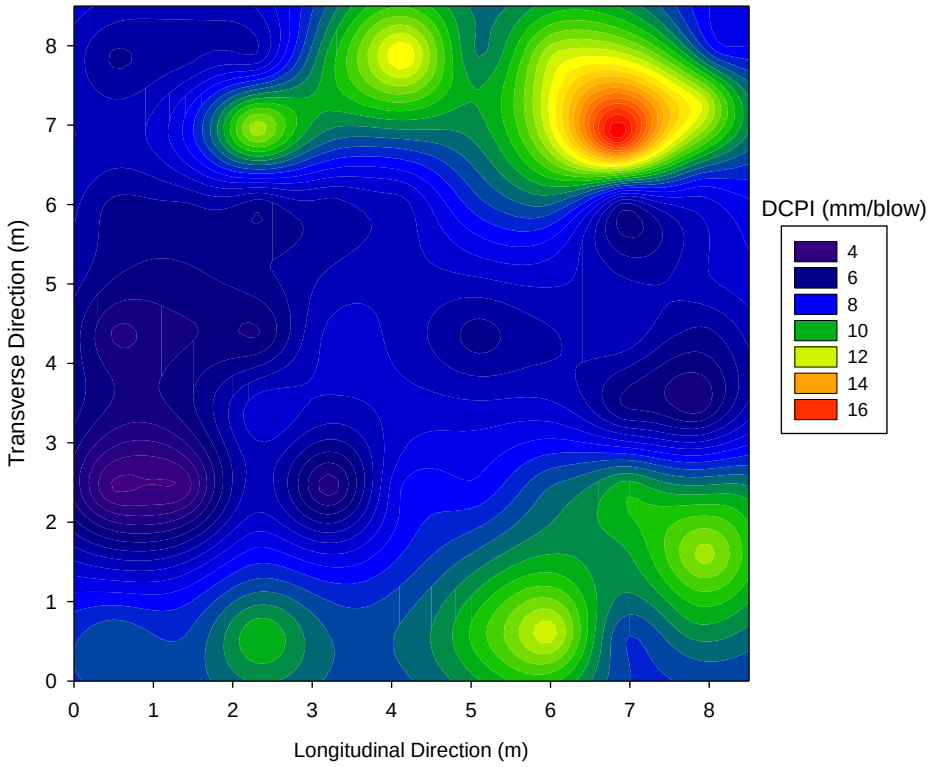

Figure B.126. Kriging contour plot with Matérn (*k*=1) model of $DCPI_{subgrade}$ for MI I-96 TS1

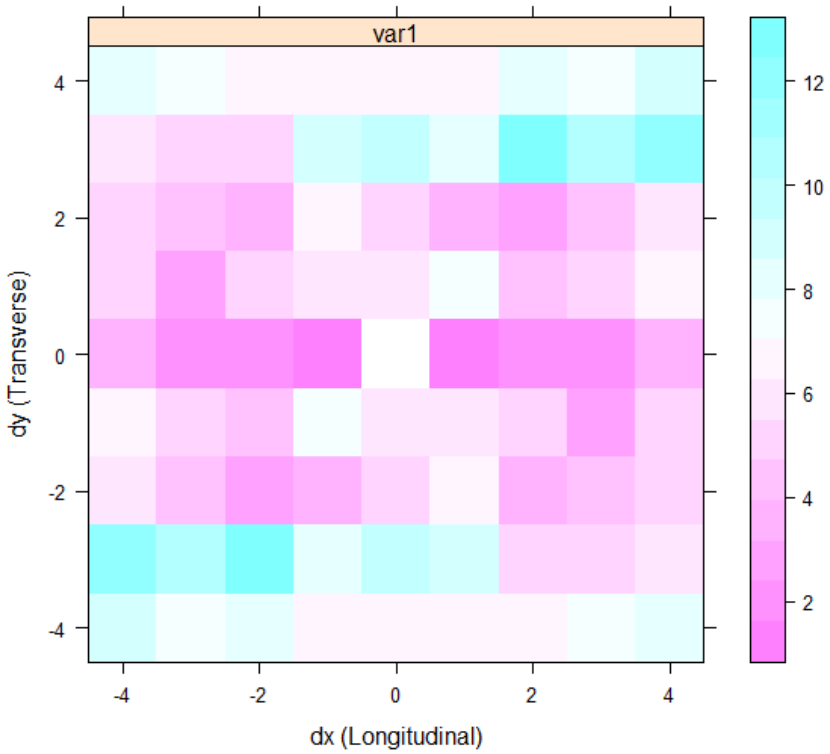

Figure B.127. Semivariogram map of $DCPI_{subgrade}$ with width =1 for MI I-96 TS1

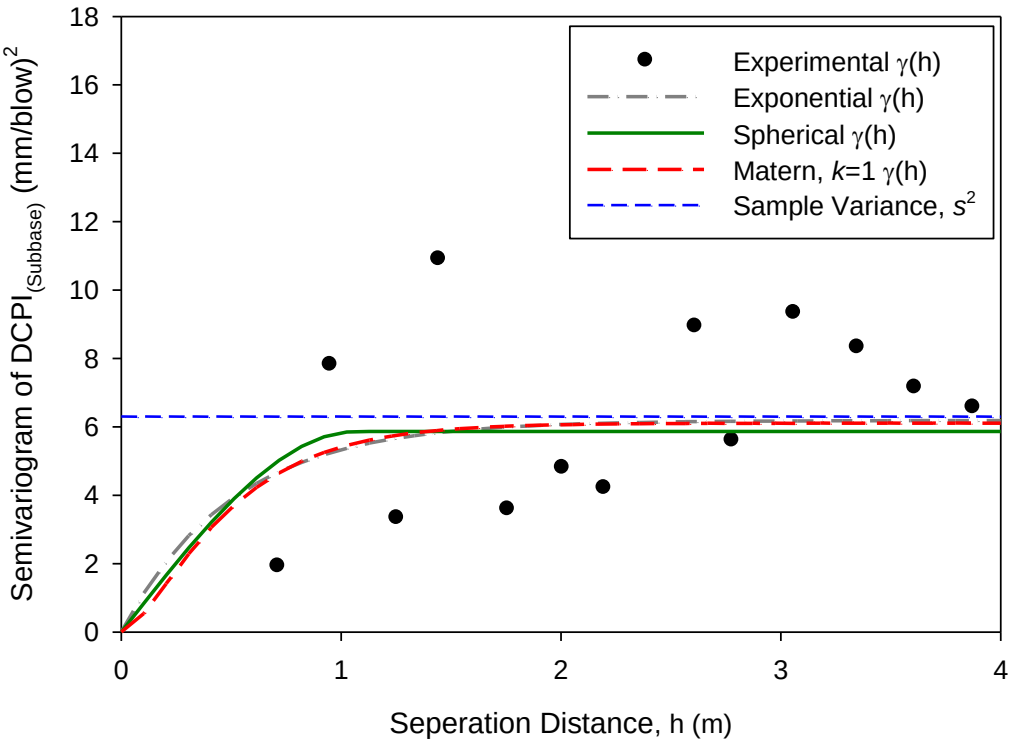

Figure B.128. Transverse direction semivariogram of $DCPI_{subgrade}$ for MI I-96 TS1

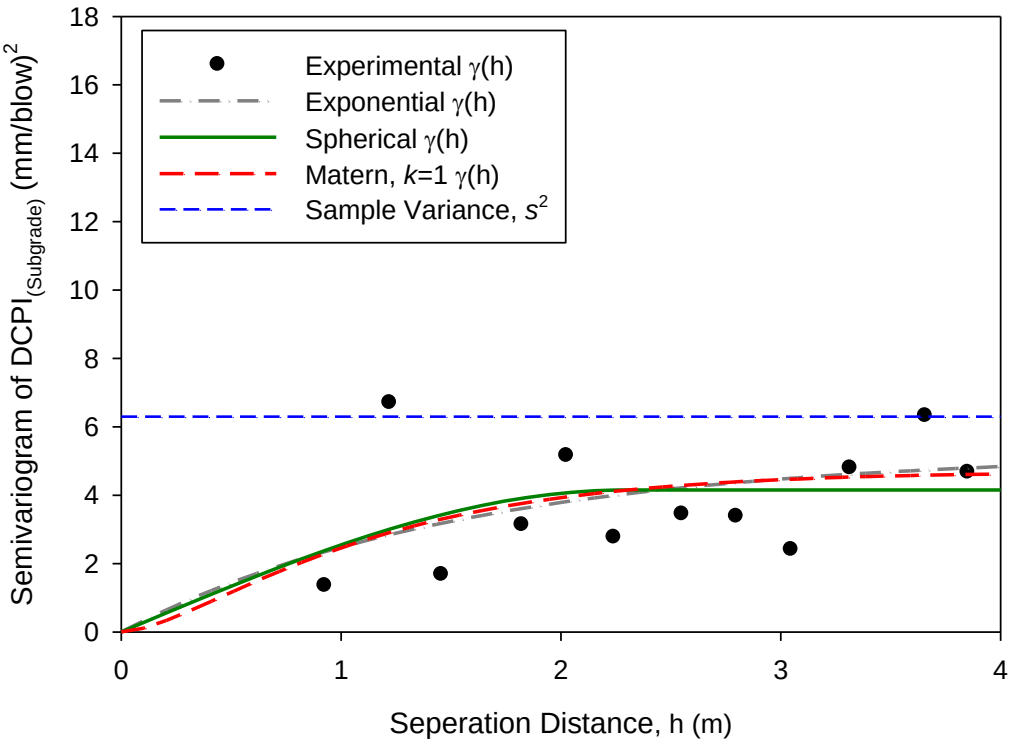

Figure B.129. Longitudinal direction semivariogram of $DCPI_{subgrade}$ for MI I-96 TS1

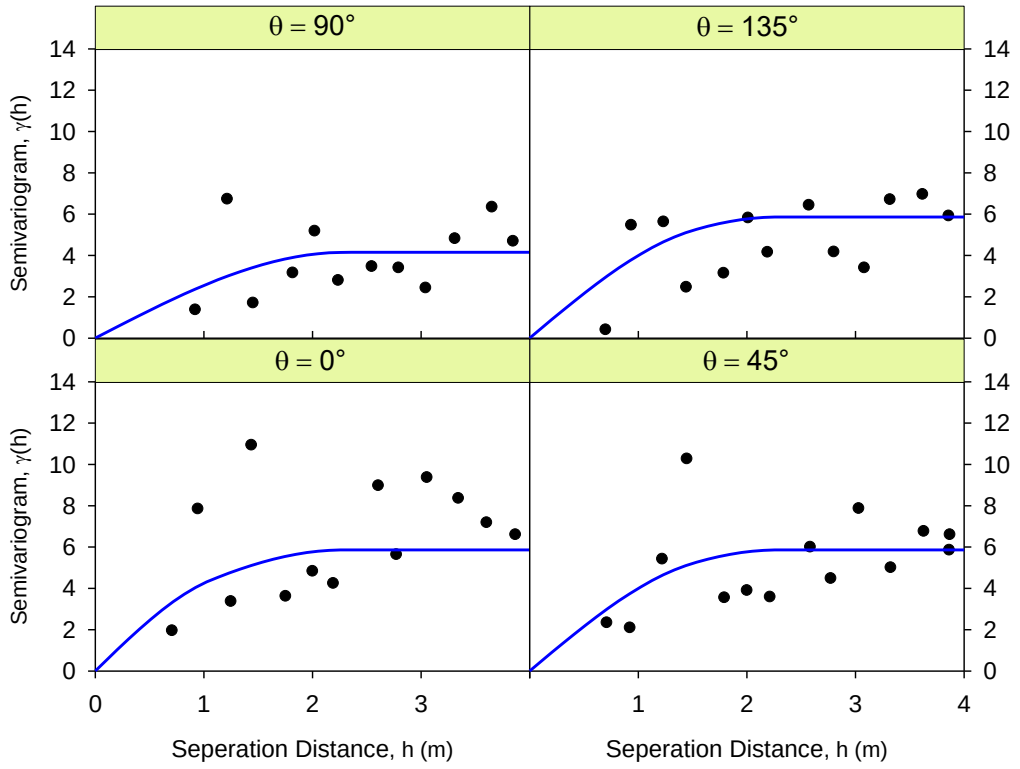

Figure B.130. Directional semivariogram with fitted zonal anisotropic model of $DCPI_{subgrade}$ for MI I-96 TS1

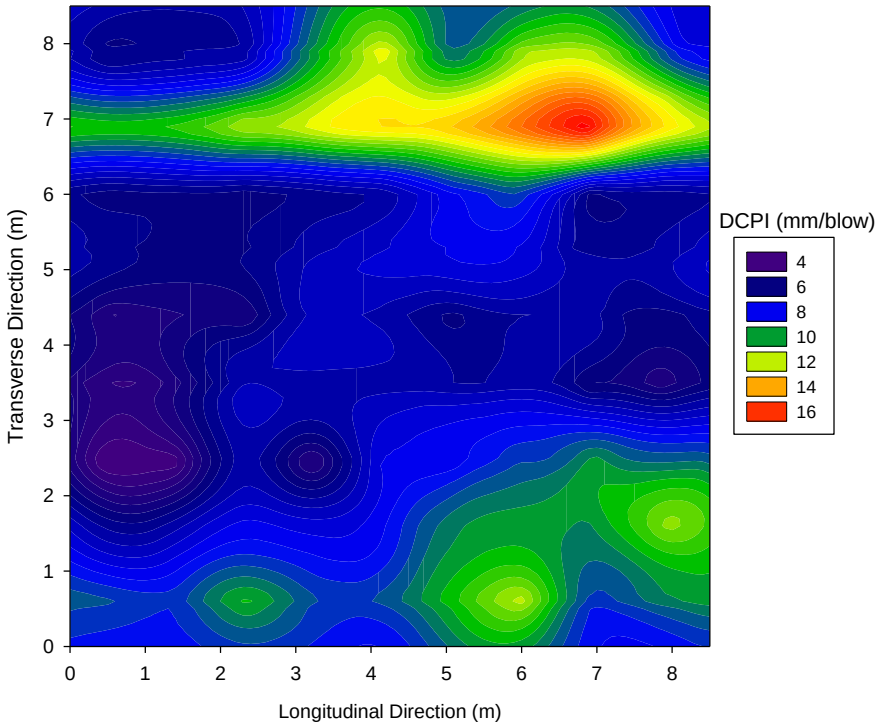

Figure B.131. Kriging contour plot with zonal anisotropic model of $DCPI_{subgrade}$ for MI I-96 TS1

B.5. MI I-96 TS2

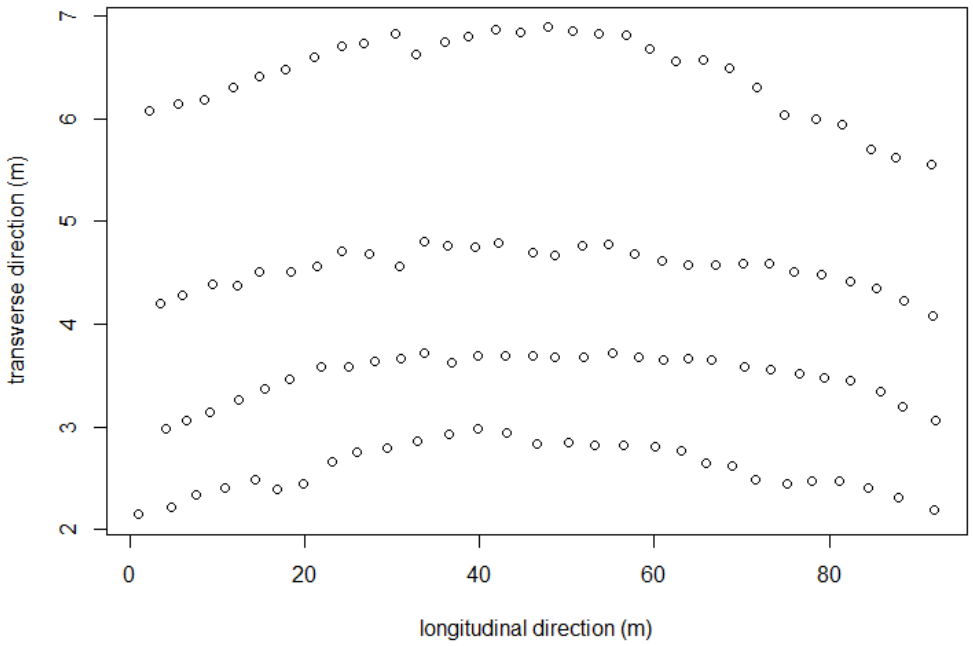

Figure B.132. Test plan for MI I-96 TS2

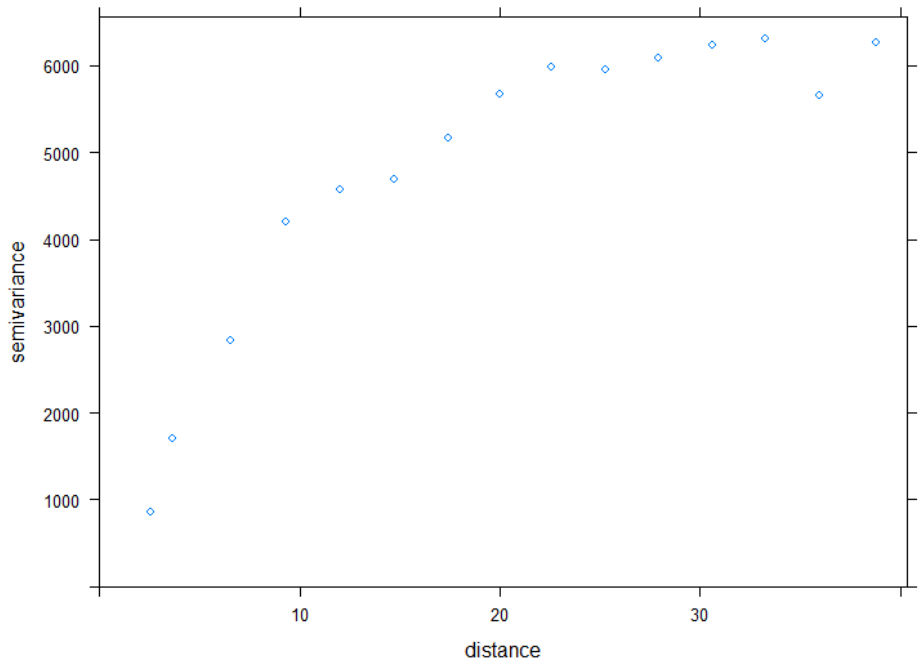

Figure B.133. Longitudinal direction experimental semivariogram of $E_{FWD\text{-}K3}$ for MI I-96 TS2

Distributions

EFWD

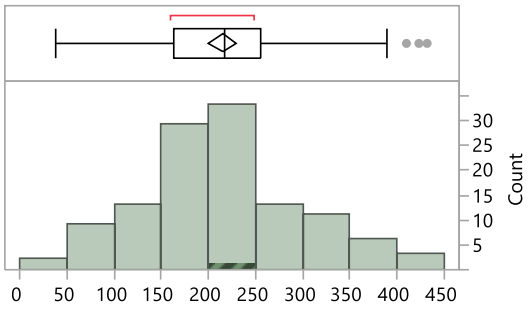

Quantiles		
100.0%	maximum	432.5138641
99.5%		432.5138641
97.5%		410.5505904
90.0%		332.9448674
75.0%	quartile	254.7691066
50.0%	median	216.9343273
25.0%	quartile	163.7840441
10.0%		101.4309344
2.5%		59.15579406
0.5%		37.64536409
0.0%	minimum	37.64536409

Summary Statistics	
Mean	214.76789
Std Dev	84.572083
Std Err Mean	7.7527101
Upper 95% Mean	230.12036
Lower 95% Mean	199.41541
N	119
Variance	7152.4372
Skewness	0.285067
CV	39.378365
Median	216.93433

rd

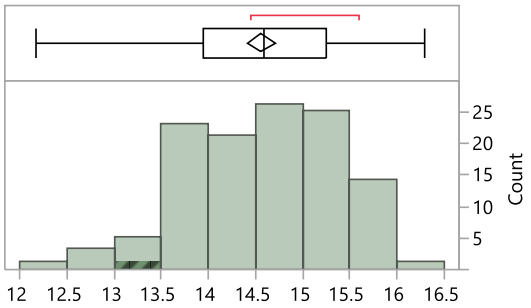

Quantiles		
100.0%	maximum	16.29137145
99.5%		16.29137145
97.5%		15.91432911
90.0%		15.58441705
75.0%	quartile	15.24664995
50.0%	median	14.58682584
25.0%	quartile	13.94271183
10.0%		13.52639424
2.5%		12.87442518
0.5%		12.16747077
0.0%	minimum	12.16747077

Summary Statistics	
Mean	14.556726
Std Dev	0.8099668
Std Err Mean	0.0742495
Upper 95% Mean	14.70376
Lower 95% Mean	14.409692
N	119
Variance	0.6560462
Skewness	-0.278736
CV	5.5642101
Median	14.586826

w

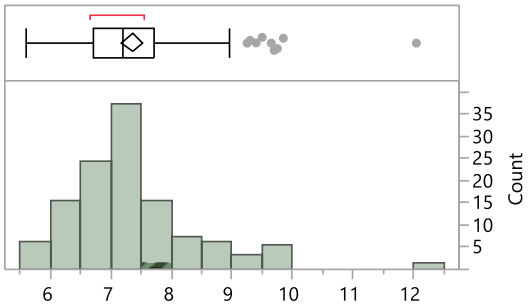

Quantiles		
100.0%	maximum	12.05
99.5%		12.05
97.5%		9.75
90.0%		8.9
75.0%	quartile	7.7
50.0%	median	7.2
25.0%	quartile	6.7
10.0%		6.3
2.5%		5.8
0.5%		5.6
0.0%	minimum	5.6

Summary Statistics	
Mean	7.3491597
Std Dev	1.0204474
Std Err Mean	0.0935443
Upper 95% Mean	7.5344028
Lower 95% Mean	7.1639166
N	119
Variance	1.0413128
Skewness	1.3954978
CV	13.885225
Median	7.2

Figure B.134. Univariate statistics summary of $E_{FWD\text{-}K3}$, γ_d, and *w* for MI I-96 TS2 (JMP)

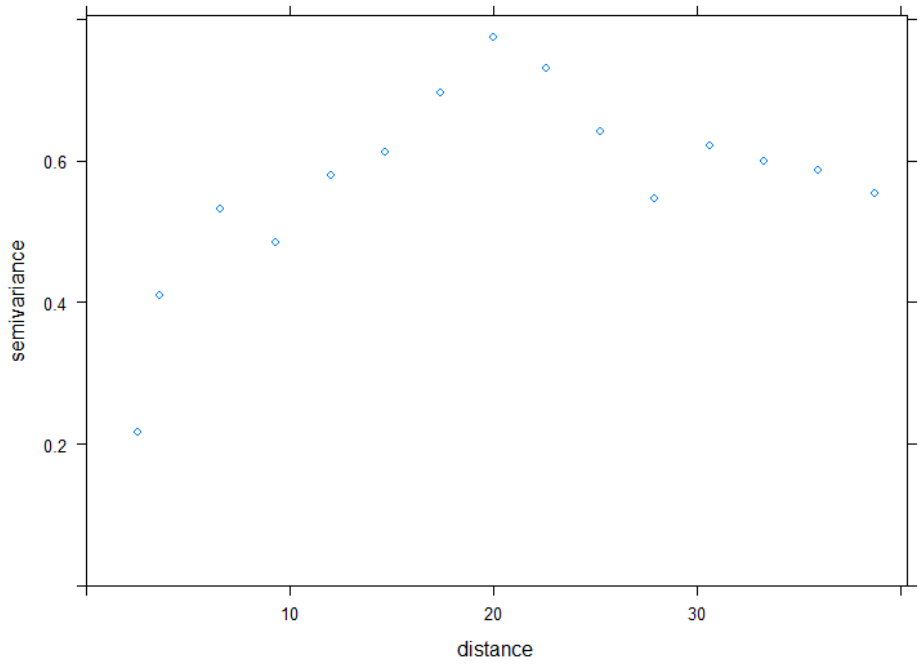

Figure B.135. Longitudinal direction experimental semivariogram of γ_d for MI I-96 TS2

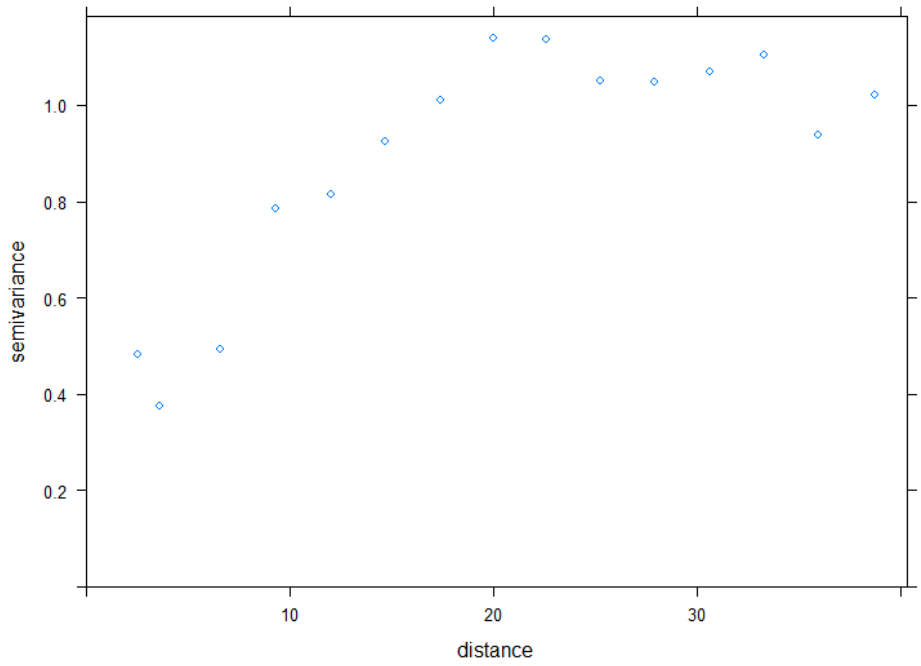

Figure B.136. Longitudinal direction experimental semivariogram of *w* for MI I-96 TS2

B.6. MI I-96 TS3

ELWD

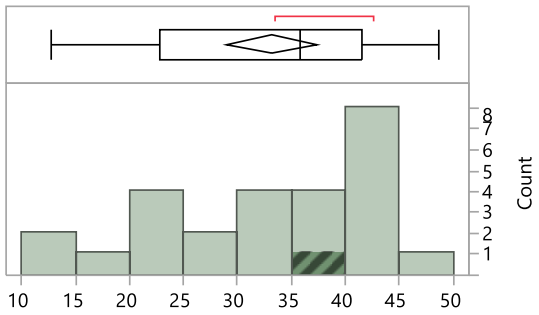

Quantiles		
100.0%	maximum	48.7185
99.5%		48.7185
97.5%		48.7185
90.0%		44.06688
75.0%	quartile	41.589
50.0%	median	35.78935
25.0%	quartile	22.78145
10.0%		16.30822
2.5%		12.7726
0.5%		12.7726
0.0%	minimum	12.7726

Summary Statistics	
Mean	33.196131
Std Dev	10.425528
Std Err Mean	2.0446142
Upper 95% Mean	37.407093
Lower 95% Mean	28.985169
N	26
Variance	108.69163
Skewness	-0.569667
CV	31.405852
Median	35.78935

rd

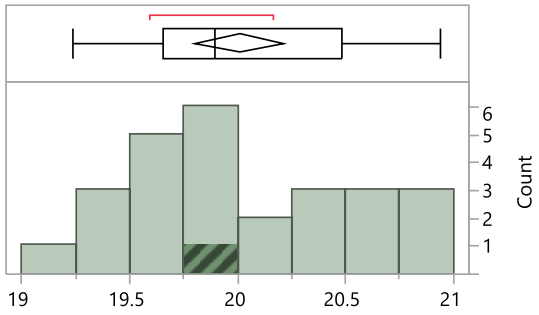

Quantiles		
100.0%	maximum	20.9416
99.5%		20.9416
97.5%		20.9416
90.0%		20.81431
75.0%	quartile	20.482075
50.0%	median	19.8929
25.0%	quartile	19.651375
10.0%		19.2999
2.5%		19.237
0.5%		19.237
0.0%	minimum	19.237

Summary Statistics	
Mean	20.011354
Std Dev	0.5087837
Std Err Mean	0.0997807
Upper 95% Mean	20.216856
Lower 95% Mean	19.805852
N	26
Variance	0.2588609
Skewness	0.297129
CV	2.5424753
Median	19.8929

w

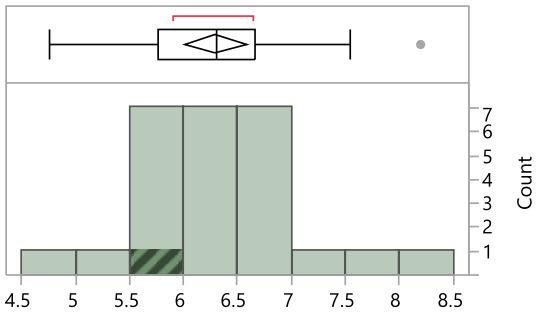

Quantiles		
100.0%	maximum	8.2
99.5%		8.2
97.5%		8.2
90.0%		7.165
75.0%	quartile	6.6625
50.0%	median	6.3
25.0%	quartile	5.7625
10.0%		5.485
2.5%		4.75
0.5%		4.75
0.0%	minimum	4.75

Summary Statistics	
Mean	6.2980769
Std Dev	0.7218699
Std Err Mean	0.1415703
Upper 95% Mean	6.5896465
Lower 95% Mean	6.0065074
N	26
Variance	0.5210962
Skewness	0.4421917
CV	11.461751
Median	6.3

Figure B.137. Univariate statistics summary of $E_{FWD\text{-}K3}$, γ_d, and *w* for MI I-96 TS3 (JMP)

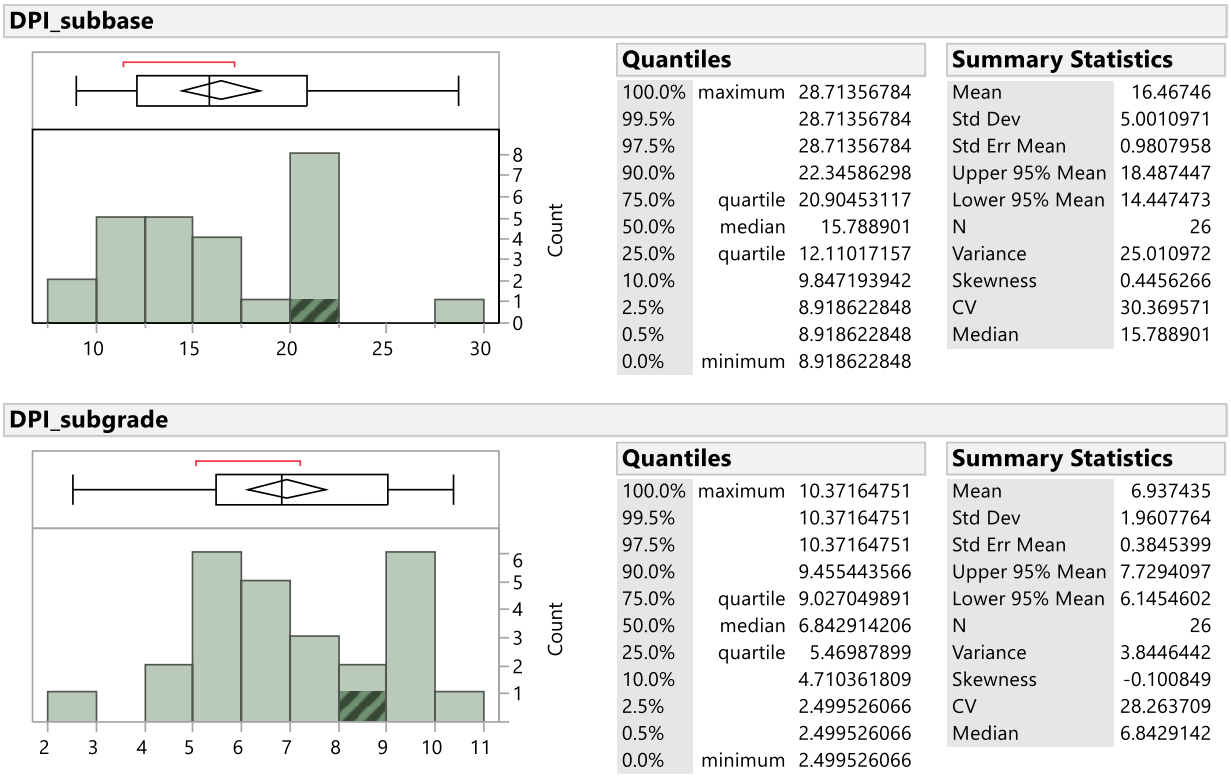

Figure B.138. Univariate statistics summary of $DCPI_{subbase}$ and $DCPI_{subgrade}$ for MI I-96 TS3 (JMP)

APPENDIX C. STATISTICAL ANALYSIS PLOTS FOR CHAPTER 3

C.1. FL I-10

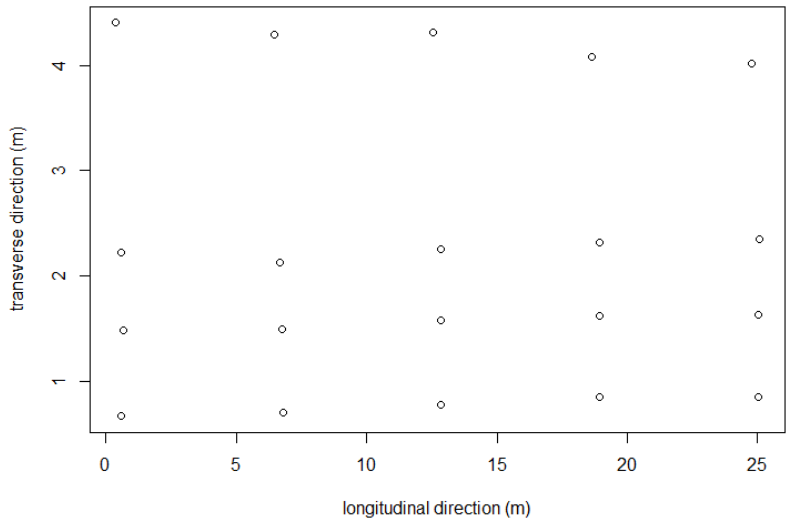

Figure C.1. Test plan for FL I-10 TS1

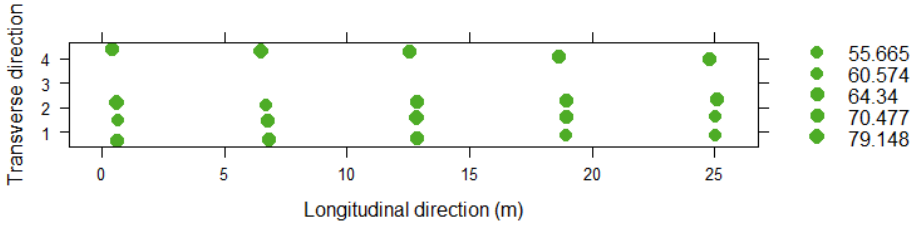

Figure C.2. Bubble plot of $E_{LWD\text{-}Z3}$ for FL I-10 TS1

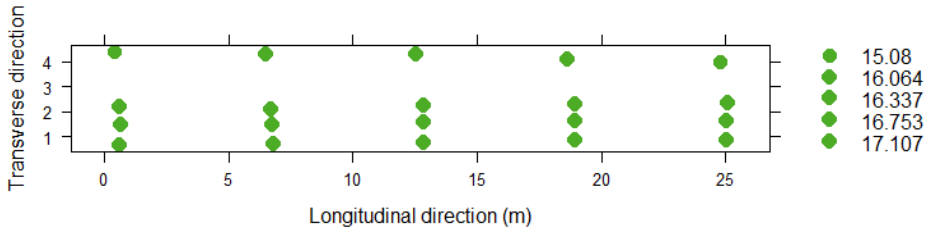

Figure C.3. Bubble plot of γ_d for FL I-10 TS1

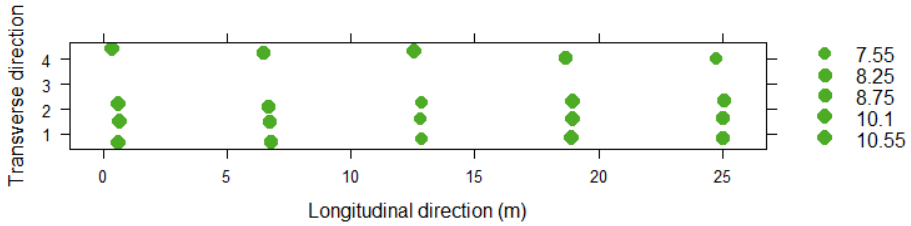

Figure C.4. Bubble plot of *w* for FL I-10 TS1

Distributions

ELWD

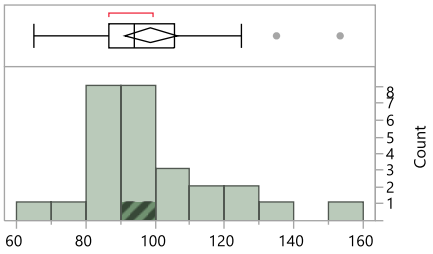

Quantiles		
100.0%	maximum	153.5
99.5%		153.5
97.5%		153.5
90.0%		127.072
75.0%	quartile	105.53
50.0%	median	93.81
25.0%	quartile	86.59
10.0%		78.39
2.5%		64.94
0.5%		64.94
0.0%	minimum	64.94

Summary Statistics	
Mean	98.726667
Std Dev	19.484089
Std Err Mean	3.7497147
Upper 95% Mean	106.43432
Lower 95% Mean	91.019018
N	27
Variance	379.62972
Skewness	0.9822321
CV	19.735386
Median	93.81

rd

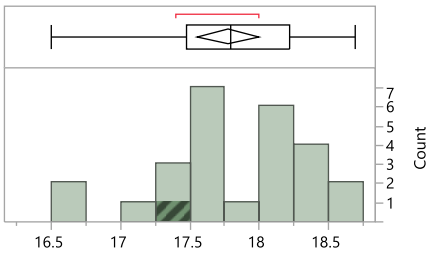

Quantiles		
100.0%	maximum	18.7
99.5%		18.7
97.5%		18.7
90.0%		18.43
75.0%	quartile	18.225
50.0%	median	17.8
25.0%	quartile	17.475
10.0%		16.91
2.5%		16.5
0.5%		16.5
0.0%	minimum	16.5

Summary Statistics	
Mean	17.776923
Std Dev	0.5428132
Std Err Mean	0.1064544
Upper 95% Mean	17.99617
Lower 95% Mean	17.557676
N	26
Variance	0.2946462
Skewness	-0.557515
CV	3.053471
Median	17.8

w%

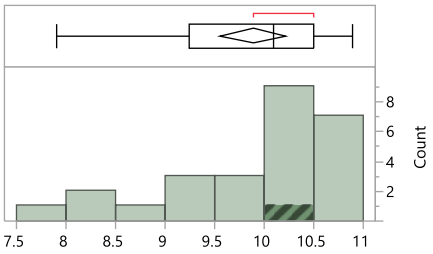

Quantiles		
100.0%	maximum	10.9
99.5%		10.9
97.5%		10.9
90.0%		10.83
75.0%	quartile	10.5
50.0%	median	10.1
25.0%	quartile	9.25
10.0%		8.37
2.5%		7.9
0.5%		7.9
0.0%	minimum	7.9

Summary Statistics	
Mean	9.8884615
Std Dev	0.8300973
Std Err Mean	0.1627955
Upper 95% Mean	10.223745
Lower 95% Mean	9.553178
N	26
Variance	0.6890615
Skewness	-0.990525
CV	8.3946052
Median	10.1

DCPI

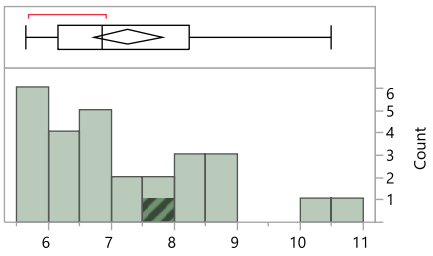

Quantiles		
100.0%	maximum	10.5
99.5%		10.5
97.5%		10.5
90.0%		9.218
75.0%	quartile	8.25
50.0%	median	6.86
25.0%	quartile	6.14
10.0%		5.77
2.5%		5.64
0.5%		5.64
0.0%	minimum	5.64

Summary Statistics	
Mean	7.2640741
Std Dev	1.3693858
Std Err Mean	0.2635384
Upper 95% Mean	7.805785
Lower 95% Mean	6.7223631
N	27
Variance	1.8752174
Skewness	0.8990973
CV	18.851484
Median	6.86

CBR

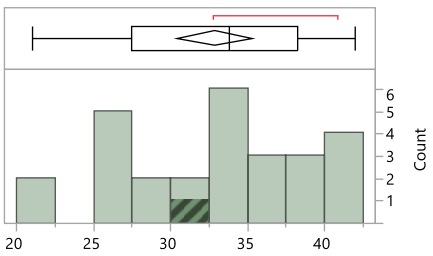

Quantiles		
100.0%	maximum	42.04398855
99.5%		42.04398855
97.5%		42.04398855
90.0%		41.03779376
75.0%	quartile	38.23032465
50.0%	median	33.79889254
25.0%	quartile	27.47605829
10.0%		24.35319976
2.5%		20.97253059
0.5%		20.97253059
0.0%	minimum	20.97253059

Summary Statistics	
Mean	32.867281
Std Dev	6.249016
Std Err Mean	1.2026237
Upper 95% Mean	35.33931
Lower 95% Mean	30.395253
N	27
Variance	39.050201
Skewness	-0.289652
CV	19.012878
Median	33.798893

Figure C.5. Univariate statistics summary for in-situ properties for FL I-10 TS1 (JMP)

Distributions

ELWD

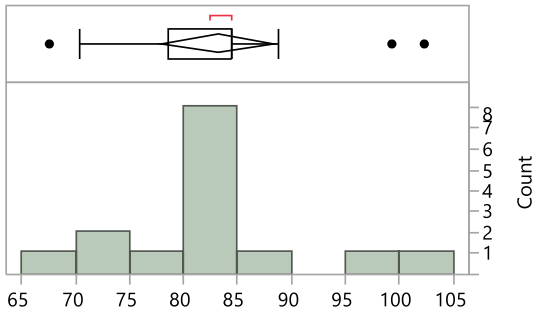

Quantiles		
100.0%	maximum	102.33
99.5%		102.33
97.5%		102.33
90.0%		100.524
75.0%	quartile	84.43
50.0%	median	84.43
25.0%	quartile	78.53
10.0%		69.226
2.5%		67.54
0.5%		67.54
0.0%	minimum	67.54

Summary Statistics	
Mean	83.203333
Std Dev	9.3678048
Std Err Mean	2.4187568
Upper 95% Mean	88.391051
Lower 95% Mean	78.015616
N	15
Variance	87.755767
Skewness	0.3850797
CV	11.25893
Median	84.43

rd

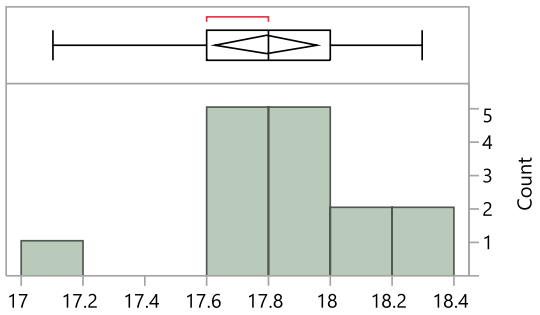

Quantiles		
100.0%	maximum	18.3
99.5%		18.3
97.5%		18.3
90.0%		18.3
75.0%	quartile	18
50.0%	median	17.8
25.0%	quartile	17.6
10.0%		17.4
2.5%		17.1
0.5%		17.1
0.0%	minimum	17.1

Summary Statistics	
Mean	17.793333
Std Dev	0.2987275
Std Err Mean	0.0771311
Upper 95% Mean	17.958763
Lower 95% Mean	17.627904
N	15
Variance	0.0892381
Skewness	-0.259729
CV	1.6788729
Median	17.8

w%

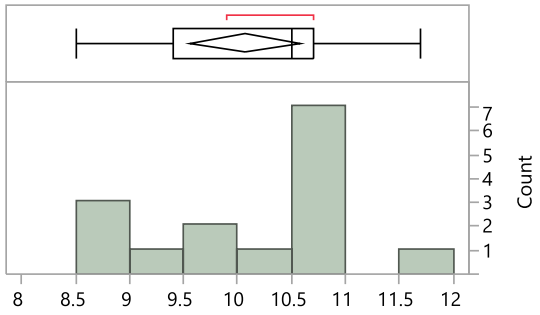

Quantiles		
100.0%	maximum	11.7
99.5%		11.7
97.5%		11.7
90.0%		11.16
75.0%	quartile	10.7
50.0%	median	10.5
25.0%	quartile	9.4
10.0%		8.56
2.5%		8.5
0.5%		8.5
0.0%	minimum	8.5

Summary Statistics	
Mean	10.066667
Std Dev	0.9317163
Std Err Mean	0.2405681
Upper 95% Mean	10.582634
Lower 95% Mean	9.5506994
N	15
Variance	0.8680952
Skewness	-0.415249
CV	9.2554598
Median	10.5

Figure C.6. Univariate statistics summary for in-situ properties for FL I-10 TS2 (JMP)

Distributions

ELWD

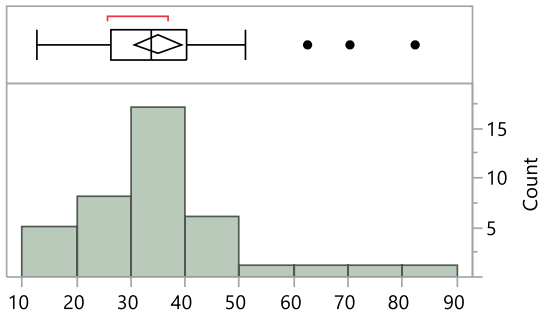

Quantiles		
100.0%	maximum	82.37
99.5%		82.37
97.5%		82.0695
90.0%		50.743
75.0%	quartile	40.0825
50.0%	median	33.61
25.0%	quartile	26.18
10.0%		17.266
2.5%		12.687
0.5%		12.6
0.0%	minimum	12.6

Summary Statistics	
Mean	34.93025
Std Dev	13.950628
Std Err Mean	2.205788
Upper 95% Mean	39.391877
Lower 95% Mean	30.468623
N	40
Variance	194.62003
Skewness	1.3784286
CV	39.93853
Median	33.61

rd

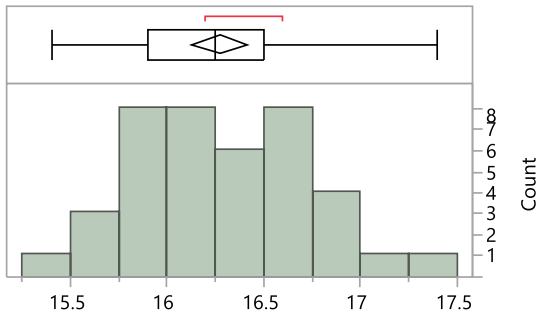

Quantiles		
100.0%	maximum	17.4
99.5%		17.4
97.5%		17.395
90.0%		16.9
75.0%	quartile	16.5
50.0%	median	16.25
25.0%	quartile	15.9
10.0%		15.62
2.5%		15.4025
0.5%		15.4
0.0%	minimum	15.4

Summary Statistics	
Mean	16.2725
Std Dev	0.4500641
Std Err Mean	0.0711614
Upper 95% Mean	16.416437
Lower 95% Mean	16.128563
N	40
Variance	0.2025577
Skewness	0.2983047
CV	2.7657957
Median	16.25

w%

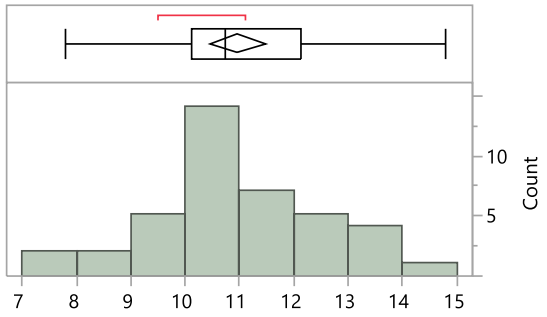

Quantiles		
100.0%	maximum	14.8
99.5%		14.8
97.5%		14.7775
90.0%		13.29
75.0%	quartile	12.125
50.0%	median	10.75
25.0%	quartile	10.125
10.0%		8.84
2.5%		7.8025
0.5%		7.8
0.0%	minimum	7.8

Summary Statistics	
Mean	10.9575
Std Dev	1.5958098
Std Err Mean	0.2523197
Upper 95% Mean	11.467865
Lower 95% Mean	10.447135
N	40
Variance	2.546609
Skewness	0.1937142
CV	14.563631
Median	10.75

Figure C.7. Univariate statistics summary for in-situ properties for FL I-10 TS3 (JMP)

Distributions

ELWD

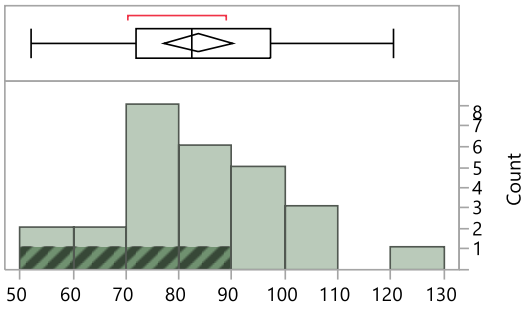

Quantiles		
100.0%	maximum	120.61
99.5%		120.61
97.5%		120.61
90.0%		104.658
75.0%	quartile	97.41
50.0%	median	82.37
25.0%	quartile	71.85
10.0%		60.832
2.5%		51.95
0.5%		51.95
0.0%	minimum	51.95

Summary Statistics	
Mean	83.623333
Std Dev	16.230109
Std Err Mean	3.1234859
Upper 95% Mean	90.043751
Lower 95% Mean	77.202916
N	27
Variance	263.41643
Skewness	0.1957163
CV	19.408589
Median	82.37

rd

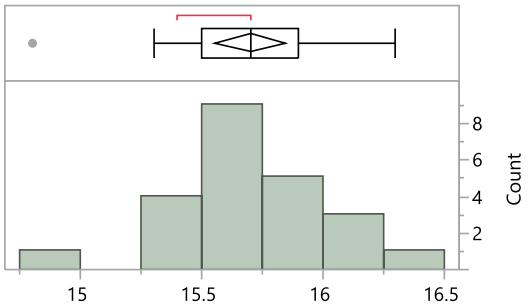

Quantiles		
100.0%	maximum	16.3
99.5%		16.3
97.5%		16.3
90.0%		16.2
75.0%	quartile	15.9
50.0%	median	15.7
25.0%	quartile	15.5
10.0%		15.34
2.5%		14.8
0.5%		14.8
0.0%	minimum	14.8

Summary Statistics	
Mean	15.7
Std Dev	0.3357488
Std Err Mean	0.0700085
Upper 95% Mean	15.845189
Lower 95% Mean	15.554811
N	23
Variance	0.1127273
Skewness	-0.434067
CV	2.1385275
Median	15.7

w%

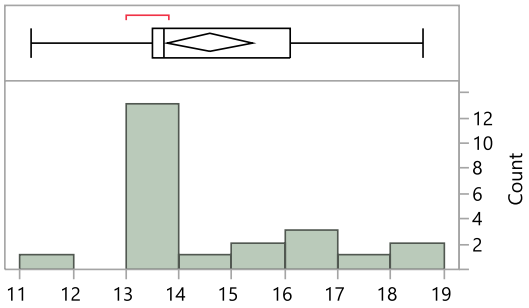

Quantiles		
100.0%	maximum	18.6
99.5%		18.6
97.5%		18.6
90.0%		17.9
75.0%	quartile	16.1
50.0%	median	13.7
25.0%	quartile	13.5
10.0%		13
2.5%		11.2
0.5%		11.2
0.0%	minimum	11.2

Summary Statistics	
Mean	14.569565
Std Dev	1.8672865
Std Err Mean	0.3893562
Upper 95% Mean	15.37704
Lower 95% Mean	13.76209
N	23
Variance	3.4867589
Skewness	0.764109
CV	12.81635
Median	13.7

Figure C.8. Univariate statistics summary of in-situ properties for FL I-10 TS4 (JMP)

C.2. IA US-30

Distributions

CBR of RPCC subbase

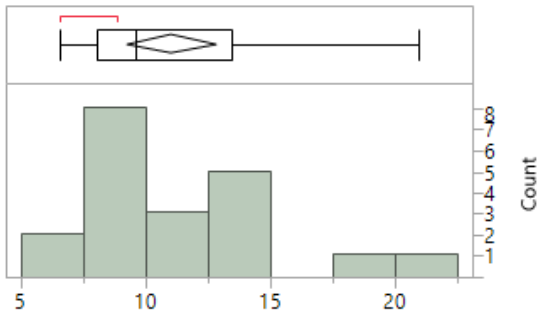

Quantiles		
100.0%	maximum	21
99.5%		21
97.5%		21
90.0%		17.38
75.0%	quartile	13.45
50.0%	median	9.55
25.0%	quartile	8
10.0%		7.23
2.5%		6.5
0.5%		6.5
0.0%	minimum	6.5

Summary Statistics	
Mean	11.03
Std Dev	3.8551538
Std Err Mean	0.8620386
Upper 95% Mean	12.834267
Lower 95% Mean	9.2257325
N	20
Variance	14.862211
Skewness	1.0767222
CV	34.95153
Median	9.55

CBR of RPCC/RAP subbase

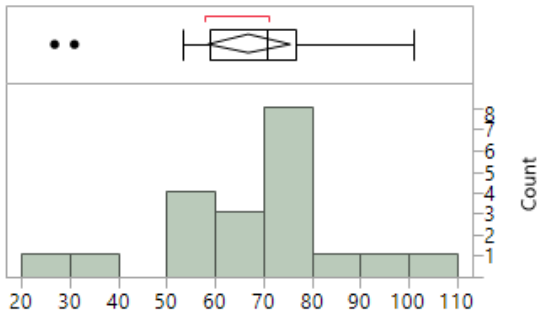

Quantiles		
100.0%	maximum	101.2
99.5%		101.2
97.5%		101.2
90.0%		97.19
75.0%	quartile	76.575
50.0%	median	70.6
25.0%	quartile	58.925
10.0%		33.15
2.5%		26.8
0.5%		26.8
0.0%	minimum	26.8

Summary Statistics	
Mean	67.04
Std Dev	18.188151
Std Err Mean	4.0669942
Upper 95% Mean	75.552317
Lower 95% Mean	58.527683
N	20
Variance	330.80884
Skewness	-0.368908
CV	27.130297
Median	70.6

CBR of subgrade

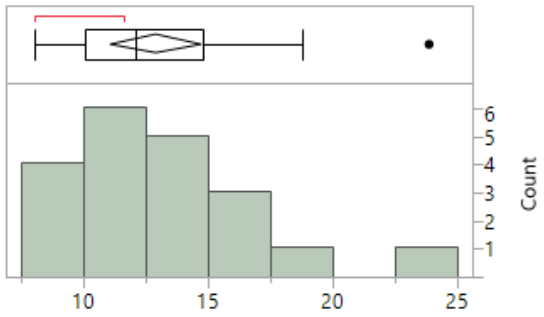

Quantiles		
100.0%	maximum	23.9
99.5%		23.9
97.5%		23.9
90.0%		18.65
75.0%	quartile	14.8
50.0%	median	12.05
25.0%	quartile	10.025
10.0%		8.66
2.5%		8
0.5%		8
0.0%	minimum	8

Summary Statistics	
Mean	12.89
Std Dev	3.9438026
Std Err Mean	0.8818611
Upper 95% Mean	14.735756
Lower 95% Mean	11.044244
N	20
Variance	15.553579
Skewness	1.247584
CV	30.595831
Median	12.05

Figure C.9. Univariate statistics summary of CBR in three layers for IA US-30 TS1 (JMP)

Distributions

ELWD_longitudinal

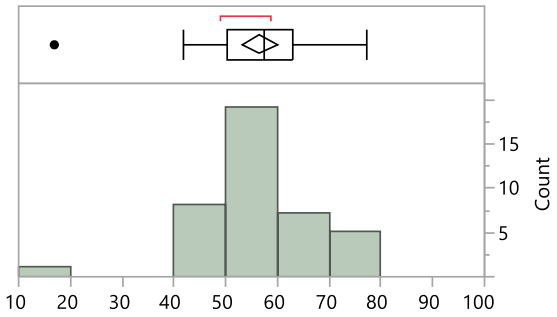

Quantiles		
100.0%	maximum	77.3
99.5%		77.3
97.5%		77.28
90.0%		73.2
75.0%	quartile	62.85
50.0%	median	57.5
25.0%	quartile	50.425
10.0%		45.74
2.5%		17.5225
0.5%		16.9
0.0%	minimum	16.9

Summary Statistics	
Mean	56.6225
Std Dev	10.981558
Std Err Mean	1.7363367
Upper 95% Mean	60.134573
Lower 95% Mean	53.110427
N	40
Variance	120.59461
Skewness	-0.812663
CV	19.394336
Median	57.5

ELWD_transverse

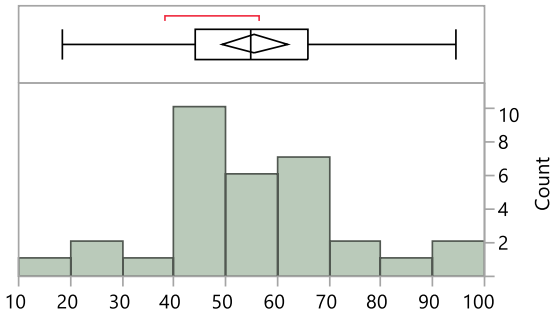

Quantiles		
100.0%	maximum	94.5
99.5%		94.5
97.5%		94.5
90.0%		84.07
75.0%	quartile	65.75
50.0%	median	54.85
25.0%	quartile	44.2
10.0%		32.28
2.5%		18.6
0.5%		18.6
0.0%	minimum	18.6

Summary Statistics	
Mean	55.59375
Std Dev	17.841397
Std Err Mean	3.1539432
Upper 95% Mean	62.02626
Lower 95% Mean	49.16124
N	32
Variance	318.31544
Skewness	0.2396138
CV	32.092451
Median	54.85

Figure C.10. Univariate statistics summary of $E_{LWD\text{-}Z3}$ in longitudinal and transverse for IA US-30 TS2 (JMP)

C.3. NC Hwy-218

Distributions

ELWD

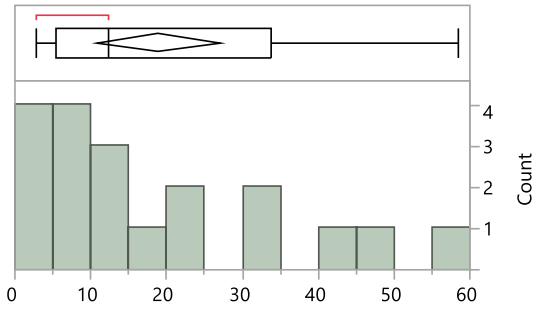

Quantiles		
100.0%	maximum	58.5
99.5%		58.5
97.5%		58.5
90.0%		48.51
75.0%	quartile	33.71
50.0%	median	12.43
25.0%	quartile	5.42
10.0%		2.85
2.5%		2.79
0.5%		2.79
0.0%	minimum	2.79

Summary Statistics	
Mean	18.903684
Std Dev	16.90576
Std Err Mean	3.8784474
Upper 95% Mean	27.052
Lower 95% Mean	10.755369
N	19
Variance	285.80474
Skewness	1.101038
CV	89.431035
Median	12.43

rd

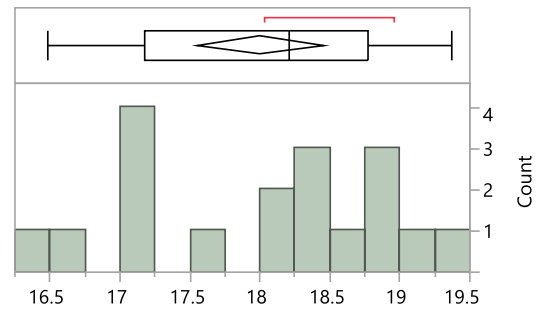

Quantiles		
100.0%	maximum	19.37
99.5%		19.37
97.5%		19.37
90.0%		19.226
75.0%	quartile	18.775
50.0%	median	18.21
25.0%	quartile	17.1775
10.0%		16.508
2.5%		16.49
0.5%		16.49
0.0%	minimum	16.49

Summary Statistics	
Mean	18.002778
Std Dev	0.9104544
Std Err Mean	0.2145961
Upper 95% Mean	18.455536
Lower 95% Mean	17.550019
N	18
Variance	0.8289271
Skewness	-0.266593
CV	5.0572993
Median	18.21

w%

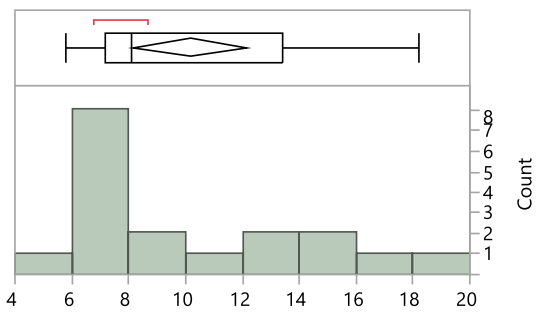

Quantiles		
100.0%	maximum	18.2
99.5%		18.2
97.5%		18.2
90.0%		17.21
75.0%	quartile	13.425
50.0%	median	8.1
25.0%	quartile	7.15
10.0%		6.52
2.5%		5.8
0.5%		5.8
0.0%	minimum	5.8

Summary Statistics	
Mean	10.172222
Std Dev	4.0034993
Std Err Mean	0.9436338
Upper 95% Mean	12.163116
Lower 95% Mean	8.1813289
N	18
Variance	16.028007
Skewness	0.853888
CV	39.357175
Median	8.1

Figure C.11. Univariate statistics summary of in-situ properties for NC Hwy-218 TS1 (JMP)

Distributions

ELWD-Z2

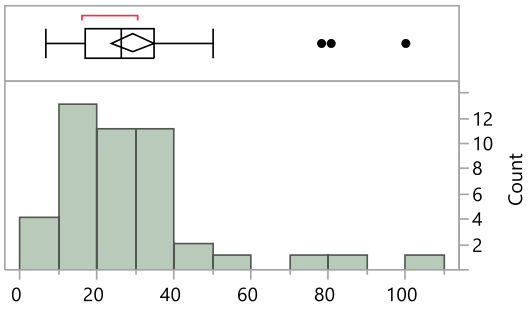

Quantiles		
100.0%	maximum	100.2
99.5%		100.2
97.5%		97.29
90.0%		47.34
75.0%	quartile	34.55
50.0%	median	26.1
25.0%	quartile	16.9
10.0%		11.44
2.5%		6.74
0.5%		6.5
0.0%	minimum	6.5

Summary Statistics	
Mean	29.204444
Std Dev	18.703499
Std Err Mean	2.7881531
Upper 95% Mean	34.823598
Lower 95% Mean	23.585291
N	45
Variance	349.82089
Skewness	2.0609863
CV	64.043332
Median	26.1

rd

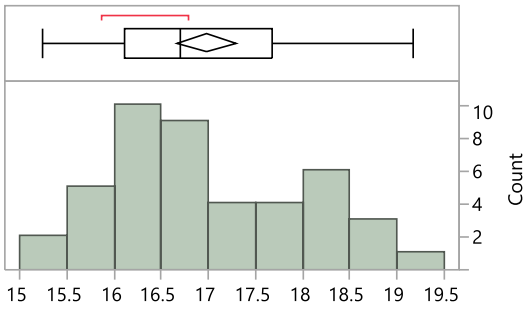

Quantiles		
100.0%	maximum	19.18
99.5%		19.18
97.5%		19.15625
90.0%		18.555
75.0%	quartile	17.6825
50.0%	median	16.705
25.0%	quartile	16.11
10.0%		15.875
2.5%		15.2575
0.5%		15.24
0.0%	minimum	15.24

Summary Statistics	
Mean	16.979091
Std Dev	1.0370751
Std Err Mean	0.156345
Upper 95% Mean	17.294391
Lower 95% Mean	16.663791
N	44
Variance	1.0755247
Skewness	0.4687687
CV	6.1079541
Median	16.705

w%

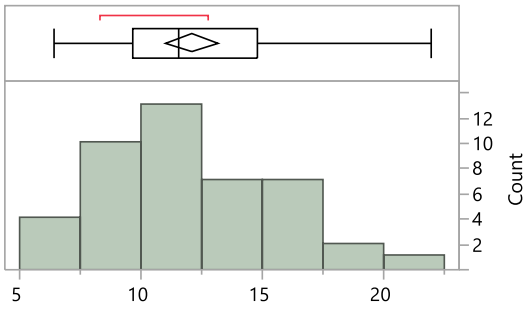

Quantiles		
100.0%	maximum	22
99.5%		22
97.5%		21.525
90.0%		17
75.0%	quartile	14.825
50.0%	median	11.55
25.0%	quartile	9.625
10.0%		7.3
2.5%		6.45
0.5%		6.4
0.0%	minimum	6.4

Summary Statistics	
Mean	12.109091
Std Dev	3.6055395
Std Err Mean	0.5435555
Upper 95% Mean	13.205275
Lower 95% Mean	11.012907
N	44
Variance	12.999915
Skewness	0.5023179
CV	29.775477
Median	11.55

DCPI_subgrade

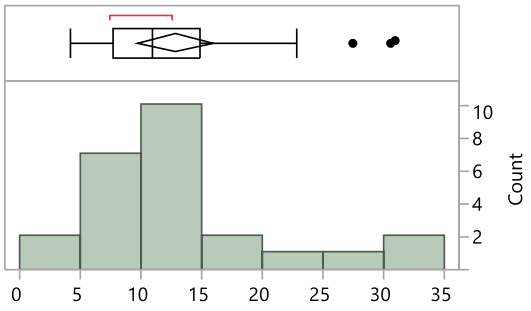

Quantiles		
100.0%	maximum	31
99.5%		31
97.5%		31
90.0%		28.752
75.0%	quartile	14.9
50.0%	median	10.87
25.0%	quartile	7.72
10.0%		5.146
2.5%		4.14
0.5%		4.14
0.0%	minimum	4.14

Summary Statistics	
Mean	12.8472
Std Dev	7.5921629
Std Err Mean	1.5184326
Upper 95% Mean	15.981091
Lower 95% Mean	9.7133092
N	25
Variance	57.640938
Skewness	1.3623956
CV	59.095857
Median	10.87

Figure C.12. Univariate statistics summary of in-situ properties for NC Hwy-218 TS2 (JMP)

Distributions

ELWD-z2

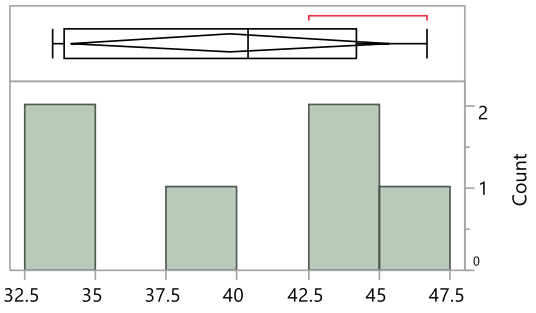

Quantiles		
100.0%	maximum	46.71
99.5%		46.71
97.5%		46.71
90.0%		46.71
75.0%	quartile	44.2125
50.0%	median	40.405
25.0%	quartile	33.875
10.0%		33.47
2.5%		33.47
0.5%		33.47
0.0%	minimum	33.47

Summary Statistics	
Mean	39.73
Std Dev	5.3613841
Std Err Mean	2.1887759
Upper 95% Mean	45.356428
Lower 95% Mean	34.103572
N	6
Variance	28.74444
Skewness	-0.04907
CV	13.494549
Median	40.405

ELWD-z3

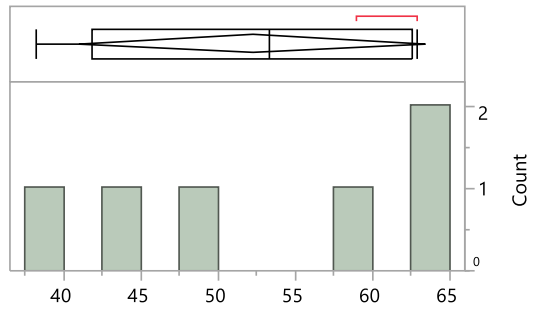

Quantiles		
100.0%	maximum	62.88
99.5%		62.88
97.5%		62.88
90.0%		62.88
75.0%	quartile	62.6475
50.0%	median	53.315
25.0%	quartile	41.81
10.0%		38.15
2.5%		38.15
0.5%		38.15
0.0%	minimum	38.15

Summary Statistics	
Mean	52.21
Std Dev	10.67484
Std Err Mean	4.357985
Upper 95% Mean	63.412557
Lower 95% Mean	41.007443
N	6
Variance	113.9522
Skewness	-0.249308
CV	20.445967
Median	53.315

rd

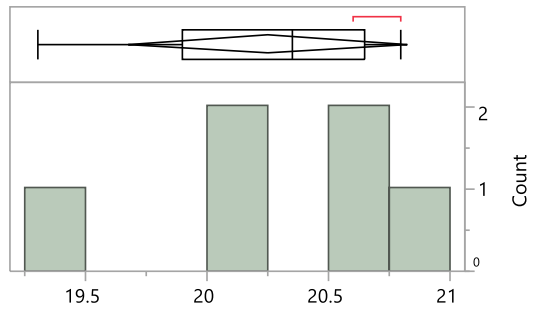

Quantiles		
100.0%	maximum	20.8
99.5%		20.8
97.5%		20.8
90.0%		20.8
75.0%	quartile	20.65
50.0%	median	20.35
25.0%	quartile	19.9
10.0%		19.3
2.5%		19.3
0.5%		19.3
0.0%	minimum	19.3

Summary Statistics	
Mean	20.25
Std Dev	0.5468089
Std Err Mean	0.2232338
Upper 95% Mean	20.823841
Lower 95% Mean	19.676159
N	6
Variance	0.299
Skewness	-1.122964
CV	2.700291
Median	20.35

DCPI_base

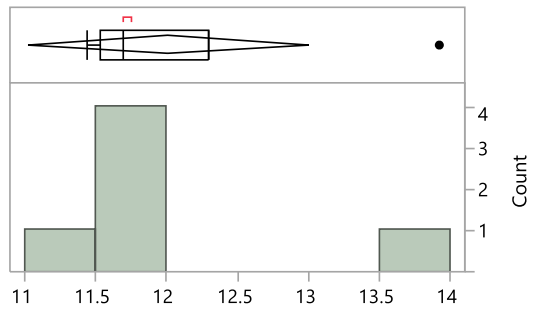

Quantiles		
100.0%	maximum	13.93
99.5%		13.93
97.5%		13.93
90.0%		13.93
75.0%	quartile	12.295
50.0%	median	11.69
25.0%	quartile	11.53
10.0%		11.44
2.5%		11.44
0.5%		11.44
0.0%	minimum	11.44

Summary Statistics	
Mean	12.01
Std Dev	0.9472275
Std Err Mean	0.386704
Upper 95% Mean	13.004054
Lower 95% Mean	11.015946
N	6
Variance	0.89724
Skewness	2.3715262
CV	7.8869903
Median	11.69

Figure C.13. Univariate statistics summary of in-situ properties for NC Hwy-218 TS3a (JMP)

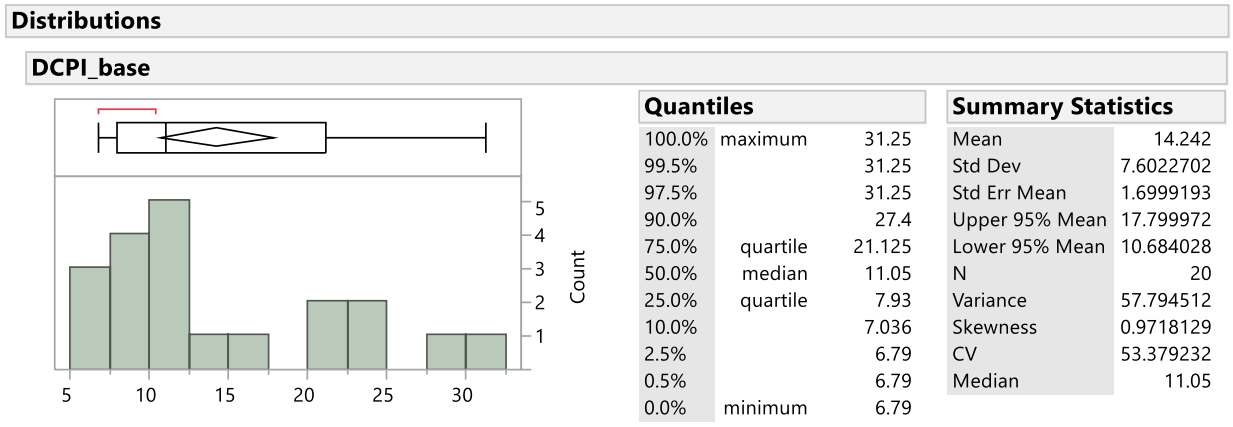

Quantiles		
100.0%	maximum	31.25
99.5%		31.25
97.5%		31.25
90.0%		27.4
75.0%	quartile	21.125
50.0%	median	11.05
25.0%	quartile	7.93
10.0%		7.036
2.5%		6.79
0.5%		6.79
0.0%	minimum	6.79

Summary Statistics	
Mean	14.242
Std Dev	7.6022702
Std Err Mean	1.6999193
Upper 95% Mean	17.799972
Lower 95% Mean	10.684028
N	20
Variance	57.794512
Skewness	0.9718129
CV	53.379232
Median	11.05

Figure C.14. Univariate statistics summary of in-situ properties for NC Hwy-218 TS3b (JMP)

C.4. WI US-10

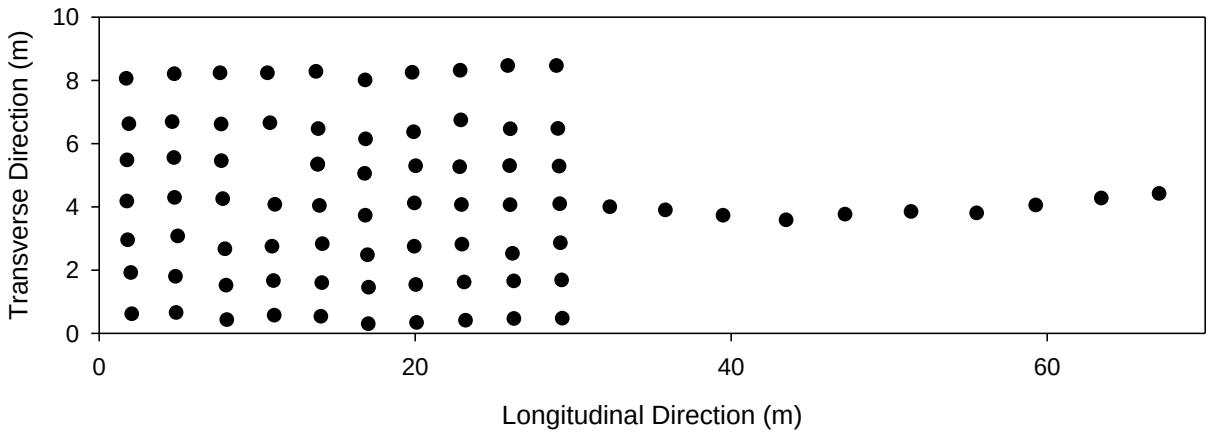

Figure C.15. Test plan for WI US-10 TS2

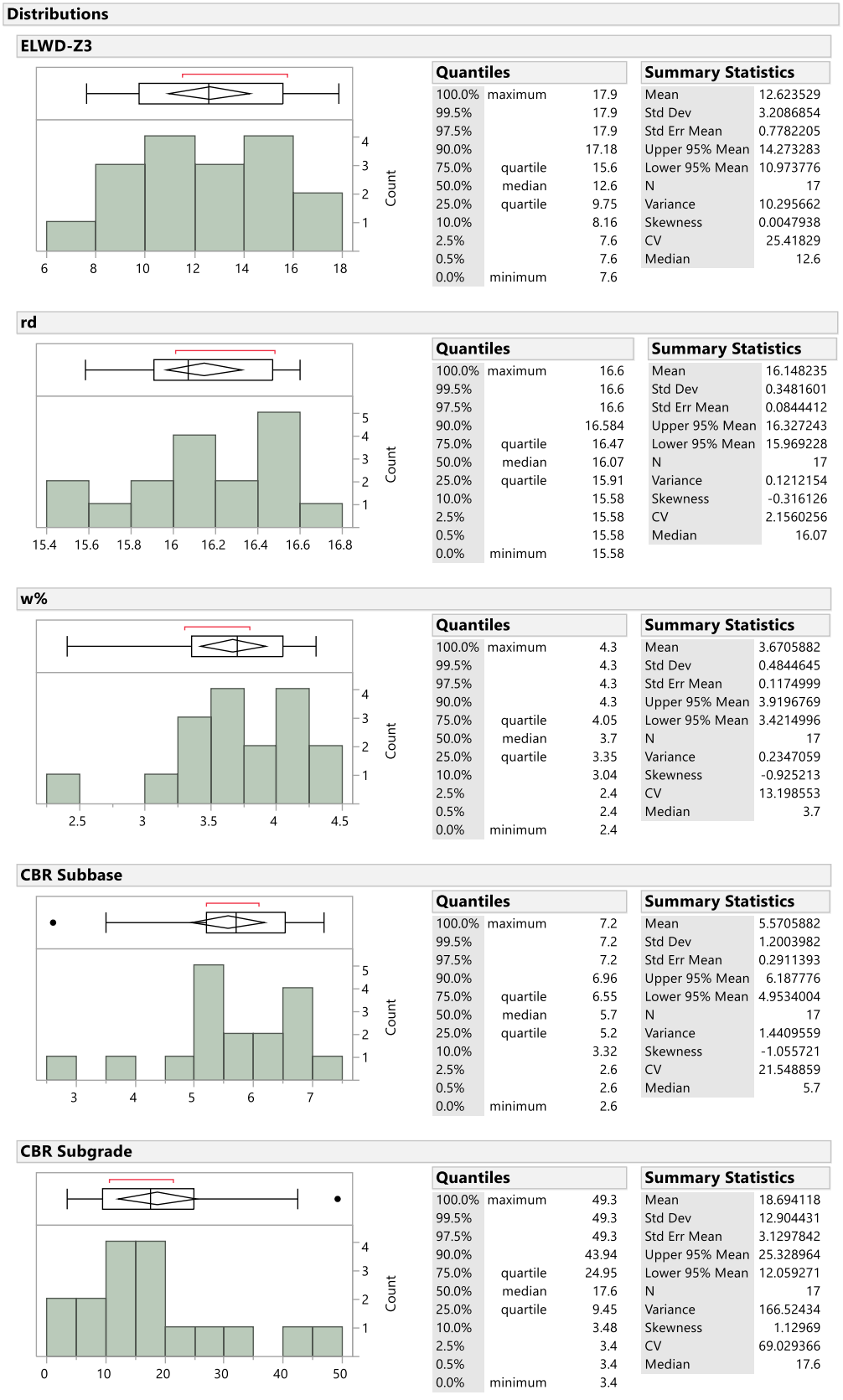

Figure C.16. Univariate statistics summary of in-situ properties for WI US-10 TS1 (JMP)

Distributions

ELWD-Z3

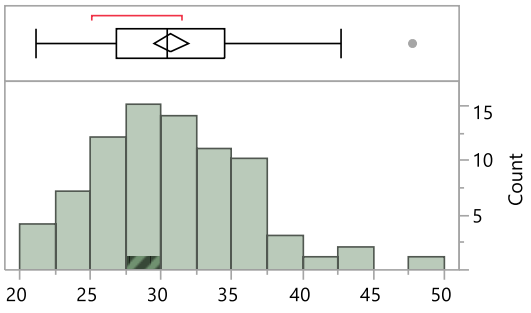

Quantiles		
100.0%	maximum	47.8
99.5%		47.8
97.5%		42.7
90.0%		37.13
75.0%	quartile	34.45
50.0%	median	30.4
25.0%	quartile	26.8
10.0%		24.5
2.5%		21.8
0.5%		21.1
0.0%	minimum	21.1

Summary Statistics	
Mean	30.695
Std Dev	5.3171778
Std Err Mean	0.5944786
Upper 95% Mean	31.87828
Lower 95% Mean	29.51172
N	80
Variance	28.27238
Skewness	0.6233142
CV	17.322619
Median	30.4

rd

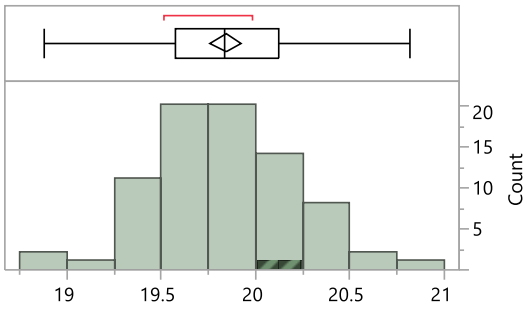

Quantiles		
100.0%	maximum	20.82
99.5%		20.82
97.5%		20.63
90.0%		20.39
75.0%	quartile	20.12
50.0%	median	19.84
25.0%	quartile	19.57
10.0%		19.39
2.5%		18.96
0.5%		18.88
0.0%	minimum	18.88

Summary Statistics	
Mean	19.840886
Std Dev	0.3827806
Std Err Mean	0.0430662
Upper 95% Mean	19.926624
Lower 95% Mean	19.755148
N	79
Variance	0.146521
Skewness	0.0635443
CV	1.9292516
Median	19.84

w%

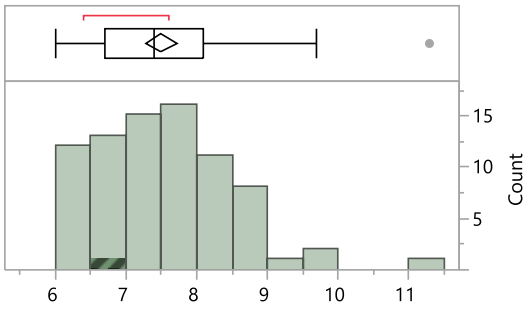

Quantiles		
100.0%	maximum	11.3
99.5%		11.3
97.5%		9.7
90.0%		8.7
75.0%	quartile	8.1
50.0%	median	7.4
25.0%	quartile	6.7
10.0%		6.3
2.5%		6.1
0.5%		6
0.0%	minimum	6

Summary Statistics	
Mean	7.4936709
Std Dev	0.9664025
Std Err Mean	0.1087288
Upper 95% Mean	7.7101333
Lower 95% Mean	7.2772085
N	79
Variance	0.9339338
Skewness	1.0101882
CV	12.89625
Median	7.4

CBR Subgrade

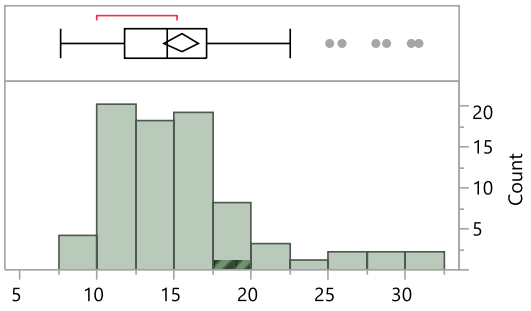

Quantiles		
100.0%	maximum	30.9
99.5%		30.9
97.5%		30.4
90.0%		22.1
75.0%	quartile	17.1
50.0%	median	14.5
25.0%	quartile	11.8
10.0%		10.1
2.5%		7.7
0.5%		7.6
0.0%	minimum	7.6

Summary Statistics	
Mean	15.446835
Std Dev	4.979312
Std Err Mean	0.5602164
Upper 95% Mean	16.562141
Lower 95% Mean	14.33153
N	79
Variance	24.793548
Skewness	1.210612
CV	32.235159
Median	14.5

Figure C.17. Univariate statistics summary of in-situ properties for WI US-10 TS2 (JMP)